

NONLOCAL ANALYSES OF ELECTROSTATIC AND ELECTROMAGNETIC WAVES IN HOT, MAGNETIZED, NONUNIFORM, BOUNDED PLASMAS

THESE No 1000 (1992)

PRESENTEE AU DEPARTEMENT DE PHYSIQUE

ECOLE POLYTECHNIQUE FEDERALE DE LAUSANNE

POUR L'OBTENTION DU GRADE DE DOCTEUR ES SCIENCES

PAR

OLIVIER SAUTER

Ingénieur physicien diplômé EPF
originaire de Vallorbe (VD) et Zurich (ZH)

acceptée sur proposition du jury :

Dr J. Vaclavic, rapporteur
Dr K. Appert, corapporteur
Prof. R. A. Cairns, corapporteur

Lausanne, EPFL
1992

ABSTRACT

Heating of tokamak plasmas up to temperatures of the order of 10 keV ($\approx 10^8$ °K) is one of the main subjects in plasma physics research. Much experimental and theoretical effort has been devoted to the improvement of the heating efficiency and to the understanding of the beam-particle or wave-particle interactions. We have studied the latter subject.

Many models describing the linear wave-particle interaction already exist, allowing one to analyze the absorption of the wave by the electrons and/or the ions. They can be separated into two main classes: ray-tracing models [Brambilla, 1986] and global wave models [Villard et al, 1986]. The latter describe the "global" wave field (sum of incident, transmitted and reflected fields) taking into account the finiteness of the plasma, the boundary conditions, the plasma-vacuum interfaces and the antenna. With this global wave approach, one is able to study scenarii where cut-off, reflected, resonant, mode converted and/or evanescent wave fields are present. Note also that this work is principally devoted to the ion cyclotron range of frequencies.

The most advanced global wave models are the "local" models which use a second-order expansion in $k_{\perp}\rho_{\sigma}$, where k_{\perp} is the perpendicular wavenumber and ρ_{σ} the Larmor radius of species σ [Appert et al, 1986a et 1987; Jaeger et al, 1988; Fukuyama et al, 1986; Edery and Picq, 1986; Brambilla and Krücken, 1988b]. In this way, one obtains a system of three second-order differential equations [Martin and Vaclavik, 1987]. However, the local models are limited to Larmor radii small compared with the wavelength or with the characteristic length of the inhomogeneous density and temperature profiles. Moreover, they are limited to frequencies lower than the third harmonic of the cyclotron frequency.

In present day experiments, the temperature of the particles is very high, especially if tails of high energy particles are created. Also, the first experiments with D-T plasmas, generating alpha particles having a temperature of the order of 1 MeV, have been performed in JET. Moreover,

increasing numbers of experiments use heating scenarii at high harmonic frequencies. Because these cases can no longer be studied using a local model, we have developed a "nonlocal" model which is not limited by the size of the Larmor radii nor by the harmonic considered. This model is based on the global wave approach and therefore can treat the variety of problems mentioned above. Nevertheless, we have limited our work to uni-dimensional geometry, Maxwellian equilibrium distribution functions and slowly-varying equilibrium magnetic field. We have also neglected k_y in the conductivity tensor, where y is the direction normal to the direction of the inhomogeneity and to the magnetostatic field.

Starting from the linearized Vlasov-Maxwell equations, we have derived the equations in the Fourier and the configuration spaces (Chaps.3 and 4), which consist, in the latter case, of a system of three second-order integro-differential equations. We have also derived a formulation of the local power absorption allowing us to determine the profile of absorption of the wave by the particles. The equations are solved numerically using the finite element method (Chap.5). We have developed two codes, SEAL and SEMAL, which calculate the wave field in the electrostatic and electromagnetic cases, respectively. These codes have been tested, and SEAL has been used to simulate an experiment which studies the interaction of a Bernstein wave with a cylindrical plasma (Chap.6). SEMAL has mainly been used to study the effects of the alpha particles on ion cyclotron heating. We have shown that the local model was inadequate and have studied in more detail the effect of temperature and the strong influence of the alpha particle concentration (Chap.7). We have also studied the excitation of an ion Bernstein wave through mode conversion at the lower-hybrid frequency in the scrape-off layer (Chap.7).

RESUME

Le chauffage d'un plasma de type tokamak à des températures de l'ordre de 10 keV ($\approx 10^8$ °K) est un des principaux sujets de recherches en physique des plasmas. Beaucoup d'efforts, tant expérimentaux que théoriques, ont été consacrés à améliorer les performances de chauffage des plasmas et la compréhension des mécanismes d'interactions faisceau-particules ou onde-particules. Ce sont ces dernières que nous avons voulu étudier.

De nombreux modèles existent permettant de simuler plus particulièrement l'interaction linéaire onde-particules et d'analyser l'absorption de l'onde par les électrons et/ou les ions. Ils peuvent être séparés en deux catégories: les méthodes de "tracé des rayons" (Ray-tracing) [Brambilla, 1986] et les méthodes "globales" [Villard et al, 1986]. Celles-ci déterminent le champ d'onde "global" (somme des ondes incidentes, transmises et réfléchies) en tenant compte de la dimension finie du plasma, des conditions aux bords, des interfaces plasma-vide et de l'antenne. Elles permettent d'étudier des réflexions, des coupures, des résonances, des conversions de mode et des régions où l'onde est évanescence. Notons encore que nous nous sommes intéressés plus particulièrement au domaine de fréquences ioniques cyclotroniques.

Les méthodes globales les plus développées à l'heure actuelle sont les modèles "locaux" qui utilisent un développement de Taylor du deuxième ordre en $k_{\perp}\rho_{\sigma}$, où k_{\perp} est le nombre d'onde perpendiculaire au champ magnétique statique et ρ_{σ} le rayon de Larmor des particules σ [Appert et al, 1986a et 1987; Jaeger et al, 1988; Fukuyama et al, 1986; Ederly et Picq, 1986; Brambilla et Krücken, 1988b]. Grâce à cette approximation, on peut obtenir un système d'équations différentielles pour le champ électrique [Martin et Vaclavik, 1987]. Néanmoins, ces modèles sont limités à des rayons de Larmor petits par rapport aux longueurs d'onde ou à la longueur caractéristique de l'inhomogénéité des profils de densité et de températures. De plus, ils sont aussi limités à des fréquences inférieures à la troisième harmonique de la fréquence cyclotronique.

Dans les expériences actuelles, la température des particules est très élevée, surtout s'il y a création de queue de particules de très haute énergie. D'autre part, les premières expériences avec du deutérium et du tritium, générant des particules alphas de l'ordre du MeV, ont eu lieu à JET. Enfin, les scénarios d'excitation des ondes utilisés dans les expériences considèrent de plus en plus les harmoniques supérieures à deux, grâce aussi au développement de sources à très hautes fréquences permettant l'accès au tokamak à l'aide d'un guide d'onde (gyrotrons). Tous ces nouveaux scénarios ne peuvent plus être étudiés avec un modèle local, c'est pourquoi nous avons développé un modèle "nonlocal" qui n'est plus limité par la taille finie du rayon de Larmor ni par l'harmonique considérée, tout en conservant les avantages de l'approche "globale" décrite ci-dessus. Nous nous sommes restreints, toutefois, à la géométrie unidimensionnelle, aux fonctions de distribution Maxwelliennes de l'équilibre et à des champs magnétiques statiques peu non-uniformes, et nous avons négligé k_y dans le calcul du courant perturbé (la direction y est normale à la direction de l'inhomogénéité et du champ magnétostatique).

En partant des équations de Vlasov-Maxwell linéarisées, nous avons dérivé les équations dans l'espace de Fourier et dans l'espace réel (Chaps. 3 et 4), dans lequel elles consistent en un système d'équations intégral-différentielles du deuxième ordre. Nous avons également dérivé une formulation de l'absorption de puissance locale permettant de déterminer le profil d'absorption de l'onde par les particules. Les équations sont résolues numériquement à l'aide de la méthode des éléments finis (Chap.5). Nous avons réalisé deux programmes, SEAL et SEMAL, qui calculent le champ d'onde dans les cas électrostatique et électromagnétique, respectivement. Ces programmes ont été testés, puis SEAL a été utilisé pour simuler une expérience étudiant l'interaction d'une onde Bernstein avec un plasma cylindrique (Chap.6). SEMAL a principalement été utilisé pour étudier l'effet des particules alphas sur le chauffage cyclotronique ionique. Nous avons montré que le modèle local était inadéquat, puis étudié plus spécifiquement l'effet de la température et l'influence considérable de la concentration des particules alpha (Chap.7). Nous avons également étudié l'excitation d'une onde Bernstein ionique à travers la conversion de mode à la fréquence hybride inférieure (Chap. 7).

TABLE OF CONTENTS

ABSTRACT	i
RESUME	iii
ACKNOWLEDGMENTS	ix
1. INTRODUCTION	1
1.1 State of research	1
1.2 Goals of the project	3
1.3 Outline of the work	4
2. FORMULATION OF THE PHYSICAL PROBLEM	7
2.1 Basic equations	7
2.2 Outline of the different models	11
2.2.1 Dispersion relation, ray-tracing model	11
2.2.2 Global wave method, local model	14
2.2.3 Global wave method, nonlocal model	18
2.3 Power absorption, basic formulae	20
3. ELECTROSTATIC APPROXIMATION	23
3.1 Equation in Fourier space	23
3.1.1 The linearized Vlasov-Poisson equations	23
3.1.2 Dispersion relation	27
3.2 Equation in configuration space	28
3.3 Local power absorption formula	32
4. ELECTROMAGNETIC PROBLEM	37
4.1 Equations in Fourier space	37
4.1.1 The linearized Vlasov-Maxwell equations	37
4.1.2 Dispersion relation	45
4.2 Equation for the electric field in configuration space	46
4.3 Local power absorption formula	49
4.4 Extension to $k_y \neq 0$	51

5.	NUMERICAL METHOD	55
5.1	Finite element method	55
5.1.1	Mathematical basis and general comments	55
5.1.2	Application to the integro-differential equation	59
5.1.3	Pollution problems	60
5.2	Boundary conditions	66
5.2.1	Plasma-vacuum-antenna-wall interfaces	67
5.2.2	Plasma-waveguide interface	70
5.3	Numerical integration of the kernel	72
5.4	Local power absorption	77
6.	RESULTS OBTAINED WITH SEAL	83
6.1	Benchmarks	83
6.1.1	Convergence study	83
6.1.2	Discussion on guiding center profiles and integration limits	85
6.1.3	Comparison of the solution with the local dispersion relation	87
6.2	Comparison with experiment	90
7.	RESULTS OBTAINED WITH SEMAL	93
7.1	Benchmarks	93
7.1.1	Convergence study	93
7.1.2	Comparison with ISMENE	95
7.2	Effects of alpha particles on ICRF heating	97
7.2.1	Limitations of the local model	98
7.2.2	Influence of T_α and modelling of non-Maxwellian distribution functions	100
7.2.3	Effects of k_z and alpha particle concentration	103
7.2.4	Summary of the results on the effects of alpha particles on ICRF heating	105
7.3	IBW launching through mode conversion at the lower-hybrid layer	106

8. CONCLUSION	109
Appendix A: Main structures of SEMAL and SEAL	A.1
Appendix B: Kernel contribution to matrix	B.1
Appendix C: Dispersion relation code DISPAL	C.1
Appendix D: Solution of the linearized Vlasov equation using the method of the characteristics	D.1
Appendix E: Discretized dispersion relation	E.1
REFERENCES	R.1
FIGURES	
CURRICULUM VITAE	

ACKNOWLEDGMENTS

This work has been very interesting and it is in great part thanks to Drs. J. Vaclavik and K. Appert, leaders of the RF group in CRPP. I am particularly grateful to Dr. J. Vaclavik, with whom it is very pleasant to work and stimulating to discuss. He has a great knowledge in physics theory and is always willing to share his experience.

I am thankful to Dr. K. Appert who is also always available for discussion and I have greatly benefited from his experience in computing. I have appreciated the enthusiastic spirit he brings to the group. I have also appreciated the very useful discussions I have had with Prof. F. Skiff.

I would like to thank the CRPP managing staff, who have facilitated my work in the institute and gave me the opportunity to attend international conferences. I offer my thanks also to the secretaries, P. Halter, E. Grüter and R. Vincent, for all what they do "behind the scenes".

It was a great pleasure to work at the CRPP during these six years and this is due to the good relationship which exists between colleagues and the possibility to meet one another outside workhours, for example for football or basketball games, ski championships or hiking. I have especially enjoyed the friendship existing at the "baraque". I also thank Dr. A. Howling who accepted to read this (long) manuscript and correct the English.

Last but not least, I express all my gratitude to my wife, Josée, and my young children, Yannick and Damien, who supported a husband and father quite often "in the clouds" and tired, particularly during the last two months.

1. INTRODUCTION

1.1 State of research

Plasma research, oriented towards fusion reactors, is traditionally concerned with three quantities: density (n), temperature (T) and energy confinement time (τ). These parameters enter the Lawson's criterion which stipulates that, at $T=10$ keV, the condition $n\tau > 10^{20} \text{ sm}^{-3}$ should be satisfied, in a D-T plasma, in order to reach breakeven. This explains what are the main goals in reaching controlled fusion: maintaining a dense plasma as long as possible ($\tau \approx 1\text{s}$) at a very high temperature ($T_i, T_e \approx 10\text{keV}$). The first condition implies stability and confinement analyses, and the second, heating improvement. The present work is a contribution to the latter, and in particular to the theory of plasma heating using high frequency waves. Other heating methods can be used, like beams (neutral, ion, electron), compression or continuous current (ohmic heating), but they will not be considered in this work. We shall also concentrate on tokamak-like plasmas and on frequencies in the ion cyclotron range of frequencies (ICRF), even though our model is not restricted to toroidal confined plasmas or to this frequency range.

A lot of theoretical work has been done during the last thirty years: first to determine which kinds of waves may exist in a plasma, then to understand their damping mechanisms, and finally to quantify the heating efficiency of a particular scenario. For solving the last problem, one needs to analyse the wave-particle interactions, which are very complex in a tokamak geometry. Different models are being used which simplify either the physics mechanism or the geometry, but anyway both to some extent. In general, most of the models consider a steady oscillatory solution proportional to $e^{-i\omega t}$, where ω is

the antenna frequency, and describe the linear interaction in at most a 2-D toroidal geometry.

The most general equations which describe the wave-particle interactions are the Boltzmann equation, or, if collisions are neglected as in most cases, the Vlasov equation, combined with the Maxwell equations. These equations should be solved in a 3-D toroidal geometry using adequate boundary conditions taking into account the plasma vacuum interface, the antenna and the wall. In heating studies so far, the inhomogeneity parallel to the magnetostatic field has not yet been considered extensively [Itoh S.-I. et al, 1985; Brambilla and Ottaviani, 1985; Smithe et al, 1988; Batchelor et al, 1989b], first because it leads to solving an integral equation, and secondly because its effect seems to be less important than the perpendicular inhomogeneity. In 1-D and 2-D geometries, two main classes of models address this problem: ray-tracing and global wave models. The first one, described in Sec.2.2.1, follows ray trajectories and calculates the power deposited by the wave along the ray. It is a very simple model which can be used in complicated geometry, but it cannot treat correctly resonances, cut-offs, mode conversion, and global modes. The second one, described in Sec.2.2.2, does not suffer from these limitations, as it solves the differential equations in the whole plasma together with the boundary conditions. However, it is limited by the complexity of the equations and the number of discretization points needed for an accurate solution. It is also limited to second harmonic scenarii and Larmor radii small compared with the wavelength.

The most developed global wave models solve the Vlasov-Maxwell equations using a second-order expansion in $k_{\perp}\rho_{\sigma}$, where k_{\perp} is the perpendicular wavenumber and ρ_{σ} the Larmor radius of species σ , for calculating the perturbed current. These models consider either 1-D geometry

[Appert et al, 1987; Jaeger et al, 1988; Skiff et al, 1985] with the complete resulting sixth order ordinary differential equations including gradients of equilibrium parameters [Martin and Vaclavik, 1987], or 2-D geometry with simplified equations [Fukuyama et al, 1986; Edery and Picq, 1986; Brambilla and Krücken, 1988b]. Due to the expansion, these models are limited to $(k_{\perp}\rho_{\sigma})^2 \ll 1$ and to second-harmonic heating. Fig.1.1 shows a typical dispersion relation in the ion cyclotron range of frequencies (ICRF). The hatched region I corresponds to the domain which can be studied using the local models. Swanson [1981] and others [Colestock and Kashuba, 1983; Chiu and Mau, 1983; Fukuyama et al, 1983; Romero and Scharer, 1987] have derived the fourth order differential equations valid up to second order with respect to $k_{\perp}\rho_{\sigma}$. One can still mention, for the interested reader, the works by Stix [1975] and Perkins [1977] and the review paper on low frequency heating by Vaclavik and Appert [1991].

The ray-tracing models [McVey, 1979; Koch et al, 1986; Brambilla, 1986, and references therein] have been extended in the last years to arbitrary Larmor radii [Koch et al, 1989] and are valid in the whole domain II, Fig.1.1, except for many horizontal regions (not shown in the picture) when the wavelength changes too rapidly, or when there are no propagatory solutions, and in all the other cases mentioned above. But these are the most interesting cases to study and, in tokamak experiments, always exist in some parts of the plasma [Bathnagar et al, 1984]. Therefore we shall not use this kind of model.

1.2 Goals of the project

The aim of this work is to use a global wave model and extend its validity to the whole region II in Fig.1.1, without restrictions with respect to $k_{\perp}\rho_{\sigma}$ or the

harmonic number considered. This will allow us to study important questions such as the effects of alpha particles on ICRF heating, propagation and absorption of Bernstein waves, which can be directly launched into the plasma [Ono et al, 1988; Moody et al, 1988] or result from mode conversion at the lower-hybrid layer [Ono et al, 1983; Chiu et al, 1990], and higher harmonic heating, which are all scenarii used more and more in heating experiments.

Of course, the new equations are more complicated. They consist of a system of second-order integro-differential equations, which is very time-consuming to solve. This is why we have limited this work to 1-D slab geometry. Moreover, as we did not know if the problem could be solved with present-day computers, we first considered the electrostatic approximation. After having well understood this case, we have solved the full electromagnetic (E.M.) problem.

1.3 Outline of the work

We shall first present, in Chapter 2, the general physical problem with the basic equations (Sec. 2.1) and then briefly explain the different models which can be used to solve these equations (Sec.2.2). We shall also introduce the general formula for calculating the local power absorption.

In the following Chapters, except for Chapter 5, we shall always separate the electrostatic and the E.M. cases, giving more details for the first one, as it is simpler and thus easier to understand. In Chapters 3 and 4, we shall derive the equations for the electrostatic potential or the electric field in Fourier space (Sec. 3.1/4.1) and in configuration space (3.2/4.2), and for the local power absorption formula (3.3/4.3) for the electrostatic and E.M. cases respectively. In

Chapter 5, we present the numerical problems, first explaining the finite element method (Sec. 5.1) and then the boundary conditions (5.2). We detail the computations, and associated problems, of the kernel contribution in Sec. 5.3 and of the power absorption formula in Sec. 5.4.

The results obtained with the electrostatic code, SEAL, are presented in Chapter 6 and with the E.M. code, SEMAL, in Chapter 7. Finally we summarize the main results and propose some extensions of this work in Chapter 8. Note also that the main structures of SEAL and SEMAL are given in Appendix A, and that a presentation of the full hot dispersion relation code, DISPAL, is given in Appendix C.

This thesis has been written in more detail than usual for a scientific paper, and only "non specialists" (or students) in RF heating modelling need to read through the whole paper in order to understand this new model and the results obtained. However, the specialists can concentrate on Secs. 2.2.3, 2.3 and Chapters 4 and 5 concerning the theory (the electrostatic case, Chapter 3, can be seen as a particular case of the E.M. problem). The main results have been published in Sauter et al [1990a] for the electrostatic approximation case (Sec. 6.2), in Sauter and Vaclavik [1990b] for the first results of the E.M. code (7.1) and reported in Sauter and Vaclavik [1991] for the analysis of the effects of alpha particles on ICRF heating (7.2). The only results not yet published are presented in Sec. 7.3, considering the coupling of ion Bernstein waves (IBW) near the "cold lower-hybrid resonance" in the scrape-off layer.

2. FORMULATION OF THE PHYSICAL PROBLEM

2.1 Basic equations

The basic equation for the description of the wave-particle interactions in a hot plasma, using kinetic theory, is the Vlasov equation which determines the evolution of the distribution function $f_{\sigma}(\mathbf{x}, \mathbf{v}, t)$ of the particles due to a force \mathbf{F} applied to them while neglecting the effect of collisions. In the case of a plasma with no other forces than the Lorentz force, the Vlasov equation reads:

$$\left(\frac{\partial}{\partial t} + \mathbf{v} \cdot \nabla \right) f_{\sigma}(\mathbf{r}, \mathbf{v}, t) + \frac{q_{\sigma}}{m_{\sigma}} (\mathbf{E} + \mathbf{v} \times \mathbf{B}) \cdot \frac{\partial}{\partial \mathbf{v}} f_{\sigma} = 0 . \quad (2.1)$$

Closure equations are given by the Maxwell equations:

$$\nabla \times \mathbf{E} = - \frac{\partial \mathbf{B}}{\partial t} , \quad (2.2a)$$

$$\nabla \times \mathbf{B} = \mu_0 \mathbf{j} + \frac{1}{c^2} \frac{\partial \mathbf{E}}{\partial t} , \quad (2.2b)$$

$$\nabla \cdot \mathbf{E} = \frac{\rho}{\epsilon_0} , \quad (2.2c)$$

$$\nabla \cdot \mathbf{B} = 0 , \quad (2.2d)$$

where the current and charge densities are obtained in terms of the distribution function:

$$\mathbf{j} = \sum_{\sigma} q_{\sigma} \int \mathbf{v} f_{\sigma}(\mathbf{r}, \mathbf{v}, t) d^3 \mathbf{v} , \quad (2.3)$$

$$\rho = \sum_{\sigma} \rho_{\sigma} = \sum_{\sigma} q_{\sigma} \int f_{\sigma}(\mathbf{r}, \mathbf{v}, t) d^3 \mathbf{v} \equiv \sum_{\sigma} q_{\sigma} n_{\sigma}(\mathbf{r}, t). \quad (2.4)$$

The last identity determines the normalization of the distribution function. Together with adequate boundary conditions, the equations are closed and self-consistent. For the electrostatic approximation, one uses Eqs.(2.1), (2.2c) and (2.4), and for the E.M. case, Eqs.(2.1), (2.2a), (2.2b) and (2.3). Note that Eq.(2.1) is very complicated as it gives the time evolution of f_{σ} in the 6-D phase-space (\mathbf{r}, \mathbf{v}) and is nonlinear. However, what we seek is the time-asymptotic response of the plasma to a forced oscillatory perturbation. Moreover we assume that the perturbation is small as compared with the magnitude of equilibrium quantities, that is:

$$\begin{aligned} f_{\sigma} &= f_{\sigma}^{(0)} + f_{\sigma}^{(1)} \quad , \quad \text{with} \quad |f_{\sigma}^{(1)}| \ll |f_{\sigma}^{(0)}| \quad , \\ \mathbf{E} &= \mathbf{E}^{(1)} \quad , \\ \mathbf{B} &= \mathbf{B}_0 + \mathbf{B}^{(1)} \quad , \quad \text{with} \quad |\mathbf{B}^{(1)}| \ll |\mathbf{B}_0| \quad , \\ \mathbf{j} &= \mathbf{j}^{(1)} \quad , \\ \rho &= \rho^{(1)} \quad . \end{aligned} \quad (2.5)$$

Note that we have assumed that there are neither equilibrium electric fields nor current density. Using Eq.(2.5) we can linearize the above equations, which yields:

$$\mathbf{v} \cdot \nabla f_{\sigma}^{(0)} + \frac{q_{\sigma}}{m_{\sigma}} \mathbf{v} \times \mathbf{B}_0 \cdot \frac{\partial}{\partial \mathbf{v}} f_{\sigma}^{(0)} = 0 \quad , \quad (2.6a)$$

$$\left(\frac{\partial}{\partial t} + \mathbf{v} \cdot \nabla \right) f_{\sigma}^{(1)} + \frac{q_{\sigma}}{m_{\sigma}} \mathbf{v} \wedge \mathbf{B}_0 \cdot \frac{\partial}{\partial \mathbf{v}} f_{\sigma}^{(1)} = - \frac{q_{\sigma}}{m_{\sigma}} (\mathbf{E}^{(1)} + \mathbf{v} \wedge \mathbf{B}^{(1)}) \cdot \frac{\partial}{\partial \mathbf{v}} f_{\sigma}^{(0)} \quad , \quad (2.6b)$$

$$\nabla \times \mathbf{E}^{(1)} = -\frac{\partial \mathbf{B}^{(1)}}{\partial t} \quad , \quad (2.6c)$$

$$\nabla \times \mathbf{B}^{(1)} = \mu_0 \mathbf{j}^{(1)} + \frac{1}{c^2} \frac{\partial \mathbf{E}^{(1)}}{\partial t} \quad , \quad (2.6d)$$

$$\nabla \cdot \mathbf{E}^{(1)} = \frac{\rho^{(1)}}{\epsilon_0} \quad , \quad (2.6e)$$

$$\mathbf{j}^{(1)} = \sum_{\sigma} q_{\sigma} \int \mathbf{v} f_{\sigma}^{(1)}(\mathbf{r}, \mathbf{v}, t) d^3 \mathbf{v} \quad , \quad (2.6f)$$

$$\rho^{(1)} = \sum_{\sigma} q_{\sigma} \int f_{\sigma}^{(1)}(\mathbf{r}, \mathbf{v}, t) d^3 \mathbf{v} \quad . \quad (2.6g)$$

These are the equations which determine the self-consistent linear response of the particles due to a small external perturbation. We seek oscillatory solutions due to this perturbation proportional to $e^{i(k_{//}z - \omega t)}$, where $k_{//}$, determined by the antenna, is the wavenumber parallel to the equilibrium magnetic field \mathbf{B}_0 , and ω is the frequency of the antenna current. In order to respect causality, ω is assumed to have a small positive imaginary part. We always choose \mathbf{B}_0 parallel to the z-axis, which is why we use either $k_{//}$ or k_z for the wavenumber parallel to \mathbf{B}_0 .

Assuming a uniform magnetic field, the general form of the solution of Eq.(2.6a) is given by:

$$f_{\sigma}^{(0)}(\mathbf{r}, \mathbf{v}) = f_{\sigma}^{(0)}\left(X = x + \frac{v_y}{\omega_{c\sigma}}, Y = y - \frac{v_x}{\omega_{c\sigma}}, v_{\perp}, v_{//}\right) \quad . \quad (2.7)$$

The solution of Eq.(2.6b) can be derived in different ways, as will be described in Secs. 3.1 and 4.1. One obtains in general the Fourier transform of $f_{\sigma}^{(1)}$, which can be written in the following general form:

$$f_{\sigma}^{(1)}(\mathbf{k}, \mathbf{v}, \omega) = \int d\mathbf{k}'_{\perp} \mathbf{A}(\mathbf{k}'_{\perp}, k_{\parallel}, \mathbf{v}, \omega) \cdot \mathbf{E}(\mathbf{k}'_{\perp}, k_{\parallel}, \mathbf{v}, \omega) f_{\sigma}^{(0)}(\mathbf{k}_{\perp} - \mathbf{k}'_{\perp}, \mathbf{v}). \quad (2.8)$$

This solution is then introduced into the Fourier transform of Eq.(2.6f) which gives, together with Eqs.(2.6c) and (2.6d), the general form of the integral equations for the electric field in \mathbf{k} space:

$$\frac{c^2}{\omega^2} \mathbf{k} \wedge \mathbf{k} \wedge \mathbf{E}(\mathbf{k}) + (\underline{\underline{\epsilon}} \mathbf{E})(\mathbf{k}) = 0, \quad (2.9a)$$

$$(\underline{\underline{\epsilon}} \mathbf{E})(\mathbf{k}) = \mathbf{E}(\mathbf{k}) + \frac{i}{\epsilon_0 \omega} \int d\mathbf{k}' \underline{\underline{\sigma}}(\mathbf{k}, \mathbf{k}') \mathbf{E}(\mathbf{k}'). \quad (2.9b)$$

In order to obtain an explicit form of $\sigma(\mathbf{k}, \mathbf{k}')$, one has to specify $f_{\sigma}^{(0)}(\mathbf{r}, \mathbf{v})$, introduce it into Eq.(2.8) and integrate $\mathbf{v} f_{\sigma}^{(1)}$ over velocity. This is described in detail in Secs. 3.1 and 4.1 for the electrostatic and E.M. cases, respectively. At this point, it is sufficient to note that, assuming a Maxwellian equilibrium distribution function, the main \mathbf{k}, \mathbf{k}' dependence of $\underline{\underline{\sigma}}$ is involved in the modified Bessel function of order n , which is the harmonic number:

$$I_n(k_{\perp} k'_{\perp} \rho_{\sigma}^2),$$

where $\rho_{\sigma}^2 = v_{T\sigma}^2 / (2\omega_{c\sigma}^2)$, $v_{T\sigma}^2 = 2T_{\sigma}/m_{\sigma}$, $\omega_{c\sigma} = q_{\sigma}B_0/m_{\sigma}$ are the Larmor radius squared, thermal velocity squared and cyclotron frequency of species σ , respectively.

To describe the coupling between an antenna and the plasma, one needs to solve the equations in configuration space. Up to now there has been two ways for deriving equations for the electric field in \mathbf{x} space and then solving them:

ray-tracing and global wave models. These models will be briefly presented in the next two subsections and the new model developed in this thesis in Sec.2.2.3.

2.2 Outline of the different models

2.2.1 Dispersion relation, ray-tracing model

The leading idea of ray-tracing models is based on geometrical optics considerations. One assumes that the local background plasma parameters do not change much over one wavelength. Therefore one can consider the plasma as made up of multiple adjacent homogeneous plasma layers, in which one can easily solve for the electric field using the local values of the plasma parameters.

Note that for an infinite homogeneous plasma, Eq.(2.9) reduces to :

$$\underline{\underline{D}} \mathbf{E} = \left(\frac{c^2}{\omega^2} \mathbf{k} \wedge \mathbf{k} \wedge + \underline{\underline{\epsilon}} \right) \mathbf{E} = \left[-\frac{\mathbf{k}^2 c^2}{\omega^2} \left(\underline{\underline{I}} - \frac{\mathbf{k} \cdot \mathbf{k}}{k^2} \right) + \underline{\underline{\epsilon}} \right] \mathbf{E}, \quad (2.10a)$$

with

$$\underline{\underline{\epsilon}} = \left(\underline{\underline{I}} + \frac{i}{\epsilon_0 \omega} \underline{\underline{\sigma}} \right) \mathbf{E}.$$

In this case, we have a non-trivial solution if:

$$\det \underline{\underline{D}}(\omega, \mathbf{k}_\perp, k_\parallel) = 0, \quad (2.10b)$$

which defines the general dispersion relation. In other words, the solution of

Eq.(2.9) in the case of an infinite homogeneous plasma is a plane wave of the form $\mathbf{E}(\mathbf{x},t) = \mathbf{E}_0 e^{i(\mathbf{k}\mathbf{x}-\omega t)}$, with \mathbf{k} and ω satisfying Eq (2.10b) for the given plasma parameters. If we assume that the plasma parameters are slowly varying compared with the wavelength of the perturbation, than one can seek a solution of the form:

$$\mathbf{E}(\mathbf{x}, t) = \mathbf{E}_0(\mathbf{x}) e^{i(S(\mathbf{x})-\omega t)}, \quad (2.11)$$

where \mathbf{E}_0 is the slowly varying amplitude and S is the rapidly varying phase. Following the work of Bernstein [1975] and Brambilla [1986], we can briefly show the main features of ray-tracing models, assuming small dissipation. First, one assumes $S \sim 1/\delta$ and $\nabla \sim \delta$, where δ is a small quantity. Then Eq.(2.11) is inserted into Eq.(2.9) which is solved order by order. The lowest order equation yields the dispersion relation, Eq.(2.10), with $\mathbf{k}=\nabla S(\mathbf{x})$. This is not astonishing, as the lowest order corresponds to assuming an infinite homogeneous plasma with the plasma parameters equal to those at position \mathbf{x} . If the anti-Hermitian part of $\underline{\underline{D}}$, $\underline{\underline{D}}^A$, is of the order of δ relative to the Hermitian part $\underline{\underline{D}}^H$ (small dissipation), then Eq.(2.10b) is equivalent to:

$$H(\mathbf{k}, \omega, \mathbf{x}) = \det \underline{\underline{D}}^H(\mathbf{k}, \omega, \mathbf{x}) = 0. \quad (2.12)$$

The ray-tracing equations are obtained by introducing a parametrization τ of \mathbf{k} and \mathbf{x} . One obtains the following ray equations:

$$\begin{aligned} \frac{d\mathbf{x}}{d\tau} &= \frac{\partial H}{\partial \mathbf{k}}, \\ \frac{d\mathbf{k}}{d\tau} &= -\frac{\partial H}{\partial \mathbf{x}}. \end{aligned} \quad (2.13)$$

Note that $d\mathbf{x}/d\tau$ is parallel to the group velocity $\mathbf{v}_g = \partial\omega/\partial\mathbf{k} = -\frac{\partial H}{\partial \mathbf{k}} / \frac{\partial H}{\partial \omega}$. Thus, the direction of the rays is the direction of the group velocity, which may differ from the direction of \mathbf{k} . Given initial conditions for the rays satisfying Eq.(2.12) at some initial wavefront $\mathbf{x}_0=\mathbf{x}(\tau_0)$, for example $S(\mathbf{x}_0)=0$, we obtain the value of S at the wavefront $\mathbf{x}(\tau)$ with:

$$S(\mathbf{x}) = \int_{\tau_0}^{\tau} dt \mathbf{k} \cdot \frac{\partial H}{\partial \mathbf{k}} . \quad (2.14)$$

The equation for the amplitude $\mathbf{E}_0(\mathbf{x})$ is obtained from the next order approximation which can be written as follows [Brambilla, 1986]:

$$\nabla \cdot \mathbf{P} = -2\gamma |\mathbf{E}_0|^2 , \quad (2.15)$$

where

$$\mathbf{P} = \frac{1}{2\mu_0} \text{Re}(\mathbf{E}_0^* \wedge \mathbf{B}_0) - \frac{\omega \epsilon_0}{4} \mathbf{E}_0^* \frac{\partial \underline{\epsilon}^H}{\partial \mathbf{k}} \mathbf{E}_0 , \quad (2.16)$$

and

$$\gamma = \frac{\omega \epsilon_0}{4|\mathbf{E}_0|^2} \mathbf{E}_0^* \underline{\epsilon}^A \mathbf{E}_0 .$$

The solution of Eqs.(2.13-16) together with adequate initial conditions, give the new position of the ray \mathbf{x} , the wavenumber \mathbf{k} , the phase S and the power P . They are solved, in general, using a Runge-Kutta procedure.

The range of validity of ray-tracing models is limited to regions where the

changes of the plasma parameters and amplitude of the electric field are small over one wavelength, as mentioned above. That is, the characteristic length, L , of the inhomogeneity must be much larger than the wavelength λ :

$$\frac{L}{\lambda} \gg 1. \quad (2.17)$$

This condition is not satisfied close to resonances, cut-offs, mode conversion and in evanescent regions. These are, however, the most interesting regions for studying wave-plasma interactions. They are often modelled with simplified equations and coupled to the ray-tracing code. On the other hand, Eqs.(2.13-16) are simple and can therefore be solved in rather complicated geometries. This is why these models have been extensively used [Brambilla, 1986, and references therein]. Another important feature is the fact that it is straightforward to extend ray-tracing models from a cold or warm model to a full hot model, by simply extending the validity of the dispersion relation, Eq.(2.12). This is why these models have been extended to higher harmonic heating without great problems [Koch et al, 1989], apart from the fact that it involves a summation over Bessel functions. We shall see in the next subsections that the extension of global wave models to higher harmonic heating and large Larmor radii is much more complicated and is the purpose of this work.

2.2.2 Global wave method, local model

The idea of the global wave method is to solve the equations for the electric field throughout the plasma, including adequate boundary conditions at the walls and at any existing plasma-vacuum interfaces. Therefore, one does not seek a propagating ray, but the solution of a system of ordinary differential equations in terms of the electric field. The first immediate advantage is that

one can treat evanescent fields as well, if one uses appropriate numerical methods. Moreover, these models are not restricted by the condition (2.17) and thus can correctly describe mode conversion, resonances and cut-offs. Finally, these models are able to describe global modes of the system [Appert et al, 1982], which is also why they are called "global" wave models.

The crucial point of this method is to obtain the equations for the electric field in configuration space, in order to be able to supplement them with the boundary conditions imposed by an antenna, a plasma-vacuum interface, or a conducting shell. Therefore one has to calculate the inverse Fourier transform of Eq.(2.9). However, it is not possible in general to integrate over \mathbf{k}_\perp an integrand of the form:

$$e^{i\mathbf{k}_\perp \cdot \mathbf{x}_\perp} k_\perp^m I_n(k_\perp k'_\perp \rho_\sigma^2) \exp\left[-\frac{1}{2}(k_\perp^2 + k'^2_\perp) \rho_\sigma^2\right], \quad (2.18)$$

which is what appears in $\underline{g}(\mathbf{k}_\perp, \mathbf{k}'_\perp)$ as mentioned in Sec.2.1. One way to resolve this problem is to expand the modified Bessel function $I_n(k_\perp k'_\perp \rho_\sigma^2)$ as well as the exponential term. Thus, it reduces to calculating the inverse integral of a polynomial of k_\perp , and k'_\perp , which gives a series of differential operators. The terms proportional to k'_\perp are transformed back to derivatives of the field, the terms proportional to $k_\perp - k'_\perp$ give derivatives of the equilibrium quantities, and k_\perp produces a differentiation of both. This is why we name these types of global wave models "local" models, because the solution $\mathbf{E}(\mathbf{x})$ depends on the local values and derivatives of \mathbf{E} , n_σ , T_σ , etc.

The simplest model is the well-known cold model [Stix, 1962], which is obtained by assuming zero temperature. In this case, the tensor, Eq.(2.9b), is very simple (no derivatives) and Eq.(2.9) can be solved in the complicated 2-D

toroidal geometry [Itoh et al, 1984; Villard et al, 1986].

The next orders are obtained by expanding I_n to second order, that is neglecting terms $O(k_{\perp}^3 k'_{\perp} \rho_{\sigma}^6)$. Many codes are based on equations obtained using this kind of approximation, either in 1-D, solving the complete sixth order ordinary differential equations including gradients of the equilibrium quantities [Appert et al, 1986a and 1987; Jaeger et al, 1988] or in 2-D, using simplified equations in toroidal geometry [Fukuyama et al, 1986; Edery and Picq, 1986; Brambilla and Krücken, 1988b]. These models are able to describe waves which exist only with finite temperature like the kinetic Alfvén wave [Hasegawa and Chen, 1975; Hasegawa and Uberoi, 1982], or the conversion to the Bernstein wave at the ion-ion hybrid resonance [Appert et al, 1986a].

Note that these models are limited to second harmonic, as they neglect the contribution due to $n \geq 3$, because $I_n(x) \sim O(x^n)$. Therefore the domain of application of the local models in global wave calculations can be sketched as in Fig.1.1 (hatched region I). It is limited by the two conditions:

$$k_{\perp}^2 \rho_{\sigma}^2 \ll 1, \quad (2.19a)$$

and

$$n \leq 2. \quad (2.19b)$$

However, in this domain, it is not restricted by the presence of cut-offs, resonances, conversion layers or evanescent fields, as in ray-tracing models.

In order to extend the region I (Fig.1.1), one could expand the equations to next order in $k_{\perp}^2 \rho_{\sigma}^2$. There are three main reasons for avoiding this method:

1) The dielectric tensor, taking into account terms of the second order in the inhomogeneity of the equilibrium parameters, is already very complicated in a 1-D slab geometry [Martin and Vaclavik, 1987; Jaeger et al, 1988], and even more so in toroidal geometry [Brunner and Vaclavik, 1992]. Therefore, it would not be reasonable to expand the equations to next order.

2) As mentioned before, the expansion gives rise to a new dispersion relation, which is a polynomial approximation of the correct one. For example, second order expansion in the case of a 1-D slab plasma results in a system of three second-order ordinary differential equations (ODE). Thus the dispersion relation consists of a polynomial of third order in k^2 , which has always three roots. However, the correct dispersion relation, Eq.(2.10b), is a transcendental function, that is it has no definite number of roots. There are two modes in the cold plasma. Therefore, in general, there could be one spurious mode in this approximation, which can interfere with the physical modes. However, with a fourth order expansion, there could be four non-physical modes, which could significantly disturb the interpretation of the results.

3) The order of the ODE is modified by the expansion method. Thus the number of boundary conditions needed is modified accordingly. In 1-D slab geometry, the Maxwell equations need four boundary conditions (for example, E_y , E_z at each side). But, as mentioned above, the equations obtained with a second-order expansion are equivalent to a sixth order ODE and need therefore six boundary conditions. That is, two extra conditions have to be determined ad-hoc. This is not yet dramatic, but to next order, one would need eight extra boundary conditions.

Another method has been used to obtain differential equations for the electric field and solve them with the adequate boundary conditions, while avoiding spurious unphysical modes. This is to construct reduced ODE which reproduce the main characteristics of the local dispersion relation [Swanson, 1985; Sy et al, 1985; Cairns and Lashmore-Davies, 1986; Smithe et al, 1987; Lashmore-Davies et al, 1988; Batchelor et al, 1989a; Llobet et al, 1989; Jaeger et al, 1990]. In this way, for example, one is able to model mode conversion with simple equations. However, this method is somewhat in between ray-tracing and global wave models and relies on an a priori knowledge of the main features of the solution. Moreover, the equations have to be modified for studying different cases. Therefore, these models may be useful mainly for analysing some specific parts of region II in Fig.1.1 with simplified equations and avoiding the existence of too many spurious modes, but cannot be used for the whole domain II.

2.2.3 Global wave method, nonlocal model

In order to be able to derive equations valid for any values of $k_{\perp}\rho_{\sigma}$ and ω/ω_{ci} (domain II in Fig.1.1), we have to calculate the inverse Fourier transform of Eq.(2.9) without any approximation with respect to $k_{\perp}\rho_{\sigma}$. We then obtain an equation in configuration space of the form:

$$-\frac{c^2}{\omega^2} \nabla \wedge \nabla \wedge \mathbf{E}(\mathbf{x}) + (\underline{\underline{\epsilon}} \mathbf{E})(\mathbf{x}) = 0, \quad (2.20a)$$

$$(\underline{\underline{\epsilon}} \mathbf{E})(\mathbf{x}) = \mathbf{E}(\mathbf{x}) + \frac{i}{\epsilon_0 \omega} \int d\mathbf{x}' \underline{\underline{\sigma}}(\mathbf{x}, \mathbf{x}') \mathbf{E}(\mathbf{x}'). \quad (2.20b)$$

The derivation of $\underline{\underline{\sigma}}(\mathbf{x}, \mathbf{x}')$ will be explained in Chapters 3 and 4 for the electrostatic and electromagnetic (E.M.) cases, respectively. We see that

Eq.(2.20) is a system of three integro-differential equations of second order. The integral part is due to the perturbed current produced by the plasma particles. It takes into account the solution of the linearized Vlasov equation with the Lorentz force. The differential part ($\nabla \wedge \nabla \wedge$) is due to the Maxwell equations which self-consistently relate the perturbed current to the perturbed electric field.

In the case of the electrostatic approximation, one has to use the Poisson equation instead of the Maxwell equations and we obtain a second-order integro-differential equation for the electrostatic potential Φ of the form:

$$\nabla^2 \Phi(\mathbf{x}) + \int K(\mathbf{x}, \mathbf{x}') \Phi(\mathbf{x}') d\mathbf{x}' = 0. \quad (2.21)$$

In this case, only two boundary conditions are necessary. The boundary conditions, plasma-vacuum interface, modelling of the antenna, etc., will be described in Sec.5.2.

One should still emphasize here that the equations in \mathbf{k} space are integral equations because of the inhomogeneity of the equilibrium distribution function. This is seen in two ways: first, if we assume a homogeneous plasma, then one sees from Eqs.(2.9) and (2.10) that the integral part disappears; second, from the Vlasov equation, Eq.(2.6b), one sees that if $f_{\sigma}^{(0)}$ is inhomogeneous, then the Fourier transform of Eq.(2.6b) will give rise to a convolution of the Fourier transform of \mathbf{E} (or $\mathbf{B}^{(1)}$) and $f_{\sigma}^{(0)}$, producing the integral equation. Formally, an integral equation is equivalent to an infinite order ODE [Ferraro and Fried, 1988; Shokair et al, 1988]. So far, the local models have cut the series of derivatives assuming $k_{\perp} \ll 1/\rho_{\sigma}$. Now, the series is kept complete and there are no restrictions with respect to $k_{\perp} \rho_{\sigma}$ in this new

model. Thus it extends to the whole domain II in Fig.1.1.

Finally, this model is called "nonlocal", because, as can be seen from Eq.(2.20), $\mathbf{E}(\mathbf{x})$ depends on values of \mathbf{E} at \mathbf{x}' throughout the plasma. This is due to the finite Larmor radius of the particles. We shall see, in Secs.3.2 and 4.2, that the non-locality is limited to a half-width of about 10 to 20 ρ_σ .

2.3 Power absorption, basic formulae

As the main goal of studying the linear plasma-wave interaction is to quantify the wave absorption and determine its mechanisms, we need a well-defined power absorption formula. Well-defined means that it has a definite sign and can become negative only if the plasma is unstable.

The standard way for deriving the energy balance equation in kinetic theory is to multiply the Vlasov equation, Eq.(2.1), by $\frac{1}{2} m_\sigma v^2$ and integrate over velocity. It yields:

$$\frac{\partial}{\partial t} \int \frac{1}{2} m_\sigma v^2 f_\sigma d^3\mathbf{v} = \frac{1}{2} q_\sigma \mathbf{E} \cdot \int \mathbf{v} f_\sigma d^3\mathbf{v} - \int \frac{1}{2} m_\sigma v^2 \mathbf{v} \cdot \nabla f_\sigma d^3\mathbf{v}. \quad (2.22)$$

The first term corresponds to the variation in time of the mean energy of the particles σ and the second term gives the work done by the electric field on these particles. The third term is not a real source or sink of energy, it is just the flux of energy of particles streaming in and out of the volume element. It can have either sign.

In order to take out the contribution of the particles streaming through the volume element considered, one should transform Eq.(2.22) into Lagrangian

coordinates which follow particles along unperturbed orbits [Mc Vey et al, 1985; Vaclavik and Appert, 1987]. One can easily show that in these coordinates, the number of particles in the volume element is conserved [Vaclavik and Appert, 1987]. Following this work, one obtains a general formula for the local power absorption as:

$$P_L(\mathbf{x}_\perp) = \frac{q\sigma}{2} \int d^3\mathbf{v} \operatorname{Re} \langle \mathbf{E}^*(\mathbf{x}'_\perp) \cdot \mathbf{v}' f^{(1)}(\mathbf{x}'_\perp, \mathbf{v}'_\perp) \rangle_t. \quad (2.23)$$

The notation $\langle \dots \rangle_t$ means the averaging over time [Vaclavik and Appert, 1987]. This formula will be calculated in Secs.3.3 and 4.3 in the electrostatic and E.M. cases, respectively.

We can relate this power absorption formula to the power emitted by an antenna in vacuum, which is relevant for the E.M. case. Using the standard procedure [Vaclavik and Appert, 1991], we multiply Eq.(2.20) by $-i\epsilon_0\omega\mathbf{E}^*(\mathbf{x})/2$ and integrate over the plasma volume V_p . We obtain:

$$\begin{aligned} i\omega \frac{1}{2} \int_{V_p} d^3\mathbf{x} \left(\frac{|\mathbf{B}|^2}{\mu_0} - \epsilon_0 |\mathbf{E}|^2 \right) + \frac{1}{2} \int_{V_p} d^3\mathbf{x} \mathbf{E}^* \cdot \int d^3\mathbf{x}' \underline{\underline{g}}(\mathbf{x}, \mathbf{x}') \mathbf{E}(\mathbf{x}') \\ = -\frac{1}{2} \int_{\Sigma_p} d\Sigma \frac{\mathbf{E}^* \wedge \mathbf{B}}{\mu_0} \mathbf{n}_p \equiv -\frac{1}{2} \int_{\Sigma_p} d\Sigma \mathbf{S} \cdot \mathbf{n}_p, \end{aligned} \quad (2.24)$$

where Σ_p is the bounding surface of the region V_p , \mathbf{n}_p its outward normal vector, and \mathbf{S} the complex Poynting vector. Likewise, if we assume an antenna current \mathbf{j}_a in the vacuum region V_v surrounding the plasma volume V_p , we obtain:

$$i\omega \frac{1}{2} \int_{V_v} d^3\mathbf{x} \left(\frac{|\mathbf{B}|^2}{\mu_0} - \epsilon_0 |\mathbf{E}|^2 \right) + \frac{1}{2} \int_{V_a} d^3\mathbf{x} \mathbf{E}^* \cdot \mathbf{j}_a = -\frac{1}{2} \int_{\Sigma_v} d\Sigma \mathbf{S} \cdot \mathbf{n}_v, \quad (2.25)$$

where \mathbf{E} and \mathbf{B} are the solutions in vacuum, and V_a the volume including the antenna inside V_v . If there is no surface current, both tangential components of \mathbf{E} and \mathbf{B} are continuous and we obtain, by taking the real parts of Eqs.(2.24-25) and assuming a perfectly-conducting shell surrounding V_v :

$$\begin{aligned} \operatorname{Re} \frac{1}{2} \int_{V_p} d^3\mathbf{x} \mathbf{E}^* \cdot \int d^3\mathbf{x}' \underline{\underline{g}}(\mathbf{x}, \mathbf{x}') \mathbf{E}(\mathbf{x}') &= \int_{V_p} d^3\mathbf{x} P_L(\mathbf{x}) \\ &= -\frac{1}{2} \operatorname{Re} \int_{V_a} d^3\mathbf{x} \mathbf{E}^* \cdot \mathbf{j}_a. \end{aligned} \quad (2.26)$$

The minus sign expresses the fact that the energy lost by the antenna is gained by the plasma particles.

3. ELECTROSTATIC APPROXIMATION

As mentioned in the introduction, we started the study of this new model using the electrostatic approximation because we did not know how difficult the full E.M case would be and if it would be at all solvable with present day computers. Even though it formally takes more time to study first a simpler model and then the complete one, it turned out to be a sensible choice as many different ideas, concerning mainly the numerical method used to integrate the kernel of the integral equation, had to be tried and tested before obtaining the correct solution. This would have been much more complicated if we had started directly with the full E.M. problem.

This is why we present first the electrostatic case which allows us to give more details, because there is only one scalar equation. The electrostatic approximation being a particular case of the E.M. problem, the reader may skip this Chapter and come back to it only if some more details are needed. In order to facilitate this, the next Chapter on the full E.M. case is structured in the same way as this one, and we use the same number (ii) for corresponding equations in the electrostatic approximation, Eq.(3.ii), and in the E.M. case, Eq.(4.ii). This matching obliges us to skip some numbers, and we hope that the reader will not be too disoriented by this ordering scheme.

3.1 Equation in Fourier space

3.1.1 The linearized Vlasov-Poisson equations

The linearized Vlasov equations are given by Eqs.(2.6a, b) which yield in

the electrostatic approximation:

$$\mathbf{v} \cdot \nabla f_{\sigma}^{(0)} + \frac{q_{\sigma}}{m_{\sigma}} (\mathbf{v} \times \mathbf{B}_0) \cdot \frac{\partial}{\partial \mathbf{v}} f_{\sigma}^{(0)} = 0, \quad (3.1a)$$

$$\left(\frac{\partial}{\partial t} + \mathbf{v} \cdot \nabla \right) f_{\sigma}^{(1)} + \frac{q_{\sigma}}{m_{\sigma}} (\mathbf{v} \times \mathbf{B}_0) \cdot \frac{\partial}{\partial \mathbf{v}} f_{\sigma}^{(1)} = \frac{q_{\sigma}}{m_{\sigma}} \nabla \Phi(\mathbf{x}, t) \cdot \frac{\partial}{\partial \mathbf{v}} f_{\sigma}^{(0)}(\mathbf{x}, \mathbf{v}, t), \quad (3.1b)$$

where $\Phi(\mathbf{x}, t)$ is the electrostatic potential defined by $\mathbf{E} \equiv -\nabla \Phi$. Eq.(3.1a) is of course independent of the type of perturbation and is the same in both electrostatic and E.M. cases. Its general solution is given by Eq.(2.7), where $f_{\sigma}^{(0)}(X, Y, v_{\perp}, v_{\parallel})$ is the equilibrium distribution function of the guiding centers. Note that taking the Fourier transform of Eq.(2.7) decouples the Larmor precession of the particles from the guiding center trajectory:

$$\begin{aligned} \text{F.T.} \{ f_{\sigma}^{(0)}(\mathbf{x} + \mathbf{v}_y / \omega_{c\sigma}, y - v_x / \omega_{c\sigma}, v_{\perp}, v_{\parallel}) \} \\ = f_{\sigma}^{(0)}(\mathbf{k}_{\perp}, v_{\perp}, v_{\parallel}) \exp\left(i \frac{(\mathbf{k}_{\perp} \times \mathbf{v}_{\perp})_{\parallel}}{\omega_{c\sigma}}\right), \end{aligned} \quad (3.2)$$

where the Fourier transform is defined by:

$$g(\mathbf{x}, t) = \int d^3 \mathbf{k} \int d\omega g(\mathbf{k}, \omega) e^{i(\mathbf{k} \cdot \mathbf{x} - \omega t)} .$$

In the case of a Maxwellian distribution function with the inhomogeneity only along x , we obtain:

$$f_{\sigma}^{(0)}(\mathbf{k}_{\perp}, v_{\perp}, v_{\parallel}) = f_{\sigma}^{(0)}(\mathbf{k}_{\mathbf{x}}, v_{\perp}, v_{\parallel}) = \frac{1}{2\pi^{5/2}} \int dx'' \frac{n_{\sigma}(x'')}{v_{T\sigma\perp}^2(x'') v_{T\sigma\parallel}(x'')} \quad (3.3)$$

$$\times \exp \left\{ -\frac{v_{\perp}^2}{v_{T\sigma\perp}^2(x'')} - \frac{v_{\parallel}^2}{v_{T\sigma\parallel}^2(x'')} \right\} e^{-i\mathbf{k}_{\mathbf{x}} x''},$$

where $n_{\sigma}(x'')$, $v_{T\sigma}^2(x'')=2T_{\sigma}(x'')/m_{\sigma}$ and $T_{\sigma}(x'')$ are the density, thermal velocity squared and temperature of the guiding centers. We shall always keep x'' as the variable for the guiding center coordinate.

There are different ways to solve Eq.(3.1b) such as integrating over unperturbed orbits (Krall and Trivelpiece [1973], p. 396), or introducing cylindrical coordinates for the velocity $\mathbf{v}=(v_{\perp}, \alpha, v_{\parallel})$ and solving, in \mathbf{k} space, the inhomogeneous first-order differential equation in α [Yasseen and Vaclavik, 1983]. We have used the first method in the general E.M. case and the calculus is presented in Appendix D. The electrostatic approximation can be deduced from Eq.(D.11) assuming $\mathbf{E}(\mathbf{k})=-i\mathbf{k}\Phi(\mathbf{k})$, or can be taken directly from Yasseen and Vaclavik [1983]:

$$f_{\sigma}^{(1)}(\mathbf{k}, \mathbf{v}, \omega) = -\frac{q_{\sigma}}{m_{\sigma}} \sum_{j,n,p} \frac{\exp[i(\alpha-\varphi)(j-n)]}{\omega - k_{\parallel} v_{\parallel} - n\omega_{c\sigma}} J_j\left(\frac{k_{\perp} v_{\perp}}{\omega_{c\sigma}}\right) J_{n+p}\left(\frac{k_{\perp} v_{\perp}}{\omega_{c\sigma}}\right)$$

$$\times \int d^2\mathbf{k}'_{\perp} \Phi(\mathbf{k}_{\perp} - \mathbf{k}'_{\perp}, k_{\parallel}, \omega) \exp[ip(\varphi - \varphi')] J_p\left(\frac{k'_{\perp} v_{\perp}}{\omega_{c\sigma}}\right) \quad (3.4)$$

$$\times \left[k_{\parallel} \frac{\partial}{\partial v_{\parallel}} + \frac{n\omega_{c\sigma}}{v_{\perp}} \frac{\partial}{\partial v_{\perp}} - i \frac{(\mathbf{k}_{\perp} \times \mathbf{k}'_{\perp})_{\parallel}}{\omega_{c\sigma}} \right] f_{\sigma}^{(0)}(\mathbf{k}'_{\perp}, v_{\perp}, v_{\parallel}),$$

where J_m is the Bessel function of the first kind of order m , and cylindrical coordinates have been used: $\mathbf{v}=(v_{\perp}, \alpha, v_{\parallel})$; $\mathbf{k}=(k_{\perp}, \varphi, k_{\parallel})$; $\mathbf{k}'=(k'_{\perp}, \varphi', k'_{\parallel})$. While solving for the perturbed distribution function, we have to introduce a small positive imaginary part to ω to satisfy the causality condition (Appendix D). It

means, with $\omega = \omega_r + i\epsilon$, $\epsilon > 0$, that we "turn on" the perturbation at $t = -\infty$.

The closure equation is given by the Poisson equation in Fourier space:

$$\mathbf{k}^2 \Phi(\mathbf{k}, \omega) = \sum_{\sigma} \frac{q_{\sigma}}{\epsilon_0} \int f_{\sigma}^{(1)}(\mathbf{k}, \mathbf{v}, \omega) d^3 \mathbf{v} . \quad (3.5)$$

At this point, we assume $k_y = 0$ and an isotropic Maxwellian equilibrium distribution function. These assumptions are not yet necessary, but we keep the general formulation only for the E.M. case, for simplicity. Introducing Eqs.(3.3) and (3.4) into (3.5), and using the following formulae for the Bessel functions [Gradshteyn, 1965, pp.980 and 718]

$$\sum_j J_{m \mp j}(a) J_j(b) = J_m(a \pm b) , \quad (3.6a)$$

$$\int_0^{\infty} t dt J_n(\alpha t) J_n(\beta t) e^{-t^2/\mu^2} = \frac{\mu^2}{2} \exp\left\{-\frac{\alpha^2 + \beta^2}{4} \mu^2\right\} I_n\left(\frac{\alpha\beta\mu^2}{2}\right) , \quad (3.6b)$$

where I_n is the modified Bessel function, we obtain:

$$(\mathbf{k}_x^2 + k_{//}^2) \Phi(\mathbf{k}_x) + \int \mathbf{K}(\mathbf{k}_x, \mathbf{k}'_x) \Phi(\mathbf{k}'_x) d\mathbf{k}'_x = 0 , \quad (3.7)$$

with

$$\begin{aligned} \mathbf{K}(\mathbf{k}_x, \mathbf{k}'_x) = & \sum_{\sigma, n} \frac{q_{\sigma}^2}{2\pi\epsilon_0} \int d\mathbf{x}'' \frac{n_{\sigma}(\mathbf{x}'')}{T_{\sigma}(\mathbf{x}'')} \left[1 + \frac{\omega}{|k_{//}| v_{T\sigma}(\mathbf{x}'')} Z_{n\sigma}(\mathbf{x}'') \right] \\ & \times I_n\left(\rho_{\sigma}^2(\mathbf{x}'') k_x k'_x\right) \exp\left\{-\frac{1}{2} \rho_{\sigma}^2(\mathbf{x}'') (k_x^2 + k_x'^2)\right\} e^{-i(\mathbf{k}_x - \mathbf{k}'_x) \cdot \mathbf{x}''} , \end{aligned}$$

where $Z_{n\sigma} = Z(\xi_{n\sigma}) \equiv Z[(\omega - n\omega_{c\sigma}) / (|k_{//}| v_{T\sigma})]$ is the plasma dispersion function [Fried and Conte, 1961] and $\rho_{\sigma}^2 = v_{T\sigma}^2 / 2\omega_{c\sigma}^2$ is the Larmor radius squared. This is the integral equation in Fourier space for $\Phi(\mathbf{k}_x)$, assuming arbitrary inhomogeneous density and temperature profiles. We see that if we assume no dissipation, i.e. $Z_{n\sigma}$ real, then the kernel is hermitian, $K(\mathbf{k}_x, \mathbf{k}'_x) = K^*(\mathbf{k}'_x, \mathbf{k}_x)$, as expected.

This equation, or an equivalent form, has been used to study the eigenmodes of a system, mainly to study drift-wave stability problems. Homogeneous temperature and Gaussian density profiles, with $k_y \neq 0$, were in general assumed: Davidson [1976], Gerver et al [1977], Watanabe et al [1979], Sanuki et al [1980], Berk and Pfirsch [1980], Watanabe et al [1981], Linsker [1981], Marchand et al [1983], Chaudry [1983], Berk and Dominguez [1983], Ferraro et al [1985], Chow et al [1990]. This list is not exhaustive, but other references can be found therein.

3.1.2 Dispersion relation

The dispersion relation, as mentioned in Chapter 2, is obtained from Eq.(3.7) by assuming a homogeneous infinite plasma. In this way, the integral over x'' gives a Dirac distribution $\delta(\mathbf{k}_x - \mathbf{k}'_x)$ and one can integrate over \mathbf{k}'_x , which yields:

$$D(\mathbf{k}_x) = k_x^2 + k_{//}^2 + \sum_{\sigma, n} \frac{(1 + \frac{\omega}{|k_{//}| v_{T\sigma}} Z_{n\sigma})}{\lambda_{D\sigma}^2} I_n(k_x^2 \rho_{\sigma}^2) e^{-k_x^2 \rho_{\sigma}^2} = 0 \quad (3.8)$$

This is a general dispersion relation for the electrostatic waves valid to all orders in Larmor radii, assuming a Maxwellian equilibrium distribution

function. Note that Eq.(3.8) has no solution for k_x^2 very large, as $I_n(k_x^2 \rho_\sigma^2) \exp[-k_x^2 \rho_\sigma^2]$ is proportional to $1/k_x \rho_\sigma$ for $|k_x^2 \rho_\sigma^2| \gg 1$ and $|\omega Z_{n\sigma} / k_{//} v_{T\sigma}| \ll 1$ for large n . Therefore, there is a finite number of roots of Eq.(3.8) for a given value of ω , $k_{//}$, n , T and B_0 . This confirms the fact that, as mentioned in Sec.2.2.2, models based on a polynomial approximation of the dispersion relation will produce additional non-physical modes at high order.

3.2 Equation in configuration space

As explained in Sec.2.2.3, the inversion of the equation in Fourier space must be calculated exactly in order to keep the equation valid in the whole region II in Fig.1.1. That is, no approximation or elimination at small terms should be used in the integral over k . This is possible by using an integral representation of the modified Bessel function I_n [Abramowitz and Stegun, 1964, p. 376]:

$$I_n(k_x k'_x \rho_\sigma^2) = \frac{1}{\pi} \int_0^\pi e^{k_x k'_x \rho_\sigma^2 \cos \theta} \cos(n\theta) d\theta \quad . \quad (3.9)$$

In this way, k_x and k'_x appear only as polynomials or in exponents and therefore the inversion integral of Eq.(3.7) can be calculated analytically. We obtain:

$$-\frac{d^2}{dx^2} \Phi(x) + k_{//}^2 \Phi(x) + \int K(x,x') \Phi(x') dx' = 0 \quad , \quad (3.10)$$

with

$$K(\mathbf{x}, \mathbf{x}') = \frac{1}{2\pi^2} \sum_{\sigma, n} \int d\mathbf{x}'' \frac{[1 + \frac{\omega}{|\mathbf{k}_{//}| v_{T\sigma}(\mathbf{x}'')} Z_{n\sigma}(\mathbf{x}'')]}{\lambda_{D\sigma}^2(\mathbf{x}'') \rho_{\sigma}^2(\mathbf{x}'')} \int_0^{\pi} d\theta \frac{\cos(n\theta)}{\sin\theta} \\ \times \exp \left\{ -\frac{(\mathbf{x}-\mathbf{x}')^2 (1 + \cos\theta)}{4 \rho_{\sigma}^2(\mathbf{x}'') \sin^2\theta} \right\} \exp \left\{ -\frac{(\mathbf{x}'' - \frac{\mathbf{x}+\mathbf{x}'}{2})^2 (1 - \cos\theta)}{\rho_{\sigma}^2(\mathbf{x}'') \sin^2\theta} \right\} ,$$

where $\lambda_{D\sigma}^2 = \epsilon_0 T_{\sigma} / n_{\sigma} q_{\sigma}^2$ and $\omega_{p\sigma}^2 = n_{\sigma} q_{\sigma}^2 / \epsilon_0 m_{\sigma}$ are the Debye length and the plasma frequency squared. This equation is valid to all orders in Larmor radii (electrons and ions) and arbitrary density and temperature profiles. It assumes a Maxwellian equilibrium distribution function, which is not so restrictive as shall be shown in Sec.7.3, and $k_y=0$. This latter assumption means that we cannot study drift wave problems, but this is anyway out of the scope of this work which is principally devoted to ICRF heating ($\omega/\omega_{ci} \gg k_y \rho_{\sigma}$). However, our model is also valid between the Alfvén and electron cyclotron range of frequencies, if relativistic effects are negligible. In this range, we may also extend the validity of Eq.(3.10) to slowly-varying equilibrium magnetic field $B_0(\mathbf{x}'')$ such that, for tokamak simulations, $(k_{//} R_0)^2 \gg 1$ [Cairns et al, 1991], where R_0 is the major radius of the tokamak. In this way, if $(k_y \rho_{\sigma})^2 \ll 1$ as is usually the case, the drift due to the nonuniform magnetic field can also be neglected as it leads to the condition: $(k_{//} R_0)^2 \gg (k_y \rho_{\sigma})^2$.

In order to close Eq.(3.10), two boundary conditions are needed. We shall discuss them in more detail in Chapter 5. We shall see that, since we use the finite element method to solve Eq.(3.10), any boundary conditions involving $\Phi(\mathbf{x})$ and $\Phi'(\mathbf{x})$ can easily be introduced in the code. The limits of integration for \mathbf{x} , \mathbf{x}' and \mathbf{x}'' integrals are discussed in Sec.6.1.2.

For the contribution due to the electrons, we can assume in many cases that $(k_{\perp} \rho_e)^2 \ll 1$. Expanding Eq.(3.7) up to second order and taking the inverse

Fourier transform gives (keeping only the main contributions):

$$\int K^{\text{exp.}}(\mathbf{x}, \mathbf{x}') \Phi(\mathbf{x}') d\mathbf{x}' \approx \frac{d}{dx} \frac{\omega}{|k_{//}| v_{Te}(\mathbf{x})} Z_{0e}(\mathbf{x}) \frac{\omega_{pe}^2(\mathbf{x})}{\omega_{ce}^2(\mathbf{x})} \frac{d}{dx} \Phi(\mathbf{x}) + \frac{1 + \frac{\omega}{|k_{//}| v_{Te}(\mathbf{x})} Z_{0e}(\mathbf{x})}{\lambda_{De}^2(\mathbf{x})} \Phi(\mathbf{x}).$$

Thus, the contribution due to the electrons can be calculated either with this expanded formula, which is much less time-consuming, or with the complete integral form, Eq.(3.10).

Let us point out different characteristics of the kernel $K(\mathbf{x}, \mathbf{x}')$. We see that it is symmetric, $K(\mathbf{x}, \mathbf{x}') = K(\mathbf{x}', \mathbf{x})$, and that it is written in the form:

$$K(\mathbf{x}, \mathbf{x}') = K(\mathbf{x} - \mathbf{x}', \frac{\mathbf{x} + \mathbf{x}'}{2}).$$

One sees from Eq.(3.10) that the $(\mathbf{x} + \mathbf{x}')/2$ dependence is directly related to the guiding center variable \mathbf{x}'' , that is, to the local plasma parameters. Note also that Berk and Pfirsch [1980] have proposed a method, based on the WKB theory, to solve an integral equation in configuration space with a kernel of that form.

The exponential terms in the kernel $K(\mathbf{x}, \mathbf{x}')$ limit the non-locality of the integral equation. $\Phi(\mathbf{x})$ depends on the value of Φ at \mathbf{x}' everywhere in the plasma, but the first exponential term, in particular, limits the influence of points far away from each other:

$$|\mathbf{x} - \mathbf{x}'| < \alpha \frac{2\rho_{\sigma} \sin \theta}{\sqrt{1 + \cos \theta}} = \alpha 2\sqrt{2} \rho_{\sigma} \sin \theta/2. \quad (3.11)$$

A typical value of α is between 4 and 7, as $\exp[-4^2] \approx 10^{-7}$. Therefore, one sees that the contribution of points 10 to 20 Larmor radii away from x is negligible. The second exponential limits the contribution of the guiding centers:

$$\left| x'' - \frac{x+x'}{2} \right| < \beta \frac{\rho_{\sigma}(x'') \sin \theta}{\sqrt{1 - \cos \theta}} = \beta \sqrt{2} \rho_{\sigma}(x'') \cos \theta/2, \quad (3.12)$$

where β is again chosen between 4 and 7. Note that this latter relation is implicit, as ρ_{σ} depends on x'' . These two relations are connected and express the fact that x , x' and x'' cannot be too far apart, otherwise they no longer contribute to the kernel. One can also see Eq.(3.11) as a relation between the characteristic length of the field and the Larmor radius. If $\Phi(x')$ does not change much over about $30\rho_{\sigma}$, then the potential can be expanded around x and the x' integral can be performed, reducing Eq.(3.10) to a differential equation, as in the local model. On the other hand, Eq.(3.12) determines under which conditions the inhomogeneity of the plasma parameters can be neglected or expanded.

Another feature that appears in the kernel $K(x,x')$ is a singularity at the points:

$$\begin{aligned} (a) \quad x=x', \quad \theta \rightarrow 0, \\ (b) \quad x'' = \frac{x+x'}{2}, \quad \theta \rightarrow \pi, \end{aligned} \quad (3.13)$$

where the integrand is proportional to $1/\sin\theta$. Note, however, that this is an integrable singularity, as can be shown with two successive changes of variable. Let us first define:

$$x'' \rightarrow z = \frac{x'' - \frac{x + x'}{2}}{\sqrt{2} \cos \theta/2} ; x''(z) = \sqrt{2} z \cos \theta/2 + \frac{x + x'}{2} .$$

The kernel is then proportional to:

$$K(x, x') \approx \int_0^\pi d\theta \int_{z_{pl}}^{z_{pr}} dz \frac{\cos n\theta}{\sqrt{2} \sin \theta/2} \exp\left(-\frac{z^2}{\rho_\sigma^2}\right) \exp\left[-\frac{(x-x')^2 (1+\cos \theta)}{4 \rho_\sigma^2 \sin^2 \theta}\right],$$

with

$$z_v = \frac{x''_v - \frac{x + x'}{2}}{\sqrt{2} \cos \theta/2} , v = pl, pr ,$$

and where x''_{pl} , x''_{pr} are the left and right limits of the guiding center density profiles. We see that the second singularity, Eq.(3.13b), disappears and is replaced by limits of integration becoming infinite as $\theta \rightarrow \pi$. But, due to the term $\exp[-z^2/\rho_\sigma^2]$, the integral is still well defined. The other singular point, Eq.(3.13a), can be removed in the same way by using the following change of variable:

$$x' \rightarrow y = \frac{x' - x}{2 \sqrt{2} \sin \theta/2} .$$

3.3 Local power absorption formula

We shall derive the local power absorption formula, $P_L(x)$, valid for all orders in Larmor radii, using the electrostatic approximation, assuming a 1-D slab plasma, Maxwellian equilibrium distribution function, slowly varying magnetic field, $k_y=0$, and arbitrary density and temperature profiles. We have

to introduce the perturbed distribution function, Eq.(3.4), using Eq.(3.3), into the general formula, Eq.(2.23), evaluated for a 1-D slab geometry:

$$\begin{aligned}
 P_L(\mathbf{x}) &= \sum_{\sigma} \frac{q_{\sigma}}{2} \int d^3 \mathbf{v}' \operatorname{Re} \left\langle \mathbf{E}^* (\mathbf{x}'_{\perp}) \cdot \mathbf{v}' f_{\sigma}^{(1)} (\mathbf{x}'_{\perp}, \mathbf{v}'_{\perp}) \right\rangle_t \\
 &= \operatorname{Re} \sum_{\sigma} \frac{i q_{\sigma}}{2} \int d^3 \mathbf{v}' dk_x dk_x''' \Phi^* (\mathbf{k}_x''') \\
 &\quad \times \left\langle (\mathbf{k}_x''' \mathbf{v}'_{\perp} + \mathbf{k}_x''' v'_{\parallel}) f_{\sigma}^{(1)} (\mathbf{k}_x, \mathbf{v}') e^{i (\mathbf{k}_x - \mathbf{k}_x''') \cdot \mathbf{x}'} \right\rangle_t,
 \end{aligned} \tag{3.14}$$

where we have introduced the electrostatic approximation and the Fourier transform of Φ and $f_{\sigma}^{(1)}$. The coordinates of the unperturbed trajectory are given by:

$$\begin{aligned}
 \mathbf{x}' &= \mathbf{x} + \frac{v_{\perp}}{\omega_{c\sigma}} [(\sin \alpha - \sin \alpha') \mathbf{e}_x - (\cos \alpha - \cos \alpha') \mathbf{e}_y] + v_{\parallel} \tau \mathbf{e}_z, \\
 \mathbf{v}' &= v_{\perp} (\cos \alpha' \mathbf{e}_x + \sin \alpha' \mathbf{e}_y) + v_{\parallel} \mathbf{e}_z, \\
 \alpha' &= \alpha - \omega_{c\sigma} \tau, \\
 \mathbf{v} &= (v_{\perp}, \alpha, v_{\parallel}), \\
 \tau &= t' - t.
 \end{aligned} \tag{3.15}$$

We see that the average over t is the same as the average over τ . We first calculate this average and integrate over α , using Eq.(3.6a) and the following relation [Gradshteyn and Ryzhik, 1980, p. 973]:

$$e^{i \xi \sin \alpha} = \sum_p J_p(\xi) e^{i p \alpha}. \tag{3.16}$$

Then, introducing the inverse Fourier transform of Φ and changing from \mathbf{k}_x to $\mathbf{k}_x + \mathbf{k}_x'''$, we obtain:

$$\begin{aligned}
 P_L(\mathbf{x}) = \text{Re} \frac{iq_\sigma^2}{4\pi^{7/2} m_\sigma} \int v_\perp dv_\perp dv_{//} dx'' dx' dx''' dk_x dk'_x dk''_x \frac{(k_{//v//} + n\omega_{c\sigma})^2}{\omega k_{//v//} - n\omega_{c\sigma}} \\
 \times \frac{n(\mathbf{x}'')}{v_{T\sigma}^5(\mathbf{x}'')} \exp\left(-\frac{v^2}{v_{T\sigma}^2}\right) J_0(\xi) J_n(\xi') J_n(\xi''') \quad (3.17) \\
 \times e^{ik_x(x-x'')} e^{ik'_x(x'-x'')} e^{ik''_x(x''-x''')} \Phi^*(\mathbf{x}''') \Phi(\mathbf{x}') ,
 \end{aligned}$$

where $\xi^v = k_\perp^v v_\perp / \omega_{c\sigma}$. In order to be able to integrate over the k variables without any approximation, we introduce the following integral representations of the Bessel function:

$$\begin{aligned}
 J_0(\xi) &= \frac{1}{\pi} \int_0^\pi e^{i\xi \cos\theta} d\theta, \\
 J_n(\xi') &= \frac{i^n}{\pi} \int_0^\pi e^{-i\xi' \cos\theta'} \cos(n\theta') d\theta', \quad (3.18) \\
 J_n(\xi''') &= \frac{-i^n}{\pi} \int_0^\pi e^{i\xi''' \cos\theta'''} \cos(n\theta''') d\theta'''.
 \end{aligned}$$

We obtain three different Dirac distributions, $\delta(z)$, from the k_x , k'_x and k''_x integrals:

$$\begin{aligned}
 2^3 \int d\theta d\theta' d\theta''' \cos n\theta' \cos n\theta''' \\
 \times \delta(x-x'' + \frac{v_\perp}{\omega_{c\sigma}} \cos\theta) \delta(x'-x'' + \frac{v_\perp}{\omega_{c\sigma}} \cos\theta') \delta(x'''-x'' + \frac{v_\perp}{\omega_{c\sigma}} \cos\theta''') .
 \end{aligned}$$

We use the first Dirac distribution for the integral over v_\perp , the second for x' and the third for x''' . The integration over v_\perp gives the condition:

$$\frac{x'' - x}{\cos \theta} \omega_{c\sigma} > 0,$$

which imposes the limits of the integral over θ to 0 and $\pi/2$. For example, if $(x''-x)\omega_{c\sigma}<0$, then θ has to be integrated only between $\pi/2$ and π . Changing θ to $\gamma=\pi-\theta$ it gives:

$$\int_0^\pi d\theta \int_0^\infty dv_\perp v_\perp \delta(x - x'' + \frac{v_\perp}{\omega_{c\sigma}} \cos \theta) g(v_\perp)$$

$$= \int_0^{\pi/2} d\gamma \frac{|\omega_{c\sigma}|}{|\cos \gamma|} \frac{(x'' - x) \omega_{c\sigma}}{-\cos \gamma} g\left(\frac{(x'' - x) \omega_{c\sigma}}{-\cos \gamma}\right).$$

if $(x'' - x) \omega_{c\sigma} < 0$

The extra minus sign is used to transform $-(x''-x)\omega_{c\sigma}$ to $|x''-x| |\omega_{c\sigma}|$. This then multiplies $\cos \theta'$ and $\cos \theta''$ by $\omega_{c\sigma} / |\omega_{c\sigma}|$ in the remaining δ -distributions. If $|\omega_{c\sigma}|<0$, this factor is eliminated by changing θ' to $\gamma'=\pi-\theta'$, which also transforms $\cos n\theta'$ to $(-1)^n \cos n\gamma'$. However, introducing the same change of variable for θ'' cancels the term $(-1)^n$.

The $v_{//}$ integral has still to be performed. As ω has a small positive imaginary part ε (Sec.2.1), we have:

$$\text{Re} \left\{ \lim_{\varepsilon \rightarrow 0^+} \frac{i}{\omega_r - k_{//} v_{//} - n\omega_{c\sigma} + i\varepsilon} \right\} = \pi \delta(\omega_r - k_{//} v_{//} - n\omega_{c\sigma}) .$$

We then easily obtain the final form for $P_L(x)$, omitting the subscript r of ω :

$$\begin{aligned}
 P_L(\mathbf{x}) = & \sum_{n,\sigma} \frac{2q_\sigma^2}{\pi^{5/2} m_\sigma} \frac{\omega^2}{|k_{//}|} \int d\mathbf{x}'' \int_0^\pi d\theta \frac{n_\sigma(\mathbf{x}'') \omega_{c\sigma}^2(\mathbf{x}'')}{v_{T\sigma}^5(\mathbf{x}'')} \frac{|\mathbf{x} - \mathbf{x}''|}{\cos^2 \theta} e^{-\xi_{n\sigma}^2(\mathbf{x}'')} \\
 & \times \exp \left\{ -\frac{(\mathbf{x} - \mathbf{x}'')^2}{2\rho_\sigma^2 \cos^2 \theta} \right\} \left| \int_0^\pi d\theta' \cos n\theta' \Phi \left(\mathbf{x}'' - \frac{|\mathbf{x} - \mathbf{x}''|}{\cos \theta} \cos \theta' \right) \right|^2 .
 \end{aligned} \tag{3.19}$$

This formula has the same domain of validity as Eq.(3.10) and is therefore consistent with the solution $\Phi(\mathbf{x})$. Note that $P_L(\mathbf{x})$ is positive-definite, as it should be with $k_y=0$ and thus no instabilities present. This shows, as mentioned in Sec.2.3, that the contribution of streaming particles is not taken into account.

From Eq.(3.19), we can define two quantities, first the local power absorption of species σ , $P_{L\sigma}(\mathbf{x})$, which is simply the contribution of the species σ to $P_L(\mathbf{x})$, and the integrated power absorption $\bar{P}_L(\mathbf{x})$:

$$\bar{P}_{L\sigma}(\mathbf{x}) = \int_{x_{pr}}^{\mathbf{x}} P_{L\sigma}(\mathbf{x}') d\mathbf{x}' \quad ; \quad \bar{P}_L(\mathbf{x}) = \sum_{\sigma} \bar{P}_{L\sigma}(\mathbf{x}) , \tag{3.20}$$

which is the power absorbed by the particles between the right-hand side of the plasma and \mathbf{x} . We integrate from x_{pr} , because we shall always put the source on the right-hand side of the plasma. This can be somewhat misleading, as $\bar{P}_L(\mathbf{x})$ is then always negative. In this way, $\bar{P}_L(x_{pl})$ represents the total power absorbed in the plasma and would be equal, in the E.M. case, to the Poynting flux $\text{Re}(S_x)$ delivered by the source, which is also negative as it flows in the opposite x direction, Eq.(2.24).

4. ELECTROMAGNETIC PROBLEM

In this Chapter we present the derivation of the equations for the three components of the electric field $\mathbf{E}(\mathbf{x})$. As mentioned in the introduction and at the beginning of Chapter 3, the method is the same as in the electrostatic case, except that we end up with a 3x3 dielectric tensor instead of one scalar. This is why we shall not give as many details as in the last Chapter. The reader can easily refer to the equivalent equation in the electrostatic case and to the details related to it, as we have kept the same numbering for corresponding equations. In doing this, we have had to skip a few numbers, hoping that this will not disturb the reader too much.

The E.M. problem being the general case of the interaction of a wave with the plasma, we have kept the equations as general as possible and for as long as we were able to, in order to facilitate later generalization. For example, in Sec.4.1, we derive the integral equation in Fourier space valid for anisotropic temperature, $T_{\perp} \neq T_{\parallel}$, and $k_y \neq 0$, and the corresponding general dispersion relation in Sec.4.1.2. We limit ourselves to $k_y = 0$ only from Sec.4.2 on. The extension to $k_y \neq 0$ is discussed in Sec.4.4.

4.1 Equations in Fourier space

4.1.1 The linearized Vlasov-Maxwell equations

The solution of the Vlasov equation for the perturbed distribution function, Eq.(2.6b), has been obtained using the method of characteristics in the general E.M. case, with a general inhomogeneous equilibrium distribution function, anisotropic temperature and $k_y \neq 0$. The derivation is presented in Appendix D

and we have checked that the expression derived recovers the result of Yasseen and Vaclavik [1986] obtained with a different method. It reads, Eqs.(D.11,12):

$$\begin{aligned}
 f_{\sigma}^{(1)}(\mathbf{k}, \mathbf{v}, \omega) = & - \frac{i q_{\sigma}}{m_{\sigma}} e^{i \frac{(\mathbf{k} \wedge \mathbf{v})_{\parallel}}{\omega_{c\sigma}}} \sum_n \frac{e^{-in\alpha}}{\omega - k_{\parallel} v_{\parallel} - n \omega_{c\sigma}} \int d\mathbf{k}'_{\perp} \\
 & \times \left\{ P_x^n \left[E_x \frac{\partial}{\partial v_{\perp}} + \frac{g(\mathbf{v})}{\omega} (k_{\parallel} E_x - k'_x E_{\parallel}) - i \frac{v_{\perp} (k_x - k'_x)}{\omega \omega_{c\sigma}} (k'_x E_y - k'_y E_x) \right] \right. \\
 & + P_y^n \left[E_y \frac{\partial}{\partial v_{\perp}} + \frac{g(\mathbf{v})}{\omega} (k_{\parallel} E_y - k'_y E_{\parallel}) - i \frac{v_{\perp} (k_y - k'_y)}{\omega \omega_{c\sigma}} (k'_x E_y - k'_y E_x) \right] \quad (4.4) \\
 & + J_n \left[E_{\parallel} \left(\frac{v_{\parallel}}{v_{\perp}} \frac{\partial}{\partial v_{\perp}} + \frac{g(\mathbf{v})}{v_{\perp}} \right) + i \left(1 - \frac{k_{\parallel} v_{\parallel}}{\omega} \right) \frac{(k_x - k'_x) E_y - (k_y - k'_y) E_x}{\omega_{c\sigma}} \right. \\
 & \left. \left. - i \frac{v_{\parallel} E_{\parallel}}{\omega \omega_{c\sigma}} (k_x (k_y - k'_y) - k_y (k_x - k'_x)) \right] \right\} f_{\sigma}^{(0)}(\mathbf{k}_{\perp} - \mathbf{k}'_{\perp}, v_{\perp}, v_{\parallel}),
 \end{aligned}$$

with

$$\begin{aligned}
 \mathbf{v} &= (v_{\perp}, \alpha, v_{\parallel}) \quad , \quad \mathbf{E} = \mathbf{E}(\mathbf{k}'_{\perp}, k_{\parallel}, \omega), \\
 P_x^n &= P_x^n(\mathbf{k}'_{\perp}) = \frac{1}{2} [J_{n+1}(\mathbf{k}'_{\perp}) + J_{n-1}(\mathbf{k}'_{\perp})], \\
 P_y^n &= P_y^n(\mathbf{k}'_{\perp}) = -\frac{i}{2} [J_{n+1}(\mathbf{k}'_{\perp}) - J_{n-1}(\mathbf{k}'_{\perp})], \\
 J_n &= J_n(\mathbf{k}'_{\perp}) = J_n \left(\frac{k'_{\perp} v_{\perp}}{\omega_{c\sigma}} \right) e^{in\phi'}, \\
 g(\mathbf{v}) &= v_{\perp} \frac{\partial}{\partial v_{\parallel}} - v_{\parallel} \frac{\partial}{\partial v_{\perp}} \quad ,
 \end{aligned}$$

where the terms divided by ω come from the $\mathbf{v} \wedge \mathbf{B}^{(1)}$ term and the others from $\mathbf{E}^{(1)}$. Therefore, the results for the electrostatic approximation, Eq.(3.4), are easily identified from the electric field contribution by introducing $\mathbf{E}(\mathbf{k}') = -i\mathbf{k}'\Phi(\mathbf{k}')$. Note also that we have replaced the term $E_{\parallel} \frac{\partial}{\partial v_{\parallel}}$ by $E_{\parallel} \left[\frac{v_{\parallel}}{v_{\perp}} \frac{\partial}{\partial v_{\perp}} + \frac{1}{v_{\perp}} g(\mathbf{v}) \right]$

in the first term proportional to J_n . This simplifies the equations afterwards.

We have to integrate $\mathbf{v} f_{\sigma}^{(1)}$ over velocities, in order to obtain the perturbed current, Eq.(2.6f), and introduce it in the closure equation, Eqs.(2c, d) in Fourier space:

$$\mathbf{k} \wedge \mathbf{k} \wedge \mathbf{E}(\mathbf{k}, \omega) + \frac{\omega^2}{c^2} \mathbf{E}(\mathbf{k}, \omega) + \sum_{\sigma} i \mu_0 \omega q_{\sigma} \int \mathbf{v} f_{\sigma}^{(1)}(\mathbf{k}, \mathbf{v}, \omega) d^3 \mathbf{v} = 0. \quad (4.5)$$

As $f_{\sigma}^{(1)}(\mathbf{k}, \mathbf{v}, \omega)$ depends on the electric field, we can define $\underline{\sigma} \mathbf{E}(\mathbf{k}, \omega) \equiv \mathbf{j}^{(1)}(\mathbf{k}, \omega)$ and Eq.(4.5) has the standard form.

We have seen in Sec.3.1.1 that the Fourier transform of the equilibrium distribution function $f_{\sigma}^{(0)}(\mathbf{k}_{\perp} - \mathbf{k}'_{\perp}, v_{\perp}, v_{\parallel})$ of the guiding center has no dependence on α . Therefore we can integrate over α the terms dependent on α in $f_{\sigma}^{(1)}(\mathbf{k}, \mathbf{v}, \omega)$, Eq.(4.4), multiplied by $\mathbf{v} = (v_{\perp} \cos \alpha, v_{\perp} \sin \alpha, v_{\parallel})$. The result is proportional to:

$$\mathbf{A}_n \equiv \begin{pmatrix} v_{\perp} P_x^{n*}(\mathbf{k}_{\perp}) \\ v_{\perp} P_y^{n*}(\mathbf{k}_{\perp}) \\ v_{\parallel} J_n^*(\mathbf{k}_{\perp}) \end{pmatrix}.$$

Using the recurrence relation for the Bessel function, we can write \mathbf{A}_n more explicitly as:

$$\mathbf{A}_n = e^{-in\varphi} \begin{pmatrix} \cos \varphi \frac{n\omega_{c\sigma}}{k_{\perp}} J_n + i \sin \varphi v_{\perp} J'_n \\ -i \cos \varphi v_{\perp} J'_n + \sin \varphi \frac{n\omega_{c\sigma}}{k_{\perp}} J_n \\ v_{\parallel} J_n \left(\frac{k_{\perp} v_{\perp}}{\omega_{c\sigma}} \right) \end{pmatrix}.$$

Thus we have:

$$\begin{aligned} \mathbf{j}^{(1)}(\mathbf{k}, \mathbf{v}, \omega) = \sum_{\sigma, n} \frac{-iq_{\sigma}^2 2\pi}{m_{\sigma}} \int v_{\perp} dv_{\perp} dv_{\parallel} d\mathbf{k}'_{\perp} \\ \times \mathbf{A}_n(\mathbf{k}_{\perp}, v_{\perp}, v_{\parallel}) \mathbf{B}_n(\mathbf{k}'_{\perp}, k_{\parallel}, v_{\perp}, v_{\parallel}, \omega) f_{\sigma}^{(0)}(\mathbf{k}_{\perp} - \mathbf{k}'_{\perp}, v_{\perp}, v_{\parallel}), \end{aligned} \quad (4.6)$$

where $\mathbf{B}_n(\mathbf{k}'_{\perp}, k_{\parallel}, v_{\perp}, v_{\parallel}, \omega)$ is the term in brackets, { }, in Eq.(4.4). At this point we need to specify the velocity dependence of $f_{\sigma}^{(0)}$, which we assume to be bi-Maxwellian. We also assume that the density and temperature profiles are inhomogeneous only in the x-direction. Thus we have:

$$f_{\sigma}^{(0)}(\mathbf{k}_{\perp} - \mathbf{k}'_{\perp}, v_{\perp}, v_{\parallel}) = f_{\sigma}^{(0)}(k_x - k'_x, v_{\perp}, v_{\parallel}) \delta(k_y - k'_y),$$

where $f_{\sigma}^{(0)}(k_x - k'_x, v_{\perp}, v_{\parallel})$ is defined in Eq.(3.3). Integrating over v_{\perp} is a lengthy process, but not very complicated. One makes extensive use of Eq.(3.6b) and its derivatives with respect to α and β . The calculus is too long to be detailed here or even in an Appendix. We need to introduce the angle ψ between \mathbf{k}_{\perp} and \mathbf{k}'_{\perp} , in the same way as Watanabe [1981], except for the sign. We have:

$$\psi = \varphi' - \varphi,$$

$$\cos \psi = \frac{\mathbf{k}_{\perp} \cdot \mathbf{k}'_{\perp}}{k_{\perp} k'_{\perp}} = \frac{(k_x k'_x + k_y^2) \rho_{\sigma}^2}{z},$$

$$\sin \psi = \frac{(\mathbf{k}_{\perp} \wedge \mathbf{k}'_{\perp})_{\parallel}}{k_{\perp} k'_{\perp}} = \frac{(k_x - k'_x) k_y \rho_{\sigma}^2}{z},$$

$$z = k_{\perp} k'_{\perp} \rho_{\sigma}^2.$$

The integral over v_{\parallel} is performed using the plasma dispersion function as defined by Fried and Conte [1961]:

$$Z(\xi) = \frac{1}{\sqrt{\pi}} \int_{-\infty}^{+\infty} dw \frac{e^{-w^2}}{w - \xi}, \quad \text{Im } \xi > 0,$$

noting that $\xi_{n\sigma} = (\omega - n\omega_{c\sigma}) / (|k_{\parallel}| v_{T\parallel\sigma})$ has a small positive imaginary part due to ω .

We can then write the equation in \mathbf{k} space for the electric field, valid for a 1-D inhomogeneous plasma, anisotropic temperature, $k_y \neq 0$ and bi-Maxwellian distribution function:

$$\mathbf{k} \wedge \mathbf{k} \wedge \mathbf{E}(\mathbf{k}) + \frac{\omega^2}{c^2} (\underline{\underline{\epsilon}} \mathbf{E})(\mathbf{k}) = 0, \quad (4.7a)$$

with

$$\begin{aligned}
 (\underline{\underline{\epsilon}}\mathbf{E})(\mathbf{k}) &= \underline{\underline{I}}\mathbf{E}(\mathbf{k}) + \sum_{\sigma,n} \int dx'' dk'_x \frac{\omega_{p\sigma}^2(x'')}{2\pi\omega^2} e^{-i(\mathbf{k}_x - \mathbf{k}'_x)x''} e^{-\frac{1}{2}(\beta - \beta')} e^{in\psi} \\
 &\times \left\{ \left[\frac{\omega - i\omega_{\sigma}^*}{|\mathbf{k}_{//}|v_{T\sigma//}} Z(\xi_{n\sigma}) - (1 + \xi_{n\sigma} Z(\xi_{n\sigma})) \left(1 - \frac{T_{\sigma\perp}}{T_{\sigma//}}\right) \right] \underline{\underline{M}} + \delta_{0n}^{Kr.} \underline{\underline{D}} e^{z \cos \psi} \right\} \mathbf{E}(\mathbf{k}', \omega),
 \end{aligned} \tag{4.7b}$$

where

$$\begin{aligned}
 M_{xx}(\mathbf{k}_x, \mathbf{k}'_x) &= \left[\frac{n^2}{z} \cos \psi + 2k_y^2 \rho_{\sigma}^2 - i \frac{n}{z} (k_x k'_x - k_y^2) \rho_{\sigma}^2 \sin \psi \right] I_n \\
 &\quad - \left[i \sin \psi + \frac{k_y^2 \rho_{\sigma}^2}{z} (\beta + \beta') \right] I'_n,
 \end{aligned}$$

$$\begin{aligned}
 M_{yy}(\mathbf{k}_x, \mathbf{k}'_x) &= \left[\frac{n^2}{z} \cos \psi + 2k_x k'_x \rho_{\sigma}^2 + i \frac{n}{z^2} (k_x \beta - k'_x \beta') k_y \rho_{\sigma}^2 \right] I_n \\
 &\quad - \left[i \sin \psi + \frac{k_x k'_x \rho_{\sigma}^2}{z} (\beta + \beta') \right] I'_n,
 \end{aligned}$$

$$M_{zz}(\mathbf{k}_x, \mathbf{k}'_x) = \Xi_{n\sigma}^2 I_n,$$

$$\begin{aligned}
 M_{xy}(\mathbf{k}_x, \mathbf{k}'_x) &= \left[\frac{n^2}{z} \sin \psi + 2k_y k'_x \rho_{\sigma}^2 - i \frac{n}{z^2} (k_y^2 \beta + k_x k'_x \beta') \rho_{\sigma}^2 \right] I_n \\
 &\quad + \left[i \cos \psi + \frac{k_y k'_x \rho_{\sigma}^2}{z} (\beta + \beta') \right] I'_n,
 \end{aligned}$$

$$M_{xz}(\mathbf{k}_x, \mathbf{k}'_x) = \Xi_{n\sigma} \left\{ \left[\frac{n}{z^2} k_x \rho_{\sigma} \beta' - i k_y \rho_{\sigma} \right] I_n + i \frac{k_y \rho_{\sigma}}{z} \beta' I'_n \right\},$$

$$M_{yz}(\mathbf{k}_x, \mathbf{k}'_x) = \Xi_{n\sigma} \left\{ \left[\frac{n}{z^2} k_y \rho_{\sigma} \beta' + i k_x \rho_{\sigma} \right] I_n - i \frac{k_x \rho_{\sigma}}{z} \beta' I'_n \right\},$$

$$M_{ij}(\mathbf{k}_x, \mathbf{k}'_x) = M_{ji}^*(\mathbf{k}'_x, \mathbf{k}_x),$$

and

$$\underline{\underline{D}} = \begin{pmatrix} 0 & 0 & 0 \\ 0 & -(k_x - k'_x)^2 \rho_\sigma^2 & -i(k_x - k'_x) \frac{\omega - i\omega_\sigma^*}{k_{//} \omega_{c\sigma}} \\ 0 & D_{yz} & \frac{(\omega - i\omega_\sigma^*)^2}{(k_{//} v_{T\sigma//})^2} \frac{2T_{\sigma//}}{T_{\sigma\perp}} \end{pmatrix},$$

with

$$\Xi_{n\sigma} = \frac{\omega - n\omega_{c\sigma}}{k_{//} \omega_{c\sigma}} \frac{1}{\rho_\sigma},$$

$$\omega_\sigma^* = \omega_{c\sigma} k_y (k_x - k'_x) \rho_\sigma^2,$$

$$I_n = I_n(z), \quad z = k_\perp k'_\perp \rho_\sigma^2, \quad \beta = k_\perp^2 \rho_\sigma^2, \quad \beta' = k'_\perp^2 \rho_\sigma^2,$$

$$\omega_{p\sigma}^2 = \frac{n_\sigma q_\sigma^2}{\epsilon_0 m_\sigma}, \quad v_{T\sigma(\perp//)}^2 = \frac{2T_{\sigma(\perp//)}}{m_\sigma}, \quad \rho_\sigma = \frac{v_{T\sigma\perp}}{\sqrt{2} |\omega_{c\sigma}|}.$$

The dielectric tensor ($\underline{\underline{\epsilon}}\mathbf{E}$)(\mathbf{k}), which is an integral operator, has been checked with the one obtained by Watanabe [1981]. We have been able to greatly simplify the formula by combining some terms differently.

A few remarks should be made about this equation. First, the tensor $\underline{\underline{D}}$ is obtained by summing over n the terms independent of $Z(\xi_{n\sigma})$, using the following relation [Abramowitz, 1964, p.376]:

$$\sum_n \cos n\psi I_n(z) = e^{z \cos \psi}.$$

That is why \underline{D} is multiplied by the Kronecker delta such that: $\sum_n \delta_{0n}^{Kr} = 1$. As an example, D_{zz} is obtained by separating the sum $\sum_n e^{in\psi} \xi_{n\sigma} (1 + \xi_{n\sigma} Z_n) I_n$, which appears in ϵ_{zz} , into two terms:

$$\sum_n e^{in\psi} \xi_{n\sigma} I_n = \frac{\omega - i\omega_\sigma^*}{|k_{//}| v_{T\sigma//}} e^{z \cos \psi} \quad \text{and} \quad \sum_n e^{in\psi} \xi_{n\sigma}^2 Z_{n\sigma} I_n,$$

which contribute to D_{zz} and M_{zz} . In this way, we are able to define the same matrix \underline{M} for the isotropic and anisotropic contributions.

As $(i\omega_\sigma^*)$ of (k_x, k'_x) does not change sign when we interchange k_x and k'_x and take its complex conjugate, we see that the kernel in Eq.(4.7b) is hermitian if we assume $Z_{n\sigma}$ real (no dissipation).

In order to recover the equation for the electrostatic potential from the general E.M. one, we have to take the divergence of Eq.(2.6d). This yields:

$$\nabla \cdot \nabla \wedge \mathbf{B} = 0 = \mu_0 \nabla \cdot \mathbf{j} + \frac{1}{c^2} \frac{\partial}{\partial t} \nabla \cdot \mathbf{E}. \quad (4.7.2)$$

Introducing Eq.(2.6e), we obtain:

$$\frac{\partial}{\partial t} \rho + \nabla \cdot \mathbf{j} = 0,$$

which is the charge conservation law. Or, otherwise stated, replacing $\nabla \cdot \mathbf{j}$ by $-\partial\rho/\partial t$ in Eq.(4.7.2), due to the conservation of the charge, we obtain the Poisson equation. Therefore, in \mathbf{k} space, we have to take the scalar product of Eq.(4.7) with \mathbf{k} , and introduce the electrostatic potential $\mathbf{E}(\mathbf{k}) = -i \mathbf{k} \Phi(\mathbf{k})$. We have verified that, with $k_y=0$ and $T_\perp=T_{//}$, we recover Eq.(3.7). The interested reader can easily

obtain the general electrostatic integral equation in \mathbf{k} space by following this procedure with the complete form of Eq.(4.7).

4.1.2 Dispersion relation

In the case of an infinite homogeneous plasma, Eq.(4.7) becomes:

$$\mathbf{k} \wedge \mathbf{k} \wedge \mathbf{E}(\mathbf{k}) + \frac{\omega^2}{c^2} \underline{\underline{\epsilon}} \cdot \mathbf{E}(\mathbf{k}) = 0, \quad (4.8)$$

with

$$\begin{aligned} \underline{\underline{\epsilon}} = \underline{\underline{I}} + \sum_{\sigma, n} \frac{\omega_{p\sigma}^2}{\omega^2} \left[\frac{\omega}{|k_{//}| v_{T\sigma//}} Z(\xi_{n\sigma}) - (1 + \xi_{n\sigma} Z(\xi_{n\sigma})) \left(1 - \frac{T_{\sigma\perp}}{T_{\sigma//}}\right) \right] \underline{\underline{M}} \\ + \sum_{\sigma} \frac{\omega_{p\sigma}^2}{\omega^2} \Xi_{0\sigma}^2 \mathbf{e}_z \cdot \mathbf{e}_z, \end{aligned}$$

and

$$\underline{\underline{M}} = \begin{pmatrix} \frac{n^2}{\beta} \Lambda_n - 2k_y^2 \rho_{\sigma}^2 \Lambda'_n & (2k_y k_x \rho_{\sigma}^2 + in) \Lambda'_n & \Xi_{n\sigma} \left(n \frac{k_x \rho_{\sigma}}{\beta} \Lambda_n + i k_y \rho_{\sigma} \Lambda'_n \right) \\ M_{xy}^* & \frac{n^2}{\beta} \Lambda_n - 2k_x^2 \rho_{\sigma}^2 \Lambda'_n & \Xi_{n\sigma} \left(n \frac{k_y \rho_{\sigma}}{\beta} \Lambda_n - i k_x \rho_{\sigma} \Lambda'_n \right) \\ M_{xz}^* & M_{yz}^* & \Xi_{n\sigma}^2 \Lambda_n \end{pmatrix},$$

where

$$\Lambda_n = \Lambda_n(\beta) = e^{-\beta} I_n(\beta) \quad , \quad \Lambda'_n = \frac{d}{d\beta} \Lambda_n(\beta),$$

and with the same notation as for Eq.(4.7). Note also that $\Sigma_n \Lambda_n = 1$, which is why we obtain an extra term in ϵ_{zz} from D_{zz} . The dispersion relation is obtained by setting to zero the determinant of the matrix multiplying $\mathbf{E}(\mathbf{k})$ in Eq.(4.8). It is valid to all orders in Larmor radii, $k_y \neq 0$, and $T_{\perp} \neq T_{\parallel}$. We have constructed a code, DISPAL, solving the real part of the dispersion relation for the local plasma parameters $n_{\sigma}(\mathbf{x})$, $T_{\sigma}(\mathbf{x})$, $B_0(\mathbf{x})$, for given values of k_y , k_z , and ω . This gives an idea of the possible values of k_x^2 in the plasma. If the WKB approximation is valid, this gives already a very good idea of the solution. This code is detailed in Appendix C, where we also show a few examples of dispersion relations.

4.2 Equation for the electric field in configuration space

As detailed in Sec.3.2, we use an integral representation for the modified Bessel function I_n , Eq.(3.9), in order to be able to calculate the inversion integrals. We also neglect k_y , which corresponds to assuming $\omega_{\sigma}^* / \omega \ll 1$, where ω_{σ}^* is defined in Eq.(4.7). This approximation is valid for the frequencies considered here. It is of course not valid for drift wave problems. We discuss the extension to non zero k_y in Sec.4.4.

Assuming $k_y = 0$ in $\underline{\epsilon}$, but keeping $T_{\perp} \neq T_{\parallel}$, we can calculate the inverse Fourier transform of Eq.(4.7), using Eq.(3.9), and we obtain:

$$\nabla \wedge \nabla \wedge \mathbf{E}(\mathbf{x}) - \frac{\omega^2}{c^2} (\underline{\epsilon} \mathbf{E})(\mathbf{x}) = 0, \quad (4.10)$$

with

$$\nabla = \left(\frac{d}{dx}, i k_y, i k_z \right),$$

$$\begin{aligned}
 (\underline{\underline{\epsilon}}\mathbf{E})(\mathbf{x}) &= \underline{\underline{I}}\mathbf{E}(\mathbf{x}) + \sum_{\sigma} \int dx'' \frac{\omega_{p\sigma}^2(x'')}{\sqrt{2\pi}\omega^2\rho_{\sigma}} \exp\left[-\frac{(\mathbf{x}-\mathbf{x}'')^2}{2\rho_{\sigma}^2}\right] \underline{\underline{D}}\mathbf{E}(\mathbf{x}) \\
 &+ \sum_{\sigma,n} \int dx'' dx' \int_0^{\pi} d\theta \frac{\omega_{p\sigma}^2(x'')}{2\pi^2\omega^2\rho_{\sigma}^2(x'')} \exp\left\{-\frac{(\mathbf{x}''-\frac{\mathbf{x}+\mathbf{x}'}{2})^2(1-\cos\theta)}{\rho_{\sigma}^2(x'')\sin^2\theta}\right\} \\
 &\times \exp\left\{-\frac{(\mathbf{x}-\mathbf{x}')^2(1+\cos\theta)}{4\rho_{\sigma}^2(x'')\sin^2\theta}\right\} \left[\frac{\omega}{|k_{//}|v_{T\sigma//}} Z_{n\sigma} - (1+\xi_{n\sigma} Z_{n\sigma})\left(1-\frac{T_{\sigma\perp}}{T_{\sigma//}}\right)\right] \underline{\underline{M}}\mathbf{E}(\mathbf{x}')
 \end{aligned}$$

where

$$\underline{\underline{M}} = \begin{pmatrix} n \sin n\theta & -i \frac{\sin n\theta}{\sin^2\theta} \frac{(\mathbf{x}'-\mathbf{x}'')}{\rho_{\sigma}^2} \times \\ & \times [(\mathbf{x}-\mathbf{x}'')\cos\theta - (\mathbf{x}'-\mathbf{x}'')] & i \frac{\sin n\theta}{\sin^2\theta} \Xi_{n\sigma} \times \\ & & \times \frac{[(\mathbf{x}-\mathbf{x}'')\cos\theta - (\mathbf{x}'-\mathbf{x}'')]}{\rho_{\sigma}} \\ M_{xy}^*(\mathbf{x}',\mathbf{x}) & \frac{\cos n\theta}{\sin\theta} \frac{(\mathbf{x}-\mathbf{x}'')(\mathbf{x}'-\mathbf{x}'')}{\rho_{\sigma}^2} & -\frac{\cos n\theta}{\sin\theta} \Xi_{n\sigma} \frac{(\mathbf{x}-\mathbf{x}'')}{\rho_{\sigma}} \\ M_{xz}^*(\mathbf{x}',\mathbf{x}) & M_{yz}^*(\mathbf{x}',\mathbf{x}) & \frac{\cos n\theta}{\sin\theta} \Xi_{n\sigma}^2 \end{pmatrix},$$

$$\underline{\underline{D}} = \begin{pmatrix} 0 & 0 & 0 \\ 0 & -1 + \frac{(\mathbf{x}-\mathbf{x}'')^2}{\rho_{\sigma}^2} & -\Xi_0 \frac{(\mathbf{x}-\mathbf{x}'')}{\rho_{\sigma}} \\ 0 & D_{yz} & \Xi_0^2 \end{pmatrix}.$$

Note that one can easily relate the terms D_{yz} , D_{zz} and M_{yz} , M_{zz} with the following relation:

$$\begin{aligned} \sum_n \int dx' \int_0^\pi d\theta \exp \left\{ -\frac{(x-x')^2 (1+\cos\theta)}{4\rho_\sigma^2(x'') \sin^2\theta} \right\} \exp \left\{ -\frac{(x'' - \frac{x+x'}{2})^2 (1-\cos\theta)}{\rho_\sigma^2(x'') \sin^2\theta} \right\} \frac{\cos n\theta}{\sin\theta} \\ = \pi \sqrt{2\pi} \rho_\sigma \exp \left\{ -\frac{(x-x'')^2}{2\rho_\sigma^2} \right\}. \end{aligned}$$

Therefore, ϵ_{yz} and ϵ_{zz} can also be written as :

$$(\epsilon_{yz} E_z) = \sum_{\sigma, n} \int dx'' \dots \frac{\omega}{k_{//} v_{T\sigma//}} \frac{2\omega_{c\sigma}}{v_{T\sigma\perp}} \sqrt{\frac{T_{//}}{T_{\perp}}} (1 + \xi_{n\sigma} Z_{n\sigma}) \frac{\cos n\theta}{\sin\theta} (x-x'') E_z(x''),$$

and

$$(\epsilon_{zz} E_z) = E_z(x) + \sum_{\sigma, n} \int dx' \dots \frac{\omega}{|k_{//}| v_{T\sigma//}} \frac{2T_{//}}{T_{\perp}} \xi_{n\sigma} (1 + \xi_{n\sigma} Z_{n\sigma}) \frac{\cos n\theta}{\sin\theta} E_z(x'),$$

which are equivalent, for $T_{\perp}=T_{//}$, to the formula reported by Sauter and Vaclavik [1991]. On the other hand, the term D_{yy} cannot be related simply to M_{yy} and is, in this respect, really an extra non-resonant term. It is due to the inhomogeneity and to the bounded character of the plasma. Indeed, if we assume a homogeneous plasma, we can integrate over x'' :

$$\int_{x''_{pl}}^{x''_{pr}} dx'' \left[\frac{(x-x'')^2}{\rho_\sigma^2} - 1 \right] \exp \left\{ -\frac{(x-x'')^2}{2\rho_\sigma^2} \right\} = (x-x'') \exp \left\{ -\frac{(x-x'')^2}{2\rho_\sigma^2} \right\} \Big|_{x''_{pl}}^{x''_{pr}}.$$

We see that the contribution is maximum near the edge of the guiding center

profiles and negligible further away or if the plasma is infinite. However, this non-resonant term does not contribute to the local power absorption (Sec.4.3).

The system of integro-differential equations for the three components of the electric field \mathbf{E} is valid to all orders in Larmor radii, for arbitrary density and anisotropic temperature profiles. It assumes a 1-D slab plasma, bi-Maxwellian equilibrium distribution function, and neglects k_y in the perturbed current. As discussed in Sec.3.2, for the problems considered in this work, we can assume the equilibrium magnetic field B_0 to be slowly varying if $(k_{\parallel}R_0)^2 \gg 1$, where R_0 is the characteristic length of the inhomogeneity of B_0 , which is typically the size of the major radius of the tokamak.

In order to close the set of Eq.(4.10), one needs to specify adequate boundary conditions. These will be detailed in Sec.5.2. They correspond to the standard boundary conditions used for the Maxwell equations, because the differential part of Eq.(4.10) is only due to the differential part of the Maxwell equations. Therefore no extra boundary conditions are needed, as is often the case with local models (see Sec.2.2.2).

For the other characteristics of Eq.(4.10), one can refer to the remarks made about the electrostatic case, Eq.(3.10), in particular regarding the limitation of the width of the non-locality due to the exponential terms in $(\underline{\epsilon}\mathbf{E})(\mathbf{x})$.

4.3 Local power absorption formula

Following the same procedure as in Sec.3.3, we introduce Eq.(4.4) into Eq.(2.23), assume $k_y=0$, and obtain the local power absorption with the same domain of validity as Eq.(4.10):

$$\begin{aligned}
 P_L(\mathbf{x}) = & \sum_{n,\sigma} \frac{2q_\sigma^2}{\pi^{5/2} m_\sigma} \int d\mathbf{x}'' \int_0^\pi d\theta \frac{n_\sigma(\mathbf{x}'')}{|k_{//}| v_{T\sigma//}(\mathbf{x}'')} \frac{\omega_{c\sigma}^4(\mathbf{x}'')}{v_{T\sigma\perp}^4(\mathbf{x}'')} \frac{|\mathbf{x} - \mathbf{x}''|^3}{\cos^4\theta} \\
 & \times e^{-\xi_{n\sigma}^2} \exp\left\{-\frac{(\mathbf{x} - \mathbf{x}'')^2}{2\rho_\sigma^2 \cos^2\theta}\right\} \frac{T_{\sigma\perp}}{T_{\sigma//}} \left[1 - \frac{n\omega_{c\sigma}}{\omega} \left(1 - \frac{T_{\sigma//}}{T_{\sigma\perp}}\right)\right] \quad (4.19) \\
 & \times \left| \int_0^\pi d\theta' \left[E_x \sin\theta' \sin n\theta' + i \cos n\theta' (\cos\theta' E_y + \frac{(\omega - n\omega_{c\sigma}) \cos\theta}{k_{//} \omega_{c\sigma} |\mathbf{x} - \mathbf{x}''|} E_{//}) \right] \right|^2,
 \end{aligned}$$

with $\mathbf{E} = \mathbf{E}[\mathbf{x}'' - \frac{|\mathbf{x} - \mathbf{x}''|}{\cos\theta} \cos\theta']$. We can rewrite the θ' integrand such as to exhibit the $E_+ = E_x + i E_y$ and $E_- = E_x - i E_y$ contributions:

$$\frac{1}{2} \left[E_+ \cos(n-1)\theta' - E_- \cos(n+1)\theta' \right] + i \cos n\theta' \frac{(\omega - n\omega_{c\sigma}) \cos\theta}{k_{//} \omega_{c\sigma} |\mathbf{x} - \mathbf{x}''|} E_z.$$

We see that both enter into the perpendicular contribution. Once again, the local power absorption is positive-definite for $T_{\sigma\perp} = T_{\sigma//}$. If $T_{\sigma\perp} > 2T_{\sigma//}$ and $\omega > \omega_{c\sigma}/2$, kinetic instabilities may exist in some special cases when

$$1 - \frac{n\omega_{c\sigma}}{\omega} \left(1 - \frac{T_{\sigma//}}{T_{\sigma\perp}}\right) < 0,$$

and if ω is not too far from a harmonic frequency [Mikhailovski, 1974, p. 194].

We have verified that this formula reduces to Eq.(3.19) in the electrostatic case with $T_{\sigma\perp} = T_{\sigma//}$. The same definitions are used for $P_{L\sigma}(\mathbf{x})$, $\bar{P}_{L\sigma}(\mathbf{x})$, and $\bar{P}_L(\mathbf{x})$ as in the electrostatic case, Eq.(3.20).

Note that $P_L(\mathbf{x})$ is called the local power absorption because it is the power

absorbed by the particles between x and $x+dx$, but it is nonlocal in the sense that its value depends on the value of the field throughout the plasma. However, the width of this nonlocal contribution is limited by the term $\exp[-(x-x'')^2 / (2 \rho_\sigma^2 \cos^2\theta)]$.

Finally, we see that only the resonant particles, characterized by $\exp(-\xi_{n\sigma}^2)$, contribute to $P_L(x)$. The non-resonant terms, matrix $\underline{\underline{D}}$ of Eq.(4.10), contribute only to the circulating power, defined by taking the imaginary part in Eq.(2.23) instead of the real part.

4.4 Extension to $k_y \neq 0$

We have assumed $k_y=0$ for calculating Eq.(4.10) and (4.19), because it enables us to easily perform the inversion integrals. Indeed, we have Bessel functions of the type $J_n(\mathbf{k}_\perp)$, Eq.(D.9) (Appendix D), which we have transformed using the integral representation of the Bessel functions. If we keep k_y , we have a $(k_x^2+k_y^2)^{1/2} \rho_\sigma$ in the exponent and we can no longer integrate analytically. One would have either to stay in 2-D geometry and use cylindrical coordinates for \mathbf{k} , or to expand the Bessel functions in terms of k_y . This latter method would enable us to stay in a 1-D geometry.

One should use different methods for calculating the expansion with respect to $k_y \rho_\sigma$ of the equation for \mathbf{E} and of the local power absorption. The first is obtained by expanding Eq.(4.7), and then integrating over $k_x, v_\perp, v_\parallel$ as before. For example, if we kept the first order contribution, we would have the following additional terms:

$$e^{in\psi} = (\cos \psi + i \sin \psi)^n \approx 1 + i n \sin \psi ,$$

$$\sin \psi = \frac{k_y (k_x - k'_x) \rho_\sigma^2}{z} ,$$

$$\omega - \omega^* = \omega - i \omega_{c\sigma} k_y (k_x - k'_x) \rho_\sigma^2 ,$$

and the Bessel function $I_n(k_\perp k'_\perp \rho_\sigma^2)$ would reduce to $I_n(k_x k'_x \rho_\sigma^2)$. There are also all the terms in $\underline{\underline{M}}$ and $\underline{\underline{D}}$ which explicitly depend on k_y . These terms can be identified from the equation for the perturbed distribution function, Eq.(4.4). As a first approximation, one could keep only the terms which are known to be important in the local model approximation, for example from the expanded form of Martin and Vaclavik [1987]. They should also constitute the main contribution in the case of large Larmor radii.

The extension of the local power absorption formula to $k_y \neq 0$ would be much more complicated, as it involves more terms. In order to expand all the terms to the same order, one would have to start from the E.M. equation equivalent to Eq.(3.17), which is proportional to $\mathbf{A}_n \cdot \mathbf{E}^* B_n$ (\mathbf{A}_n, B_n being defined in Eq.(4.6)), and where the Bessel functions $J_n(\xi^v)$ would have to be replaced by the "vector Bessel" functions $\mathbf{J}_n(\mathbf{k}_\perp^v)$, Eq.(D.9). Then, using the summation theorem, Eq.(D.10), with $\mathbf{k}_\perp = k_x \mathbf{e}_x + k_y \mathbf{e}_y$, we would have:

$$\begin{aligned} \mathbf{J}_n(\mathbf{k}_\perp) &= \sum_{m=-\infty}^{+\infty} \mathbf{J}_{m+n}(k_x \mathbf{e}_x) \mathbf{J}_m^*(k_x (-\mathbf{e}_y)) \\ &= \sum_{m=-\infty}^{+\infty} \mathbf{J}_{m+n}\left(\frac{k_x v_\perp}{\omega_{c\sigma}}\right) \mathbf{J}_m\left(\frac{k_y v_\perp}{\omega_{c\sigma}}\right) e^{im\pi/2} . \end{aligned} \tag{4.20}$$

This formula would enable us to expand the Bessel functions directly without introducing k_y/k_x terms, which would otherwise be the case if we used a Taylor

expansion of $J_n(k_\perp v_\perp / \omega_{c\sigma})$. Therefore, the first order contribution would give:

$$J_n(\mathbf{k}_\perp) = J_n(\xi_x) + i J_1(\xi_y) [J_{n+1}(\xi_x) - J_{n-1}(\xi_x)] \approx J_n(\xi_x) - \xi_y P_y^n(\xi_x),$$

where $\xi_w = k_w v_\perp / \omega_{c\sigma}$ and P_y^n is defined in Eq.(4.4). Inserting this into Eq.(3.17), we could perform the $k_x, v_\perp, v_{||}$ integrals as before. Note that we could not keep the summation over m of Eq.(4.20), because it would introduce additional Bessel functions and rule out the possibility to integrate analytically over v_\perp .

As there are many different products of $J_n, P_x^n,$ and $P_y^n,$ even the first order contribution would involve many terms. This would not be worthwhile to evaluate and one should concentrate on Eq.(4.19). The first approximation, however, neglecting k_y in the argument of the "vector Bessel functions" and keeping only the terms which depend explicitly on k_y in the bracket $\{ \},$ Eq.(4.4), could be useful.

The analysis of drift wave problems is beyond the scope of this work and so we leave this extension for future development of our model. Note that there have been many publications on this subject using Eq.(3.7), or (4.7), with gaussian density profiles, and solving for the eigenmodes and eigenfrequencies, as mentioned in Sec.3.1.1.

5. NUMERICAL METHOD

We use the finite element method to solve Eqs.(3.10) and (4.10). This method is first presented in a general way and then applied to our specific problem (Sec.5.1). In Sec.5.2 we discuss the boundary conditions, mainly for the E.M. case, the computation of the contribution of the kernel to the matrix and of the local power absorption formula. We do not separate the electrostatic and E.M. cases, as the numerical method is the same for both.

5.1 Finite element method

5.1.1 Mathematical basis and general comments

Let us consider the following simple 1-D problem:

$$\left\{ \begin{array}{l} -u''(x) + c(x)u(x) = f(x), \quad 0 < x < 1, \quad c(x) \geq 0, \\ u'(0) = 0, \quad u'(1) = 0. \end{array} \right. \quad (5.1a)$$

$$(5.1b)$$

We multiply this equation by a test function $v(x)$, once differentiable in $[0,1]$, and integrate over the interval $[0,1]$. We obtain:

$$\int_0^1 v'(x) u'(x) dx + \int_0^1 v(x) c(x) u(x) dx - v(1) u'(1) + v(0) u'(0) = \int_0^1 v(x) f(x) dx .$$

Imposing the boundary conditions, Eq.(5.1b), it gives:

$$\int_0^1 v'(x) u'(x) dx + \int_0^1 v(x) c(x) u(x) dx = \int_0^1 v(x) f(x) dx . \quad (5.2)$$

If we consider the space V of continuous functions in $[0,1]$, once differentiable, and satisfying Eq.(5.1b), we can formulate the following problem:

find a solution $u \in V$ of Eq.(5.2) for all $v \in V$.

This problem is called the "weak form" of Eq.(5.1). These two problems are equivalent, except that the solution $u(x)$ of the differential equation must be more regular, twice differentiable, than the solution of Eq.(5.2). The weak form in this case is also called the variational form, or principle, as it is equivalent to searching for a solution $u \in V$ which minimizes the following quantity:

$$J(w) = \frac{1}{2} \int_0^1 w'^2(x) dx + \frac{1}{2} \int_0^1 c(x) w^2(x) dx - \int_0^1 w(x) f(x) dx , w \in V . \quad (5.3)$$

The finite element method is based on the weak form, whereas the finite difference method is based on the differential equation.

Let us consider $\phi_1, \phi_2, \dots, \phi_N$, N linearly independent functions which span a subspace V_h of V . That is, V_h is defined by the following class of functions $g(x)$:

$$g(x) = \sum_{i=1}^N g_i \phi_i(x) , g_i \in \mathcal{R} .$$

Thus, an approximation of the weak form problem is the following:

find a function $u_h \in V_h$ such that, for all $v_h \in V_h$:

$$\int_0^1 v'_h(x) u'_h(x) dx + \int_0^1 v_h(x) c(x) u_h(x) dx = \int_0^1 v_h(x) f(x) dx . \quad (5.4)$$

This is the Galerkin approximation, which is why the finite element method is also called the Galerkin method. We see that, as $u_h \in V_h$, we can write:

$$u_h(x) = \sum_{j=1}^N u_j \varphi_j(x) ,$$

and choose in Eq.(5.4) the basis functions $\varphi_i(x)$ as test functions v_h , which gives:

$$\underline{\underline{A}} \mathbf{u} = \mathbf{b} , \quad (5.5)$$

with

$$A_{ij} = \int_0^1 \varphi'_i(x) \varphi'_j(x) dx + \int_0^1 \varphi_i(x) c(x) \varphi_j(x) dx ,$$

$$b_i = \int_0^1 \varphi_i(x) f(x) dx ,$$

$$\mathbf{u} = (u_1, u_2, \dots, u_N) .$$

Thus, the finite element method consists in constructing the matrix $\underline{\underline{A}}$ and the right-hand side vector \mathbf{b} , and solving the linear system Eq.(5.5).

The basis functions are chosen such as to maximize the number of zeros in $\underline{\underline{A}}$ and minimize the error of u_h compared with the exact solution $u(x)$. In general, one discretizes the domain in x_i nodes, $i=1, \dots, N$, and define $\varphi_i(x)$ such

that it is non zero only in $[x_{i-1}, x_{i+1}]$. Fig.5.1 shows the most commonly used basis functions: piece-wise constant, linear, quadratic, and Hermite-cubic. Note that for the cubics, the two types of basis functions represent the function and its first derivative at the node x_i . Of course, the use of higher order polynomials allows for better accuracy and convergence properties. For example, numerical schemes using piece-wise constant and linear basis converge like $1/N^2$, whereas the two others like $1/N^4$. Moreover, some global quantities can show super-convergence properties. This method can be generalized to multi-dimensional space as well. Note also that one does not need to use the same basis functions for the different unknowns, as shall be done in our codes, or even for an unknown and its derivatives (non-conforming approximation [Gruber and Rappaz, 1985]).

We list below some of the attractive features of the finite element method [Morton, 1986]:

- a strong mathematical basis, leading to a good error analysis of the method
- it divides the domain into finite elements (in general intervals, triangles or quadrilaterals), allowing one to handle complex geometries.
- different simple basis functions defined on the same finite elements can be used, depending on the accuracy needed.
- The mesh can easily be packed where it is needed.
- It approximates the global solution and therefore does not matter if it is an evanescent or propagating solution. Therefore it can be used in cut-off regions as well.
- It is rather straightforward to program.

5.1.2 Application to the integro-differential equation

We apply the finite element method to Eq.(4.10), which is equivalent to the following equation:

$$\nabla \wedge \nabla \wedge \mathbf{E}(\mathbf{x}) - \frac{\omega^2}{c^2} \mathbf{E}(\mathbf{x}) - \int_{x_{pl}}^{x_{pr}} \underline{\underline{K}}(\mathbf{x}, \mathbf{x}') \mathbf{E}(\mathbf{x}') d\mathbf{x}' = 0. \quad (5.6)$$

Multiplying by a test function $\mathbf{G}^*(\mathbf{x})$ and integrating over $[x_{pl}, x_{pr}]$, we obtain the weak form:

$$\begin{aligned} & \int_{x_{pl}}^{x_{pr}} \nabla \wedge \mathbf{G}^* \cdot \nabla \wedge \mathbf{E} d\mathbf{x} - \frac{\omega^2}{c^2} \int_{x_{pl}}^{x_{pr}} \mathbf{G}^* \cdot \mathbf{E} d\mathbf{x} \\ & - \int_{x_{pl}}^{x_{pr}} d\mathbf{x} \int_{x_{pl}}^{x_{pr}} d\mathbf{x}' \mathbf{G}^*(\mathbf{x}) \underline{\underline{K}}(\mathbf{x}, \mathbf{x}') \mathbf{E}(\mathbf{x}') = \mathbf{G}^* \wedge (\nabla \wedge \mathbf{E}) \cdot \mathbf{e}_x \Big|_{x_{pl}}^{x_{pr}}. \end{aligned} \quad (5.7)$$

We then discretize $[x_{pl}, x_{pr}]$ in N intervals of arbitrary length and choose piecewise constant and linear basis functions, χ_i and φ_i :

$$\chi_i(\mathbf{x}) = \left\{ \begin{array}{l} 1 \text{ if } \mathbf{x} \in [x_{i-1}, x_i] \\ 0 \text{ otherwise} \end{array} \right\}, \quad i = 2, \dots, N, \quad (5.8a)$$

$$\chi_1(\mathbf{x}) \equiv 0,$$

$$\varphi_i(\mathbf{x}) = \left\{ \begin{array}{l} \frac{x - x_{i-1}}{x_i - x_{i-1}} \text{ if } \mathbf{x} \in [x_{i-1}, x_i] \\ \frac{x_{i+1} - x}{x_{i+1} - x_i} \text{ if } \mathbf{x} \in [x_i, x_{i+1}] \\ 0 \text{ otherwise} \end{array} \right\}, \quad i = 1, \dots, N, \quad (5.8b)$$

and approximate $\mathbf{E}(\mathbf{x})$ as follows:

$$\begin{aligned} \mathbf{E}_x(\mathbf{x}) &= \sum_{j=1}^N \mathbf{E}_x^j \chi_j(\mathbf{x}), \\ \mathbf{E}_{y,z}(\mathbf{x}) &= \sum_{j=1}^N \mathbf{E}_{y,z}^j \varphi_j(\mathbf{x}). \end{aligned} \tag{5.9}$$

We choose different basis function for \mathbf{E}_x and $\mathbf{E}_y, \mathbf{E}_z$ because Eq.(5.6) is a system of one first-order integro-differential equation for \mathbf{E}_x and two second-order for \mathbf{E}_y and \mathbf{E}_z . It is shown in the next subsection that one should use a basis function of one degree less in x for \mathbf{E}_x , in order to recover the correct dispersion relation. Otherwise, the discretized dispersion relation is polluted.

The boundary conditions have still to be incorporated into the weak form or imposed on the resulting matrix. This is discussed in the Sec.5.2.

5.1.3 Pollution problems

In this subsection we discuss the problem of mode pollution arising from the numerical method used to discretize the differential equation. This study is based on the work by Llobet et al [1990]. We extend it to the Maxwell equations in vacuum:

$$\nabla \wedge \nabla \wedge \mathbf{E}(\mathbf{x}) - \frac{\omega^2}{c^2} \mathbf{E}(\mathbf{x}) = 0, \tag{5.10}$$

considered in a 1-D slab geometry, assuming $\mathbf{E}(\mathbf{x}) = \mathbf{E}(x) \exp[i(k_z z - \omega t)]$ for simplicity and without loss of generality. Assuming a solution of Eq.(5.10) of

the form:

$$\mathbf{E}(\mathbf{x}) = \mathbf{E}_0 e^{i \mathbf{k} \cdot \mathbf{x}}, \quad (5.11)$$

we obtain the exact dispersion relation (EDR) for Eq.(5.10):

$$\frac{\omega^2}{c^2} = k^2 + k_z^2. \quad (5.12)$$

We want to compare it with the discretized dispersion relation (DDR) obtained with the finite element method. The matrix representing Eq.(5.10) is obtained by multiplying the equation by $\hat{\mathbf{e}}_v \eta_i^v(\mathbf{x})$, $v=x,y,z$, and integrating over x between x_{i-1} and x_{i+1} , which is the finite support of $\eta_i^v(\mathbf{x})$. We then make the ansatz that the solutions have the following form:

$$\mathbf{E}_w(\mathbf{x}) \approx \sum_j e^{i \mathbf{k} \cdot \mathbf{x}_j} \eta_j^w(\mathbf{x}), \quad w=x, y, z, \quad (5.13)$$

where $\eta_j^w(\mathbf{x})$ is the basis function used for approximating the component E_w . We then obtain the DDR, $\det \underline{\underline{D}}=0$, with:

$$D_{vw} = \sum_j e^{i \mathbf{k} \cdot \mathbf{x}_j} \int_{x_{i-1}}^{x_{i+1}} dx \left[(\nabla \wedge \hat{\mathbf{e}}_v \eta_i^v(\mathbf{x})) \cdot (\nabla \wedge \hat{\mathbf{e}}_w \eta_j^w(\mathbf{x})) - \frac{\omega^2}{c^2} \eta_i^v \delta_{vw} \eta_j^w \right], \quad (5.14)$$

where $\nabla=(d/dx, 0, ik_z)$, δ_{vw} is the Kronecker delta and $v,w=x,y,z$. We first take linear basis functions for each component, $\eta_i(x)=\varphi_i(x)$ (Fig.5.1b), and we obtain:

$$\underline{\underline{D}} = \begin{pmatrix} \left(\frac{\omega^2}{c^2} - k_z^2\right) \tilde{G}_0 & 0 & -i k_z G_1 \\ 0 & \left(\frac{\omega^2}{c^2} - k_z^2\right) \tilde{G}_0 + G_2 & 0 \\ -i k_z G_1 & 0 & \frac{\omega^2}{c^2} \tilde{G}_0 + G_2 \end{pmatrix},$$

where

$$\tilde{G}_0 = \frac{2 + \cos kh}{3},$$

$$G_1 = i \frac{\sin kh}{h},$$

$$G_2 = -\frac{2(1 - \cos kh)}{h^2},$$

$$h = x_i - x_{i-1} = x_{i+1} - x_i.$$

Thus, for the "linear—linear" case, the DDR is defined by:

$$\begin{aligned} \left\{ \left(\frac{\omega^2}{c^2} - k_z^2\right) \tilde{G}_0 + G_2 \right\} \times \left\{ \frac{\omega^2}{c^2} \tilde{G}_0 \left[\left(\frac{\omega^2}{c^2} - k_z^2\right) \tilde{G}_0 + G_2 \right] - k_z^2 (\tilde{G}_0 G_2 - G_1^2) \right\} \\ \equiv DYY_{||} \times DXZ_{||} = 0. \end{aligned} \quad (5.15)$$

As

$$\tilde{G}_0 G_2 = -\frac{2}{3h^2} (2 - \cos kh - \cos^2 kh) \neq G_1^2 = -\frac{(1 - \cos^2 kh)}{h^2},$$

we see that the second term in Eq.(5.15), $DXZ_{||}$, gives rise to a different DDR than the first term $DYY_{||}$. This is clearly seen in Fig.5.2, where the EDR, $DYY_{||}=0$, and $DXZ_{||}=0$, normalized to k_z^2 , are plotted. Note that this last

equation produces two extra non-physical roots, which is the spectral pollution due to the numerical scheme.

To avoid this pollution, one should use a different basis function for E_x , of one degree less in x , as the differential equation is only first-order in E_x and second-order in the other components. Using a piece-wise constant basis for E_x and linear ones for E_y, E_z , referred as the "piece-wise constant—linear" case, we obtain:

$$\underline{\underline{D}} = \begin{pmatrix} \frac{\omega^2}{c^2} - k_z^2 & 0 & -i k_z \frac{1 - e^{-ikh}}{h} \\ 0 & (\frac{\omega^2}{c^2} - k_z^2) \tilde{G}_0 + G_2 & 0 \\ i k_z \frac{1 - e^{ikh}}{h} & 0 & \frac{\omega^2}{c^2} \tilde{G}_0 + G_2 \end{pmatrix},$$

which gives the following DDR:

$$DYY_{11} \times \left\{ \frac{\omega^2}{c^2} DYY_{11} - k_z^2 (G_2 + 2 \frac{1 - \cos kh}{h^2}) \right\} = \frac{\omega^2}{c^2} DYY_{11}^2 = 0,$$

as $G_2 = -2 \frac{(1 - \cos kh)}{h^2}$. The DDR is no longer polluted.

In the case of Hermite-cubic basis functions, it becomes much more complicated to calculate the DDR, as we have to integrate all the combinations of γ, ψ and their first derivatives. This has been done with the software Mathematica, and the resulting matrices are given in Appendix E. The matrix $\underline{\underline{D}}$ can be schematically written as:

$$\underline{\underline{D}} = \begin{pmatrix} \underline{\underline{d}}_{xx} & 0 & \underline{\underline{d}}_{xz} \\ 0 & \underline{\underline{d}}_{yy} & 0 \\ \underline{\underline{d}}_{zx} & 0 & \underline{\underline{d}}_{zz} \end{pmatrix},$$

where $\underline{\underline{d}}_{vw}$ are 4x4 matrices as there are two basis functions per node and per component:

$$E_w = \sum_j E_w^{j,1} \eta_j^1(x) + E_w^{j,2} \eta_j^2(x), \quad w = x, y, z,$$

where $\eta_j^1(x)$ and $\eta_j^2(x)$ are the two basis functions shown in Fig.5.1d. In this case, DYY_{cc} and DXZ_{cc} are defined by:

$$\begin{aligned} DYY_{cc} &= \det(\underline{\underline{d}}_{yy}), \\ DXZ_{cc} &= \det\left(\begin{array}{cc} \underline{\underline{d}}_{xx} & \underline{\underline{d}}_{xz} \\ \underline{\underline{d}}_{zx} & \underline{\underline{d}}_{zz} \end{array}\right). \end{aligned} \tag{5.16}$$

Their complete expressions are given in Appendix E, Eq.(E.2). They are plotted in Fig.5.3. We see that $DYY_{cc}=0$, Fig.5.3a, reproduces well the EDR, whereas $DXZ_{cc}=0$, Fig.5.3b, has an additional root in the evanescent region, i.e. when $\omega^2/c^2 k_z^2 < 1$. With the same argument as before, we use quadratic basis functions for E_x and Hermite-cubics for E_y, E_z . In this case, DXZ_{qc} , Eq.(E.4), is such that:

$$DXZ_{qc} = \frac{2\omega^2}{45c^2} (3 - \cos kh) DYY_{qc}.$$

Thus $DXZ_{qc}=0$ is equivalent to $DYY_{qc}=0$ and the DDR in the "quadratic—cubic" case reproduces well the EDR without any spurious mode.

We have introduced these different possibilities of approximating the solution in the code ISMENE [Appert et al, 1986a and 1987], taking out the plasma contribution, and we solve Eq.(5.12) with $\omega/c=0.016$ m/s (which corresponds to $\omega/\omega_{cD}=0.1$, with $B_0=1T$) and $k_z=0.03$ m⁻¹. The EDR gives $k_x=\pm i 0.0254$ m⁻¹ and the spurious modes obtained from $DXZ_{ll,cc} = 0$ with $h=0.01$ m, Eq.(5.15) or (5.16), in the two polluted cases are:

$$\begin{aligned} \text{linear—linear} & : \quad k_x = 165.6 \text{ m}^{-1} \Rightarrow 26.4 \text{ wavelengths in } [0,1]; \\ \text{cubic—cubic} & : \quad k_x = 116.3 \text{ m}^{-1} \Rightarrow 18.5 \text{ wavelengths in } [0,1]. \end{aligned}$$

We see in Figs.5.4a and c that the numerical results do exhibit the corresponding spurious mode and that the solution obtained with piece-wise constant—linear and quadratic—cubic basis are pollution free (Figs.5.4.b, d).

Note that we have plotted the imaginary part of dE_x/dx in Fig.5.4 instead of E_x , because the spurious mode has a small amplitude in the cubic—cubic case and cannot be seen on the function itself. But due to the large value of the wavenumber of the unphysical mode, it appears on the derivative. This seems in fact quite general for the cubic—cubic numerical scheme and means that the pollution is not so dramatic in this case, except if one explicitly needs the derivatives for a diagnostic.

We can also calculate, with the DDR defined by $DYY_{ll,cc}=0$, the minimum value of points per wavelength, λ/h , needed to obtain a relative error of 1% and 0.1%, for example, of the exact value. This gives us an idea of the accuracy of the finite element method using linear or cubic basis functions, which can be useful for the complete problem as well. We have done this for two cases: $k_z=3$ m⁻¹ and $\omega^2/c^2=51$ or 0.1 m²/s². We obtain typical values of $\lambda/h(1\%)=2$ and $\lambda/h(0.1\%)=2-3$, with cubic basis functions; $\lambda/h(1\%)=13$ and $\lambda/h(0.1\%)=40$

with linear basis. Thus, with 2 or 3 points per wavelength the numerical result is very accurate with cubics, whereas one needs 13 to 40 points with the linear basis to obtain the same accuracy. Therefore, the use of quadratic—cubic is much more advantageous than piece-wise constant—linear. In our case, however, we have used the latter method, because of simplicity and especially because the explicit expression of the basis functions is used in a lengthy analytical calculation for evaluating the kernel contribution (Sec.5.3). However, with the help of a software like Mathematica and with the know-how acquired during this work, the introduction of quadratic—cubic basis functions could be a worthwhile future improvement of the code.

5.2 Boundary conditions

There are many different possible boundary conditions. In the electrostatic case, it makes no real sense to assume that the source is in vacuum. Thus we specify the boundary conditions at x_{pl} and x_{pr} . The weak form of Eq.(3.10) is of the form:

$$\int dx v'(x) \Phi'(x) + k_{//}^2 \int dx v(x) \Phi(x) + \int dx v(x) \int dx' K(x, x') \Phi(x') = v(x) \Phi'(x) \Big|_{x_{pl}}^{x_{pr}} . \quad (5.17)$$

Thus, for simplicity, we choose the following natural boundary conditions:

$$\begin{cases} \Phi'(x_{pl}) = 0, \\ \Phi'(x_{pr}) = 1, \end{cases} \quad (5.18)$$

which simulates an oscillating surface charge on the right-hand side of the

plasma. These boundary conditions are called "natural", because they can be introduced directly in the boundary term of the weak form resulting from the integration by parts.

In the E.M. case, we shall use two kinds of boundary conditions. First, we assume that the plasma is surrounded by vacuum, in which there is an infinitely thin sheet of antenna current in the (y,z) plane, with radial feeders and imposing $\nabla \cdot \mathbf{j} = 0$ for simplicity. The vacuum is bounded by perfectly-conducting walls. This set-up (Fig.5.5) is adequate to simulate waves launched by antennae in the ICRF. It allows one to compute the power emitted by the antenna and its impedance. The other set-up is used to simulate waveguide launching. In this case, we specify the tangential component of the electric field at the boundaries. Note that, with the finite element method, it is very easy to implement new boundary conditions.

5.2.1 Plasma-vacuum-antenna-wall interfaces

We assume the set-up shown in Fig.5.5, which simulates a diameter of a tokamak cross-section. The antenna current is defined by:

$$\mathbf{j}_a = (J_y \mathbf{e}_y + J_z \mathbf{e}_z) \delta(x - x_a) + j_x H(x - x_a) \mathbf{e}_x, \quad (5.19)$$

with $j_x = -i(k_y J_y + k_z J_z)$, assuming $\nabla \cdot \mathbf{j} = 0$, and where $\mathbf{j}_a = \mathbf{j}_a \exp[i(k_y y + k_z z - \omega t)]$, $\delta(x - x_a)$ is the Dirac distribution, and $H(x - x_a)$ the Heaviside function. The term j_x represents the current in radial feeders between the antenna and the wall which closes the loop. Thus one has to solve the Maxwell equations in vacuum with an external current \mathbf{j}_a . The boundary conditions are the following, assuming no surface currents at the plasma-vacuum interfaces:

plasma-vacuum ($x=x_{pl}$ and $x=x_{pr}$):

$$E_y, E_z \text{ continuous,} \quad (5.20a)$$

$$B_y, B_z \text{ continuous;} \quad (5.20b)$$

sheet antenna at $x=x_a$:

$$E_{y,z}(x_a^-) = E_{y,z}(x_a^+), \quad (5.21)$$

$$\mathbf{e}_x \wedge \mathbf{B}(x_a^+) - \mathbf{e}_x \wedge \mathbf{B}(x_a^-) = \mu_0 (J_y \mathbf{e}_y + J_z \mathbf{e}_z);$$

perfectly-conducting shells ($x=x_{sl}$ and $x=x_{sr}$):

$$E_y, E_z = 0. \quad (5.22)$$

With these sixteen boundary conditions, we can solve the Maxwell equations in the four regions $[x_{sl}, x_{pl}]$, $[x_{pl}, x_{pr}]$, $[x_{pr}, x_a]$, and $[x_a, x_{sr}]$, and connect the solutions.

In a 1-D slab geometry, it is simple to solve the Maxwell equations in vacuum with a current given by Eq.(5.19), using 1-D Green's function or the solution of the homogeneous equation. We obtain the following relations for B_y , B_z in terms of E_y , E_z at the plasma-vacuum interfaces [Vaclavik and Appert, 1991, p.1957-1960]:

$$B_y(x_{pr}) = -\frac{i}{\omega} \frac{H_p}{H'_p} [k_y k_z E_y(x_{pr}) + (\frac{\omega^2}{c^2} - k_y^2) E_z(x_{pr})] \quad (5.23a)$$

$$+ \frac{\mu_0}{\kappa^2} [\frac{\omega^2}{c^2} \frac{F_a}{F_p} J_z + k_y k_z \frac{H'_a}{H'_p} \eta_0],$$

$$B_z(x_{pr}) = \frac{i}{\omega} \frac{H_p}{H'_p} \left[\left(\frac{\omega^2}{c^2} - k_z^2 \right) E_y(x_{pr}) + k_y k_z E_z(x_{pr}) \right] + \mu_0 \frac{H'_a}{H'_p} \eta_0, \quad (5.23b)$$

with

$$\kappa^2 = k_z^2 - \frac{\omega^2}{c^2}, \quad k_x^2 = \kappa^2 + k_y^2,$$

$$\eta_0 = J_y - i \frac{k_y}{k_x} j_x,$$

$$F(x) = \frac{\sinh [k_x(x - x_{sr})]}{k_x}, \quad F_p = F(x_{pr}), \quad F_a = F(x_a),$$

$$H(x) = \cosh [k_x(x - x_{sr})], \quad H_p = H(x_{pr}), \quad H_a = H(x_a),$$

$$G(x) = \frac{\sinh [k_x(x - x_a)]}{k_x}, \quad G_p = G(x_{pr}).$$

The values of B_y , B_z at $x=x_{pl}$ are obtained by replacing x_{pr} by x_{pl} and setting $J_y=J_z=0$ in Eq.(5.23).

The power emitted by the antenna in the "volume" V_a between x_a and x_{sr} , defined by the right-hand side of Eq.(2.26):

$$\tilde{P} = P + iP_c = -\frac{1}{2} \int_{V_a} dV \mathbf{E}^* \cdot \mathbf{j}_a = -\frac{1}{2} \int_{V_a} dV [\operatorname{Re}(\mathbf{E}^* \cdot \mathbf{j}_a) + i \operatorname{Im}(\mathbf{E}^* \cdot \mathbf{j}_a)],$$

is also directly obtained in terms of $E_y(x_{pr})$ and $E_z(x_{pr})$:

$$\tilde{P} = \frac{1}{2} \frac{\omega^2}{c^2 \kappa^2} J_z E_z^*(x_a) + \frac{1}{2} \frac{i\omega}{c \kappa^2} \eta_0 B_z^*(x_a) + \frac{1}{2} i \omega \mu_0 \frac{(x_{sr} - x_a)}{k_x^2} |j_x|^2, \quad (5.24)$$

where

$$E_z^*(x_a) = \frac{F_a}{F_p} (E_z^*(x_{pr}) + i\mu_0 \omega J_z^* G_p),$$

$$B_z^*(x_a) = -\frac{i}{\omega} \frac{H'_a}{H'_p} \left[\left(\frac{\omega^2}{c^2} - k_z^2 \right) E_y^*(x_{pr}) + k_z^2 E_z^*(x_{pr}) \right] - \mu_0 \eta_0 \frac{H'_a}{H_a} \left(1 - \frac{H'_a G'_p}{H'_p} \right).$$

At this point, we have to solve Eq.(5.7) with the four boundary conditions expressing the continuity of B_y , B_z at x_{pl} and x_{pr} , Eq.(5.20b). Note that B_y , B_z come naturally in the boundary term of Eq.(5.7). After solving Eq.(5.7), we obtain $\mathbf{E}(\mathbf{x})$ in the plasma and we can introduce the value of $E_y(x_{pr})$, $E_z(x_{pr})$ in Eq.(5.24) to obtain the power emitted by the antenna.

Note also that for a pure helical antenna without feeders ($j_x=0$), or for an antenna with $J_z=0$, one can define the total current in the antenna as [Vaclavik and Appert, 1991, p.1959]:

$$I = J_y \int_{-\frac{\pi}{2k_z}}^{\frac{\pi}{2k_z}} e^{ik_z z} dz = \frac{2}{k_z} J_y, \quad (5.25)$$

and therefore we can define the antenna impedance Z by:

$$Z = \frac{2\tilde{P}}{I^2} = \frac{k_z^2 \tilde{P}}{2|J_y|^2}. \quad (5.26)$$

5.2.2 Plasma-waveguide interface

In this case, we assume that the plasma reaches the waveguide at $x=x_{pr}$, and impose the value of E_y , E_z corresponding to the waveguide spectrum for

each k_y, k_z . At the left-hand side ($x=x_{pl}$), we also impose the value of E_y and E_z . Note that there can still be vacuum near the waveguide if the density of the guiding centers $n(x)$ vanishes at $x''=x''_{pr} < x_{pr}$. But it is solved numerically within Eq.(5.7), for simplicity, and thus does not give rise to additional boundary conditions. Note that in this case, the boundary conditions are called essential conditions, because they have to be imposed on the functional space spanned by the basis functions.

Solving the equations twice and calculating $\mathbf{B}(x_{pr})$, we can determine the admittance matrix defined by:

$$\begin{pmatrix} B_y \\ B_z \end{pmatrix} (x_{pr}) = \underline{\underline{Y}}(k_y, k_z) \begin{pmatrix} E_y \\ E_z \end{pmatrix} (x_{pr}), \quad (5.27)$$

or the impedance matrix $\underline{\underline{Z}}(k_y, k_z) = \underline{\underline{Y}}^{-1}(k_y, k_z)$. This matrix can be used to analyse the matching between the waveguide and the plasma. If a complete k_y, k_z spectrum needs to be solved, one has to solve Eq.(5.7) for each k_y, k_z and then reconstruct the total tangential fields. Note that this can also be done with an antenna spectrum in the case discussed in Sec.5.2.1.

From the solution in the plasma, we can also compute the power absorbed by the particles, as well as the reactive power in the plasma, $\bar{P}_c(x_{pl})$, by using Eq.(4.19) and an equation obtained by taking the imaginary part in Eq.(2.23) instead of the real part. In this way, we can define a quality factor Q :

$$Q = \frac{\text{total reactive power}}{\text{total absorbed power}} = \frac{\bar{P}_c(x_{pl})}{\bar{P}_L(x_{pl})}, \quad (5.28)$$

where we have used the definition given in Eq.(3.20). This quality factor can be

defined in the same way as for an antenna, using the imaginary and real parts of \tilde{P} . This allows us to study the effect of different parameters on Q , where smaller values of Q denote better coupling conditions.

5.3 Numerical integration of the kernel

The contribution of the kernel to the matrix, obtained by introducing Eqs.(5.8) and (5.9) into (5.7), is given by:

$$\sum_{w=x,y,z} \sum_{j=1}^N \int_{x_{j-1}}^{x_{j+1}} dx \eta_i^v(x) \int_{x_{j-1}}^{x_{j+1}} dx' K_{vw}(x, x') \eta_j^w(x'),$$

(5.29)

for $i=1, \dots, N; v=x, y, z,$

where

$$\eta_m^t(x) = \begin{cases} \chi_m(x), & \text{for } t = x, \\ \phi_m(x), & \text{for } t = y \text{ and } z. \end{cases}$$

In this Section we shall only discuss the computation of the integral part of Eq.(4.10), symbolized by Eq.(5.29), using the finite element method described in Sec.5.1 with the basis functions given in Eq.(5.8). The other contributions, from $\nabla \wedge \mathbf{G}^* \cdot \nabla \wedge \mathbf{E}$ and $\omega^2/c^2 \mathbf{G}^* \cdot \mathbf{E}$, are straightforward to calculate. We generally use Gaussian quadrature formulae with 2, 4 or 6 points in our codes for computing the different integrals.

However, due to the singular points mentioned in Sec.3.2, Eq.(3.13), we cannot integrate over θ the kernel ($\underline{\epsilon} \mathbf{E}$), Eq.(4.10), as it stands, because near the

singular points it reduces to integrating a $1/\theta$ function. One solution is to perform the changes of variables $x'' \rightarrow z$ and $x' \rightarrow y$, proposed in Sec.3.2, and integrate with Gaussian quadrature over x , θ , y , and z . In this way the integrand is regular, but the limits of integration for y and z depend on the other variables and thus have variable length. This needs a little analytical work, is easy to program, but is very time-consuming. Therefore, we have used another method which consists in integrating analytically over two variables, each integration removing one of the two singularities. In the electrostatic case, we integrate analytically over x'' and x' , where the x'' interval is cut into many small homogeneous layers. In the E.M. case, however, this method leads to small errors at each interface between two x'' sub-intervals. Therefore, we have changed the method and we integrate analytically over x' and x , and numerically over x'' and θ . We shall only describe the latter method in this Section.

Let us first note that we use explicitly the basis functions, as we integrate over x and x' analytically. Therefore we remove the flexibility of changing the basis functions for better accuracy, which normally exists in finite element methods. However, the gain in computing-time justifies this choice. Another advantage of integrating analytically is that one uses less points for x and x' , as the number of Gaussian points per interval are not needed for the quadrature.

We first integrate Eq.(5.29) over x' . We shall detail here the calculation of the zz contribution, in order to show the procedure and exhibit the difficulties. The terms dependent on x' in the $[x_j, x_{j+1}]$ interval are:

$$A_v \equiv \int_{x_j}^{x_{j+1}} dx' \varphi_v^z(x') \exp \left\{ - \frac{(x-x')^2 (1+\cos\theta)}{4\rho_\sigma^2 \sin^2\theta} - \frac{(x'' - \frac{x+x'}{2})^2 (1-\cos\theta)}{\rho_\sigma^2 \sin^2\theta} \right\}, \quad (5.30)$$

with, for $v=j, j+1$ and $x' \in [x_j, x_{j+1}]$:

$$\begin{aligned}\varphi_j^z(x') &= \frac{x' - x_{j+1}}{x_j - x_{j+1}} \equiv \frac{x' - \bar{x}_{j+1}}{\Delta_{jj+1}} \equiv \bar{\varphi}_j(x', \bar{x}_{j+1}), \\ \varphi_{j+1}^z(x') &= \frac{x' - x_j}{x_{j+1} - x_j} = -\frac{x' - \bar{x}_j}{\Delta_{jj+1}} = -\bar{\varphi}_j(x', \bar{x}_j).\end{aligned}$$

Thus, replacing $\varphi_j^z(x')$ by $\bar{\varphi}_j(x', \bar{x}_{j+1})$, one can define $\bar{A}_j(\bar{x}_{j+1})=A_j$. In this way, A_{j+1} is directly obtained with $A_{j+1} = -\bar{A}_j(\bar{x}_j)$. Note that the sign $\bar{\quad}$ superposed is only to point out which term has to be substituted. Integrating Eq.(5.30) we obtain:

$$\bar{A}_j(\bar{x}_{j+1}) = \frac{\exp\left[-\frac{(x-x'')^2}{2\rho_\sigma^2}\right]}{\Delta_{jj+1}} \left[-\frac{\varepsilon}{2} e^{-x'^2} + (\Omega - \bar{x}_{j+1}) \frac{\sqrt{\pi}}{2} \operatorname{erf}(x') \right]_{(x_j - \Omega)/\varepsilon}^{(x_{j+1} - \Omega)/\varepsilon}, \quad (5.31)$$

with

$$\begin{aligned}\varepsilon &= \sqrt{2} \rho_\sigma \sin \theta, \\ \Omega &= \Omega(x) = x \cos \theta + x'' (1 - \cos \theta).\end{aligned}$$

Then, in the same way, we have to integrate the following terms over x (for the $[x_i, x_{i+1}]$ interval):

$$B_i = \bar{B}_i(\bar{x}_{i+1}) \equiv \int_{x_i}^{x_{i+1}} dx \bar{\varphi}_i(x, \bar{x}_{i+1}) \bar{A}_j = \bar{B}_i^1(\bar{x}_{i+1}) + \bar{B}_i^2(\bar{x}_{i+1}),$$

where we have separated \bar{A}_j , Eq.(5.31), into two terms: one obtained with the

$\exp(-x'^2)$ term, contributing to $\bar{B}_i^1(\bar{x}_{i+1})$, and one with the $\text{erf}(x')$, $\bar{B}_i^2(\bar{x}_{i+1})$. The first term can be integrated exactly and it yields:

$$\bar{B}_i^1(\bar{x}_{i+1}) = -\frac{\varepsilon}{2 \Delta_{ii+1} \Delta_{jj+1}} \left\{ [c_{j+1}(x, \bar{x}_{i+1})]_{g_i^{j+1}}^{g_{i+1}^{j+1}} - [c_{j+1}(x, \bar{x}_{i+1})]_{g_i^{j+1}}^{g_{i+1}^{j+1}} \right\}, \quad (5.32)$$

with

$$c_v(x, \bar{x}_{i+1}) = e^{-\alpha_v^2} \left[-\frac{\varepsilon}{2} e^{-x^2} + (p_v - \bar{x}_{i+1}) \frac{\sqrt{\pi}}{2} \text{erf}(x) \right],$$

$$\alpha_v^2 = \frac{(x'' - x_v)^2}{2 \rho_\sigma^2},$$

$$p_v = x_v \cos \theta + x'' (1 - \cos \theta),$$

$$g_\mu^v = \frac{x_\mu - p_v}{\varepsilon},$$

$$\mu = i, i+1 \quad , \quad v = j, j+1.$$

On the other hand, the second term, $\bar{B}_i^2(\bar{x}_{i+1})$, cannot be integrated analytically because of the error function. Nevertheless, as the error function does not vary much over its argument and even less over x , we can neglect its x dependence in the interval and evaluate it at the middle point. In the code, we have cut $[x_i, x_{i+1}]$ into two equal intervals and calculate the error function at $x=x_{i+1}/4$ and $x=x_{i+3}/4$, but here we report only the result using one interval for simplicity. The term $\bar{B}_i^2(\bar{x}_{i+1})$ can be integrated and it yields:

$$\bar{B}_i^2(\bar{x}_{i+1}) = \frac{\sqrt{2} \rho_\sigma}{\Delta_{ii+1} \Delta_{jj+1}} (\Delta \text{erf}) \left[\cos \theta H_1^{ij}(\bar{x}_{i+1}) + (x'' - \bar{x}_{i+1}) H_0^{ij}(\bar{x}_{i+1}) \right], \quad (5.33)$$

where

$$(\Delta \text{erf}) = \text{erf} \left[\frac{x_{j+1} - x''(1 - \cos \theta) - x_{i+1/2} \cos \theta}{\epsilon} \right] - \text{erf} \left[\frac{x_j - x''(1 - \cos \theta) - x_{i+1/2} \cos \theta}{\epsilon} \right],$$

$$H_0^{ij}(\bar{x}_{i+1}) = \left[-\frac{\rho_\sigma}{\sqrt{2}} e^{-x^2} + (x'' - \bar{x}_{i+1}) \frac{\sqrt{\pi}}{2} \text{erf } x \right]_{e_i}^{e_{i+1}},$$

$$H_1^{ij}(\bar{x}_{i+1}) = \frac{\rho_\sigma}{\sqrt{2}} \left[-(\sqrt{2} \rho_\sigma x + x'' - \bar{x}_{i+1}) e^{-x^2} + \frac{\rho_\sigma}{\sqrt{2}} \sqrt{\pi} \text{erf } x \right]_{e_i}^{e_{i+1}},$$

$$x_{i+1/2} = \frac{x_i + x_{i+1}}{2}, \quad e_\mu = \frac{x_\mu - x''}{\sqrt{2} \rho_\sigma}.$$

Note that the contribution B_{i+1} is easily obtained with:

$$B_{i+1} = -\bar{B}_i(\bar{x}_i) = -\bar{B}_i^1(\bar{x}_i) - \bar{B}_i^2(\bar{x}_i).$$

The contribution of the integral part of Eq.(4.10) to the zz component of the matrix is given by Eqs.(5.32) and (5.33). One sees that these terms are already quite long, even though the zz term of ($\underline{\epsilon}\mathbf{E}$) is rather simple. This explains why we did not use the quadratic—cubic basis functions. Note also that we have verified that the approximation with respect to the x-dependence of the error functions does not give a different result than when one integrates numerically over x, θ , y and z.

Repeating this procedure, we obtain all the terms of Eq.(5.29). They are reported in Appendix B as a reference for eventual future modification of the code SEMAL.

5.4 Local power absorption

The computation of the local power absorption $P_L(x)$, Eq.(4.19) or (3.19), is not as straightforward as it may appear at first glance. First, for each point x considered, one needs to compute three integrals over x'' , θ and θ' and two explicit summations over σ and n , which requires even more computing than for the kernel contribution. Moreover, we have to compute first the θ' integral and it needs the value of the field \mathbf{E} at points dependent on x , x'' and θ , which takes time to interpolate. Therefore, even though $P_L(x)$ is in fact only a diagnostic and does not require very high accuracy, the cpu-time needed is comparable, if not longer, with the time needed to solve Eq.(4.10). This is why we will discuss some numerical difficulties in computing $P_L(x)$ in this Section.

The integral over θ' needs to be examined in detail. First, when the harmonic number n is large, $\sin n\theta'$ and $\cos n\theta'$ are highly oscillatory and if \mathbf{E} is approximately constant in the interval $[x'' - |x-x''|/\cos\theta, x'' + |x-x''|/\cos\theta]$, the contribution integrates to zero. We see that there is a relation between n and the variation of the field, that is its derivatives. This can be seen by expanding \mathbf{E} around x'' in the θ' integrand of Eq.(4.19). It gives for the term proportional to E_x :

$$\sum_{k=0}^{\infty} \frac{1}{k!} \frac{\partial^k E_x(x'')}{\partial x^k} \left(\frac{|x-x''|}{\cos \theta} \right)^k \int_0^{\pi} d\theta' \cos^k \theta' \sin \theta' \sin n \theta' , \quad (5.34)$$

and similar terms for E_y and E_z . In this way, we can integrate over θ' [Gradshteyn, 1980, p.374]:

$$\int_0^\pi d\theta' \cos^k \theta' \sin \theta' \sin n \theta' = \frac{n}{k+1} \int_0^\pi d\theta' \cos^{k+1} \theta' \cos n \theta' \quad (5.35)$$

$$= \begin{cases} 0, & \text{if } k+1 < n \text{ or if } (k+1-n) \text{ is odd,} \\ \frac{\pi}{2^n}, & \text{if } k+1 = n, \\ \frac{\pi}{2^{k+1}} \frac{n}{k+1} \binom{k+1}{\frac{k+1-n}{2}}, & \text{if } k+1 \geq n+2, \end{cases}$$

where

$$\binom{m}{n} = \frac{m(m-1)\dots(m-n+1)}{n!}, \quad \binom{m}{0} = 1.$$

It gives for Eq.(5.34):

$$\sum_{\substack{k=n-1 \\ k+1-n \text{ even}}}^{\infty} \frac{1}{k!} \frac{\partial^k \mathbf{E}_x(\mathbf{x}'')}{\partial \mathbf{x}^k} \left(\frac{|\mathbf{x}-\mathbf{x}''|}{\cos \theta} \right)^k \frac{\pi}{2^{k+1}} \frac{n}{k+1} \binom{k+1}{\frac{k+1-n}{2}}. \quad (5.36)$$

Therefore, if $|\mathbf{x}-\mathbf{x}''|/\cos\theta$ is smaller than the characteristic length of the field, the first term contributing to the local power absorption for \mathbf{E}_x is the $(n-1)$ th derivative. It is the same for \mathbf{E}_y , but it is the n th derivative for the \mathbf{E}_z contribution. Thus, in this case, the numerical quadrature used for the θ' integral must be able to extract the contribution of the $(n-1)$ th or n th derivative of the field, which is quite difficult for $n \geq 4$. In order to obtain the best accuracy, the θ' mesh must be not only symmetric with respect to $\pi/2$ but also equidistant. This is similar to numerical Fourier series decomposition. However, if

$|x-x''|/\cos\theta$ is of the same order or greater than the characteristic length of the field, then Eq.(5.34) is useless but the numerical integration is much more accurate, as already the function itself contributes.

Note that we obtain the same result as in Eq.(5.36) if we first expand the Bessel functions $J_n(\xi')$ and $J_n(\xi'')$ in Eq.(3.17) (calculated in E.M. case) before calculating the inversion integrals. This can be seen from the fact that, due to the exponential term in Eq.(4.19), $|x-x''|/\cos\theta$ is of the order of ρ_σ , thus:

$$\frac{\partial^n E_x}{\partial x^n} \left(\frac{|x-x''|}{\cos\theta} \right)^n \approx k_x^n \rho_\sigma^n,$$

which is proportional to the lowest order of $J_n(k_x \rho_\sigma)$.

Using the same procedure for E_y, E_z and keeping the first two-lowest order contributing terms, we obtain:

$$P_L(x) = P_L^{n=0}(x) + \sum_{\sigma, n \neq 0} \int dx'' \int_0^{\pi/2} d\theta A_{n\sigma}(x, x'', \theta)$$

$$\left| \frac{\pi}{2^m(m-1)!} \left(\frac{|x-x''|}{\cos\theta} \right)^{m-1} \left\{ \frac{\partial^{m-1}}{\partial x^{m-1}} (E_x + i \frac{n}{|n|} E_y) - i \frac{(\omega - n\omega_{c\sigma})}{k_z n \omega_{c\sigma}} \frac{\partial^m E_z}{\partial x^m} \right. \right. \quad (5.37)$$

$$\left. \left. + \frac{|x-x''|^2}{4(m+1)\cos^2\theta} \left[\frac{\partial^{m+1}}{\partial x^{m+1}} (E_x + i \frac{m+2}{n} E_y) - i \frac{(\omega - n\omega_{c\sigma})}{k_z n \omega_{c\sigma}} \frac{\partial^{m+2} E_z}{\partial x^{m+2}} \right] \right\} \right|^2,$$

where

$$m = |n|,$$

$$A_{n\sigma} = \frac{2 n_{\sigma} q_{\sigma}^2 \omega_{c\sigma}^4}{\pi^{5/2} m_{\sigma} |k_z| v_{T\sigma//} v_{T\sigma\perp}^4} \frac{|x-x''|^4}{\cos^4 \theta} \exp \left[- \frac{(x-x'')^2}{2 \rho_{\sigma}^2 \cos^2 \theta} \right] e^{-\xi_{n\sigma}^2},$$

and

$$P_L^{n=0}(x) = \sum_{\sigma} \int dx'' \int_0^{\pi/2} d\theta A_{n\sigma}(x, x'', \theta) \left| \frac{\pi |x-x''|}{2 \cos \theta} \left[\frac{\partial E_y}{\partial x} - \frac{2\omega}{k_z \omega_{c\sigma}} \left(\frac{\cos^2 \theta}{|x-x''|^2} E_z + \frac{1}{4} \frac{\partial^2 E_z}{\partial x^2} \right) + \frac{|x-x''|^2}{8 \cos^2 \theta} \frac{\partial^3 E_y}{\partial x^3} \right] \right|^2.$$

One can easily identify the lowest order terms, for $n=0,1$ and 2 , with parts of the formula by Jaun and Vaclavik [1990], which is valid up to second order in $k_{\perp} \rho_{\sigma}$ but limited to $n=2$. Eq.(5.37) gives, for any harmonic, the two lowest-order terms of Eq.(4.19) with respect to the fields. That is, as we have kept the integral representation for $J_0(\xi)$ which relates ρ_{σ} with the characteristic length of the equilibrium parameters, Eq.(5.37) is only limited by the approximation of $J_m(\xi')$ which relates ρ_{σ} with the characteristic length of the fields. We show in Fig.5.6 the approximation of three Bessel functions, J_1 , J_3 and J_5 , with one (dotted lines) and two (dashed lines) terms. One clearly sees, in the second case, that the approximation is good for x larger than one, even for J_1 . In table 1, we show the points at which the relative error is equal to 10%. We see that the limit of validity of the expansion, fixed here at 10% of relative error, is approximately doubled if we keep the first two lowest-order terms. In this case, the limit of validity varies like $\sqrt{1.5n+2}$, and is larger than one already for $n=0$ with two terms. Therefore, the formula given in Eq.(5.37) is also valid for $k_x \rho_{\sigma}$ up to about this value, where k_x is the maximum wavenumber of the fields. Note that as we do not expand $J_0(\xi)$ and we keep the θ integral, we are not limited by

this term. This can save a lot of computing time because the complete formula, Eq.(4.19), is very time-consuming. It also eliminates computation errors which may appear at high n values and $k_x \rho_\sigma < \sqrt{1.5n+2}$, as mentioned above.

n	1 term	2 terms
0	0.6	1.4
1	0.87	1.89
3	1.23	2.6
5	1.51	3.14
10	2.04	4.21

Table 1: x values at which $|J_n(x)-f(x)|/J_n(x)=0.1$, where $f(x)$ is given by the first or two first terms in the expansion of $J_n(x)$

6. RESULTS OBTAINED WITH SEAL

In this Chapter we present the results obtained with the electrostatic code SEAL, which solves the electrostatic wave equation valid to all orders in Larmor radii, Eq.(3.10). Most of them have been reported by Sauter et al [1990a], but the first results were published at the EPS-conference in Dubrovnik [Sauter and Vaclavik, 1988]. Note that we had presented the model at the 2nd European Fusion Theory Conference in Varenna, Italy, in December 1987, which was the very beginning of this work.

6.1 Benchmarks

The main part of the study presented in this Chapter, Sec.6.2, is the comparison of the results obtained with our code SEAL and with the LMP experiment [Skiff et al, 1987], done at our institute, in which ion acoustic waves (IAW) and IBW are launched. This is why we choose the same parameters for the different studies presented in this Section. They are those of an argon plasma, with a charge number $Z_i=1$, density $n=10^{17}\text{m}^{-3}$, $T_e=14\text{ eV}$, $T_i=0.1\text{ eV}$, $B_0=0.2\text{T}$, and $k_z=100\text{m}^{-1}$. We first show a convergence study, Sec.6.1.1, and discuss the limits of integration for x , x' , and x'' in Eq.(3.10), Sec.6.1.2. Then we compare the wavelengths of the solution obtained with inhomogeneous temperature, density and magnetic field, with those obtained from the local dispersion relation, Sec.6.1.3.

6.1.1 Convergence study

A typical solution is shown in Fig.6.1. One sees that there is a sharp drop near the antenna, corresponding to the Debye screening effect. We have

zoomed the solution near the antenna in Fig.6.1b and we show how the mesh points were packed in order to verify that we resolve correctly this drop and that it has indeed a characteristic length of the order of the Debye length ($\lambda_{De}=9\cdot 10^{-5}m$, $\lambda_{Di}=7\cdot 10^{-6}m$, $\rho_e=4.4\cdot 10^{-5}m$). In the code, we automatically pack $N/10$ points in 10 Debye lengths on the right- and left-hand side of the plasma. The rest of the points are generally equally spaced in between, but can be packed as well if needed. For example, for $N=192$ points, we have packed 19 points at each side, i.e. about two points per Debye length, which leaves 154 points inside. Note that the characteristic length of the screening has a scale governed by ρ_e , λ_{De} and λ_{Di} . Therefore, in the code, we may pack mesh points near the edge according to any of these parameters. We cannot make a definite statement as to which parameter dominates, but it is in most cases the electron Larmor radius ρ_e .

The convergence study of the values of the real and imaginary parts of Φ at the antenna, i.e. at $x=x_{pr}$, is shown in Fig.6.2. We see that it starts to converge as $1/N^2$ for $N>192$, that is, as the solution has 25 short wavelengths in the plasma, when there are about 6 to 8 points per wavelength. This is a typical minimum number of points per wavelength with linear basis functions. This can also be seen on the whole solution in Fig.6.3, where we have cut off the points near the antenna. We show in this picture the real part of $\Phi(x)$ obtained with $N=160$ (dashed line), 192 (continuous line) and 256 (dots) points.

We also check the local power absorption formula, Eq.(3.19), and the accuracy of its computation. For this purpose, we compare it, for the electrons, with the expanded formula [Vaclavik and Appert, 1987] evaluated with the electrostatic approximation. In this case, $P_{Le}(x)$ should recover the expanded formula as $k_x\rho_e\approx 0.07$, except near the edge where the sharp drop is of the order of ρ_e . In Fig.6.4, we show $P_{Le}(x)$ calculated for $n=0$, and where a change of

variable from θ' to $x' = x'' - |x - x''| \cos \theta' / \cos \theta$ was performed, corresponding to the original formula published by Sauter et al [1990a]. We see that if we take enough points, $P_L(x)$ recovers exactly the expanded formula (Fig.6.4b). With a coarser mesh, $P_L(x)$ is much more oscillatory around the correct result, but if we compare the integrated power profile, $\bar{P}_{Le}(x)$, in Fig.6.5a, we see that there is less than 5% error and that the numerical oscillations are integrated out. Thus, for computing the diagnostic $\bar{P}_L(x)$, the coarse mesh is sufficient and is much less time consuming. Fig.6.5b shows how the power is distributed between the ions and the electrons in this case.

6.1.2 Discussion on guiding center profiles and integration limits

The limits of integration of x' and x'' have not been specified in Eq.(3.10). We discuss them in this Section in order to assess the problem of "particles which would hit the wall due to their very large Larmor radii". The limits for x and x' are the same and are specified by x_{pl} and x_{pr} . They are the limits of the interval over which Eq.(3.10) is solved. The limits of x'' are independent and are defined by x''_{pl} and x''_{pr} . They correspond to the points at which the guiding center density profile vanishes. However, the density of the particles does not vanish at x''_{pl} , x''_{pr} , due to their finite Larmor radius. Therefore, in general, $[x''_{pl}, x''_{pr}]$ should be included in $[x_{pl}, x_{pr}]$. The difference between them is determined by the density of the particles:

$$n_{\text{part}}(x) = \int d^3v f_{\sigma}^{\text{GC}} \left(x + \frac{vy}{\omega_{c\sigma}}, v_{\perp}, v_{\parallel} \right),$$

where f_{σ}^{GC} is the guiding center equilibrium distribution function. Assuming an isotropic Maxwellian:

$$n_{\text{part}}(\mathbf{x}) = \int d^3\mathbf{v} \frac{n_{\sigma\text{GC}}(\mathbf{x} + \mathbf{v}_y/\omega_{c\sigma})}{\pi^{3/2} v_{T\sigma\text{GC}}^3(\mathbf{x} + \mathbf{v}_y/\omega_{c\sigma})} \exp\left[-\frac{v_{\perp}^2 + v_{\parallel}^2}{v_{T\sigma\text{GC}}^2(\mathbf{x} + \mathbf{v}_y/\omega_{c\sigma})}\right],$$

where $n_{\sigma\text{GC}}$ and $v_{T\sigma\text{GC}}$ are determined by the density and temperature of the guiding centers. Assuming step profiles:

$$\begin{cases} n_{\sigma\text{GC}}(\mathbf{x}) = n_0, & T_{\sigma\text{GC}}(\mathbf{x}) = T_0, & \text{for } \mathbf{x} \in [x''_{\text{pl}}, x''_{\text{pr}}], \\ n_{\sigma\text{GC}}(\mathbf{x}) \equiv 0, & T_{\sigma\text{GC}}(\mathbf{x}) \equiv 0, & \text{otherwise,} \end{cases}$$

we obtain the following density profile for the particles:

$$n_{\text{part}}(\mathbf{x}) = \frac{n_0}{2} \left[\operatorname{erf}\left(\frac{x''_{\text{pr}} - x}{\sqrt{2} \rho_{\sigma}}\right) - \operatorname{erf}\left(\frac{x''_{\text{pl}} - x}{\sqrt{2} \rho_{\sigma}}\right) \right].$$

Both density profiles (G.C. and n_{part}) are plotted near x''_{pr} in Fig.6.6. We see that the density of the particles drops from n_0 to about zero in between $x''_{\text{pr}} - 2\rho_{\sigma}$ and $x''_{\text{pr}} + 2\rho_{\sigma}$. Therefore, $n_{\text{part}}(\mathbf{x})=0$ for $x > x''_{\text{pr}} + 2\rho_{\sigma}$, even though it never vanishes exactly. Thus, the x interval should be such that $x_{\text{pl}} < x''_{\text{pl}} - 2\rho_{\sigma}$ and $x_{\text{pr}} > x''_{\text{pr}} + 2\rho_{\sigma}$, if we want to connect to vacuum, in particular in the E.M. case. This is seen in Fig.6.7, where we have introduced a source at $x=0$, inside the plasma, and specified $[x_{\text{pl}}, x_{\text{pr}}]$ much larger than $[x''_{\text{pl}}, x''_{\text{pr}}]$. The solution behaves as if there is a plasma in between $x''_{\text{pl}} - 2\rho_{\sigma}$ and $x''_{\text{pr}} + 2\rho_{\sigma}$, and vacuum outside. However, one should mention that the solution inside $[x''_{\text{pl}} + 2\rho_{\sigma}, x''_{\text{pr}} - 2\rho_{\sigma}]$ is not modified if we take $x_{\text{pl}} = x''_{\text{pl}}$ and $x_{\text{pr}} = x''_{\text{pr}}$. Note that in the case of Fig.6.7, we have imposed $\Phi' = 0$ at $x_{\text{pl}}, x_{\text{pr}}$ as boundary conditions.

We can also calculate the perpendicular temperature profile of the particles, which determines the Larmor radius squared profile, defined by:

$$T_{\perp}^{\text{part}}(\mathbf{x}) = \frac{m_{\sigma}}{2 n_{\text{part}}(\mathbf{x})} \int d^3 \mathbf{v} v_{\perp}^2 f_{\sigma}^{\text{GC}} \left(\mathbf{x} + \frac{v_y}{\omega_{c\sigma}}, v_{\perp}, v_{\parallel} \right),$$

which yields:

$$W_{\perp}^{\text{part}} \equiv n_{\text{part}}(\mathbf{x}) T_{\perp}^{\text{part}}(\mathbf{x}) = \frac{n_0 T_0}{2} \left[\text{erf} \left(\frac{x''_{\text{pr}} - x}{\sqrt{2} \rho_{\sigma}} \right) - \text{erf} \left(\frac{x''_{\text{pl}} - x}{\sqrt{2} \rho_{\sigma}} \right) \right] \\ - \frac{T_0}{2 \sqrt{2\pi} \rho_{\sigma}} \left\{ (x''_{\text{pr}} - x) \exp \left[-\frac{(x''_{\text{pr}} - x)^2}{2 \rho_{\sigma}^2} \right] - (x''_{\text{pl}} - x) \exp \left[-\frac{(x''_{\text{pl}} - x)^2}{2 \rho_{\sigma}^2} \right] \right\}.$$

W_{\perp}^{part} and T_{\perp}^{part} are also shown in Fig.6.6 (dashed and dotted lines). We see that only the particles with very large Larmor radius (temperature) can exist at $x > x''_{\text{pr}}$, but the total perpendicular energy carried by these particles, W_{\perp}^{part} , is about zero at $x''_{\text{pr}} + 3\rho_{\sigma}$.

In all the results presented in this work, we have taken $x''_{\text{pl}} = x_{\text{pl}}$ and $x''_{\text{pr}} = x_{\text{pr}}$ for simplicity. It may be a little inaccurate within two Larmor radii of the edge, but it does not change the solution inside. Moreover, for realistic temperature profiles, the Larmor radius at the edge is very small anyway.

6.1.3 Comparison of the solution with the local dispersion relation

The dispersion relation, Eq.(3.8), obtained with the parameters defined at the beginning of this Chapter is shown in Fig.6.8. Two modes are present: the IAW, which is not sensitive to harmonic frequencies because the ratio T_e/T_i is large, and the IBW, which exists only above the fundamental. We have chosen these parameters because the two waves are "decoupled", which allows us to identify them more easily. The solution in a homogeneous plasma with these parameters and $\omega = 3.5\omega_{ci}$ was already shown in Sec.6.1.1 (Fig.6.1). At this

frequency, we obtain from Fig.6.8:

$$\lambda_{\text{ion ac.}}^{\text{WKB}} = 2.45 \text{ cm} \quad , \quad \lambda_{\text{Bernstein}}^{\text{WKB}} = 2.37 \text{ mm} \quad ,$$

where the superscript "WKB" means that it is the wavelength obtained from the local dispersion relation. The wavelength measured on the solution shown in Fig.6.3 are:

$$\lambda_{\text{ion ac.}}^{\text{sol.}} = 2.40 \pm 0.1 \text{ cm} \quad , \quad \lambda_{\text{Bernstein}}^{\text{sol.}} = 2.40 \pm 0.03 \text{ mm} \quad ,$$

which are in very good agreement with the local dispersion relation.

We shall now compare the solution with the local dispersion relation for two cases with a weak inhomogeneity, such that the WKB approximation is valid. First we study the case of inhomogeneous temperature profiles. As the IAW is sensitive mainly to electrons and the IBW to ions , we assume both T_e and T_i profiles inhomogeneous :

$$T_{\sigma}(x) = \frac{T_{\sigma}(x_{pl}) - T_{\sigma}(x_{pr})}{4 x_p^3} (x + x_p)^3 - 3 \frac{T_{\sigma}(x_{pl}) - T_{\sigma}(x_{pr})}{4 x_p^2} (x + x_p)^2 + T_{\sigma}(x_{pl}) ,$$

where $x_{pr} = -x_{pl} = x_p = 3 \text{ cm}$. That is, we take cubic profiles with zero slopes at the edges and :

$$\begin{aligned} T_e(x_{pl}) &= 30 \text{ eV}, & T_e(x_{pr}) &= 2.0 \text{ eV} , \\ T_i(x_{pl}) &= 0.5 \text{ eV}, & T_i(x_{pr}) &= 0.05 \text{ eV} . \end{aligned}$$

From the dispersion relation, we obtain the following wavelengths for both waves:

at $x = x_{pl} = -3$ cm	:	$\lambda_{ion\ ac.} = 3.8$ cm	$\lambda_{Bernstein} = 6.3$ mm ,
$x = 0$ cm	:	$\lambda_{ion\ ac.} = 2.4$ cm	$\lambda_{Bernstein} = 2.9$ mm ,
$x = x_{pr} = 3$ cm	:	$\lambda_{ion\ ac.} = 0.9$ cm	$\lambda_{Bernstein} = 2.1$ mm .

We see in Fig.6.9 that the solution agrees well with these values.

The second case is that of a nonuniform magnetic field. We introduce a "toroidal" profile proportional to $1/(R_0 \pm x)$, depending on whether the antenna is on the low field side (LFS) or the high field side (HFS) respectively. Note that this profile is slowly varying as assumed above. We have chosen $R_0 = 0.647$ m, such that for the HFS case $\omega/\omega_{ci} = 3.95$ at $x = x_{pl}$ and 3.60 at $x = x_{pr}$, and vice versa for the LFS case. From the dispersion relation, we expect the following wavelengths for the HFS case :

at $x = x_{pl}, \omega/\omega_{ci} = 3.95$:	$\lambda_{ion\ ac.} = 2.1$ cm	$\lambda_{Bernstein} = 4.3$ mm ,
$x = 0$ cm, $\omega/\omega_{ci} = 3.775$:	$\lambda_{ion\ ac.} = 2.2$ cm	$\lambda_{Bernstein} = 4.2$ mm ,
$x = x_{pr}, \omega/\omega_{ci} = 3.60$:	$\lambda_{ion\ ac.} = 2.4$ cm	$\lambda_{Bernstein} = 2.9$ mm .

The imaginary part of the solution from the SEAL code is shown in Fig.6.10. We expect a strong ion cyclotron damping of the ion Bernstein wave when ω is close to a harmonic, i.e. when ω/ω_{ci} approaches 4. This is clearly shown in Fig.6.10a, where the antenna is in a region where ω is far from a harmonic. Therefore both waves are well excited, but as the waves approach the left-hand side, the cyclotron damping is enhanced and the IBW is damped. On the other hand, when the antenna is on the LFS, (Fig.6.10b), i.e. in a region of a high ion cyclotron damping, only the IAW is launched. We see, however, that the IBW is reemitted on the left boundary, but naturally with a smaller amplitude than via direct launching (Fig.6.10a).

We have shown in this Section that our code SEAL gives correct results for different homogeneous and inhomogeneous profiles. We have discussed the convergence properties of the code in Sec.6.1.1 and the effect of the guiding center profiles in Sec.6.1.2. We shall now use this code to compare its results with those obtained in a Q-machine experiment performed in our institute.

6.2 Comparison with experiment

In this experiment, electrostatic waves are launched in a homogeneous cylindrical plasma of 2.5 cm radius and 5 meters length [Skiff et al, 1987]. Two plasmas have been studied : the first with argon, $n \cong 10^{17} \text{ m}^{-3}$, $B_0 \cong 0.2 \text{ T}$, $\omega/\omega_{ci} \cong 3.5$, $k_{//} \cong 200 \text{ m}^{-1}$, $T_e \cong 18 \text{ eV}$, and $T_i \cong 0.03 \text{ eV}$ and the second with barium, $n \cong 10^{16} \text{ m}^{-3}$, $B_0 \cong 0.25 \text{ T}$, $\omega/\omega_{ci} \cong 3.05$, $k_{//} \cong 30 \text{ m}^{-1}$, and $T_e = T_i \cong 0.1 \text{ eV}$.

The wave electrostatic potential in the argon plasma is shown in Fig.6.11a taken from Skiff et al [1987]. The corresponding numerical result is presented in Fig.6.11b and shows very good agreement. This is not, however, very surprising, as in this case the solution is approximately the sum of the two modes found in solving the dispersion relation. This was already done with a simpler model, Skiff et al [1987] and is due to the high ratio T_e/T_i and the decoupling of the modes in the dispersion relation, as mentioned before.

In the case of the barium Q-plasma, however, both temperatures are equal, which changes the dispersion relation dramatically (Fig.6.12). In isothermal plasmas, it is difficult to distinguish between the ion acoustic and the Bernstein branches, i.e. between the forward and backward propagating waves respectively. Another difficulty is the fact that the experimental plasma is drifting along the cylindrical axis with a non-negligible velocity v_{drift} .

Therefore there is a Doppler shift of the frequency, $k_{//} v_{\text{drift}}$, between the plasma and laboratory frames. Thus we expect an influence of the $k_{//}$ spectrum of the antenna, as a change in $k_{//}$ changes also the effective frequency of the wave. The antenna is made of two plates at the plasma edge with oscillating charges. The parallel wavenumber is determined by the size and separations of the plates along the magnetic field. Therefore $k_{//}$ is not uniquely defined, which is why we have computed the solutions for different $k_{//}$, introducing the Doppler shift. The sum of these solutions gives the final solution shown in Fig.6.13b. We can compare it with the experimental result, Fig.6.13a [Anderegg and Good, 1989], where we see that the wave has a very different behavior than in the case of argon. First, it seems that only one mode is present: in this case it is the IAW. Secondly, as the ion cyclotron damping is important, the wave is rather quickly damped over a few wavelengths. Fig.6.13 shows that both features, as well as the relative amplitudes along the wave, are well represented by the numerical result. It should be emphasized that no instabilities have been observed in the experiment, which is why our 1-D model was successful in describing it.

7. RESULTS OBTAINED WITH SEMAL

In this Chapter, we present the results obtained with the code SEMAL, which solves the E.M. Eq.(4.10), valid to all orders in Larmor radii. Note that we have not studied the effect of anisotropic temperature. In the first Section, we show a few benchmarks and check our code using the code ISMENE [Appert et al, 1986a and 1987]. Most of these results have been published by Sauter and Vaclavik [1990b], whereas the study of the nonlocal effects of α particles on second-harmonic heating, presented in Sec.7.2, have been reported by Sauter and Vaclavik [1991]. In Sec.7.3, we analyse the mode conversion of a plasma wave into an IBW near the cold lower-hybrid resonance in the scrape-off layer.

7.1 Benchmarks

7.1.1 Convergence study

We have studied the convergence properties of the code SEMAL in the Alfvén range of frequencies (AWRF). The plasma parameters are the following: $B_0=1$ T, $n_e=n_D=10^{19}$ m⁻³, $T_e=1000$ eV, $T_D=10$ eV, $k_y=0$ m⁻¹, $k_z=3$ m⁻¹, $\omega/\omega_{cD}=0.298$. The density and temperature profiles are parabolic, the equilibrium magnetic field is uniform and the antenna is purely poloidal ($J_z=0$). The ion temperature is taken very low to make sure that $k_{\perp}\rho_{\sigma}\ll 1$ and thus that we can compare the local and the nonlocal models. The imaginary part of E_x is shown in Fig.7.1, obtained with $N_x=16, 32$ and 64 points. With more than 64 points, we can no longer distinguish the solutions. In Fig.7.2 we show the real power emitted by the antenna, which is two orders of magnitude smaller than the imaginary part and is proportional to the real part of $E_y(x_{pr})$

in this case. We first compare, in Fig.7.2a, the results obtained with an equidistant mesh, but with two different numerical method for the x'' integration. With $NXPP=NX/2$, where $NXPP$ and NX are the number of intervals for the x'' and x meshes respectively, we take the Gaussian quadrature formula with two points, whereas with $NXPP=NX$, that is with the same mesh for x and x'' , we use a one middle-point formula, which just computes the value at the middle point times the interval width. Therefore, the two methods have the same number of integration points, but not the same accuracy, since the Gaussian formula is supposed to be better. However, in our case, due to the exponentials and the error function, and the relation which exists within the equations between x , x' and x'' , it is much better to take an equidistant integration point method. Note that one should not take the points $x''=x$ as integration points, because they would have too much weight, except if the Larmor radius scale is well resolved. This explains why the solution is very oscillatory with the Gaussian formula when the number of points is increased. Note that it is even worse when we take $NXPP=NX$ with the two Gaussian points formula. In Fig.7.2b, we have taken $NX=NXPP$, but used an equidistant mesh (circles) and a mesh packed very close to the plasma edge, within $10\rho_e$, like in the electrostatic case (Fig.6.1).

The convergence of $E_x(x_{pr})$ is much better, as seen in Fig.7.3. It is the same for $E_z(x_{pr})$. We compare here only the two different x'' meshes. We see that with a uniform mesh for the x'' integration points, $NXPP=NX$, both the real and imaginary parts of E_x converge like $1/NX^2$, as is the case with a linear basis function and a standard ODE.

The typical cpu-time needed is very difficult to specify exactly. Most of the time is spent in computing the kernel contribution, because it involves many nested loops. As mentioned in Sec.3.2, we do not calculate the contribution for

mesh points such that Eqs.(3.11-12) are not satisfied, that is for x , x' and x'' points too far apart. Thus, the number of times that the kernel is computed is proportional to the number of points per Larmor radius needed, which depends on λ/ρ_σ . For the cases presented in this Section, with equidistant mesh, the cpu-time is about $25 (NX/400)^2$ secs. However this number is much higher in the cases shown in Sec.7.2, because the alpha particle Larmor radius is much larger, of the order of 6 cm, which gives a width over which the kernel has to be calculated of more than 50 cm. The cpu-time needed, in addition to the number just stated, is about proportional to $(\rho_\sigma/\Delta x)^{1.5}$, where Δx is the width of a mesh interval.

Note that, due to this cutting, Eqs.(3.11-12), the x and x' loops have a length around 10. That is why we have used the θ loop as the innermost loop, in order to improve the vectorization. Nevertheless the length of this loop, typically between 20 to 40, is very short also and the scalar to vector ratio equals 2.5-3, which is not very high. However, as different parts of the kernel can be computed independently, parallel processing could be helpful on a multi-processor machine.

7.1.2 Comparison with ISMENE

In this Section, we compare the results obtained with the code SEMAL with those obtained with ISMENE [Appert et al, 1986a and 1987], in the AWRF. In this domain, we know that the ion Larmor radius is much smaller than the wavelengths and therefore that both codes should give essentially the same results. Fig.7.4a shows a frequency scan of the power emitted by the antenna obtained with the two models. The parameters used are similar to those of the previous Section; $n_e=n_D=10^{19}m^{-3}$, $T_e=1keV$, $T_i=10eV$, $B_0=1T$, $x_{sr}=-x_{sl}=12$ cm, $x_{pr}=-x_{pl}=8$ cm, $x_a=8.8$ cm, $k_y=5$ m⁻¹, $k_z=3$ m⁻¹, $s=1$ ($J_z=0$), deuterium plasma.

Density and temperature are taken to be homogeneous. For these parameters, $k_z c_A / \omega_{cD} = 0.3$, where $c_A^2 = B^2 / \mu_0 n m$ is the Alfvén velocity squared. The peaks due to the kinetic Alfvén wave (KAW) and to the surface mode of the fast magnetosonic wave (FW) can be seen in this picture. The first mode of the KAW lies at $\omega / \omega_{ci} = 0.296$ with ISMENE and 0.298 with SEMAL, confirming that SEMAL gives correct results. The imaginary part of E_x of the corresponding solution is shown in Figs.7.5 and 7.6, respectively. As in the electrostatic case, Chap.6, there is a sharp drop at the edge, Fig.7.6b, which scales as the electron Debye length, which is equal to $7.5 \cdot 10^{-5}$ m. The small wiggles in Fig.7.5 correspond to the spurious third branch present in the local model as discussed in Sec.2.2.2.

The peak of the surface mode has a slight shift in frequency between the two codes (Fig.7.4a). This is not surprising as this mode depends strongly on the boundary conditions which are quite different in the two models. Indeed, even though the vacuum, the antenna and the infinitely conducting shell are treated in exactly the same way, the density and temperature of the particles are different at the plasma-vacuum interface. As detailed in Sec.6.1.2, the profiles of the particles are continuous in the nonlocal model, whereas in the local model they are discontinuous. This difference has a strong effect on the surface mode in this case because the profiles are homogeneous and thus the step is very large. If we take inhomogeneous density and temperature profiles, Fig.7.4b, then the peaks overlap well. Note that both the position and the amplitude are identical. The step of the particle profiles in the local model has another effect at both sides of the trace in Fig.7.4a, where the emitted power obtained with ISMENE (solid line) becomes negative. This is why we have used at the lower part of the plot a "negative logarithmic" scale; the dots illustrate that the line would be continuous with a linear scaling. This non-physical feature is due to the discontinuity mentioned above, which gives rise to a large

surface energy flux, and is removed in the code SEMAL (dashed line). It also disappears in the local model when inhomogeneous profiles are used (Fig.7.4b). However, in this latter case, one needs to incorporate the gradients of equilibrium quantities in the dielectric tensor [Martin and Vaclavik, 1987], otherwise the power at the antenna stays negative even with inhomogeneous profiles. The effect of these gradients have been studied in more detail by Jaun et al [1991].

In Fig.7.7, we show the local power absorption of the electrons for $\omega/\omega_{ci}=0.298$ and with inhomogeneous profiles. The top curve is obtained with the second order expansion [Jaun and Vaclavik, 1990], whereas the three others are obtained using Eq.(4.19) with different x'' and θ' meshes. The first lowest curve (small dashes) is obtained with 25 intervals for each mesh, the second (continuous line) with 50 and the third one (dotted line) with 150 points. We see that we converge towards the results of the expanded formula, which we have also checked by using the value of the total absorbed power.

7.2 Effects of alpha particles on ICRF heating

We shall discuss in this Section the nonlocal effects of alpha particles on heating efficiency in ICRF, in particular on second-harmonic heating. This analysis is based on the work done by Hellsten et al [1985], where they have studied the effects of alpha particles on second-harmonic heating using a local model. Note that there have been other works related to this analysis: Van Eester et al, 1990; Kay et al, 1988; Batchelor et al, 1989c; Yamagiwa and Takizuka, 1988. As the Larmor radius of the alphas is very large, they cannot be treated using a local model, as is shown in Sec.7.2.1, and our code SEMAL is needed to quantify their effect on heating scenarii. Even though we find that the alpha particles absorb much less than is predicted by the local model, they still

have a dramatic effect on second-harmonic heating for a concentration n_α/n_e greater than 2 to 3% (Sec.2.3). We have also studied the influence of k_z and of the alpha particle temperature. This latter analysis also allows us to discuss the modelling of non-Maxwellian distribution functions with our code (Sec.7.2.2).

Most of the results presented in this Section have been reported by Sauter and Vaclavik [1991].

7.2.1 Limitations of the local model

In this subsection, we compare and discuss the results obtained with SEMAL and with ISMENE for the cases presented by Hellsten et al [1985, Figs.2 and 3]. Thus, we use the same standard Jet-like plasma parameters: $x_{pr}=-x_{p1}=1.25$ m, $B_0=2.71$ T, $R_0=2.96$ m, $B(x)=B_0R_0/(R_0+x)$, $k_z=5$ m⁻¹, $k_y=0$, $n_D=n_T=0.5 \cdot 10^{20}$ m⁻³, $n_e=10^{20}$ m⁻³, $T_e=T_D=T_T=5$ keV, $T_\alpha=3.5$ MeV, $x_{sr}=-x_{s1}=1.30$ m, $x_a=1.26$ m, $s=1$. The profiles of the guiding centers are proportional to $(1-0.95(x/x_{pr})^2)^\gamma$, with $\gamma=1$ for the density and $\gamma=2$ for the temperature. We keep the electron central density fixed and calculate the ion concentrations such as to satisfy the neutrality condition while maintaining $n_D = n_T$. The alpha particle density profile is also parabolic, but the temperature is homogeneous if not otherwise stated. The concentrations are always specified relative to the electron central density n_e .

The full hot-plasma dispersion relation, valid to all orders in Larmor radii, is shown in Fig.7.8 for the standard parameters with $n_\alpha/n_e = 1\%$. Note that harmonics up to $n=\pm 20$ were needed to correctly resolve the Bernstein wave near the resonances. Two cyclotron resonances occur inside the plasma, at $x=0$ and $x=1.0$ m. At $x=0$, we have $\omega=2\omega_{cD}=2\omega_{c\alpha}=3\omega_{cT}$, and at $x=1.0$ m, $\omega=4\omega_{cT}$. The

wavelength of the fast wave is about 10 cm throughout the plasma and between 1mm and 1cm for the Bernstein wave. Note that the Bernstein wave can be excited directly from the plasma edge and that it connects to the IBW branch below $4\omega_{cT}$. Note also that, above the second-harmonic of deuterium, the fast and Bernstein wave branches connect.

The effect of alpha particle concentrations from $n_{\alpha}/n_e=0$ to 1% is shown in Fig.7.9 for the local and nonlocal models with $\omega=2\omega_{cD}$ at the center. The integrated power not yet absorbed by the particles, $1 - \bar{P}_L(x)/\bar{P}_L(x_{pl})$ (Eq.(3.20)), is plotted versus x . We see that there is a great discrepancy between the two models. For $n_{\alpha}/n_e=1\%$, the local model predicts that 100% is absorbed by the alphas and none by the deuterium, while the nonlocal model gives 44% and 31% respectively. This difference can be explained by examining the local power absorption formula. For small $k_{\perp}^2 \rho_{\sigma}^2$, $P_L(x)$ (Eq.(3.19)) is proportional to $k_{\perp}^2 \rho_{\sigma}^2$, but inversely for large $k_{\perp}^2 \rho_{\sigma}^2$, as shall be seen in Sec.7.2.2. Therefore, the power absorbed by the alphas is overestimated by the local model, as already mentioned by Hellsten et al [1985], and is sufficiently high to absorb the wave completely before it reaches the cyclotron resonance at the center (Fig.7.9a). On the other hand, with the nonlocal model, Fig.7.9b, the wave reaches the center and much more power is absorbed by the deuterium. This is clearly seen in Fig.7.10, where we compare the real part of E_x obtained in both models with $n_{\alpha}/n_e=1\%$. With the local model, code ISMENE, the wave is completely absorbed already at $x=50$ cm, whereas with the nonlocal model, code SEMAL, it reaches the cyclotron resonance ($x=0$). However, another effect can compensate this, neglected in the local model, which is absorption at harmonics lying outside the plasma. For example, in the case considered, $\omega/\omega_{cD}=2.7$ at the plasma edge. Therefore no power can be absorbed by the deuterium at the third harmonic, whereas the alphas absorb as much power at the third harmonic (21.5% of total) as at the second harmonic (22.5%), due to their broad resonance

layer. Note also that the Bernstein wave excited at the plasma edge appears on E_x , but it only deposits a little energy to the electrons.

The limit to the second harmonic is in fact one of the main drawbacks of the local model for such scenarii. This is shown in Fig.7.11, where different scenarii at $\omega=2\omega_{cH}$, $2\omega_{c^3He}$, $2\omega_{cD}$ and $2\omega_{cT}$ at the center, are compared. They all have an alpha particle concentration of 1% and in the first two cases, 20% of hydrogen or 3He has been added. With ISMENE, the scenario tuned to the second harmonic of H is found to be much better than the others, whereas it is quite the opposite with SEMAL. This difference is essentially due to higher harmonic heating. Indeed, as $2\omega_{cH} = 4\omega_{c\alpha}$, resonances at the fourth to sixth harmonic of $\omega_{c\alpha}$ occur in the plasma and absorb most of the energy, but these resonances are neglected in the local model. Moreover, if the frequency is higher, the distance between two successive resonances is shorter and the number of cyclotron resonances between the center and the edge of the plasma is increased. As an example, we show in Fig.7.12 the power absorption density of the alphas for the case with hydrogen. We see that strong off-center power absorption occurs at the 5th (39%) and 6th (13%) harmonic compared with central absorption at the $n=4$ (11%). In this case, $P_\alpha/P_{tot}=63\%$ and $P_H/P_{tot}=35\%$.

7.2.2 Influence of T_α and modelling of non-Maxwellian distribution functions

In this subsection we shall discuss the effects of T_α and of the type of distribution function, always starting from the previous standard case of a D-T- α plasma with $n_\alpha/n_e=1\%$ and $\omega=2\omega_{cD}$ at the center.

The influence of T_α is shown in Fig.7.13. In Fig.7.13b, we have taken the same bi-quadratic profile for T_α as for the other species. We see that the power absorbed by the alphas is not at all proportional to T_α , confirming the fact that

the width of the cyclotron resonance is not the main factor, for k_z not too small. In both cases, there is a small interval where P_α is larger than P_D , which is around 1MeV for the homogeneous profile and 0.5MeV for an inhomogeneous one. These intervals correspond to parameters such that $k_\perp \rho_\alpha$ is of the order of 1 in the outer part of the plasma or near the center. In order to understand this feature, let us go back to the power absorption formula. If we assume a plane wave for \mathbf{E}_\perp and neglect E_z , as $|E_z| \ll |E_\perp|$ in all our cases, $P_L(x)$ is proportional to the following expression, changing x to $y = k_x(x-x)/\cos\theta$:

$$P_L(x) = \int_0^\pi d\theta \int dy \left(\frac{n_\sigma q_\sigma^2}{4\sqrt{\pi} m_\sigma} \right) \left(\frac{e^{-\xi_{n\sigma}^2}}{|k_z| v_{T\sigma}} \right) \left(\frac{y^3}{2k_x^4 \rho_\sigma^4} e^{-\left(\frac{y}{\sqrt{2} k_x \rho_\sigma}\right)^2} |E_+ J_{n-1}(y) + E_- J_{n+1}(y)|^2 \right).$$

The second term in brackets determines the width of the resonance layer and the last term gives the contribution of the fields modified by a form factor. Note that it is indeed the product $k_x \rho_\sigma$ which enters into this formula. Due to the Bessel function, this form factor is proportional to $(k_x \rho_\sigma)^n$ for small $k_x \rho_\sigma$, inversely proportional to $k_x \rho_\sigma$ for large $k_x \rho_\sigma$ and has a maximum in between. In Fig.7.14, we have plotted the contribution of E_x to the form factor, as it is the dominant component of the field, which reads:

$$g(k_x \rho_\sigma) = \int dy \frac{y^3}{2k_x^4 \rho_\sigma^4} e^{-\left(\frac{y}{\sqrt{2} k_x \rho_\sigma}\right)^2} |E_{x0} [J_{n-1} + J_{n+1}]|^2$$

$$= |E_{x0}|^2 \int dy \frac{2n^2 y}{k_x^4 \rho_\sigma^4} e^{-\left(\frac{y}{\sqrt{2} k_x \rho_\sigma}\right)^2} J_n^2(y),$$

where we have neglected the x dependence of E_{x0} . Fig.7.14 shows that the form factor g has a maximum for $k_x \rho_\sigma$ around $n/2$, which confirms the result obtained previously (Fig.7.13). For $n=2$, we have also plotted the expanded formula, which yields $g \approx (k_x \rho_\sigma)^2$ (large dots). We clearly see that for $k_x \rho_\sigma \geq 1$, it strongly overestimates the integral form.

This has another important consequence. It means that the amount of power absorbed between x and $x+dx$ mainly depends on the effective value of ρ_σ^2 around x . Therefore, if we want to approximate a non-Maxwellian distribution function with a Maxwellian, both should have the same effective ρ_σ^2 , defined as $\rho_\sigma^2 = \langle v_\perp^2 \rangle(x) / 2\omega_{c\sigma}^2$, where the perpendicular velocity squared is averaged over the equilibrium distribution function considered:

$$\langle v_\perp^2 \rangle(x) = \int dv v_\perp^2 f_\sigma^{(0)}(x, v) .$$

Note that for a Maxwellian, $\langle v_\perp^2 \rangle(x) = v_{T\sigma}^2(x)$. In order to illustrate this, we have compared the results obtained with a single Maxwellian and with a bi-Maxwellian, that is with two alpha species. For the bi-Maxwellian, we have taken: $T_{\alpha 1} = 0.4$ MeV, $T_{\alpha 2} = 1.2$ MeV and $n_{\alpha 1}/n_e = n_{\alpha 2}/n_e = 0.5\%$; and for the single Maxwellian: $T_\alpha = 0.8$ MeV and $n_\alpha/n_e = 1\%$. These values have been chosen such that the total alpha particle density and the effective value of ρ_σ^2 are the same, and such that they approximate the slowing-down distribution defined below. Fig.7.15 shows how they approximate the distribution and also the integrand of the $\langle v_\perp^2 \rangle$ integral assuming isotropic temperature:

$$\int dv v_\perp^2 f_\sigma^{(0)}(x, v) \approx \int dv v^4 f_\sigma^{(0)}(x, v) .$$

The results obtained with SEMAL show that both alpha power absorption profiles are very similar, as well as the total absorbed power. This shows that we can approximate any distribution function using a Maxwellian with $v_{T\sigma}^2(x) = \langle v_{\perp}^2 \rangle(x)$. In particular, the alphas are expected to have a slowing-down distribution function of the form [Koch, 1991]:

$$f_{\text{slow}}^{(0)} = \frac{3}{4\pi \ln\left(1 + \left(\frac{v_0}{v_c}\right)^3\right)} \frac{1}{v + v_c} \cdot H(v_0 - v),$$

$$v_c = \left(3\sqrt{\pi} \frac{m_{\alpha} + m_i}{m_{\alpha} m_i} m_e\right)^{1/3} \left(\frac{T_e}{m_e}\right)^{1/2},$$

where $H(v_0 - v)$ is the Heaviside function and $v_0 = 1.3 \cdot 10^7 \text{m/s}$ is the birth velocity of the alphas. Using the standard parameters and this slowing-down distribution function, we obtain $\langle v_{\perp}^2 \rangle_{\text{slow}} = 3.8 \cdot 10^{13} \text{m}^2/\text{s}^2$, which corresponds to a Maxwellian with $T_{\alpha} = 0.8 \text{MeV}$, which was used in Fig.7.15. We see that this equivalent Maxwellian temperature is much smaller than the 3.5MeV of the birth temperature. This has also been found by Koch [1991], by comparing the imaginary part of K_{xx} , the first term of the dielectric tensor, obtained with a Maxwellian and the slowing-down distribution function. In Fig.7.16, we show the equivalent Maxwellian temperature defined by $T_{\alpha} = \frac{1}{2} m_{\alpha} \langle v_{\perp}^2 \rangle_{\text{slow}}$ versus T_e . We see that the "effective" temperature of the alphas varies between 0.3 and 1.4 MeV for T_e between 0.01 and 100 keV.

7.2.3 Effects of k_z and alpha particle concentration

The effect of k_z on the power absorbed by the different species is shown in Fig.7.17 for the standard case ($T_{\alpha} = 3.5 \text{MeV}$, $n_{\alpha}/n_e = 1\%$, D-T). We see that $P_{\alpha}/P_{\text{tot}}$ only varies between 20 and 40%, for k_z not too small, but the distribution of the power between electrons, deuterium and tritium changes much more. This is

the same with T_α inhomogeneous. Note that for large k_z , electron absorption is important. For small k_z , P_D is smaller than P_α at the second harmonic, as mentioned by Kay et al [1988]. For $k_z \geq 2m^{-1}$ ($k_z R_0 \geq 6$), the main effect of k_z is to determine the amount of alpha power absorption near the edge at the highest harmonic.

The concentration n_α/n_e is, of course, the main parameter which determines the degradation of heating due to alpha particles. This is clearly seen in Fig.7.18, where we have taken $T_\alpha=0.8$ MeV, which is the effective alpha temperature as seen in previous subsection. For a concentration higher than 1 to 2%, more than 50% of the power is absorbed by the alphas for the standard case considered. This was also seen by Van Eester et al [1990] in a ITER-NET D-T scenario. The dramatic effect occurring in the homogeneous T_α case, Fig.7.18a, is mainly due to the enhancement of alpha power absorption at the third harmonic near the edge such that most of the power is absorbed before it reaches the center. Once again, it is not really due to a higher absorption at the second harmonic of alpha compared with the one at the second harmonic of deuterium. As an example, for $n_\alpha/n_e=6\%$, $P_\alpha/P_{tot}=87.8\%$ at the third harmonic, but only 10.8% at the second. Moreover, note that in the outer 45 cm ($x>80$ cm), already 86% and 1.6% is absorbed by the alphas at the third and second harmonic respectively, that is 87.6% of the total power. The alpha particle power absorption is particularly strong in this case, because $k_\perp \rho_\alpha \approx 3/2$, near the edge, which corresponds to a maximum of the form factor for the third harmonic, as discussed in previous subsection (Fig.7.14). However, in the case of inhomogeneous alpha particle temperature profile, Fig.7.18b, the value of $\xi_{3\alpha}$ is too large near the edge ($|\xi_{3\alpha}| > 2.5$ for $x > 80$ cm) and not much power is absorbed at the third harmonic of the alpha cyclotron frequency. Therefore, the power is absorbed in the central region, near $\omega=2\omega_{c\alpha}$, where the electrons can also contribute to the power absorption ($\xi_{0e} < 2.5$ for $x < 90$ cm). This is why the

power is distributed very differently: at $n_\alpha/n_e=6\%$, $P_\alpha/P_{tot}=2\%$ at the third harmonic and 83.5% at the second, and $P_e/P_{tot}=13.9\%$. Note also that 73.2% of the total power is absorbed for $x<50$ cm, 65% by the alpha and 7.5% by the electrons. If the alpha particle temperature near the edge is larger, $|\xi_{3\alpha}|$ is smaller and strong absorption occurs at the third harmonic. However the overall feature shown in Figs 7.18a and b remains essentially the same, except for small alpha concentrations.

7.2.4 Summary of the results on the effects of alpha particles on ICRF heating

The analysis of the effects of alpha particles on higher harmonic heating needs a model valid to all orders in Larmor radius. We have shown that the local model was not adequate, because it strongly overestimates the power absorbed by the alpha particles, because $k_x\rho_\alpha\geq 1$. Another effect which could not be seen in the local model is the absorption at a higher harmonic not present in the plasma, but sufficiently close to the edge such that strong absorption occurs in the outer part of the plasma, due to the temperature broadening of the cyclotron resonance layer. We have shown that this effect is in fact very important in the scenarii studied here, as the alpha particle temperature is very large. This can also be the case when tails of high energy ions are generated.

We have also studied the influence of the alpha particle temperature T_α . It shows, together with a study of the dependencies of $P_L(x)$, that the main parameter is the value of $k_\perp\rho_\sigma$ and that $P_L(x)$ has a maximum near $k_\perp\rho_\sigma \approx n/2$. Thus, a non-Maxwellian distribution function can be approximated by a Maxwellian such that the average Larmor radii are the same, i.e. such that $v_{T\sigma\perp}^2 = \langle v_\perp^2 \rangle$, where v_\perp^2 is averaged over the distribution function considered. This gives for the alphas, using a typical slowing-down distribution function,

an equivalent Maxwellian temperature between 0.4 and 1.2 MeV for T_e between 0.1 and 50 keV.

We have also seen that P_α/P_{tot} is not very sensitive to the value of k_z , provided that k_z is not too small. The main parameter is, of course, the alpha particle concentration. We have shown that, even though the alphas absorb much less power than expected from local model, they have a strong influence for $n_\alpha/n_e > 2\%$. If the alpha density or temperature profile is more peaked than that of the other species it decreases the alpha power absorption near the edge and greatly improves the heating scenario.

7.3. IBW launching through mode conversion at the lower-hybrid layer

The ion Bernstein wave (IBW) can be used to heat the plasma [Ono et al, 1988; Moody et al, 1988]. One method of launching IBW, already employed in DIII-D [Chiu et al, 1990] and which will be used for the Frascati Tokamak Upgrade (FTU), is via mode conversion of a slow wave to an IBW near the lower-hybrid layer $x=x_{LH}$, where $\omega=\omega_{LH}$ [Ono et al, 1983]. We have obtained the solution, using the FTU parameters given by Cesario [1990], for a few different values of $n_{//}=k_{//}c/\omega$. We wanted to see if the electric field near the conversion point becomes large enough to produce non-linear phenomena. A next step is to study the coupling for different $n_{//}$ and different distances between the antenna, or the waveguide, and the x_{LH} . This is left for a future study.

The set-up is shown in Fig.7.19. The limiter is at $x_{lim}=30$ cm, the waveguide mouth at $x_a=35$ cm, $B_0=7.9242$, the major radius is $R_0=93$ cm and $k_y=0$. A hydrogen plasma and a frequency of 433 MHz are considered. The density and temperature profiles are given by:

$$n_e(x) = n_i(x) = n_{\text{lim}} \exp \left[-\frac{x - x_{\text{lim}}}{\lambda_s x_a} \right], \quad n_{\text{lim}} = 5 \cdot 10^{19} \text{ m}^{-3}, \quad \lambda_s = 3.1052 \cdot 10^{-2},$$

$$T_e(x) = T_i(x) = T_{\text{lim}} \exp \left[-\frac{x - x_{\text{lim}}}{\delta_s x_a} \right], \quad T_{\text{lim}} = 50 \text{ eV}, \quad \delta_s = 8.8851 \cdot 10^{-2},$$

and are also shown in Fig.7.19. With these parameters, $x_{\text{LH}}=32.7$ cm. Note that, as $\omega_{\text{LH}}^2 \cong [\omega_{\text{ce}}^2 (\omega_{\text{ci}}^2 + \omega_{\text{pi}}^2) + \omega_{\text{pe}}^2 \omega_{\text{ci}}^2] / (\omega_{\text{ce}}^2 + \omega_{\text{pe}}^2) \cong \omega_{\text{pi}}^2$, we have at $x=32.7$ cm: $\omega_{\text{LH}} \cong 4.8 \omega_{\text{cH}}$. The fifth harmonic is located just outside the antenna, at 36.75 cm, and the fourth at 10.8 cm, where the IBW will ultimately be absorbed. The dispersion relations for $n_{\parallel}=0.5, 1, \text{ and } 5$ are shown in Figs.7.20a-c. One sees that, for small n_{\parallel} , there is an evanescent region in front of the waveguide, and the fast wave is coupled to the IBW near the lower-hybrid layer. For n_{\parallel} larger than unity, the fast wave has a cut-off on the high-field side of the lower-hybrid layer and is decoupled from the slow wave, which is propagatory near the waveguide.

The fields corresponding to the two cases shown in Figs.7.20c and a are presented in Figs.7.21a-b, respectively. They have been obtained by imposing $E_y=0$ on both sides, $E_z(x_{\text{pl}})=0$, $E_z(x_{\text{pr}})=2$, and $k_y=0$. In Fig.7.21a, $n_{\parallel}=5$, we clearly see the conversion of the propagatory slow wave to the IBW. The amplitude of the field at x_{LH} can be up to about 10 times larger than its value at the antenna. In the other case, $n_{\parallel}=0.5$, the wave is evanescent near the antenna, but the IBW is nevertheless excited. However, the amplitude of the field is smaller than in the first case, Fig.7.21a, where the waveguide couples to a propagatory wave.

Another important question, since one cannot control well the density profile in the scrape-off layer, is whether one can excite the IBW if the lower-hybrid layer is behind the waveguide. We show, in Fig.7.22, the solution

obtained by imposing the boundary conditions at $x_{pr}=32.6$ cm, i.e. $x_a=32.6$ cm, for the same values of $n_{//}$ and the same units as in Fig.7.21. The two solutions are very similar in this case, because the dispersion relation of the IBW does not depend much on $n_{//}$. One also sees that, even though the wave is essentially electrostatic, there is only a small Debye screening effect, due to the fact that the wavelength of the IBW is very short. However, the amplitude of the wave field is much smaller than when the waveguide couples to the slow wave (Fig.7.21a).

8. CONCLUSION

We have developed a nonlocal model based on the global wave approach and on the linearized Vlasov-Maxwell equations. It can be used to analyse electrostatic and electromagnetic (E.M.) waves in hot, magnetized, nonuniform, bounded plasmas. It is valid for arbitrary density and anisotropic temperature profiles in 1-D bounded geometry. The boundary conditions are arbitrary provided that they are consistent with the Maxwell equations. No assumption is made with respect to the size of the Larmor radii compared with the inhomogeneity scale lengths of the field and of the equilibrium density and temperature profiles, and is therefore valid also for high harmonics. The inhomogeneity is along the x axis and the equilibrium magnetic field \mathbf{B}_0 along z . We assume $k_y=0$ in the perturbed current (because we do not consider drift wave problems), a Maxwellian distribution function and slowly-varying magnetic field. We have briefly mentioned how one can obtain the first order contribution in $k_y\rho_\sigma$ in the equations in configuration space. Note that the equation in \mathbf{k} space is still completely general, including $k_y\neq 0$ and anisotropic temperature.

The equations for the electric field consist of a system of one first-order and two second-order integro-differential equations for E_x and E_y , E_z respectively. The differential part is only due to the Maxwell equations and is therefore the same as in vacuum. The integral part is due to the contribution of the particles to the perturbed current. We use the finite element method to solve these equations. We have shown that, in vacuum, we have to use a basis function for E_x of one degree less in x than for E_y and E_z , to avoid spectral pollution problems. This is due to the asymmetry of the order of the differential operator between the different components, as mentioned above. This is why we

have used piece-wise constant basis functions for E_x and linear basis for E_y and E_z . We did not use quadratic and Hermite-cubic basis, as we integrate analytically the kernel contribution over x and x' , using explicitly the x, x' dependence of the basis functions. However, this change of basis functions might be a useful improvement of the code, because they lead to much better accuracy.

We have derived a local power absorption formula which is also valid for arbitrary density and temperature profiles and to all orders in Larmor radii. It is positive-definite if $T_{\perp\sigma} = T_{\parallel\sigma}$ as expected with $k_y = 0$. We have also calculated a simpler formula obtained by expanding the general one with respect to the field inhomogeneity, while keeping it valid to all orders with respect to the equilibrium characteristic length compared with the Larmor radii. This formula is very useful for higher harmonic heating, as it can be applied for $k_x \rho_{\sigma} < \sqrt{1.5n + 2}$.

We have shown that both codes SEAL and SEMAL, solving the electrostatic and the E.M. problems respectively, have good convergence properties and give correct results compared with the local dispersion relation. We have also compared the E.M. code, SEMAL, with the code ISMENE valid up to second order in $k_{\perp} \rho_{\sigma}$. SEAL has been used to simulate an experiment done in our institute and has been able to reproduce well the measured wave field.

SEMAL has mainly been used to study the effects of alpha particles on higher harmonic heating. We have shown that the local model was not adequate, because it greatly overestimates the alpha absorption, as $k_{\perp} \rho_{\alpha} \geq 1$, and because it neglects the contribution from harmonics higher than three, which are dominant even for second-harmonic scenarii.

We have also discussed how one should approximate a non-Maxwellian equilibrium distribution function. We have seen that the main parameter, with regard to heating, is $\rho_{\sigma}^2 = \langle v_{\perp}^2 \rangle / 2\omega_{c\sigma}^2$, where v_{\perp}^2 is averaged over the distribution function considered. This gives an equivalent "Maxwellian" temperature for the alpha particles between 0.4 and 1.2 MeV.

The study of the effect of the alpha particle concentration, n_{α}/n_e , shows that they have nevertheless a strong influence on heating efficiency already for $n_{\alpha}/n_e > 2\%$. Therefore, except if the alpha density profile is more peaked than for the other species, the ICRF heating will be rapidly inoperative with alpha particle concentration above 3%.

SEMAL can also be used to study mode conversion, ECRH scenarii, cut-off regions, etc. In this work, we have presented the simulation of an IBW launched through a mode conversion at the "cold lower-hybrid resonance" in the scrape-off layer, as will be done in FTU. We have seen that the electric field can become quite large at the conversion layer and may produce non-linear phenomena. However, we do not expect any linear absorption in this region, as the temperature is very low and the region is far from a harmonic. We have seen that the antenna, or the waveguide, can excite some IBW for $n_{\parallel} < 1$, but with a lower amplitude. The electric field shows no sharp drop due to the Debye screening of the ion Bernstein wave when the waveguide is on the high field side of the conversion layer. However, a more precise study is needed in order to determine if most of the wave is reflected into the waveguide. But one needs in fact to use a coupling code to solve the matching problem. It should take into account the different modes of the waveguide and use the impedance matrices obtained by solving Eq.(4.9) for each k_y , k_z component [Brambilla, 1988a; England et al, 1989; Chiu et al, 1990].

A large amount of work was needed for improving the numerical and analytical treatment of the integral contribution, as well as for decreasing the cpu-time needed for one run. This was also the case for the computation of the local power absorption, which would still require some care. But there are still many possibilities for improving either the numerical method or the model itself. For example, as already mentioned, one can change the basis functions, incorporate the anisotropic formulas into the code or parallelize the code if a multi-processor machine is available. On the other hand, one can couple this code to a ray-tracing code or a plasma-antenna matching code; or, if drift wave problems are considered, one can include in the equations the first order contribution of $k_y \rho_G$.

Appendix A

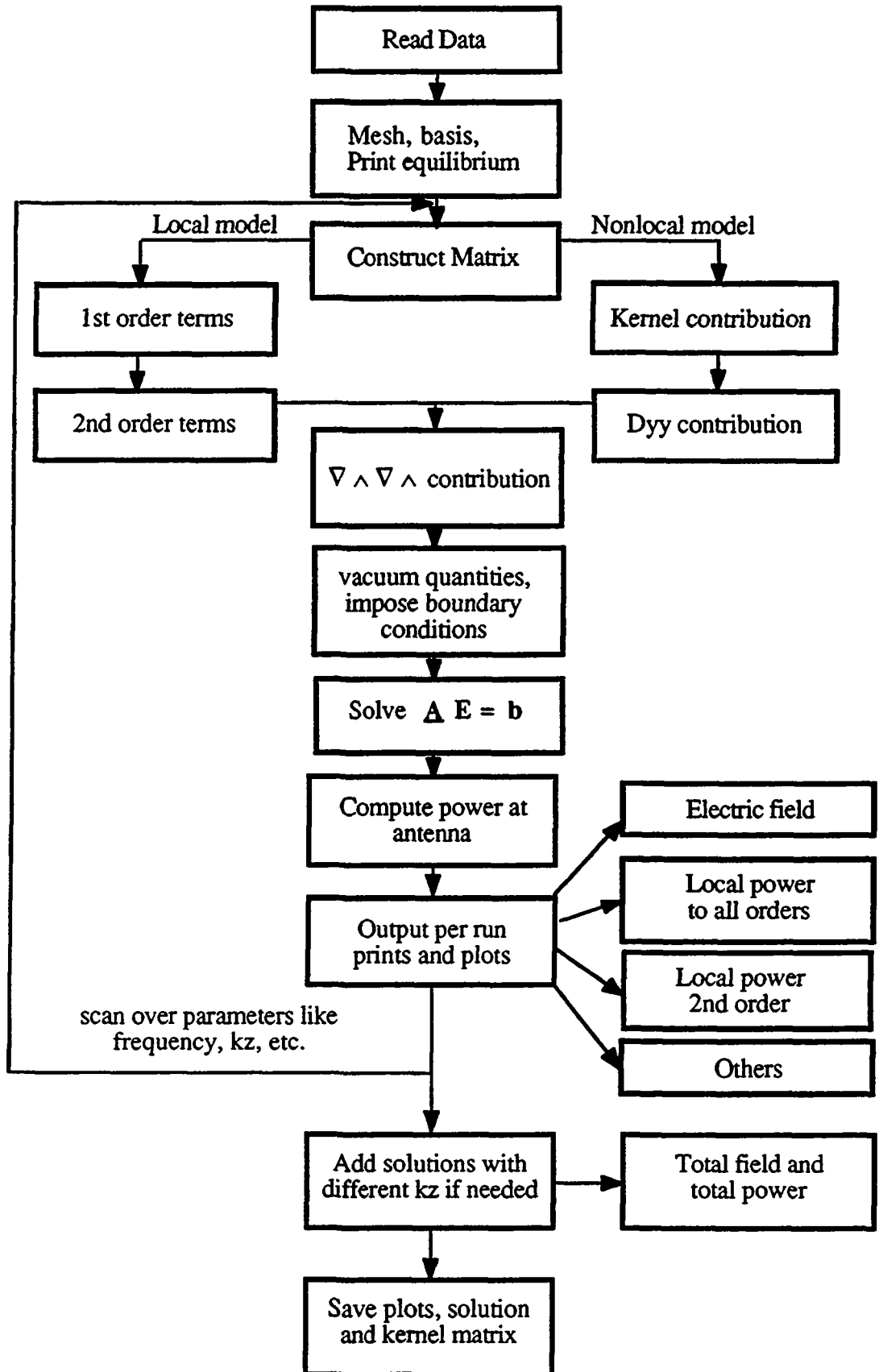
Main structure of SEMAL and SEAL

The code SEMAL solves the E.M. problem to all orders in Larmor radii. Its structure is sketched in table A.1 below. We have incorporated into the code SEMAL the code ISMENE, provided by K.Appert, where the gradients of equilibrium quantities are also included up to second order in $k_{\perp}\rho_{\sigma}$. This enables us to compute the perturbed current using either the expanded formula [Martin and Vaclavik, 1987; Appert et al, 1986a and 1987], or the complete integral form, Eq.(4.19) and (5.7). In the first case, the matrix problem is solved using the fact that it is a band matrix. Note that with this option, we can use many different basis functions: piece-wise constant—linear, linear—linear, quadratic—cubic, cubic—cubic, where the first type of basis function refers to the E_x component and the second one to E_y and E_z .

The number of harmonics computed in Eq.(4.19) is typically taken from $n=-20$ to $+20$, but it can be larger, as the summation over n is decoupled from the other loops and does not consume much cpu-time. Note that, for the IBW mode, one need in general at least contributions up to $n=\pm 10$.

We can obtain the electric field several times in the same global run, when we change only the frequency or k_z , for example. This enables us to have directly the dependence of the power on these parameters, or to reconstruct a total solution from a k_y, k_z spectrum. Note that if only k_z is modified, we incorporate the loop over k_z inside the computation of the kernel contribution, which saves about 30 to 40% of the time.

Table A.1. Structure of SEMAL



Many input parameters control the different options available as well as the shape of the profiles, the mesh packing, etc. We have tried to keep these input variables as close as possible to those of the original code ISMENE. The minimum set of parameters needed for a simulation of a plasma is the following: ion species, B_0 , R_0 , $n_{0\sigma}$, $T_{0\sigma}$, density and temperature profiles, frequency, k_z , x_{pl} , x_{pr} , and eventually x_{sl} , x_{sr} , x_a and k_y .

The code SEAL is structured exactly in the same way, except that it does not have the ISMENE option, which is replaced by the computation of the expanded kernel contribution, and the $\nabla \wedge \nabla \wedge$ and vacuum contributions.

Appendix B

Kernel contribution to matrix

In this Appendix, we write down the final form of the kernel contribution which is computed in the code SEMAL, after the analytical integration over x' and x , in that order. This is intended as a reference to the formulae coded in SEMAL, for eventual future amendments, or debugging, of the code.

The contribution to the main matrix due to the integral part of Eq.(4.10), \underline{K}_{vw}^{ij} , is given by:

$$\begin{aligned} \underline{K}^{ij} = & \sum_{\sigma} \int_0^{\pi} d\theta \int_{x''_{pl}}^{x''_{pr}} dx'' \frac{\omega_{p\sigma}^2}{\sqrt{2} \pi^2 k_{//} v_{T\sigma} \omega \rho_{\sigma}} \sum_n \underline{C}_n(x'', \theta, \sigma) \\ & \times [\underline{G}^{ij} + \underline{H}^{ij}(\tau_1=0, \tau_2=1/2) + \underline{H}^{ij}(\tau_1=1/2, \tau_2=1)] \quad (B.1) \\ & + \mathbf{e}_y : \mathbf{e}_y \sum_{\sigma} \int_{x''_{pl}}^{x''_{pr}} dx'' \frac{2 \omega_{p\sigma}^2}{\sqrt{\pi} \omega^2} D_{yy}^{ij}(\bar{x}_{i+1}, \bar{x}_{j+1}), \end{aligned}$$

with

$$\underline{C}_n(x'', \theta, \sigma) = \begin{pmatrix} n Z_{n\sigma} \sin n\theta \sin \theta & i \frac{Z_{n\sigma} \sin n\theta}{\rho_{\sigma}^2 \sin \theta} & -i \frac{2 \omega_{c\sigma}}{v_{T\sigma}} \xi_{n\sigma} Z_{n\sigma} \frac{\sin n\theta}{\sin \theta} \\ -C_{xy} & -\frac{Z_{n\sigma} \cos n\theta}{\rho_{\sigma}^2} & \frac{2 \omega_{c\sigma}}{v_{T\sigma}} (1 + \xi_{n\sigma} Z_{n\sigma}) \cos n\theta \\ C_{xz} & -C_{yz} & 2 \xi_{n\sigma} (1 + \xi_{n\sigma} Z_{n\sigma}) \cos n\theta \end{pmatrix}$$

and where i refers to the test basis function and j to the unknown basis function. Note that we have not yet coded the anisotropic temperature formula, but by comparing with Eq.(4.10), this would be straightforward to do. The matrix $\underline{\underline{G}}^{ij}$ is due to the exponential terms obtained after the x' integral, which is exactly integrable. $\underline{\underline{H}}^{ij}(\tau_1, \tau_2)$ is obtained, after integrating over x , terms involving $\text{erf}[(x_v - x''(1 - \cos\theta) - x \cos\theta)/\epsilon]$, $v=j$ or $j+1$, with $\epsilon = \sqrt{2}\rho_\sigma \sin\theta$. As mentioned in Sec.5.3, we cut the $[x_i, x_{i+1}]$ interval into two equidistant intervals and assume the error function to be constant over the half interval $[x_{i+\tau_1}, x_{i+\tau_2}]$, $\tau_1=0$ or $1/2$, $\tau_2=1/2$ or 1 , with the value at middle point:

$$\text{erf} \left[\frac{x_v - x''(1 - \cos\theta) - \frac{x_{i+\tau_1} + x_{i+\tau_2}}{2} \cos\theta}{\epsilon} \right].$$

This is why the $\underline{\underline{H}}$ contribution over the whole $[x_i, x_{i+1}]$ interval is given by $\underline{\underline{H}}^{ij}(0,1/2) + \underline{\underline{H}}^{ij}(1/2,1)$.

The D_{yy}^{ij} term comes from the extra non-resonant term due to D_{yy} in Eq.(4.10). The other terms in $\underline{\underline{D}}$ of Eq.(4.10), are introduced into the main matrix, as mentioned in Sec.4.2.

We use the following definition:

$$A_v^2 \equiv \frac{(x'' - x_v)^2}{2\rho_\sigma^2},$$

$$p_v \equiv x_v \cos\theta + x''(1 - \cos\theta),$$

$$g_v^\mu \equiv \frac{x_\mu - p_v}{\epsilon},$$

$$AG_{zz}(\bar{x}_{i+1}, j+1) = e^{-A_{j+1}^2} \left[-\frac{\varepsilon}{2} e^{-y^2} + (p_{j+1} - \bar{x}_{i+1}) \frac{\sqrt{\pi}}{2} \operatorname{erf} y \right]_{g_i^{j+1}}^{g_{i+1}^{j+1}}$$

$$AG_{yz}(\bar{x}_{i+1}, j+1) = e^{-A_{j+1}^2} \left\{ -\frac{\varepsilon}{2} e^{-y^2} [\varepsilon y + 2p_{j+1} - \bar{x}_{i+1} - x"] \right. \\ \left. + \left[\frac{\varepsilon^2}{2} + (p_{j+1} - \bar{x}_{i+1})(p_{j+1} - x") \right] \frac{\sqrt{\pi}}{2} \operatorname{erf} y \right\}_{g_i^{j+1}}^{g_{i+1}^{j+1}}$$

$$AG_{yy}(\bar{x}_{i+1}, j+1) = e^{-A_{j+1}^2} \left\{ -\frac{\varepsilon}{2} e^{-y^2} [\varepsilon^2(y^2+1) + \varepsilon y(3p_{j+1} - \bar{x}_{i+1} - 2x")] \right. \\ \left. + (p_{j+1} - x")(3p_{j+1} - x" - 2\bar{x}_{i+1}) \right. \\ \left. + [(p_{j+1} - \bar{x}_{i+1})(p_{j+1} - x")^2 + \frac{\varepsilon^2}{2}(3p_{j+1} - \bar{x}_{i+1} - 2x")] \frac{\sqrt{\pi}}{2} \operatorname{erf} y \right\}_{g_i^{j+1}}^{g_{i+1}^{j+1}}$$

$$\delta_{mt}^k \binom{3}{4} = \begin{cases} 1 & \text{if method} = \binom{3}{4} \text{ for basis function } \chi_k(x) \\ 0 & \text{otherwise} \end{cases}$$

where method=3 corresponds to taking the piece-wise constant basis $\chi_{i-1/2}$ as in Fig.5.1 , whereas method=4 corresponds to the opposite, $\chi_{i+1/2}=1$, $\chi_{i-1/2}=0$. It is in fact equivalent and we use always method=3. We always use μ to denote the test function indices i , $i+1$ and ν for the unknown basis function j , $j+1$ We can define the $G_{\nu w}^{ij}$ matrix:

$$G_{xx}^{\mu\nu} \equiv 0$$

$$G_{xy}^{ij} = -\frac{\varepsilon^4 e^{-A_{j+1}^2}}{2\Delta_{jj+1}} \left[\frac{\sqrt{\pi}}{2} \operatorname{erf} y \right]_{g_i^{j+1}}^{g_{i+1}^{j+1}} + \frac{\varepsilon^2 e^{-A_j^2}}{2\Delta_{jj+1}} \left[(x_j - x") \Delta_{jj+1} + \varepsilon^2 \right] \frac{\sqrt{\pi}}{2} \operatorname{erf} y \Big|_{g_i^j}^{g_{i+1}^j} \delta_{mt}^i$$

$$G_{xy}^{ij+1} = -\frac{\varepsilon^2 e^{-A_{j+1}^2}}{2\Delta_{jj+1}} \left[(x_{j+1} - x") \Delta_{jj+1} - \varepsilon^2 \right] \frac{\sqrt{\pi}}{2} \operatorname{erf} y \Big|_{g_i^{j+1}}^{g_{i+1}^{j+1}} - \frac{\varepsilon^4 e^{-A_j^2}}{2\Delta_{jj+1}} \left[\frac{\sqrt{\pi}}{2} \operatorname{erf} y \right]_{g_i^j}^{g_{i+1}^j} \delta_{mt}^i$$

$$G_{xz}^{ij} = \frac{\varepsilon^2}{2} e^{-A_j^2} \left[\frac{\sqrt{\pi}}{2} \operatorname{erf} y \right]_{g_i^j}^{g_{i+1}^j} \delta_{mt4}^i \quad ; \quad G_{xz}^{ij+1} = -G_{xz}^{ij} \Big|_{j \rightarrow j+1}$$

$$G_{xw}^{i+1v} = G_{xw}^{ij} \Big|_{\delta_{mt4}^i \rightarrow \delta_{mt3}^i}, \quad w = y, z$$

$$G_{yx}^{ij}(\bar{x}_{i+1}) = \Delta_{jj+1} \cos \theta G_{yz}^{ij}(\bar{x}_{i+1}) \delta_{mt4}^j$$

$$G_{zx}^{ij}(\bar{x}_{i+1}) = \Delta_{jj+1} \cos \theta G_{zz}^{ij}(\bar{x}_{i+1}) \delta_{mt4}^j$$

$$G_{vx}^{\mu j+1} = G_{vx}^{\mu j} \Big|_{\delta_{mt4}^j \rightarrow \delta_{mt3}^j}, \quad v = y, z$$

$$G_{yy}^{ij}(\bar{x}_{i+1}) = \frac{\varepsilon^2 \cos \theta}{2\Delta_{ii+1} \Delta_{jj+1}} [AG_{yy}(\bar{x}_{i+1}, j+1) - AG_{yy}(\bar{x}_{i+1}, j+1)] \\ - \frac{\varepsilon^2}{2\Delta_{ii+1}} AG_{yz}(\bar{x}_{i+1}, j)$$

$$G_{yy}^{ij+1}(\bar{x}_{i+1}) = -\frac{\varepsilon^2 \cos \theta}{2\Delta_{ii+1} \Delta_{jj+1}} [AG_{yy}(\bar{x}_{i+1}, j+1) - AG_{yy}(\bar{x}_{i+1}, j+1)] \\ + \frac{\varepsilon^2}{2\Delta_{ii+1}} AG_{yz}(\bar{x}_{i+1}, j+1)$$

$$G_{yz}^{ij}(\bar{x}_{i+1}) = \frac{\varepsilon^2}{2\Delta_{ii+1} \Delta_{jj+1}} [AG_{yz}(\bar{x}_{i+1}, j+1) - AG_{yz}(\bar{x}_{i+1}, j+1)]$$

$$G_{yz}^{ij+1}(\bar{x}_{i+1}) = -G_{yz}^{ij}(\bar{x}_{i+1})$$

$$G_{zy}^{ij}(\bar{x}_{i+1}) = \frac{\varepsilon^2}{2\Delta_{ii+1}} AG_{zz}(\bar{x}_{i+1}, j) - \cos \theta G_{yz}^{ij}(\bar{x}_{i+1})$$

$$G_{zy}^{ij+1}(\bar{x}_{i+1}) = -\frac{\varepsilon^2}{2\Delta_{ii+1}} AG_{zz}(\bar{x}_{i+1}, j+1) - \cos \theta G_{yz}^{ij+1}(\bar{x}_{i+1})$$

$$G_{zz}^{ij}(\bar{x}_{i+1}) = -\frac{\varepsilon^2}{2\Delta_{ii+1} \Delta_{jj+1}} [AG_{zz}(\bar{x}_{i+1}, j+1) - AG_{zz}(\bar{x}_{i+1}, j+1)]$$

$$G_{zz}^{ij+1}(\bar{x}_{i+1}) = -G_{zz}^{ij}(\bar{x}_{i+1})$$

$$G_{vw}^{i+1v} = -G_{vw}^{iv}(\bar{x}_i), \quad v = y, z, \quad w = x, y, z$$

For the contribution of the error function, we first define:

$$\begin{aligned} \gamma_{i+(\tau_1+\tau_2)/2}^v &= \frac{x_v - x'' (1 - \cos \theta) - x_{i+(\tau_1+\tau_2)/2} \cos \theta}{\epsilon} \\ x_{i+\tau} &= x_i + \tau(x_{i+1} - x_i) \\ (\Delta \text{erf})(\tau_1, \tau_2) &= \text{erf}(\gamma_{i+(\tau_1+\tau_2)/2}^{j+1}) - \text{erf}(\gamma_{i+(\tau_1+\tau_2)/2}^j) \\ e_{i+\tau} &= \frac{x_{i+\tau} - x''}{\sqrt{2} \rho_\sigma} \\ (\tau_1, \tau_2) &= (0, 1/2), (1/2, 1) \end{aligned}$$

which enables us to specify first the $H_{xw}^{\mu\nu}$ components:

$$\begin{aligned} \bar{H}_{xx}^{ij}(\tau_1, \tau_2) &= \frac{\sqrt{\pi}}{2} (\Delta \text{erf}) \sqrt{2} \rho_\sigma \left[\frac{\sqrt{\pi}}{2} \text{erf } y \right]_{e_{i+\tau_1}}^{e_{i+\tau_2}} \\ H_{xx}^{ij}(\tau_1, \tau_2) &= \bar{H}_{xx}^{ij}(\tau_1, \tau_2) \delta_{mt4}^i \delta_{mt4}^j ; H_{xx}^{ij+1}(\tau_1, \tau_2) = \bar{H}_{xx}^{ij}(\tau_1, \tau_2) \delta_{mt4}^i \delta_{mt3}^j \\ H_{xy}^{ij}(\bar{x}_{j+1}, \tau_1, \tau_2) &= \frac{\sqrt{\pi}}{2} (\Delta \text{erf}) \frac{\sqrt{2} \rho_\sigma \epsilon^2}{2 \Delta_{jj+1}} \left[-\sqrt{2} \rho_\sigma \cos \theta e^{-y^2} + (x'' - \bar{x}_{j+1}) \frac{\sqrt{\pi}}{2} \text{erf } y \right]_{e_{i+\tau_1}}^{e_{i+\tau_2}} \delta_{mt4}^i \\ H_{xz}^{ij}(\tau_1, \tau_2) &= \frac{\epsilon^2}{2 \Delta_{jj+1}} \bar{H}_{xx}^{ij}(\tau_1, \tau_2) \delta_{mt4}^i \\ H_{xy}^{ij+1} &= -H_{xy}^{ij}(\bar{x}_j, \tau_1, \tau_2) ; H_{xz}^{ij+1} = -H_{xz}^{ij}(\tau_1, \tau_2) \\ G_{xw}^{i+1v} &= G_{xw}^{iv} \Big|_{\delta_{mt4}^i \rightarrow \delta_{mt3}^i} , \quad w = x, y, z \end{aligned}$$

For the other terms, we still define the following "moments" involving $(x-x'')$ and the basis functions $\varphi_i(x)$.

$$\begin{aligned} AH_0^{ij}(\bar{x}_{i+1}) &= \int_{x_{i+\tau_1}}^{x_{i+\tau_2}} dx \frac{x - \bar{x}_{i+1}}{\Delta_{ii+1}} \exp\left[-\frac{(x - x'')^2}{2\rho_\sigma^2}\right] \\ &= \frac{\sqrt{2}\rho_\sigma}{\Delta_{ii+1}} \left[-\frac{\rho_\sigma}{\sqrt{2}} e^{-y^2} + (x'' - \bar{x}_{i+1}) \frac{\sqrt{\pi}}{2} \operatorname{erf} y \right]_{e_{i+\tau_1}}^{e_{i+\tau_2}} \end{aligned}$$

$$\begin{aligned} AH_1^{ij}(\bar{x}_{i+1}) &= \int_{x_{i+\tau_1}}^{x_{i+\tau_2}} dx \frac{x - \bar{x}_{i+1}}{\Delta_{ii+1}} \exp\left[-\frac{(x - x'')^2}{2\rho_\sigma^2}\right] (x - x'') \\ &= \frac{2\rho_\sigma^2}{\Delta_{ii+1}} \left[-\frac{e^{-y^2}}{2} (\sqrt{2}\rho_\sigma y + x'' - \bar{x}_{i+1}) + \frac{\rho_\sigma \sqrt{\pi}}{\sqrt{2}} \frac{\operatorname{erf} y}{2} \right]_{e_{i+\tau_1}}^{e_{i+\tau_2}} \end{aligned}$$

$$\begin{aligned} AH_2^{ij}(\bar{x}_{i+1}) &= \int_{x_{i+\tau_1}}^{x_{i+\tau_2}} dx \frac{x - \bar{x}_{i+1}}{\Delta_{ii+1}} \exp\left[-\frac{(x - x'')^2}{2\rho_\sigma^2}\right] (x - x'')^2 \\ &= \frac{2\sqrt{2}\rho_\sigma^3}{\Delta_{ii+1}} \left[-\frac{e^{-y^2}}{2} [\sqrt{2}\rho_\sigma(y^2 + 1) + (x'' - \bar{x}_{i+1})y] + \frac{(x'' - \bar{x}_{i+1})\sqrt{\pi}}{2} \frac{\operatorname{erf} y}{2} \right]_{e_{i+\tau_1}}^{e_{i+\tau_2}} \end{aligned}$$

$$\begin{aligned} AH_3^{ij}(\bar{x}_{i+1}) &= \int_{x_{i+\tau_1}}^{x_{i+\tau_2}} dx \frac{x - \bar{x}_{i+1}}{\Delta_{ii+1}} \exp\left[-\frac{(x - x'')^2}{2\rho_\sigma^2}\right] (x - x'')^3 \\ &= \frac{4\rho_\sigma^4}{\Delta_{ii+1}} \left[-\frac{e^{-y^2}}{2} [\sqrt{2}\rho_\sigma y(y^2 + \frac{3}{2}) + (x'' - \bar{x}_{i+1})(y^2 + 1)] + \frac{3\rho_\sigma \sqrt{\pi}}{2\sqrt{2}} \frac{\operatorname{erf} y}{2} \right]_{e_{i+\tau_1}}^{e_{i+\tau_2}} \end{aligned}$$

We have then:

$$H_{yx}^{ij}(\bar{x}_{i+1}) = \frac{\sqrt{\pi}}{2} (\Delta \operatorname{erf}) \sin^2 \theta AH_2^{ij}(\bar{x}_{i+1}) \delta_{mt4}^j$$

$$H_{zx}^{ij}(\bar{x}_{i+1}) = -\frac{\sqrt{\pi}}{2} (\Delta \operatorname{erf}) \sin^2 \theta AH_1^{ij}(\bar{x}_{i+1}) \delta_{mt4}^j$$

$$H_{vx}^{\mu j+1} = H_{vx}^{\mu j} \Big|_{\delta_{mt4}^j} \rightarrow \delta_{mt3}^j, \quad v = y, z$$

$$H_{yy}^{ij}(\bar{x}_{i+1}, \bar{x}_{j+1}) = -\frac{\sqrt{\pi}}{2\Delta_{jj+1}} (\Delta \text{erf}) \left[\cos^2 \theta AH_3^{ij}(\bar{x}_{i+1}) \right. \\ \left. + (x'' - \bar{x}_{j+1}) \cos \theta AH_2^{ij}(\bar{x}_{i+1}) + \frac{\varepsilon^2}{2} AH_1^{ij}(\bar{x}_{i+1}) \right]$$

$$H_{yz}^{ij}(\bar{x}_{i+1}, \bar{x}_{j+1}) = -\frac{\sqrt{\pi}}{2\Delta_{jj+1}} (\Delta \text{erf}) \left[\cos \theta AH_2^{ij}(\bar{x}_{i+1}) + (x'' - \bar{x}_{j+1}) AH_1^{ij}(\bar{x}_{i+1}) \right]$$

$$H_{zy}^{ij}(\bar{x}_{i+1}, \bar{x}_{j+1}) = \frac{\sqrt{\pi}}{2\Delta_{jj+1}} (\Delta \text{erf}) \left[\cos^2 \theta AH_2^{ij}(\bar{x}_{i+1}) \right. \\ \left. + (x'' - \bar{x}_{j+1}) \cos \theta AH_1^{ij}(\bar{x}_{i+1}) + \frac{\varepsilon^2}{2} AH_0^{ij}(\bar{x}_{i+1}) \right]$$

$$H_{zz}^{ij}(\bar{x}_{i+1}, \bar{x}_{j+1}) = \frac{\sqrt{\pi}}{2\Delta_{jj+1}} (\Delta \text{erf}) \left[\cos \theta AH_1^{ij}(\bar{x}_{i+1}) + (x'' - \bar{x}_{j+1}) AH_0^{ij}(\bar{x}_{i+1}) \right]$$

$$H_{vw}^{\mu j+1} = -H_{vw}^{\mu j}(\bar{x}_{i+1}, \bar{x}_j) , H_{vw}^{i+1v} = -H_{vw}^{iv}(\bar{x}_i, \bar{x}_{j+1}) , v, w = y, z$$

Finally. the term D_{yy}^{ij} is defined by the following integral, Eq.(4.10):

$$\sum_{\sigma} \int_{x''_{pl}}^{x''_{pr}} dx'' \frac{\omega_{p\sigma}^2}{\sqrt{2\pi} \omega^2 \rho_{\sigma}^3} \int dx \eta_i(x) \eta_j(x) [(x-x'')^2 - \rho_{\sigma}^2] \exp\left[-\frac{(x-x'')^2}{2\rho_{\sigma}^2}\right] \\ \equiv \sum_{\sigma} \int_{x''_{pl}}^{x''_{pr}} dx'' \frac{2\omega_{p\sigma}^2}{\sqrt{\pi} \omega^2} D_{yy}^{ij}(\bar{x}_{i+1}, \bar{x}_{j+1}) ,$$

which gives:

$$D_{yy}^{ij}(\bar{x}_{i+1}, \bar{x}_{j+1}) = \frac{1}{\Delta_{ii+1} \Delta_{jj+1}} \left\{ -\frac{e^{-y^2}}{2} \left[2\rho_{\sigma}^2 y^3 + \sqrt{2}\rho_{\sigma} (2x'' - \bar{x}_{i+1} - \bar{x}_{j+1})(y^2 + \frac{1}{2}) \right. \right. \\ \left. \left. + ((x'' - \bar{x}_{i+1})(x'' - \bar{x}_{i+1}) + 2\rho_{\sigma}^2) y \right] + \rho_{\sigma}^2 \frac{\sqrt{\pi}}{2} \text{erf } y \right\} \frac{\frac{x_{i+1} - x''}{\sqrt{2}\rho_{\sigma}}}{\frac{x_i - x''}{\sqrt{2}\rho_{\sigma}}} ,$$

with

$$D_{yy}^{\mu j+1} = -D_{yy}^{\mu j}(\bar{x}_{i+1}, \bar{x}_j) \text{ and } D_{yy}^{i+1\nu} = -D_{yy}^{i\nu}(\bar{x}_i, \bar{x}_{j+1}) .$$

The relations between α^{i+1j} and α^{ij} are explained by the relation between η_i and η_{i+1} in the interval $[x_i, x_{i+1}]$, as explained in Sec.5.3.

With these fourmulas, we obtain for a couple of intervals $[x_i, x_{i+1}]$ and $[x_j, x_{j+1}]$ the contributions α_{vw}^{ij} , α_{vw}^{i+1j} , α_{vw}^{ij+1} and α_{vw}^{i+1j+1} , to the matrix of each components. Scanning over all the intervals gives the total contribution of the kernel to the main matrix. Note that due to the exponential terms and the error functions, the computation of this matrix $\underline{\alpha}^{ij}$ is limited to x , x' , x'' , θ and σ satisfying the conditions of Eqs.(3.11) and (3.12).

Note also that \underline{G}^{ij} and \underline{H}^{ij} do not depend on the harmonic number n and that \underline{C} , Eq.(B.1) is independent of x and x' . This is why the summation over n can be decoupled from the loops over x and x' , and therefore is not at all time consuming.

Appendix C

Dispersion relation code DISPAL

We have constructed a code, DISPAL, which solves the dispersion relation valid to all orders in Larmor radii. It solves the following equation:

$$\text{Re} [\det D (k_x^2, x, \omega)] = 0,$$

where $D = \det \underline{\underline{D}}$ and $\underline{\underline{D}}$ is the tensor multiplying the electric field \mathbf{E} in Eq.(4.8). For given $B_0(x)$, $n_\sigma(x)$, $T_\sigma(x)$, k_y , k_z and ω , the solution for k_x^2 real is obtained for different values of x . This gives the solution of the dispersion relation throughout the plasma and indicates also the minimum of points one should use in SEMAL (about 4 to 8 points per wavelength). The input parameters are the same as for SEMAL.

The approximation of solving only the real part of the dispersion relation is valid as long as the imaginary parts of $\underline{\underline{D}}$ and ω , or k_x^2 , of the complex solution are small compared with the real parts. We check this by computing the imaginary part of ω , ω_i , using:

$$\omega_i(k_x^2, x, \omega_r) = - \frac{\text{Im} [D(k_x^2, x, \omega_r)]}{\partial D / \partial \omega |_{\omega = \omega_r}},$$

and verifying that ω_i/ω_r is small. Note that as we solve for k_x^2 , we can also find purely evanescent modes, $k_x^2 < 0$.

An example of the result of DISPAL is shown in Fig.C.1, for the case of a

mode conversion at the ion-ion hybrid frequency. We have used similar parameters as in Appert et al [1986b], i.e. D-³He, with $n^3\text{He}/n_e=6.4\%$ and $n_D=2.8\cdot 10^{19} \text{ m}^{-3}$, $T_e=T_D=2000 \text{ eV}$, $T_{3\text{He}}=600 \text{ eV}$, $B_0=3.4 \text{ T}$, $R_0=3 \text{ m}$, $f=33 \text{ MHz}$, minor radius of 1.25 m , $k_y=0 \text{ m}^{-1}$, $k_z=3 \text{ m}^{-1}$, parabolic density profiles and bi-quadratic temperature profiles. For comparison, in Fig.C.2, we show the dispersion relation obtained using the code ISMENE, which approximates the dispersion relation with a third order polynomial in k_x^2 , where k_x^2 is complex. We see that the effect of the polynomial approximation is to fill in the regions where there are less than three physical roots, but apart from that, the main features are well represented. Fig.C.3 has been obtained with $k_z=10 \text{ m}^{-1}$ and it illustrates that the dispersion relation can become rather complicated. The dispersion relation obtained with ISMENE in this case is shown in Fig.C.4. The main features are also well represented, even if the large gap in between the cold ion-ion hybrid resonance and the first harmonic of the deuterium is removed. This difference is seen on the wave-field as well as, with the local model, the slow wave propagates further away from the conversion layer than with the nonlocal model. However, this does not change much the power deposition profile.

Another example is shown in Fig.C.5, where one sees the O and X mode near the electron cyclotron and upper hybrid, ω_{uH} , frequencies. We have used TCV (Tokamak à configurations variables, Lausanne) parameters: $B_0=1.43 \text{ T}$, $n_e=n_D=10^{19} \text{ m}^{-3}$, $T_e=T_D=1500 \text{ eV}$, $k_y=0 \text{ m}^{-1}$, $k_z=140 \text{ m}^{-1}$, $f=39 \text{ GHz}$, $R_0=0.87 \text{ m}$, minor radius 0.24 m .

Apart from the same standard input variables as in SEMAL, we control the number of points in x and k_x^2 , as well as the limits x_{\min} , x_{\max} , $k_{x\min}^2$, $k_{x\max}^2$, in between which DISPAL searches for a root. In this way, we can concentrate on small intervals, when a very fine mesh is needed, without increasing too much the number of points, i.e. the cpu-time used. The roots are

written in a simple way such that the results of different runs, giving roots in different x intervals, can be copied one after the other in a new file. Then, they are read by another code, called READPOINTS, which sorts all the modes in increasing order with respect to x and plot them. The roots corresponding to the same mode are grouped together and joined by a continuous line on the plot.

We have added two special graphic features to these codes, in order to obtain a plot easier to study. First, we use an inverse hyperbolic sinus for the y -axis scale. It has the nice properties to be linear near zero and logarithmic for large values, and moreover it is well-defined for positive and negative values. In this way, we can clearly see on the same graph: low and high k_x roots, as well as propagatory and evanescent modes. The second facility is used in READPOINTS. We can inhibit the drawing of a segment between two roots, by introducing an extra root equal to zero in between. This enables us to distinguish better two separate adjacent regions, even though they belong to the same mode. For example, when there is a region where no solution exists, points at the left and at the right should not be joined together.

Appendix D

Solution of the linearized Vlasov equation using the method of the characteristics

Here we present the main steps for calculating the perturbed distribution function in the E.M. case with arbitrary inhomogeneous profiles, anisotropic temperature, but uniform magnetic field. We follow the method presented in the book of Krall and Trievpiece [1973, p.396-404].

We want to solve the following equation for the perturbed distribution function $f_{\sigma}^{(1)}$, Eq.(2.6b):

$$\left[\frac{\partial}{\partial t} + \mathbf{v} \cdot \nabla + \frac{q_{\sigma}}{m_{\sigma}} \mathbf{v} \wedge \mathbf{B}_0 \cdot \frac{\partial}{\partial \mathbf{v}} \right] f_{\sigma}^{(1)}(\mathbf{x}, \mathbf{v}, t) = -\frac{q_{\sigma}}{m_{\sigma}} \left(\mathbf{E}^{(1)} + \mathbf{v} \wedge \mathbf{B}^{(1)} \right) \cdot \frac{\partial}{\partial \mathbf{v}} f_{\sigma}^{(0)}, \quad (\text{D.1})$$

where we have assumed that $\mathbf{E}_0=0$. The equilibrium distribution function satisfies Eq.(2.6a). Let us introduce the Lagrangian coordinates \mathbf{x}' , \mathbf{v}' , t' such that:

$$\frac{d\mathbf{x}'}{dt'} = \mathbf{v}' \quad ; \quad \frac{d\mathbf{v}'}{dt'} = \frac{q_{\sigma}}{m_{\sigma}} \mathbf{v}' \wedge \mathbf{B}_0, \quad (\text{D.2a})$$

which gives (Eq.(3.15)):

$$\begin{aligned}
 \mathbf{x}' &= \mathbf{x} + \frac{\mathbf{v}_\perp}{\omega_{c\sigma}} [(\sin \alpha - \sin \alpha') \mathbf{e}_x - (\cos \alpha - \cos \alpha') \mathbf{e}_y] + v_{\parallel} \tau \mathbf{e}_z, \\
 \mathbf{v}' &= v_\perp (\cos \alpha' \mathbf{e}_x + \sin \alpha' \mathbf{e}_y) + v_{\parallel} \mathbf{e}_z, \\
 \alpha' &= \alpha - \omega_{c\sigma} \tau, \\
 \mathbf{v} &= (v_\perp, \alpha, v_{\parallel}), \\
 \tau &= t' - t,
 \end{aligned} \tag{D.2b}$$

using the following boundary conditions:

$$\begin{cases} \mathbf{x}'(t'=t) = \mathbf{x}, & \text{position of particle at time } t, \\ \mathbf{v}'(t'=t) = \mathbf{v}, & \text{velocity of particle at time } t. \end{cases} \tag{D.3}$$

In this way, Eq.(D.1) is transformed into:

$$\frac{d}{dt'} f_\sigma^{(1)}(\mathbf{x}', \mathbf{v}', t') = -\frac{q_\sigma}{m_\sigma} (\mathbf{E}^{(1)} + \mathbf{v}' \wedge \mathbf{B}^{(1)}) (\mathbf{x}', t') \cdot \frac{\partial}{\partial \mathbf{v}'} f_\sigma^{(0)}(\mathbf{x}', \mathbf{v}'). \tag{D.4}$$

We can integrate Eq.(D.4) over t' between $-\infty$ and t , and use Eq.(D.3):

$$f_\sigma^{(1)}(\mathbf{x}(t), \mathbf{v}(t), t) = f_\sigma^{(1)}(\mathbf{x}'(-\infty), \mathbf{v}'(-\infty), t'=-\infty) - \frac{q_\sigma}{m_\sigma} \int_{-\infty}^0 d\tau (\mathbf{E} + \mathbf{v}' \wedge \mathbf{B}) \cdot \frac{\partial f_\sigma^{(0)}}{\partial \mathbf{v}'}, \tag{D.5}$$

where we have suppressed the superscripts ⁽¹⁾ and changed t' to $\tau=t'-t$. We now introduce the Fourier transform defined by:

$$g(\mathbf{x}, t) = \int d^3 \mathbf{k} d\omega e^{i(\mathbf{k}\mathbf{x} - \omega t)} g(\mathbf{k}, \omega), \tag{D.6}$$

where a small positive imaginary part is assumed for ω (causality condition), such that the perturbed distribution function is zero at $t=-\infty$. This means that

the perturbation is turned on smoothly at $t=-\infty$.

Inserting Eq.(D.6) into (D.5) we obtain:

$$f_{\sigma}^{(1)}(\mathbf{k}, \mathbf{v}, \omega) = -\frac{q_{\sigma}}{m_{\sigma}} \int_{-\infty}^0 d\tau \int d\mathbf{k}'_{\perp} (\mathbf{E} + \mathbf{v}' \wedge \mathbf{B})(\mathbf{k}_{\perp} - \mathbf{k}'_{\perp}, k_{\parallel}, \omega) \cdot \frac{\partial f_{\sigma}^{(0), \text{part}}}{\partial \mathbf{v}'}(\mathbf{k}'_{\perp}, \mathbf{v}') \times e^{i[\mathbf{k}(\mathbf{x}' - \mathbf{x}) - \omega\tau]}. \quad (\text{D.7})$$

The superscript "part" has been added to emphasize that $f_{\sigma}^{(0), \text{part}}$ is the Fourier transform with respect to the particle coordinates. We have seen in Sec.3.1.1 that the precession of the particles around the guiding centers can be factorized by introducing the Fourier transform with respect to the guiding center coordinates, $f_{\sigma}^{(0), \text{GC}}(\mathbf{k}'_{\perp}, v_{\perp}, v_{\parallel})$, Eq.(3.2). We shall omit the superscript "GC" in what follows.

We then insert Eqs.(D.2b) and (3.2) into Eq.(D.7) and use Eq.(3.16), the recurrence formulae of the Bessel function J_n , as well as the summation theorem given by [Gradshteyn and Ryzhik, 1980, p. 979]:

$$e^{i n \beta} J_n(p c) = \sum_{m=-\infty}^{+\infty} J_{n+m}(p a) J_m(p b) e^{i m \gamma}, \quad (\text{D.8})$$

where p is a complex number and a, b, c are the sides of a triangle with β being the angle opposite to b and γ the angle opposite to c . We then use the same definition of the Bessel function J_n of a two-dimensional vector \mathbf{d} as Yasseen and Vaclavik [1986]:

$$J_n(\mathbf{d}) \equiv J_n\left(\frac{d v_{\perp}}{\omega_{c\sigma}}\right) e^{i n \delta}, \quad (\text{D.9})$$

where δ is the angle of \mathbf{d} with the x axis. We apply this definition to vectors in the plane (x, y) normal to \mathbf{B}_0 . In this way, the summation theorem, Eq.(D.8), can be written as:

$$\mathcal{J}_n(\mathbf{k}_\perp - \mathbf{k}'_\perp) = \sum_{m=-\infty}^{+\infty} \mathcal{J}_{m+n}(\mathbf{k}_\perp) \mathcal{J}_m^*(\mathbf{k}'_\perp). \quad (\text{D.10})$$

With all these, we can perform the integration over τ in Eq.(D.7), which yields:

$$\begin{aligned} f_\sigma^{(1)}(\mathbf{k}, \mathbf{v}, \omega) = & - \frac{i q_\sigma}{m_\sigma} e^{i \frac{(\mathbf{k} \wedge \mathbf{v})_{//}}{\omega_{c\sigma}}} \sum_n \frac{e^{-in\alpha}}{\omega - \mathbf{k}_{//} \mathbf{v}_{//} - n \omega_{c\sigma}} \int d\mathbf{k}'_\perp \\ & \times \left\{ P_x^n \left[E_x \frac{\partial}{\partial v_\perp} + \frac{g(v)}{\omega} (k_{//} E_x - k'_x E_{//}) - i \frac{v_\perp (k_x - k'_x)}{\omega \omega_{c\sigma}} (k'_x E_y - k'_y E_x) \right] \right. \\ & + P_y^n \left[E_y \frac{\partial}{\partial v_\perp} + \frac{g(v)}{\omega} (k_{//} E_y - k'_y E_{//}) - i \frac{v_\perp (k_y - k'_y)}{\omega \omega_{c\sigma}} (k'_x E_y - k'_y E_x) \right] \quad (\text{D.11}) \\ & + \mathcal{J}_n \left[E_{//} \left(\frac{v_{//}}{v_\perp} \frac{\partial}{\partial v_\perp} + \frac{g(v)}{v_\perp} \right) + i \left(1 - \frac{k_{//} v_{//}}{\omega} \right) \frac{(k_x - k'_x) E_y - (k_y - k'_y) E_x}{\omega_{c\sigma}} \right. \\ & \left. \left. - i \frac{v_{//} E_{//}}{\omega \omega_{c\sigma}} (k_x (k_y - k'_y) - k_y (k_x - k'_x)) \right) \right] \left. \right\} f_\sigma^{(0)}(\mathbf{k}_\perp - \mathbf{k}'_\perp, v_\perp, v_{//}), \end{aligned}$$

with

$$\begin{aligned}
 \mathbf{E} &= \mathbf{E}(\mathbf{k}'_{\perp}, k_{\parallel}, \omega), \\
 P_x^n &= P_x^n(\mathbf{k}'_{\perp}) = \frac{1}{2} [\mathcal{J}_{n+1}(\mathbf{k}'_{\perp}) + \mathcal{J}_{n-1}(\mathbf{k}'_{\perp})], \\
 P_y^n &= P_y^n(\mathbf{k}'_{\perp}) = -\frac{i}{2} [\mathcal{J}_{n+1}(\mathbf{k}'_{\perp}) - \mathcal{J}_{n-1}(\mathbf{k}'_{\perp})], \\
 \mathcal{J}_n &= \mathcal{J}_n(\mathbf{k}'_{\perp}) = J_n\left(\frac{\mathbf{k}'_{\perp} v_{\perp}}{\omega_{c\sigma}}\right) e^{in\phi'}, \\
 g(v) &= v_{\perp} \frac{\partial}{\partial v_{\parallel}} - v_{\parallel} \frac{\partial}{\partial v_{\perp}},
 \end{aligned} \tag{D.12}$$

and where we have decomposed the term $E_{\parallel} \frac{\partial}{\partial v_{\parallel}}$ into $E_{\parallel} \left(\frac{v_{\parallel}}{v_{\perp}} \frac{\partial}{\partial v_{\perp}} + \frac{1}{v_{\perp}} g(v) \right)$, which enables us to have more symmetries in following calculations. Note that all the terms in Eq.(D.11) divided by ω are due to $\mathbf{B}^{(1)}$ and the others to $\mathbf{E}^{(1)}$. We have checked that these latter terms recover the electrostatic case, Eq.(13) of Yasseen and Vaclavik [1983] or Eq.(3.4), if we introduce $\mathbf{E}^{(1)}(\mathbf{x}, t) = -\nabla\Phi^{(1)}(\mathbf{x}, t)$. We have also verified that Eq.(D.11) is equivalent to Eq.(11) of Yasseen and Vaclavik [1986].

This equation is valid for arbitrary density and anisotropic temperature profiles and does not assume any approximation with respect to $k_{\perp}\rho_{\sigma}$, where ρ_{σ} is the Larmor radius of species σ . One should not forget that $f_{\sigma}^{(0)}(\mathbf{k}_{\perp}, v)$ is the Fourier transform of the equilibrium distribution function of the guiding centers, and not of the particles. Thus, one needs to specify the density and temperature profiles of the guiding centers.

Appendix E

Discretized dispersion relation

In this Appendix we present the discretized dispersion relation (DDR) of Maxwell's equations in vacuum, obtained using a finite element method with Hermite-cubic and quadratic-cubic basis functions. We assume solutions of the form:

$$E_w = \sum_j E_{ow}^1 e^{ikx_j} \gamma_j(x) + E_{ow}^2 e^{ikx_j} \psi_j(x) , \quad w = x, y, z, \quad (E.1a)$$

or:

$$\begin{cases} E_x = \sum_j E_{ox}^1 e^{ikx_j} \Omega_j(x) + E_{ox}^2 e^{ikx_j-1/2} \zeta_j(x) , \\ E_w = \sum_j E_{ow}^1 e^{ikx_j} \gamma_j(x) + E_{ow}^2 e^{ikx_j} \psi_j(x) , \quad w = y, z, \end{cases} \quad (E.1b)$$

where γ , ψ , Ω and ζ are sketched in Figs.5.1d and c. These two cases are referred to as the "cubic—cubic and the "quadratic—cubic" cases, respectively. We use Eq.(E.1) to construct the matrix $\underline{\underline{D}}$ (Eq.(5.14)), which leads to calculating integrals of the type:

$$\sum_{j=i-1}^{i+1} \int_{x_{j-1}}^{x_{i+1}} dx \frac{d^\alpha \eta_j(x)}{dx^\alpha} \frac{d^\beta \kappa_j(x)}{dx^\beta} , \quad \alpha = 0, 1 , \quad \beta = 0, 1 ,$$

where η and κ are one of the four basis functions mentioned above. We obtain

the following DDR for the cubic—cubic case:

$$DYY_{cc} DXZ_{cc} = 0 , \quad (E.2)$$

with

$$DYY_{cc} = \det \begin{pmatrix} \kappa^2 a_0 + \frac{6}{5} G_2 & -\kappa^2 b_1 - \frac{1}{5} G_1 \\ \kappa^2 b_1 + \frac{1}{5} G_1 & \kappa^2 b_0 - b_2 \end{pmatrix},$$

and

$$DXZ_{cc} = \det \begin{pmatrix} \underline{d}_{xx}^{cc} & \underline{d}_{xz}^{cc} \\ \underline{d}_{xz}^{cc} & \underline{d}_{zz}^{cc} \end{pmatrix},$$

$$\underline{d}_{xx}^{cc} = \begin{pmatrix} \kappa^2 a_0 & -\kappa^2 b_1 \\ \kappa^2 b_1 & \kappa^2 b_0 \end{pmatrix},$$

$$\underline{d}_{xz}^{cc} = \begin{pmatrix} -i k_z G_1 & i k_z \frac{h^2}{10} G_2 \\ -i k_z \frac{h^2}{10} G_2 & i k_z \frac{h^2}{30} G_1 \end{pmatrix},$$

$$\underline{d}_{zz}^{cc} = \begin{pmatrix} \frac{\omega^2}{c^2} a_0 + \frac{6}{5} G_2 & -\frac{\omega^2}{c^2} b_1 - \frac{1}{5} G_1 \\ \frac{\omega^2}{c^2} b_1 + \frac{1}{5} G_1 & \frac{\omega^2}{c^2} b_0 - b_2 \end{pmatrix},$$

where

$$\begin{aligned} \kappa^2 &= \frac{\omega^2}{c^2} - k_z^2, \\ a_0 &= 1 + \frac{9}{70} h^2 G_2, \\ b_0 &= \frac{h^2}{140} \left(\frac{2}{3} - h^2 G_2 \right), \\ b_1 &= \frac{13}{210} h^2 G_1, \\ b_2 &= \frac{1}{30} (6 - h^2 G_2), \\ G_1 &= i \frac{\sin kh}{h}, \\ G_2 &= - \frac{2(1 - \cos kh)}{h^2}. \end{aligned}$$

If we introduce the quadratic basis functions for approximating the E_x component, we obtain:

$$DYY_{qc} DXZ_{qc} = 0, \quad (E.3)$$

with $DYY_{qc} \equiv DYY_{cc}$, as we did not change the basis functions for E_y , and:

$$DXZ_{qc} = \det \begin{pmatrix} \underline{d}_{xx}^{qc} & \underline{d}_{xz}^{qc} \\ \underline{d}_{zx}^{qc} & \underline{d}_{zz}^{qc} \end{pmatrix},$$

where

$$\underline{d}_{xx}^{qc} = \begin{pmatrix} \kappa^2 b_2 & \frac{\kappa^2}{15} K_{+1}^+ \\ \frac{\kappa^2}{15} K_{-1}^+ & \frac{8}{15} \kappa^2 \end{pmatrix},$$

$$\underline{\underline{d}}_{xz}^{qc} = \begin{pmatrix} -i \frac{k_z}{5} G_1 & -i k_z c_1 \\ -i \frac{4k_z}{5h} K_{-1}^- & i \frac{k_z}{15} K_{-1}^+ \end{pmatrix},$$

$$\underline{\underline{d}}_{zx}^{qc} = \begin{pmatrix} -i \frac{k_z}{5} G_1 & i \frac{4k_z}{5h} K_{+1}^- \\ i k_z c_1 & -i \frac{k_z}{15} K_{+1}^+ \end{pmatrix},$$

$$\underline{\underline{d}}_{zz}^{qc} = \underline{\underline{d}}_{zz}^{cc},$$

with

$$c_1 = \frac{1}{20} \left(\frac{8}{3} - h^2 G_2 \right),$$

$$K_n^{\pm 1} = 1 \pm e^{i n k h}, \quad n = \pm 1.$$

Introducing the matrices as input to the software Mathematica and expanding the determinants, one finds the following relation between the XZ and YY contribution:

$$DXZ_{qc} = \frac{\omega^2}{c^2} \frac{2(3 - \cos kh)}{45} DYY_{qc}. \quad (E.4)$$

Therefore, $DXZ_{qc}=0$ is equivalent to $DYY_{cc}=0$ and it shows that the quadratic—cubic method is pollution free.



REFERENCES

- Abramowitz M. and Stegun I. E., Handbook of Mathematical Functions, National Bureau of Standards, Washington, DC, 1964.
- Anderegg F. and Good T. N., private communication, 1989.
- Appert K., Gruber R., Troyon F. and Vaclavik J., Plasma Phys. **24** (1982) 1147.
- Appert K., Hellsten T., Vaclavik J. and Villard L., Comput. Phys. Commun. **40** (1986a) 73.
- Appert K., Hellsten T., Sauter O., Succi S., Vaclavik J. and Villard L., Comput. Phys. Commun. **43** (1986b) 125.
- Appert K., Hellsten T., Lütjens H., Sauter O., Vaclavik J. and Villard L., in Proceedings of the International Conference on Plasma Physics, Kiev, Invited Papers, edited by A. G. Sitenko (World Scientific, Singapore, 1987), p. 1230.
- Batchelor D. B., Jaeger E. F. and Weitzner H., in Theory of Fusion Plasmas (Proc. Joint Varenna-Lausanne Int. Workshop, Chexbres, 1988), Editrice Compositori, Bologna (1989a) 691.
- Batchelor D. B., Jaeger E. F., Carreras B. A., Lynch V. E., Weitzner H., Imre K., Stevens D. C., Fuchs V. and Bers A., in Plasma Physics and Controlled Fusion Research 1988 (Proc. 12th Int. Conf. Nice, 1988), Vol. 1, IAEA, Vienna (1989b) 611.
- Batchelor D. B., Jaeger E. F. and Colestock P. L., Phys. Fluids B **1** (1989c) 1174.
- Bathnagar V. P., Koch R., Geilfus P., Kirkpatrick R. and Weynants R. R., Nucl. Fusion **24** (1984) 955.
- Berk H. L. and Pfirsch D., J. Math. Phys. **21** (1980) 2054.
- Berk H. L. and Dominguez R. R., Phys. Fluids **26** (1983) 1825.

- Bernstein I., *Phys. Fluids* **18** (1975) 320.
- Brambilla M. and Ottaviani M., *Plasma Phys. Controlled Fusion* **27** (1985) 919.
- Brambilla M., *Comput. Phys. Rep.* **4** (1986) 71. See also Brambilla M. and Cardinali A., *Plasma Phys.* **24** (1982) 1187.
- Brambilla M., *Nucl. Fusion* **28** (1988a) 549.
- Brambilla M. and Krücken T., *Nucl. Fusion* **28** (1988b) 1813.
- Brunner S. and Vaclavik J., to be reported, 1992.
- Cairns R. A. and Lashmore-Davies C. N., *Phys. Fluids* **29** (1986) 3639.
- Cairns R. A., Lashmore-Davies C. N., Dendy R. O., Harvey B. M., Hastie R. J. and Holt H., *Phys. Fluids B* **3** (1991) 2953.
- Cesario R., private communication, 1990.
- Chaudry M. B., *J. Phys. Soc. Jpn.* **52** (1983) 856.
- Chiu S. C. and Mau T. K., *Nucl. Fusion* **23** (1983) 1613.
- Chiu S. C., Mayberry M. J., Bard W. D., *Nucl. Fusion* **30** (1990) 2551.
- Chow C., Fuchs V. and Bers A., *Phys. Fluids B* **2** (1990) 1089.
- Colestock P. L. and Kashuba R. J., *Nucl. Fusion* **23** (1983) 763.
- Davidson R. C., *Phys. Fluids* **19** (1976) 1189.
- Edery D. and Picq H., *Comput. Phys. Commun.* **40** (1986) 95; Gambier D. J. and Samain A., *Nucl. Fusion* **25** (1985) 283.
- England A. C., Eldridge O. C., Knowlton S. F., Porkolab M. and Wilson J. R., *Nucl. Fusion* **29** (1989) 1527, Secs. 3.4 and 3.5.
- Ferraro R. D., Sanuki H., Littlejohn R. G. and Fried B. D., *Phys. Fluids* **28** (1985) 2181.
- Ferraro R. D. and Fried B. D., *Phys. Fluids* **31** (1988) 2594.
- Fried B. D., Conte S. D., *The Plasma Dispersion Function*, Academic, New York, 1961.

- Fukuyama A., Nishiyama S., Itoh K. and Itoh S.-I., *Nucl. Fusion* **23** (1983) 1005.
- Fukuyama A., Itoh K. and Itoh S.-I., *Comput. Phys. Rep.* **4** (1986) 137.
- Gerver M. J., Birdsall C. K., Langdon A. B. and Fuss D., *Phys. Fluids* **20** (1977) 291.
- Gradshteyn I. S. and Ryzhik M., Tables of Integrals, Series, and Products, Academic, New York, 1980.
- Gruber R. and Rappaz J., Finite Element Methods in Linear Ideal Magnetohydrodynamics, Springer-Verlag, Berlin, Heidelberg, 1985.
- Hasegawa A. and Chen L., *Phys. Rev. Lett.* **35** (1975) 370.
- Hasegawa A. and Uberoi C., The Alfvén wave, Technical Information Center, United States Department of Energy, Washington, DC (1982).
- Hellsten T., Appert K., Vaclavik J. and Villard L., *Nucl. Fusion* **25** (1985) 99.
- Itoh K., Itoh S.-I. and Fukuyama A., *Nucl. Fusion* **24** (1984) 13.
- Itoh S.-I., Fukuyama A., Itoh K. and Nishikawa K., *J. Phys. Soc. Jpn.* **54** (1985) 1800.
- Jaeger E. F., Batchelor D. B. and Weitzner H., *Nucl. Fusion* **28** (1988) 53.
- Jaeger E. F., Batchelor D. B., Carter M. D. and Weitzner H., *Nucl. Fusion* **30** (1990) 505.
- Jaun A. and Vaclavik J., in *Theory of Fusion Plasmas* (Proc. Joint Varenna-Lausanne Int. Workshop, Varenna, 1990), Editrice Compositori, Bologna (1990) 461.
- Jaun A., Vaclavik J. and Appert K., *Plasma Phys. Controlled Fusion* **33** (1991) 521.
- Kay A., Cairns R. A. and Lashmore-Davies C. N., *Plasma Phys. Controlled Fusion* **30** (1988) 471.

- Koch R., Bathnagar V. P., Messiaen A. M. and Van Eester D., *Comput. Phys. Commun.* **40** (1986) 1.
- Koch R., Nys V., Van Eester D. and Durodic F., *Ecole Royale Militaire, Brussels, LPP-ERM/KMS Rep. No. 89* (1989).
- Koch R., *Phys. Lett. A* **157** (1991) 399.
- Krall N. A. and Trivelpiece A. W., *Principles of Plasma Physics*, McGraw-Hill Book Company, New York, 1973.
- Lashmore-Davies C. N., Fuchs V., Francis G., Ram A. K., Bers A. and Gauthier L., *Phys. Fluids* **31** (1988) 1614.
- Linsker R., *Phys. Fluids* **24** (1981) 1485.
- Llobet X., Hellsten T. and Villard L., in *Theory of Fusion Plasmas* (Proc. Joint Varenna-Lausanne Int. Workshop, Chexbres, 1988), Editrice Compositori, Bologna (1989) 663.
- Llobet X., Appert K., Bondeson A. and Vaclavik J., *Comput. Phys. Commun.* **59** (1990) 199.
- Marchand R., Zhang C. F. and Lee Y. C., *Phys. Fluids* **26** (1983) 194.
- Martin Th. and Vaclavik J., *Helv. Phys. Acta* **60** (1987) 471.
- McVey B. D., *Nucl. Fusion* **19** (1979) 461.
- McVey B. D., Sund R. S. and Scharer J. E., *Phys. Rev. Lett.* **55** (1985) 507.
- Mikhailovski A. B., *Theory of Plasma Instabilities*, Vol. 1, Consultants Bureau, New York (1974).
- Moody J. D., Porkolab M., Fiore C. L., McDermott F. S., Takase Y., Terry J. and Wolfe S. M., *Phys. Rev. Lett.* **60** (1988) 298.
- Morton K. W., *Basic Course in Finite Element Methods*, First Graduate Summer Course in Computational Physics, EPFL, Lausanne, 1986.
- Ono M., Wong K. L. and Wurden G. A., *Phys. Fluids* **26** (1983) 298.

- Ono M., Beiersdorfer P., Bell R., Bernabai S., Cavallo A., Chmyga A., Cohen S., Colestock P., Gammel G., Greene G. J., Hosea J., Kaita R., Lehrman I., Mazzitelli G., Mazzucato E., McNeill D., Sato K., Stevens J., Timberlake J., Wilson J. R. and Wouters A., *Phys. Rev. Lett.* **60** (1988) 294.
- Perkins F. W., *Nucl. Fusion* **17** (1977) 1197.
- Romero H. and Scharer J., *Nucl. Fusion* **27** (1987) 363.
- Sanuki H., Watanabe T. and Watanabe M., *Phys. Fluids* **23** (1980) 158.
- Sauter O. and Vaclavik J., *Europhys. Conf. Abstr.* **12B**, Part II, (1988) 758.
- Sauter O., Vaclavik J. and Skiff F., *Phys. Fluids B* **2** (1990a) 475.
- Sauter O. and Vaclavik J., in *Theory of Fusion Plasmas* (Proc. Joint Varenna-Lausanne Int. Workshop, Varenna, 1990), Editrice Compositori, Bologna (1990b) 403.
- Sauter O. and Vaclavik J., *Lausanne Report LRP 432/91* (1991), submitted to *Nucl. Fusion*.
- Shokair I. R., Conn R. W. and Mau T. K., *Nucl. Fusion* **28** (1988) 1393.
- Skiff F., Ono M., Colestock P. and Wong K. L., *Phys. Fluids* **28** (1985) 2453; *Phys. Fluids* **31** (1988) 2030.
- Skiff F., Anderegg F., Tran M. Q., Paris P. J., Good T. N., Stern R. A. and Rynn N., in *Proceedings of the International Conference on Plasma Physics, Kiev, Invited Papers*, edited by A. G. Sitenko (World Scientific, Singapore, 1987), p. 441, and *Contributed Papers* (Naukova Dumka, Kiev, 1987), Vol. 1, p. 55.
- Smithe D. N., Colestock P. L., Kashuba R. J. and Kammash T., *Nucl. Fusion* **27** (1987) 1319.
- Smithe D. N., Colestock P. L., Kammash T. and Kashuba R., *Phys. Rev. Lett.* **60** (1988) 801.
- Stix T. H., *The Theory of Plasma Waves*, McGraw-Hill, New York (1962).

Stix T. H., Nucl. Fusion **15** (1975) 737.

Swanson D. G., Phys. Fluids **24** (1981) 2035.

Swanson D. G., Phys. Fluids **28** (1985) 1800.

Sy W. N.-C., Amano T., Ando R., Fukuyama A. and Watari T., Nucl. Fusion **25** (1985) 795.

Vaclavik J. and Appert K., Plasma Phys. Controlled Fusion **29** (1987) 257.

Vaclavik J. and Appert K., Nucl. Fusion **31** (1991) 1945.

Van Eester D., Koch R. and Nys V., in Theory of Fusion Plasmas (Proc. Joint Varenna-Lausanne Int. Workshop, Varenna, 1990), Editrice Compositori, Bologna (1990) 339.

Villard L., Appert K., Gruber R. and Vaclavik J., Comput. Phys. Rep. **4** (1986) 95.

Watanabe M., Serizawa Y., Sanuki H. and Watanabe T., J. Phys. Soc. Jpn. **50** (1981) 1738.

Watanabe T., Sanuki H. and Watanabe M., J. Phys. Soc. Jpn. **47** (1979) 286.

Yamagiwa M. and Takizuka T., Nucl. Fusion **28** (1988) 2241.

Yasseen F. and Vaclavik J., Phys. Fluids **26** (1983) 468.

Yasseen F. and Vaclavik J., Phys. Fluids **29** (1986) 450.

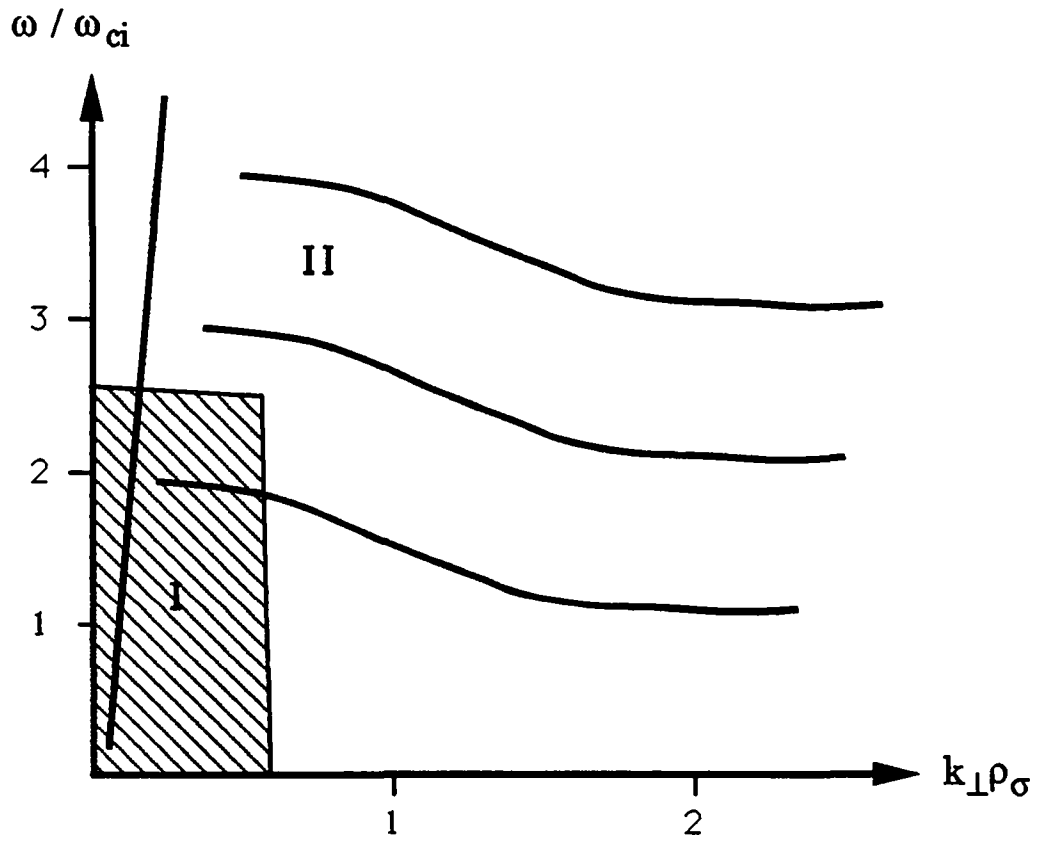


Fig.1.1: Typical dispersion relation with the domains of validity of the local (hatched region I) and nonlocal models (region II, whole domain).

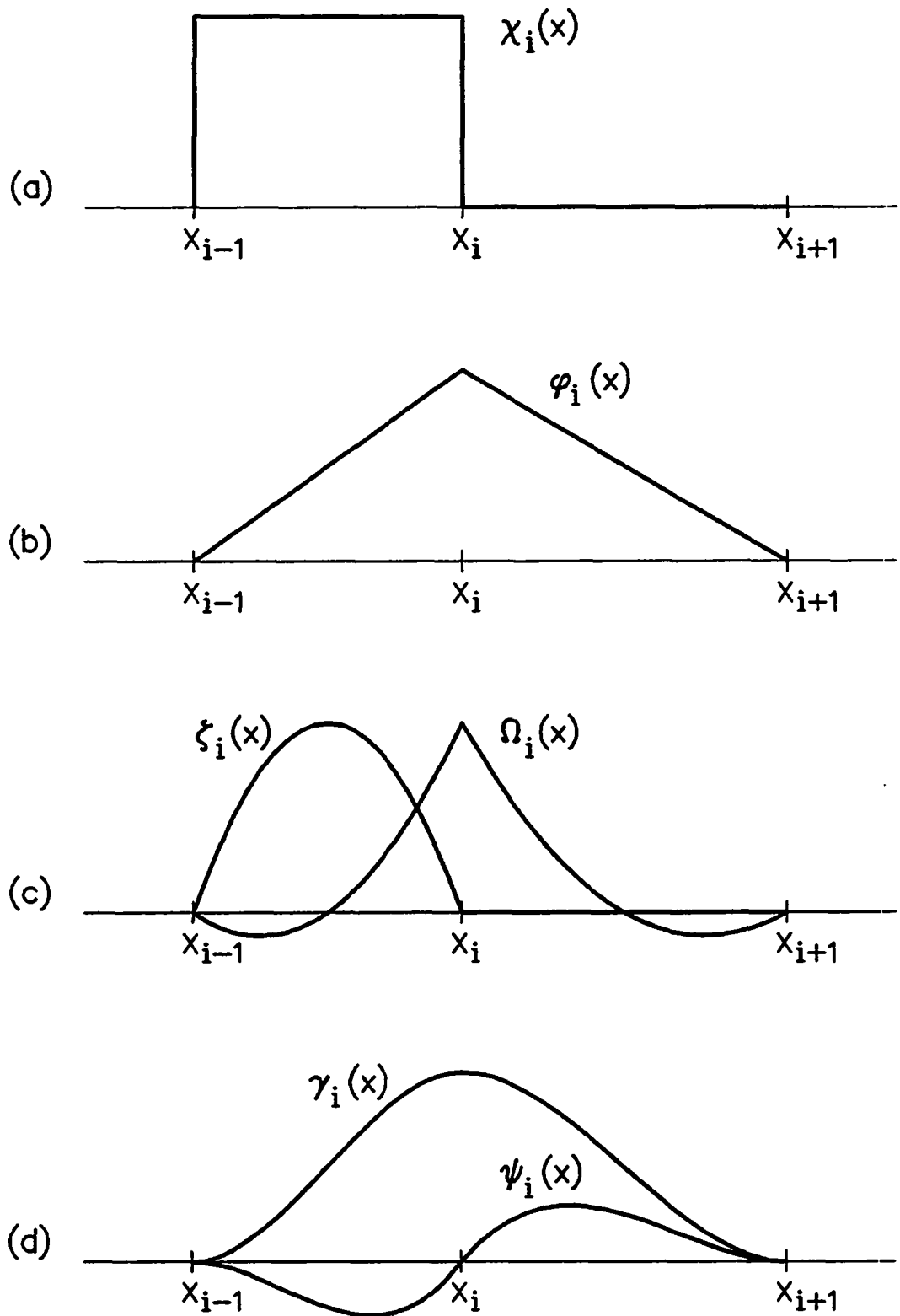


Fig.5.1: Different types of basis functions. (a) piece-wise constant: $\chi_i(x_{i-1/2})=1$; (b) linear: $\varphi_i(x_i)=1$; (c) quadratic: $\Omega_i(x_i)=1$, $\zeta_i(x_{i-1/2})=1$; (d) Hermite cubic: $\gamma_i(x_i)=1$, $\psi_i(x_{i-1/2})=1$.

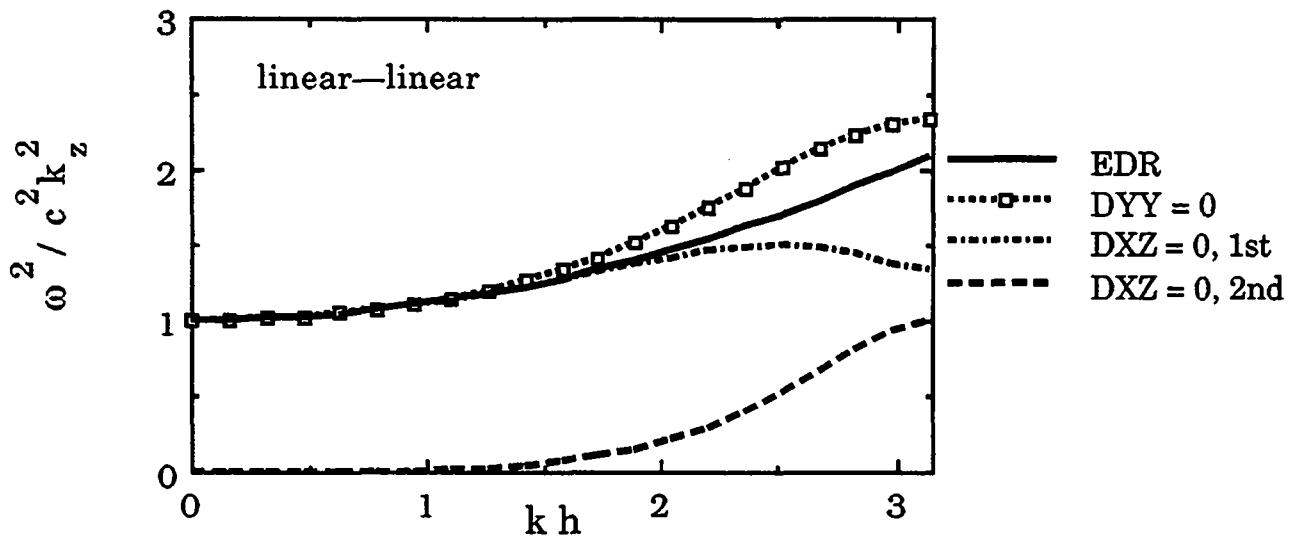


Fig.5.2: Discretized dispersion relation (DDR) with linear basis functions for E_x and E_y , E_z : $DYY_{||}=0$ and $DXZ_{||}=0$. The solid line represents the exact dispersion relation (EDR): $\omega^2/c^2 k_z^2 = k^2/k_z^2 + 1$. For $\omega^2/c^2 k_z^2 < 1$, k is purely imaginary. h is the mesh size.

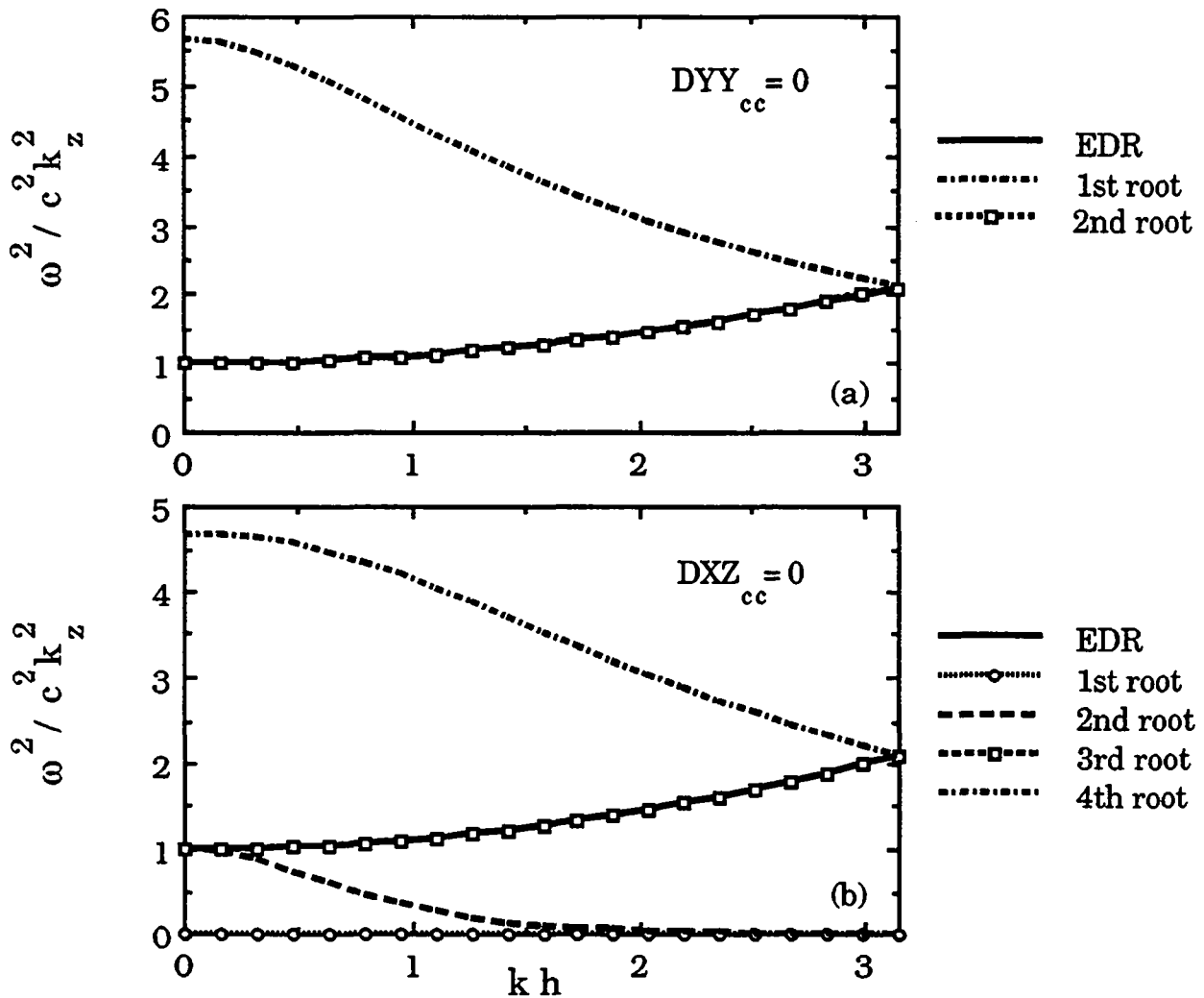


Fig.5.3: DDR with Hermite cubic basis: (a) $DYY_{cc}=0$, (b) $DXZ_{cc}=0$. Only the second root of DXZ_{cc} (long dashes) gives rise to pollution, when $\omega^2/c^2 k_z^2 < 1$.

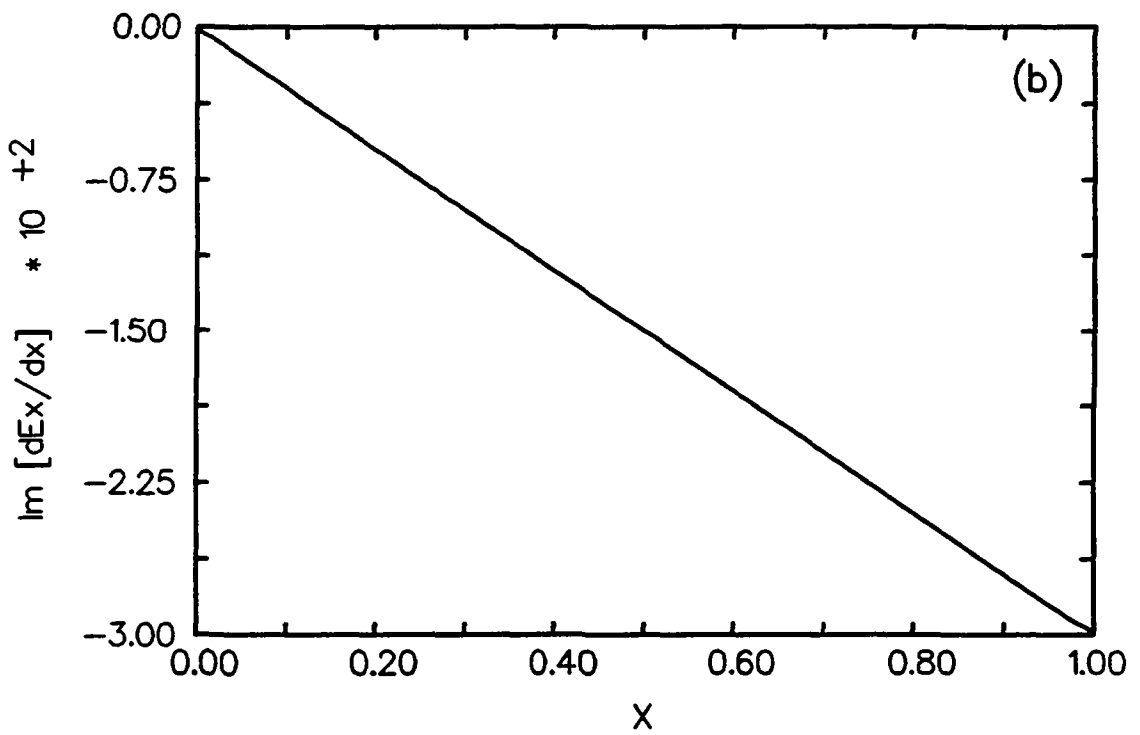
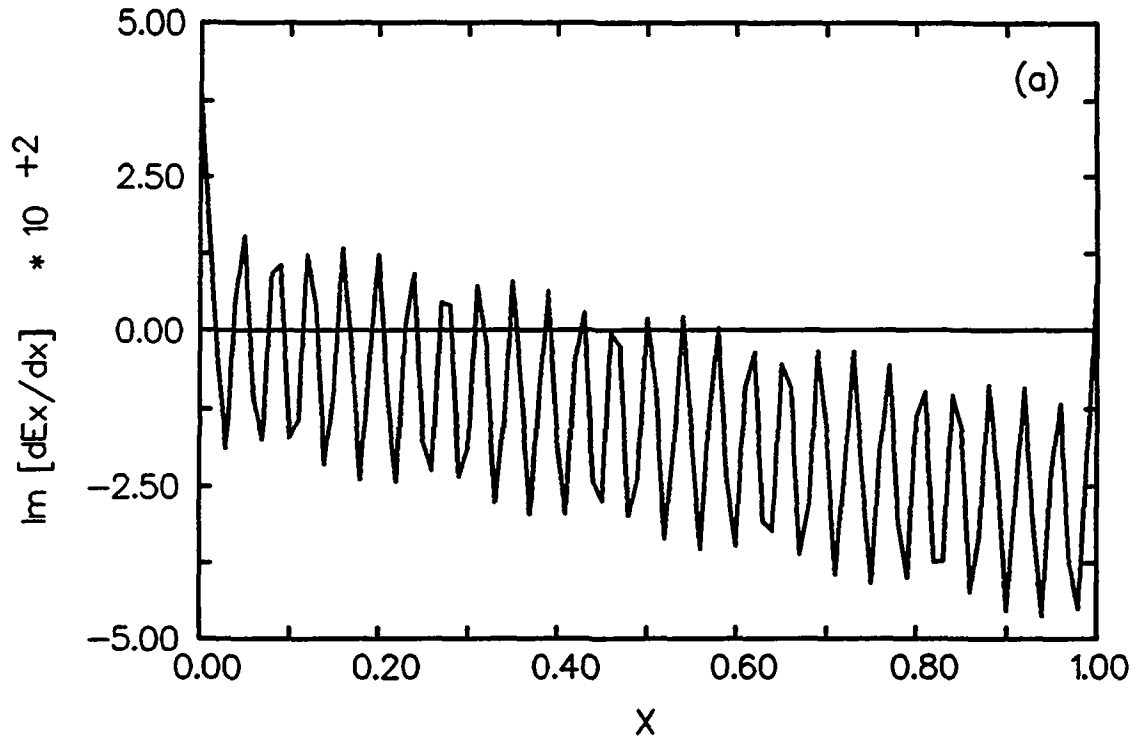


Fig.5.4a, b: Imaginary part of the wave field E_x vs x [m] in vacuum, with $\omega/c=0.016$ m/s and $k_z=0.03$ m^{-1} .(a) Solution obtained with linear basis functions for E_x and E_y , E_z , and (b) with piece-wise constant for E_x and linear for E_y , E_z .

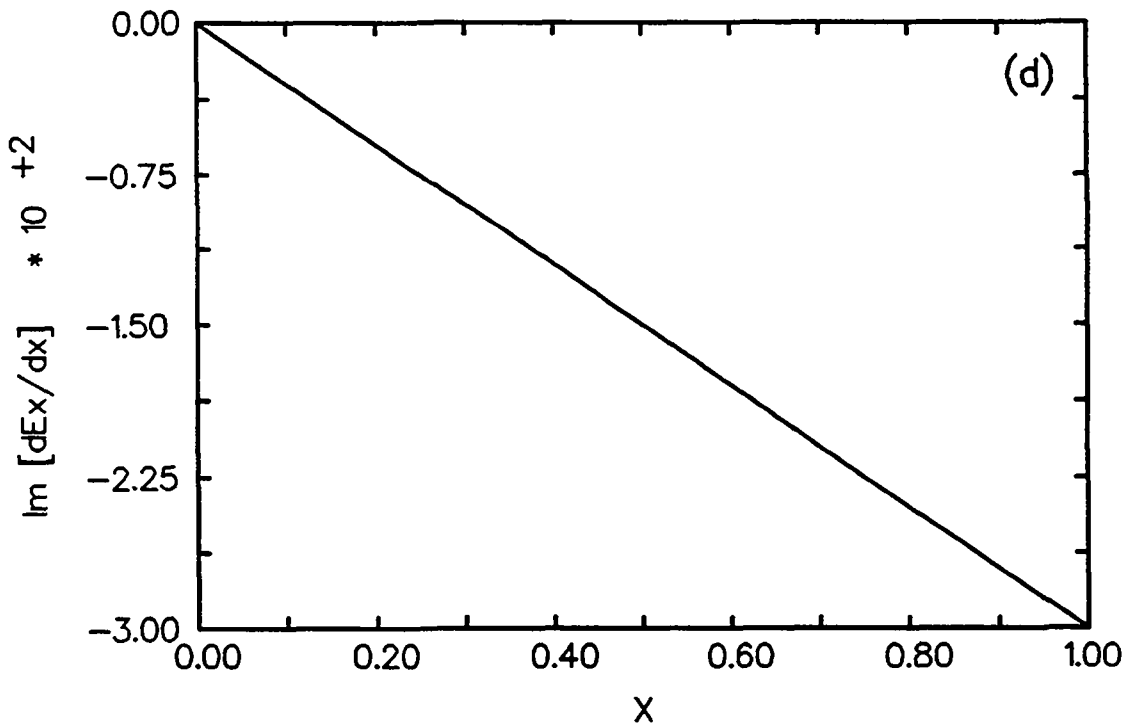
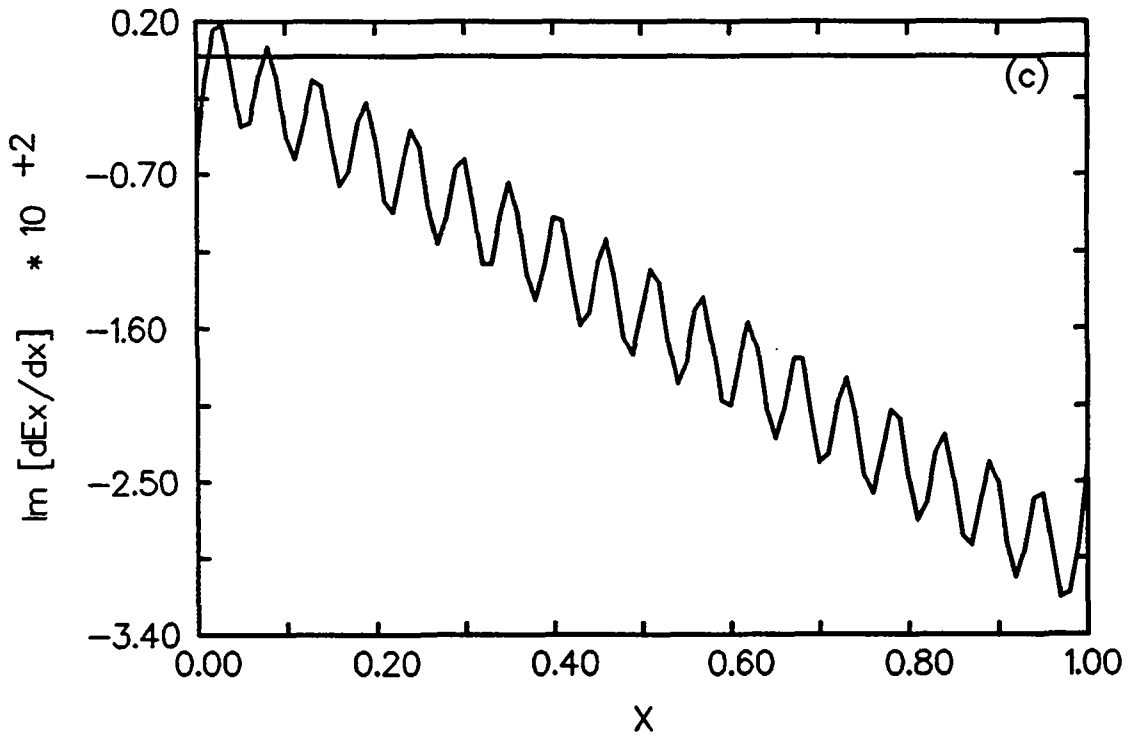


Fig.5.4c, d: The same plot as in Fig.5.4a, b, but with: (c) Hermite cubic basis for the three components and (d) quadratic for E_x and Hermite cubic for E_y, E_z .

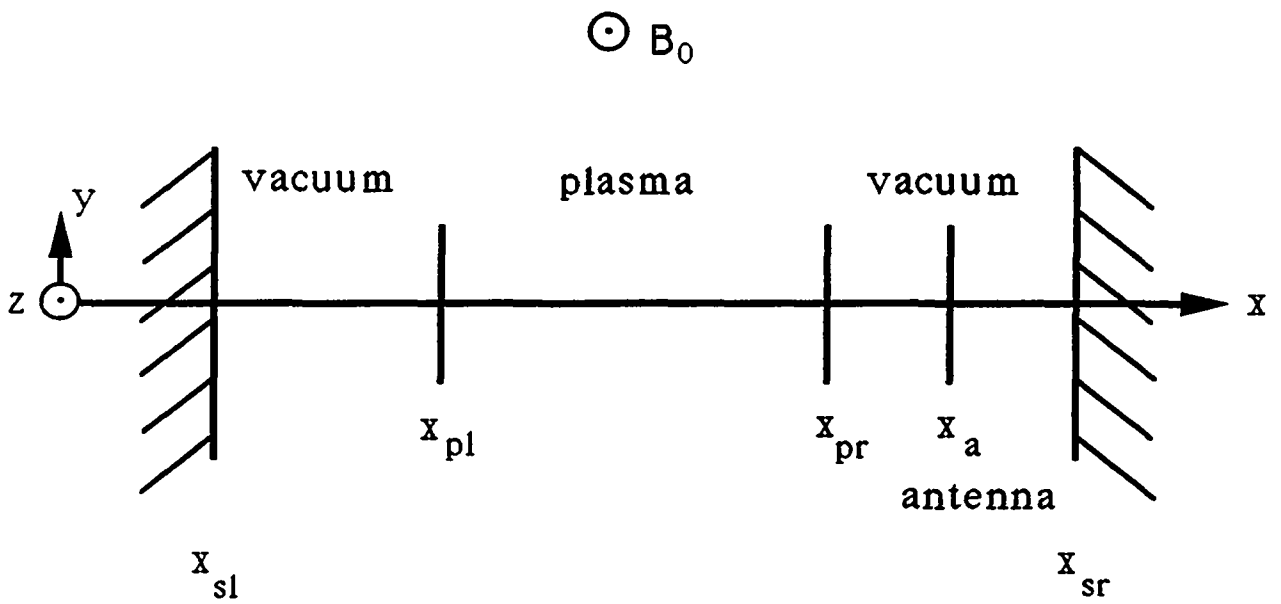


Fig.5.5: Configuration of the slab model. The plasma is situated between two vacuum regions which are limited by perfectly-conducting walls. An idealized antenna is located in vacuum on the right-hand side of the plasma. The current flows in the (y, z) plane. The equilibrium magnetic field $B_0(x)=B_0R_0/(R_0\pm x)$ is parallel to the z -axis.

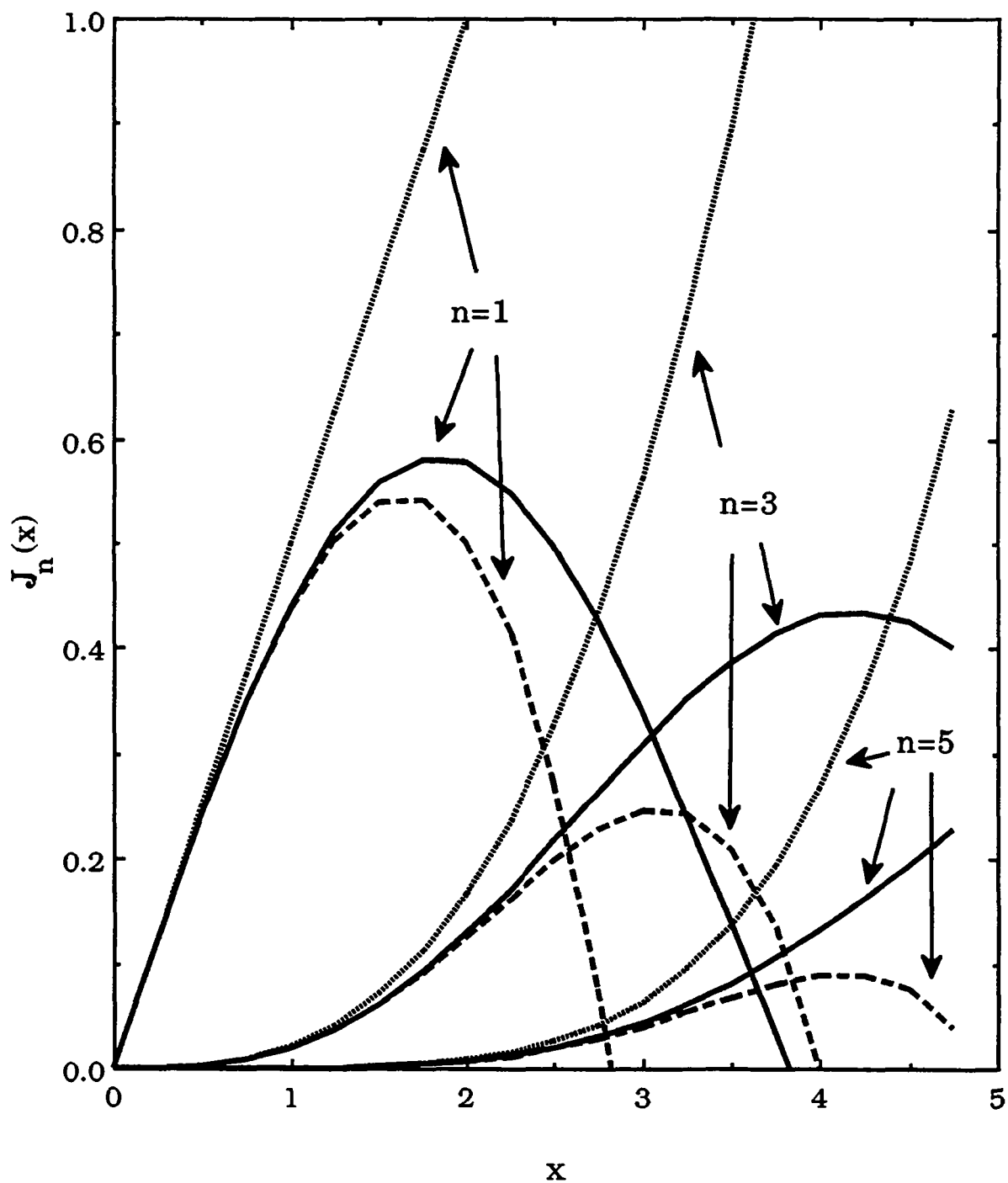


Fig.5.6: Approximation of the Bessel function $J_n(x)$ using the lowest order term, $x^n/2^n n!$ (dotted lines), and the first two lowest-order terms, $x^n[1-x^2/4(n+1)]/2^n n!$ (dashed lines), of the ascending series. The continuous lines represent the exact Bessel functions for $n=1, 3$ and 5 .

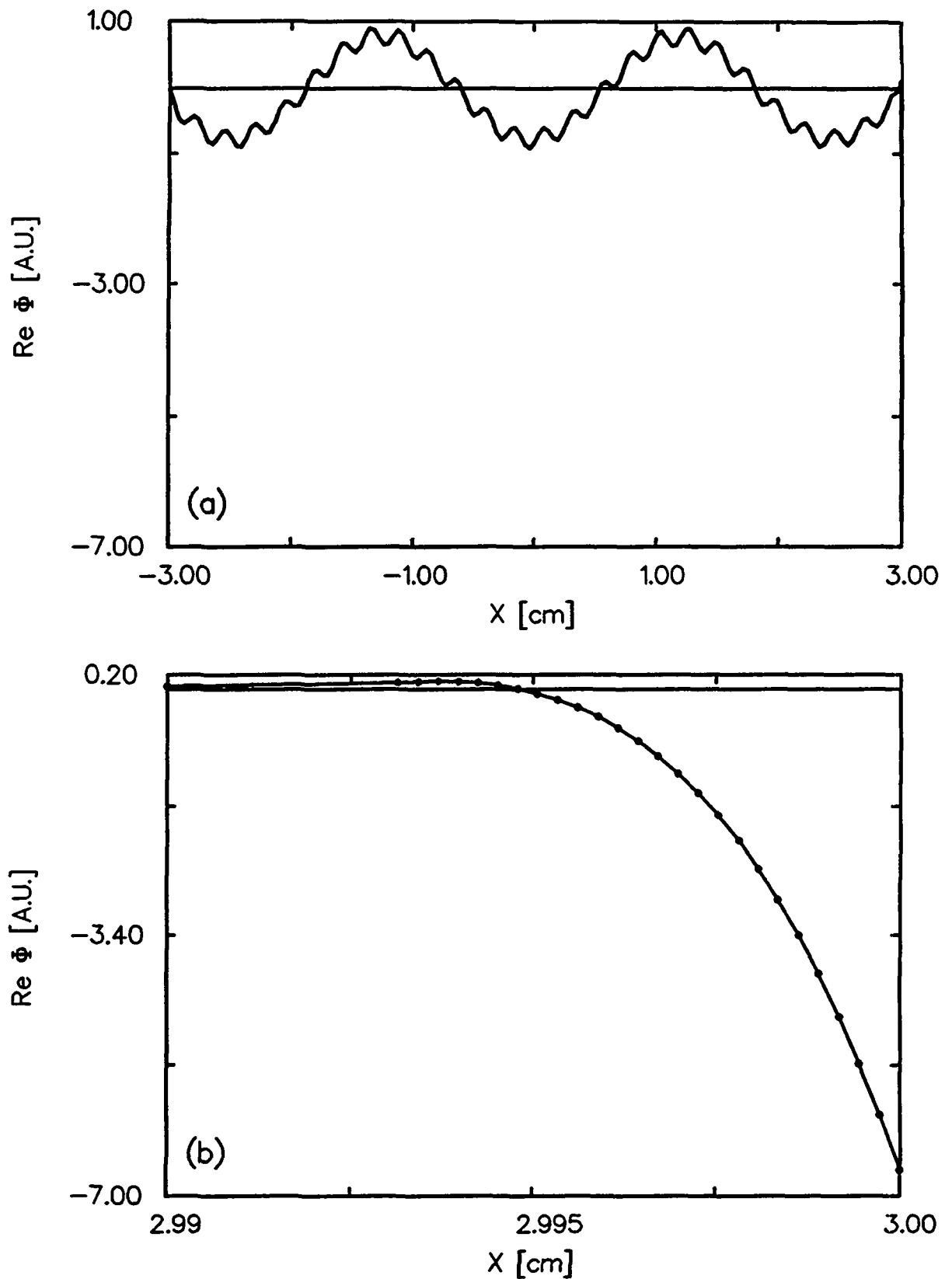


Fig.6.1: Real part of $\Phi(x)$ for a homogeneous argon plasma with: $T_e=14\text{eV}$, $T_i=0.1\text{eV}$, $B_0=0.2\text{T}$, $k_z=100\text{m}^{-1}$, $n=10^{17}\text{m}^{-3}$, $\omega/\omega_{ci}=3.5$. In Fig.6.1b, only the field very close to the right-hand side edge of the plasma is shown. The dots represent the mesh points. $\lambda_{De}=0.009\text{cm}$ and $\lambda_{Di}=0.0007\text{cm}$. The same units have been used for both plots.

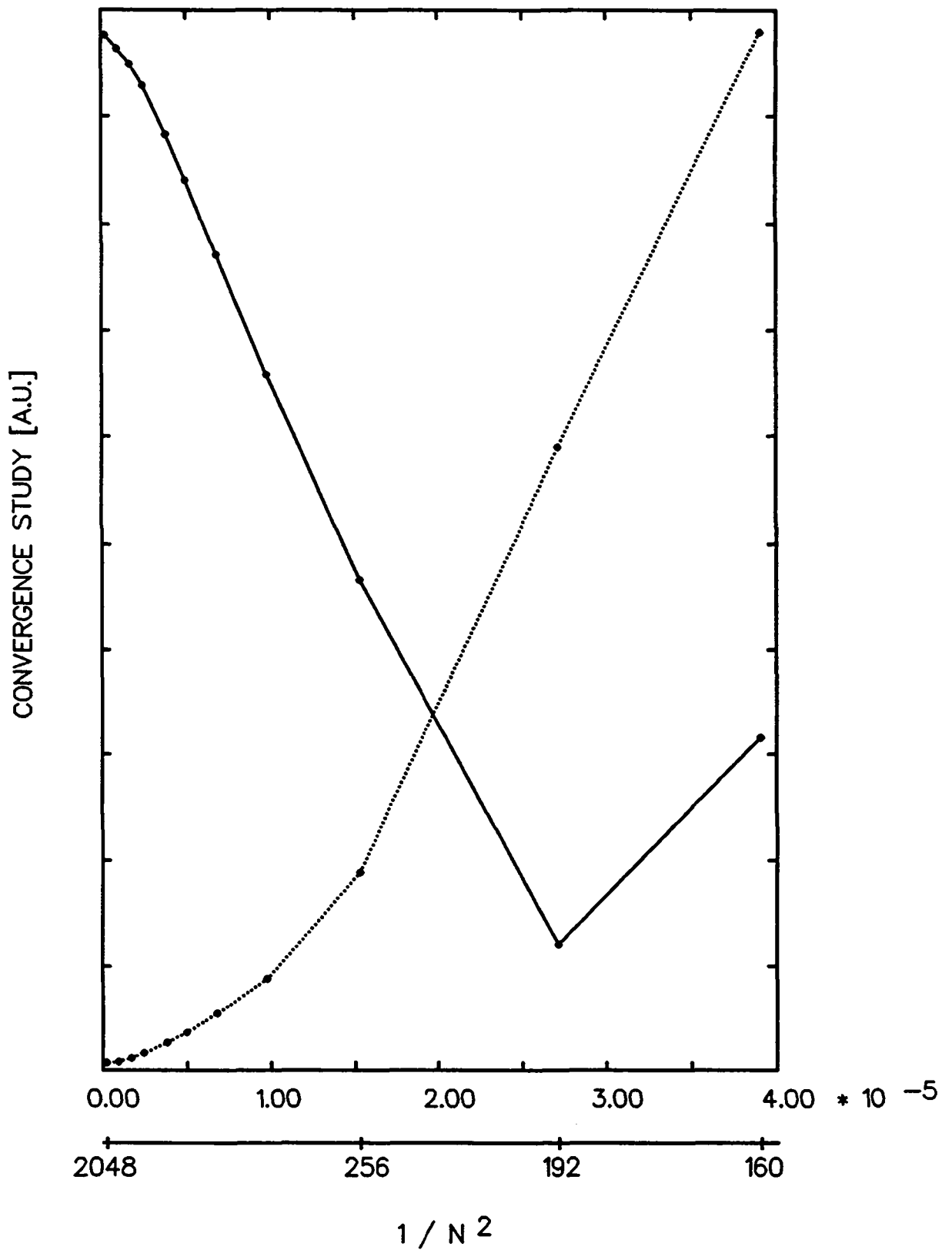


Fig.6.2: Convergence study of the real (solid line) and imaginary (dotted line) parts of $\Phi(x_{pr})$ vs $1/N^2$. A few values of N , the number of mesh intervals, are pointed out on the lower x-axis.

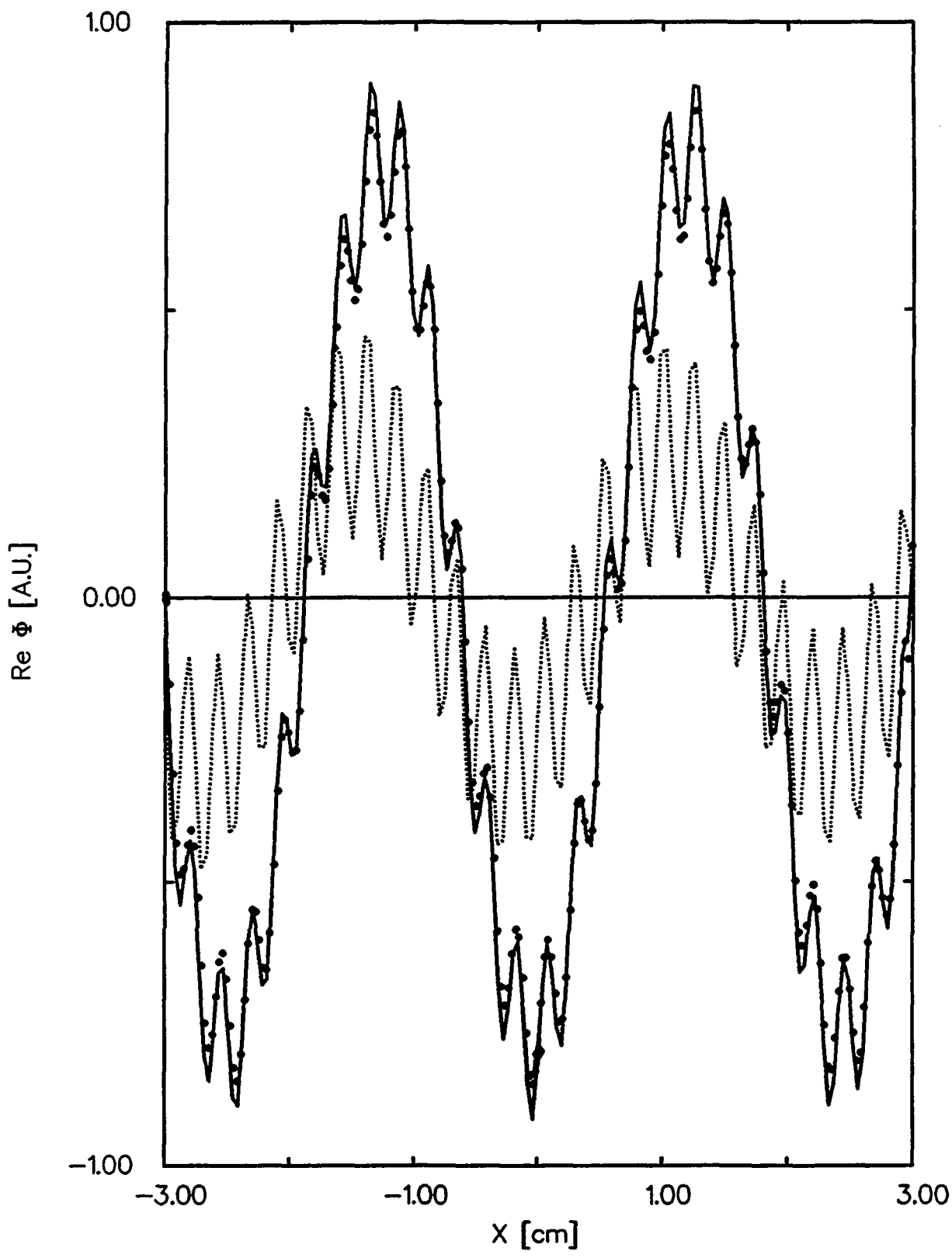


Fig.6.3: The same plot as in Fig.6.1a, but without the right-hand side drop. The wave field obtained with three different meshes is shown: $N=160$ (dotted line), $N=192$ (solid line) and $N=256$ (large dots).

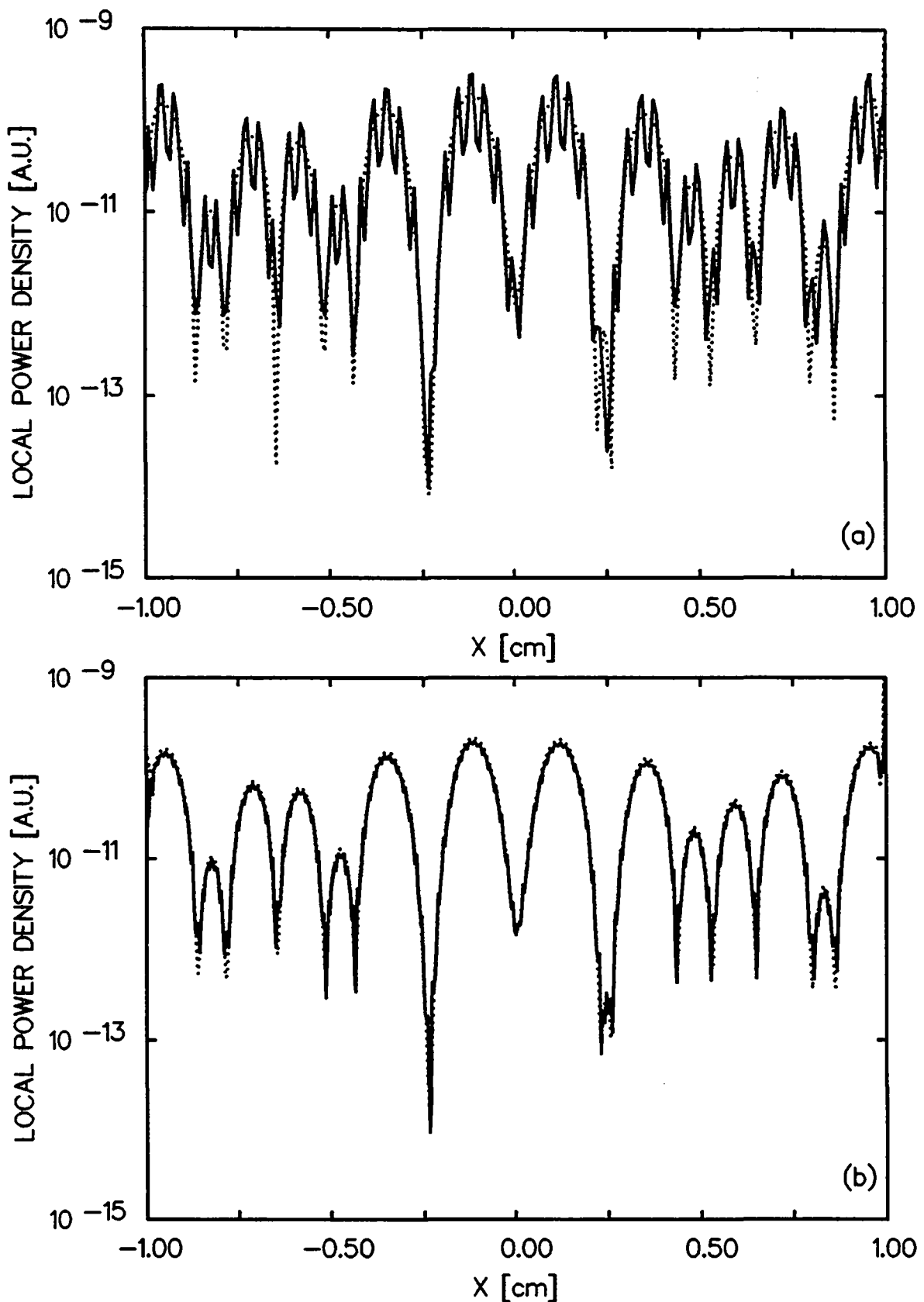


Fig.6.4: Local power absorption density $P_L(x)$, for the electrons only, with the same plasma parameters as in Fig.6.1, but with $x_{pr}=-x_{pl}=1\text{cm}$. The solid lines correspond to $P_L(x)$ and the dotted lines to the expanded formula. Two sets of meshes for x , x' and x'' have been used: (a) $N=128$, $N'=N''=64$, which took 67sec. of computing time, and (b) $N=320$, $N'=N''=160$, which took 837sec.

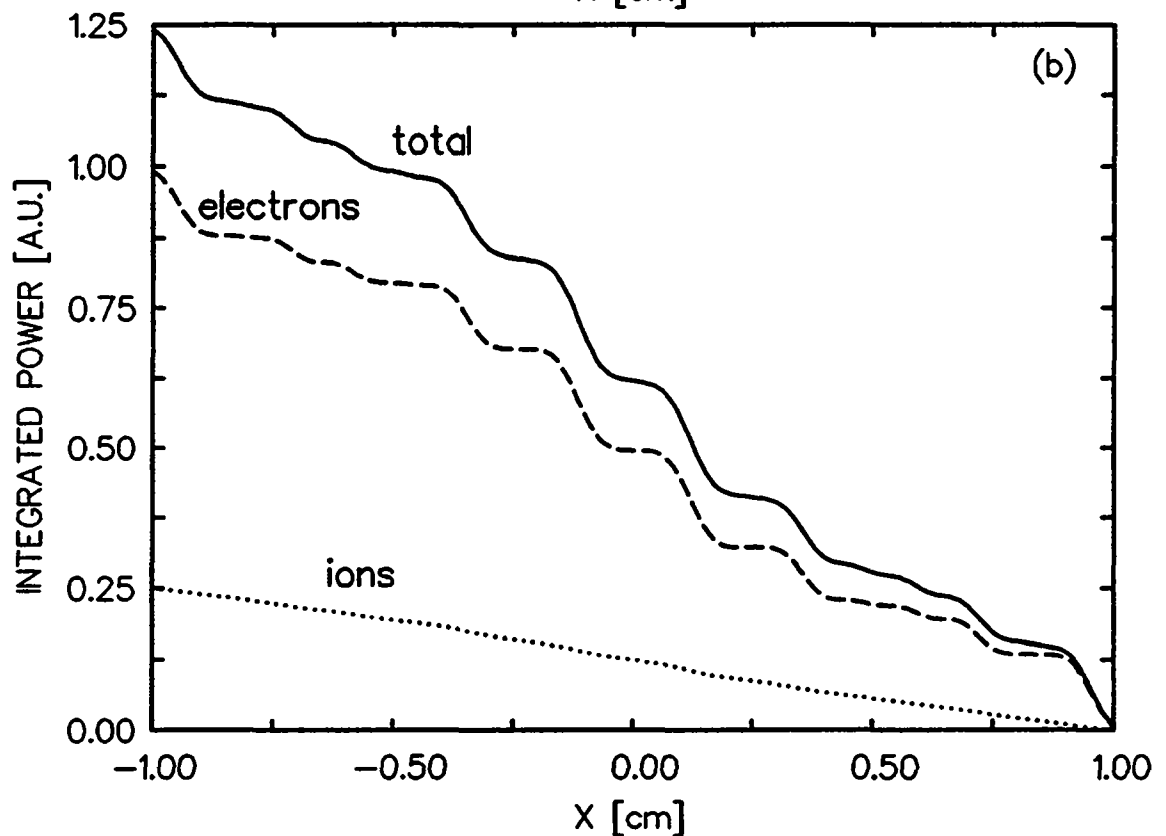
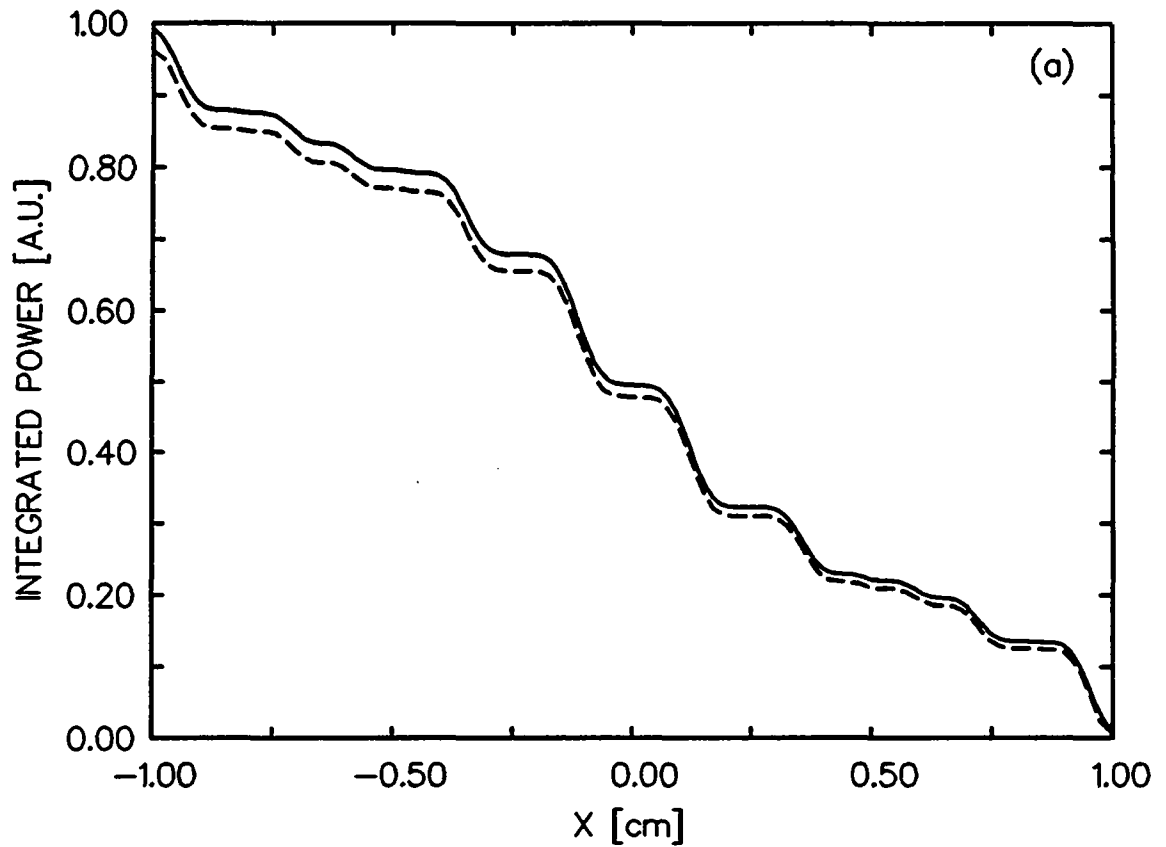


Fig.6.5: (a) Integrated power $\bar{P}_L(x)$, for electrons only, corresponding to the cases of low (dashed line) and high (solid line) resolution shown in Fig.6.4.
 (b) Ion (dotted line), electron (dashed line) and total (solid line) integrated power using the higher resolution mesh (Fig.6.4b).

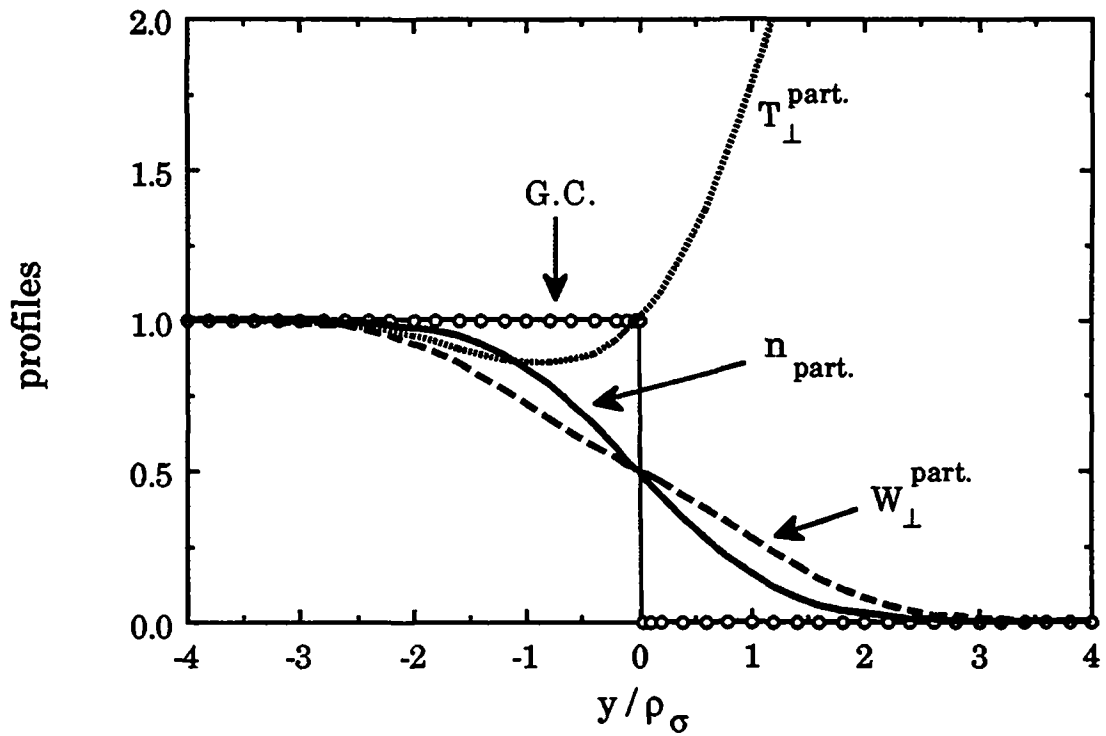


Fig.6.6: Sketch of guiding centre step profiles around $y=x-x''_{pr}$ and corresponding density and temperature profiles of the particles σ . $W_{\perp}^{part.} = n_{part.} T_{\perp}^{part.}$.

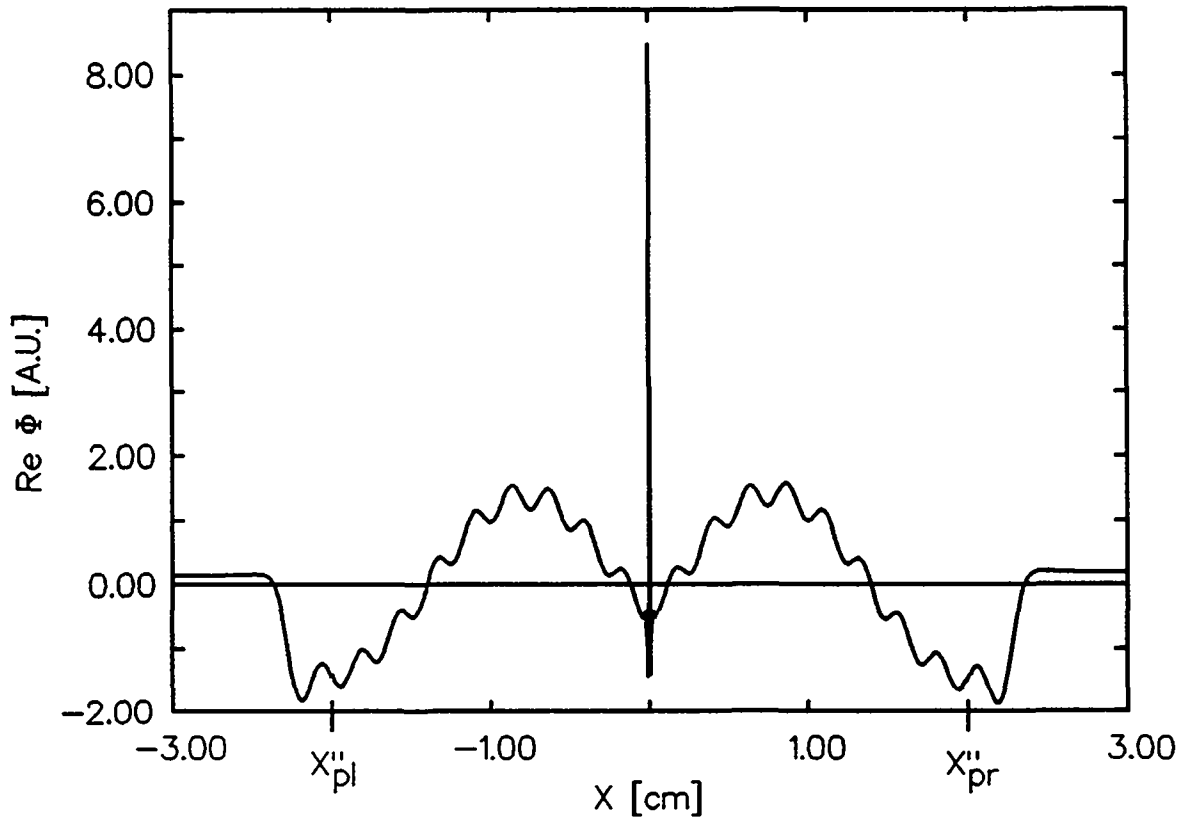


Fig.6.7: $\text{Re} [\Phi(x)]$ for the same parameters as in Fig.6.1, but with the source at $x=0$ and with the guiding centre interval $[x''_{pl}, x''_{pr}]$ shortened to $[-2, 2]$. That is, n_{GC} and T_{GC} are set to zero outside this interval. The ion Larmor radius ρ_i is equal to 1mm and the IBW wavelength about to 2.4mm.

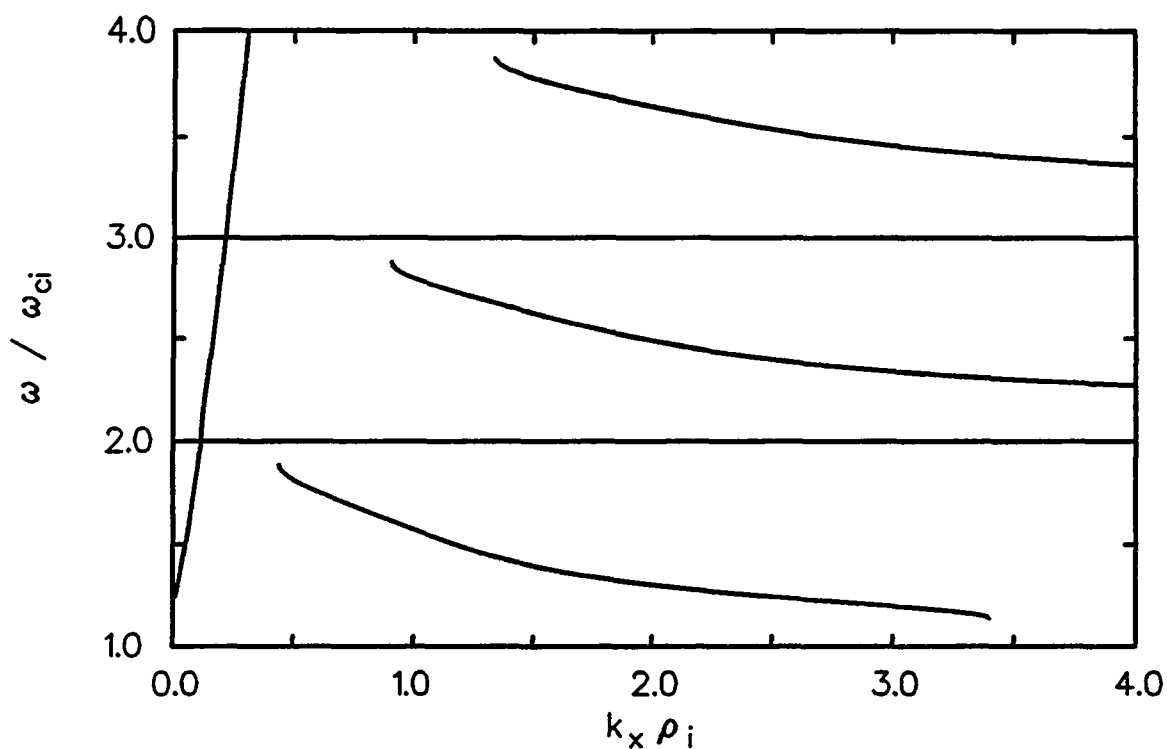


Fig.6.8: Dispersion relation of an argon plasma with the same plasma parameters as in Fig.6.1, $\rho_i \equiv 1\text{mm}$.

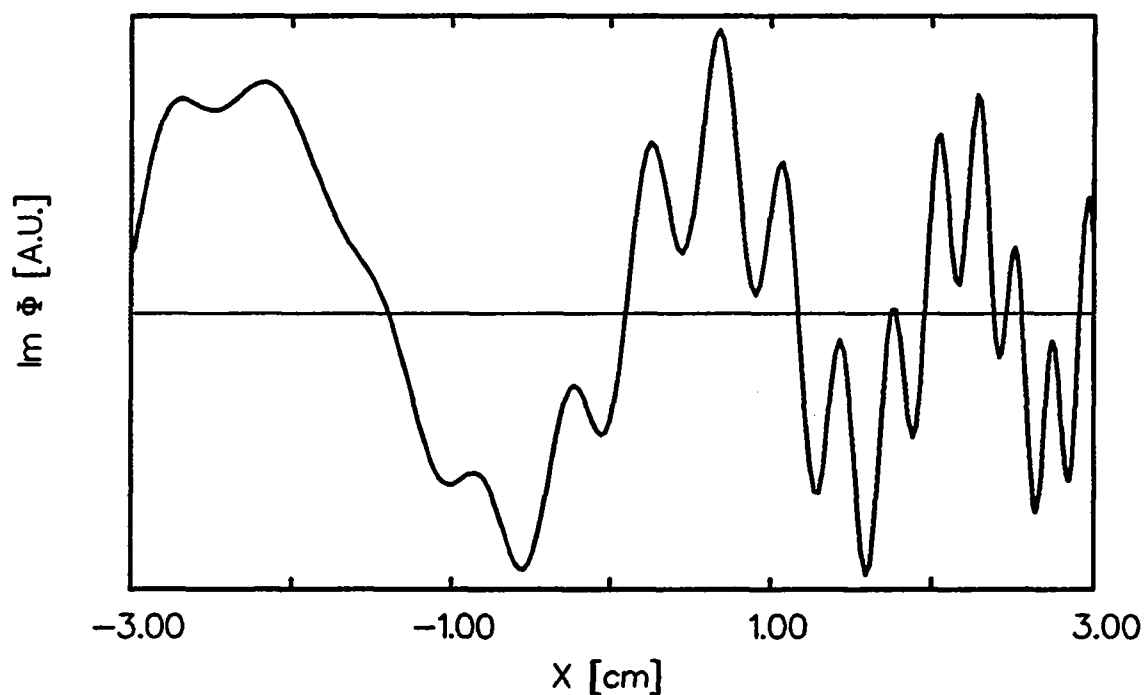


Fig.6.9: Imaginary part of $\Phi(x)$ for an argon plasma with the same parameters as in Fig.6.1, but with inhomogeneous temperature profiles. Both T_e and T_i are decreasing from left to right.

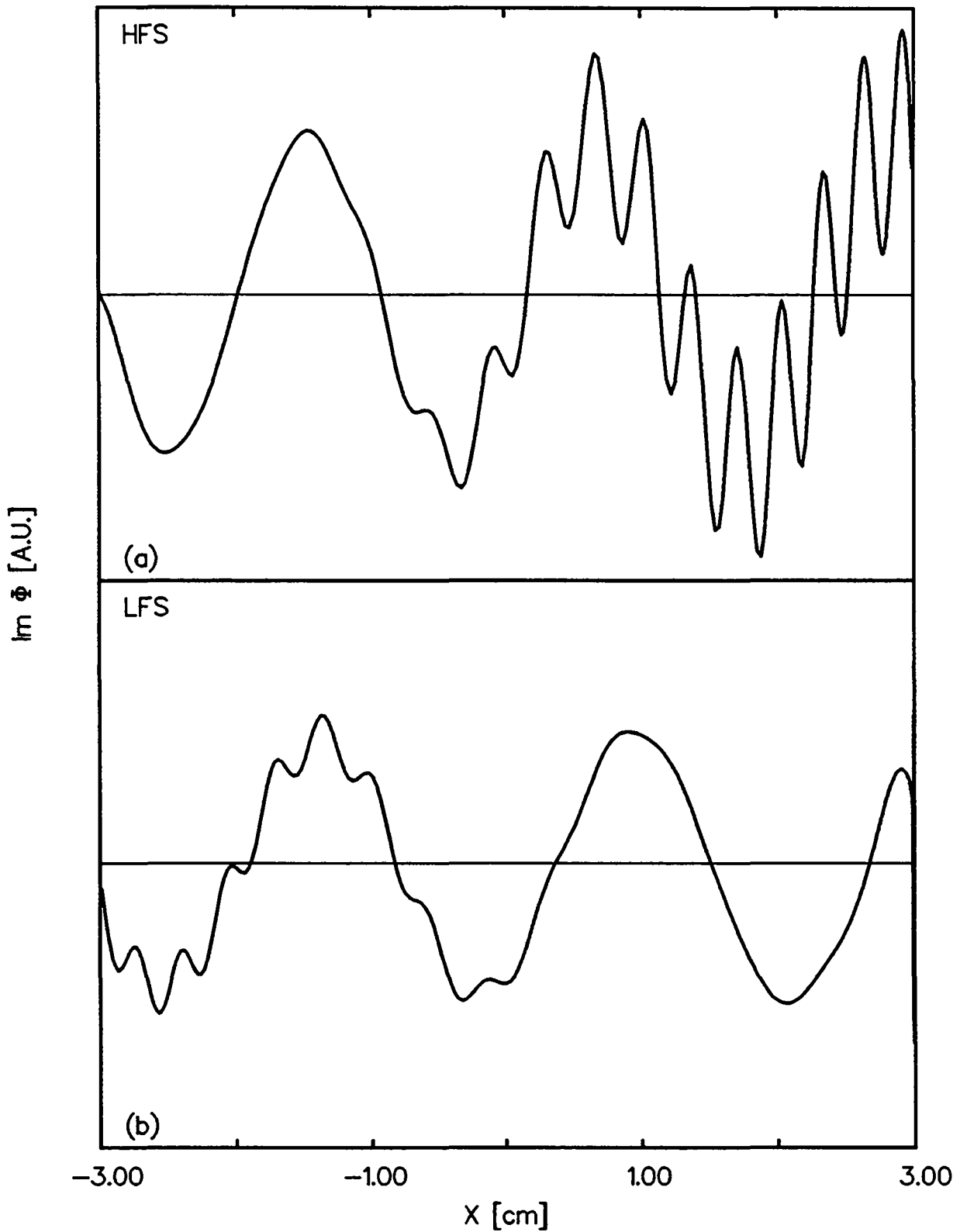
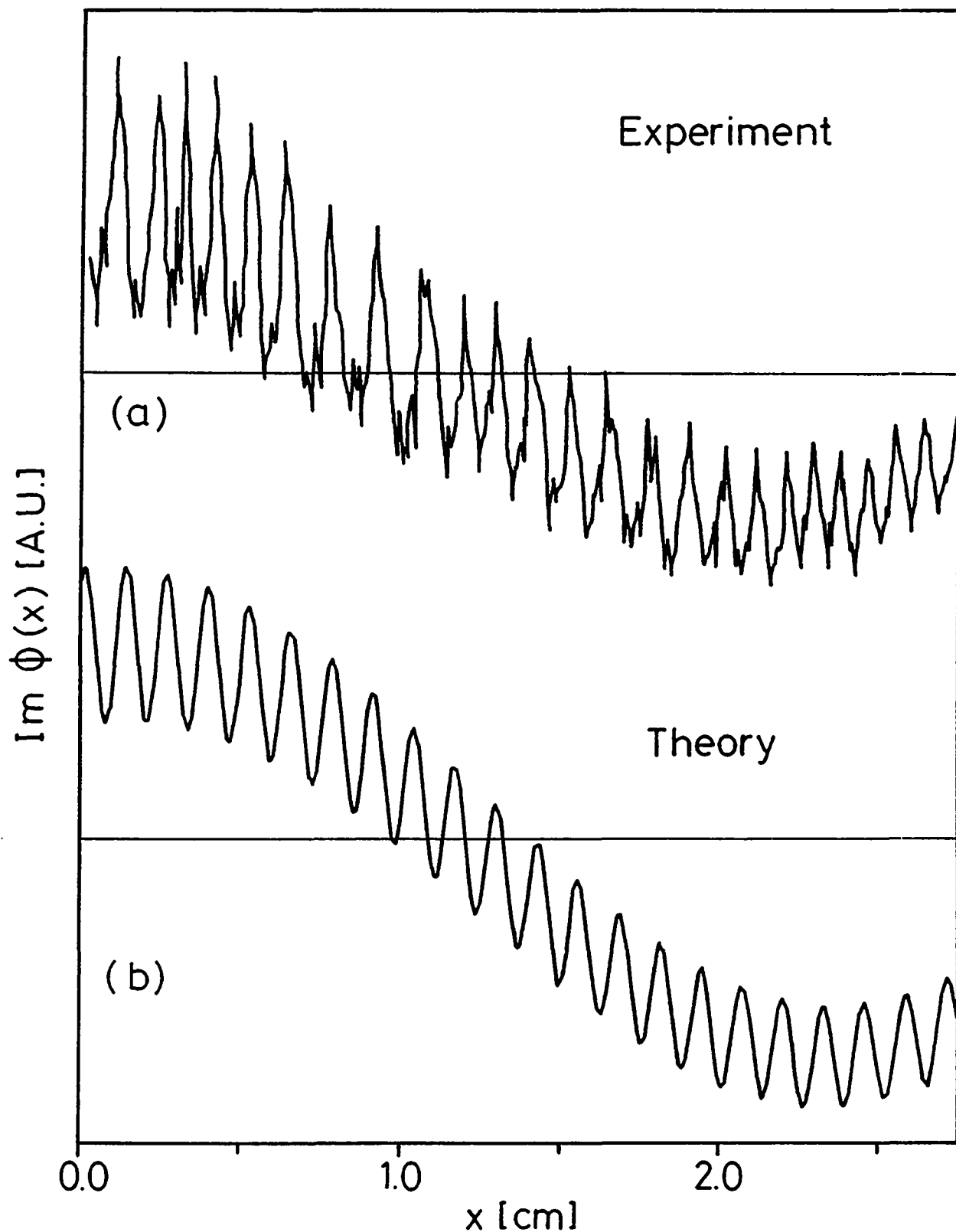


Fig.6.10: Imaginary part of $\Phi(x)$ with the same parameters as in Fig.6.1, but with a non-uniform magnetic field. $B_0(x)$ is proportional to $1/(R_0 \pm x)$, depending on whether the antenna, located at $x=3\text{cm}$, is on the low field side (LFS) or the high field side (HFS), respectively. Here $R_0=64.7\text{cm}$, such that $\omega/\omega_{ci}(x_{pl})=3.95$ and $\omega/\omega_{ci}(x_{pr})=3.60$ in (a), and vice versa in (b).

Fig.6.11: Experimental and numerical electrostatic potential in an argon plasma. The parameters used for the numerical simulation are the following: $T_e=18\text{eV}$, $T_i=0.03\text{eV}$, $B_0=0.2\text{T}$, $k_{\parallel}=200\text{m}^{-1}$, $n=10^{17}\text{m}^{-3}$, $\omega/\omega_{ci}=3.5$. They correspond, within error bars, to those of the experiment.



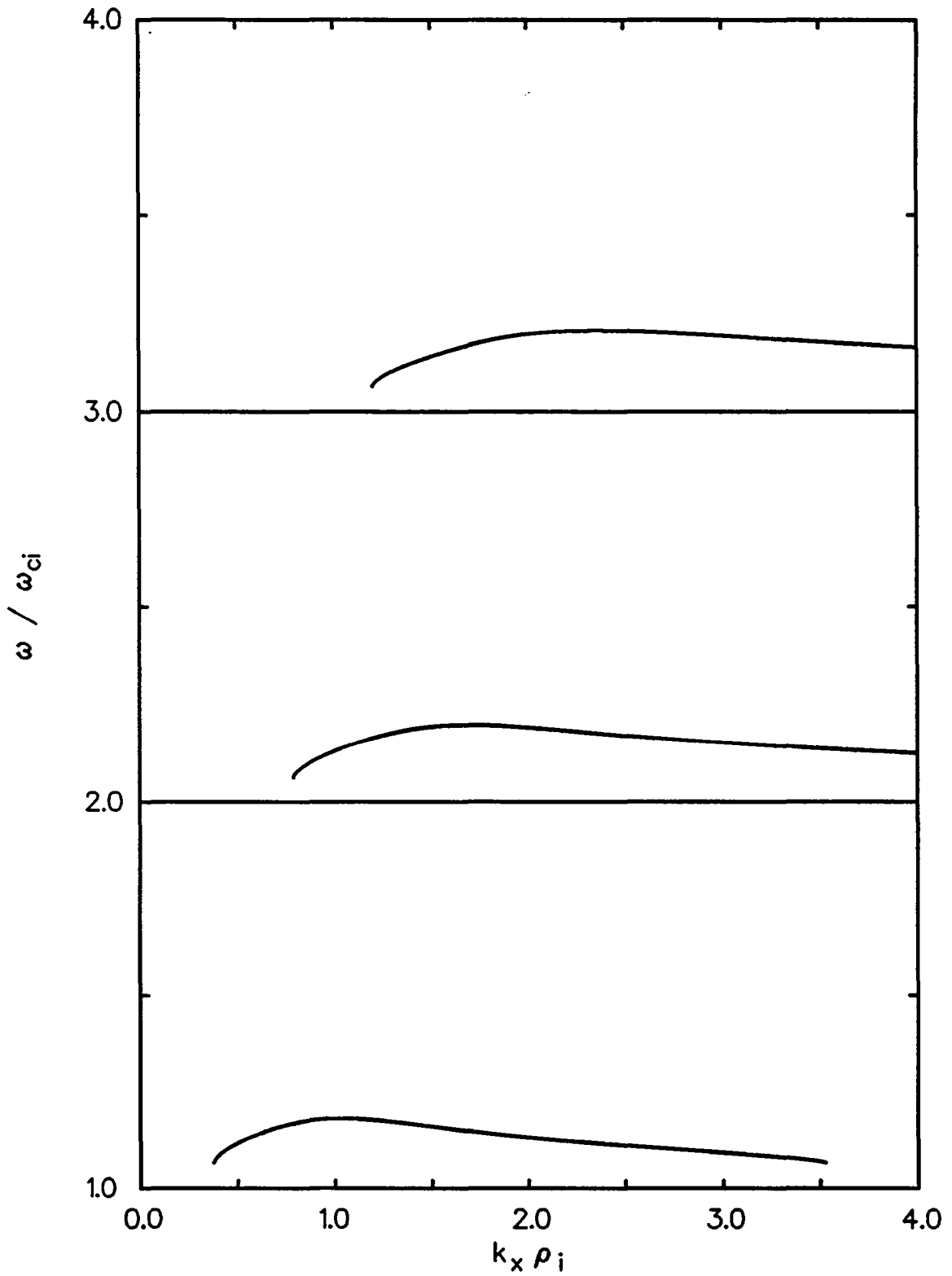
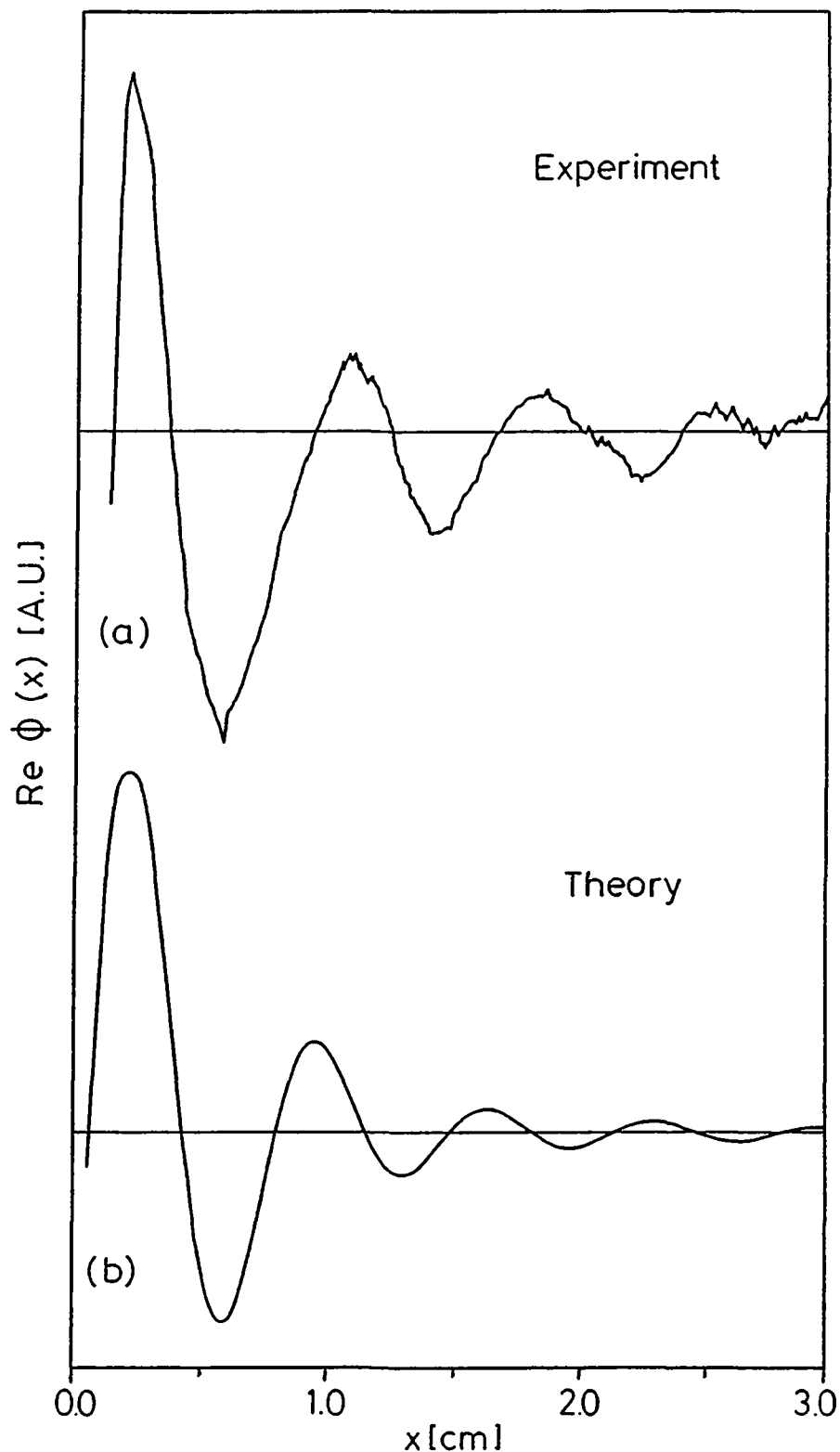


Fig.6.12: Dispersion relation of a barium plasma with $B_0=0.25\text{T}$, $k_{//}=30\text{m}^{-1}$, $T_e=T_i=0.1\text{eV}$ and $n=10^{16}\text{m}^{-3}$. In this case, $\rho_i \cong 1.5\text{mm}$.

Fig.6.13: Experimental and numerical electrostatic potential in a barium plasma, with the same parameters as in Fig.6.12. The numerical solutions with $k_{//}=25, 26, 27, 28, 29$ and 30 m^{-1} have been summed. A frequency equal to $2.6\omega_{ci}$ in the laboratory frame and a drift velocity $v_{\text{drift}}/\omega_{ci}=0.016m$ have been used. Thus, $\omega/\omega_{ci}=2.6+0.016k_{//}$ in the plasma frame is around 3.05.



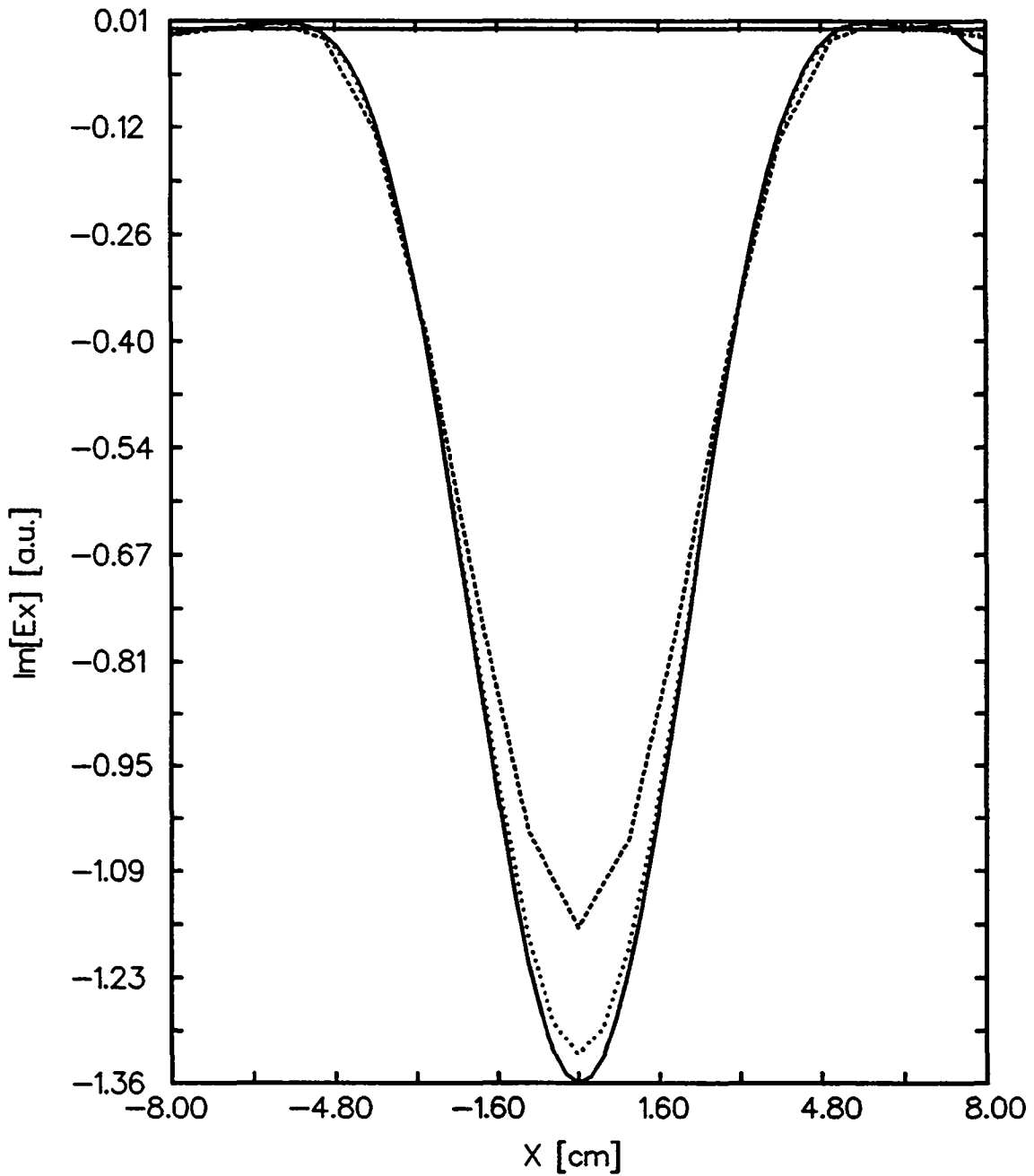


Fig.7.1: Imaginary part of E_x for a deuterium plasma with: $B_0=1\text{T}$, $n_e=n_D=10^{19}\text{m}^{-3}$, $T_e=1000\text{eV}$, $T_i=10\text{eV}$, $k_{//}=3\text{m}^{-1}$, $\omega/\omega_{cD}=0.298$, inhomogeneous density and temperature profiles. Three different meshes have been used: $NX=16$ (dashed line), $NX=32$ (dotted line) and $NX=64$ (solid line).

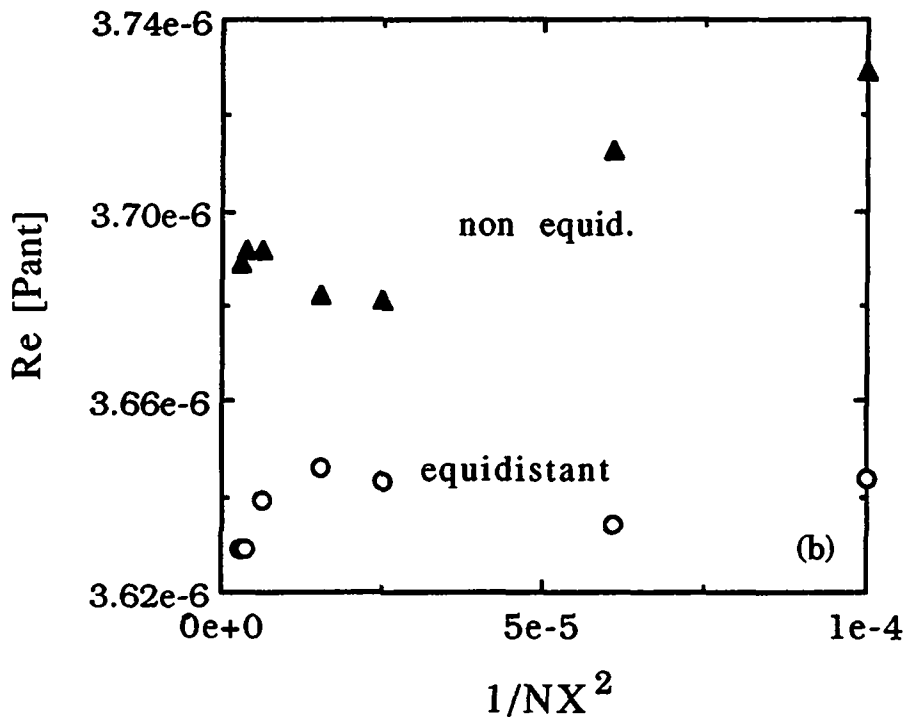
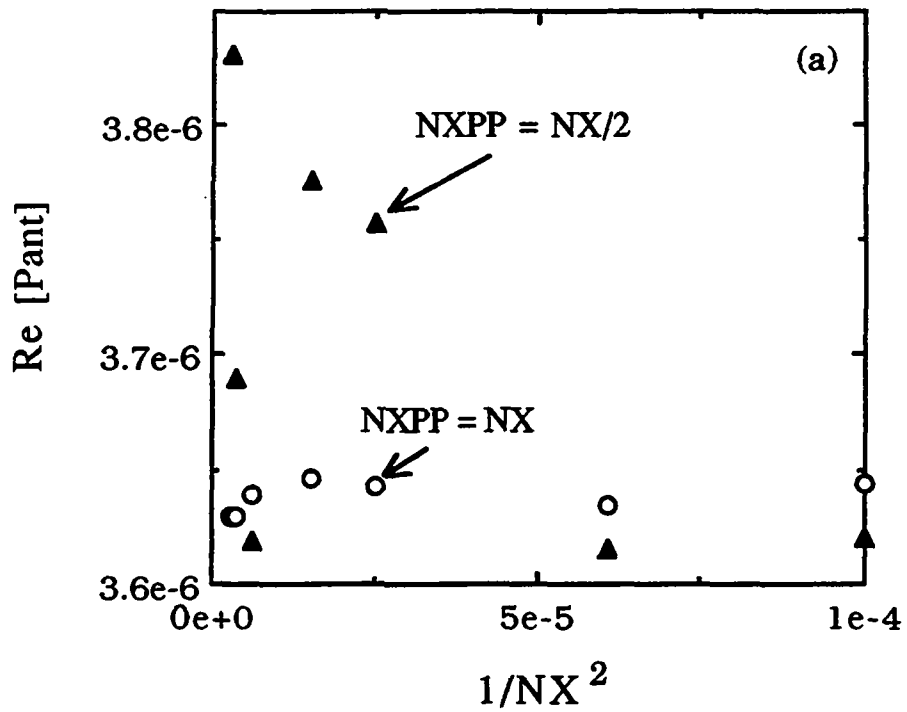


Fig.7.2: Convergence study of the power emitted by the antenna vs $1/NX^2$ with the same parameters as in Fig.7.1. (a) Equidistant mesh, but with different x'' meshes. Note that with $NXPP=NX$, the x and x'' meshes are more uniform. (b) $NX=NXPP$ case, but with an equidistant mesh (as in (a)) and a mesh packed very close to the plasma edge, within $10\rho_e$, similar to Fig.6.1b.

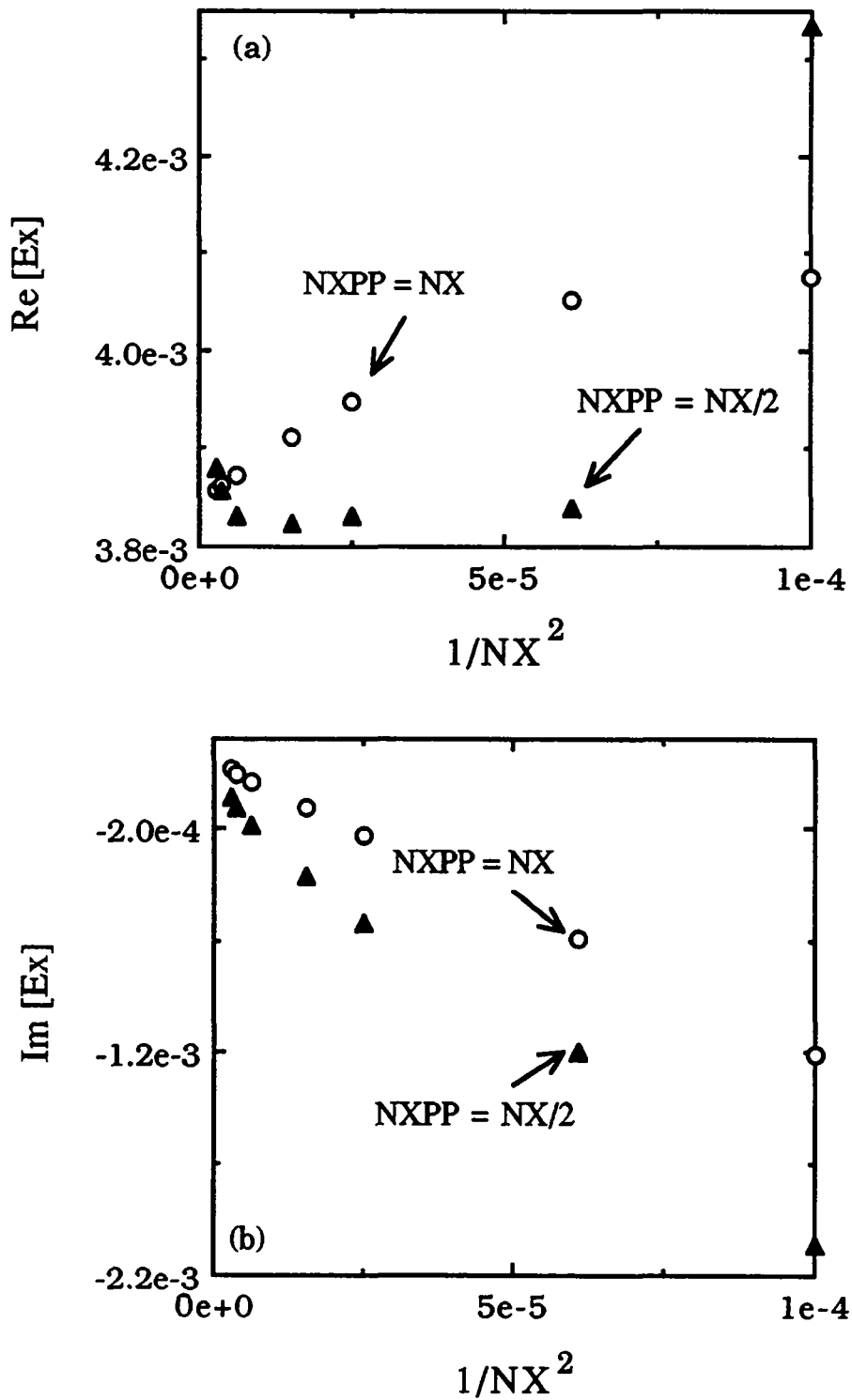


Fig.7.3: Convergence study for the same case as in Fig.7.2a, but of the real (a) and imaginary (b) parts of $E_x(x_{pr})$.

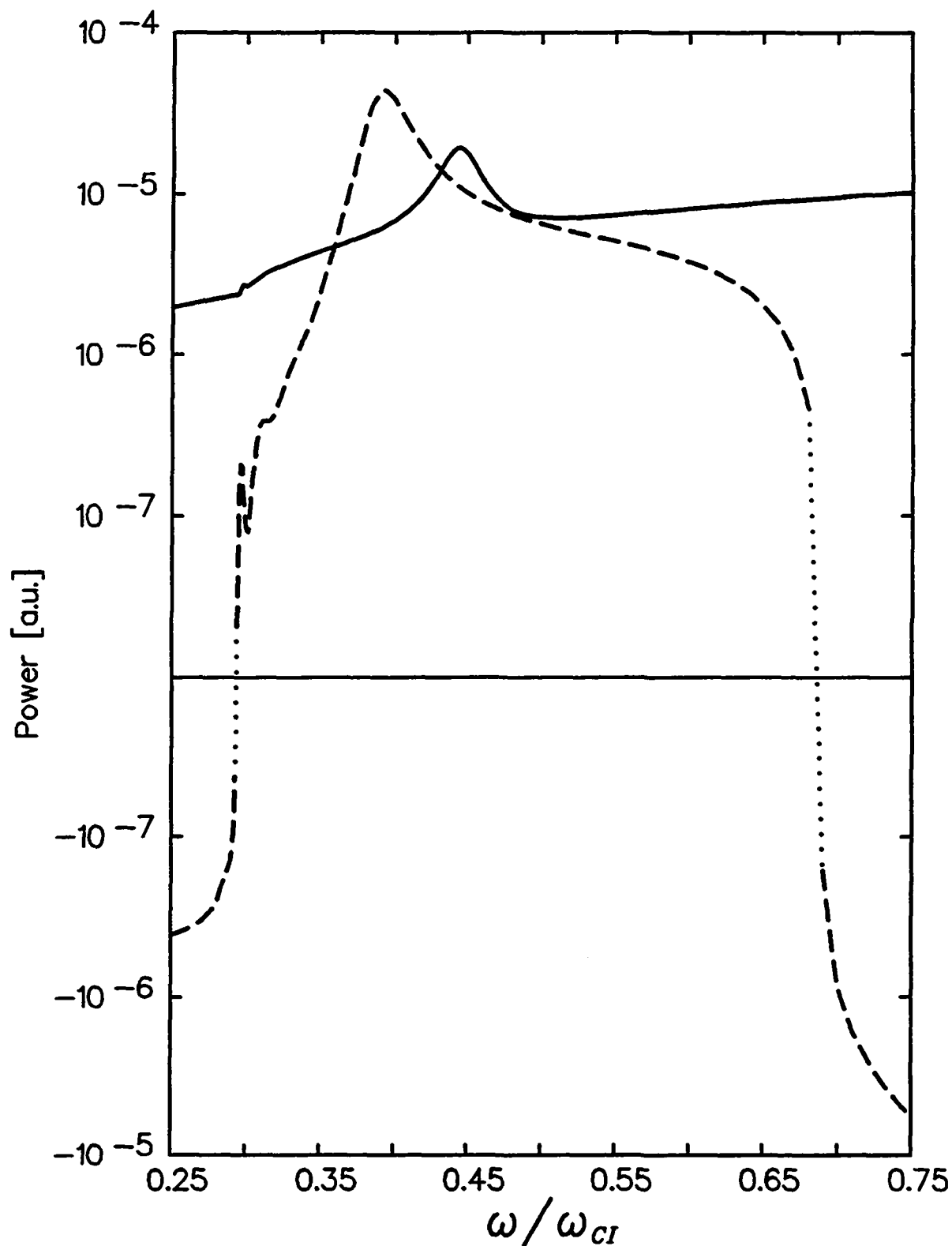


Fig.7.4a: Power emitted by the antenna vs ω/ω_{ci} obtained with ISMENE (dashed line) and SEMAL (solid line) for the same parameters as in Fig.7.1, but with homogeneous profiles. The small peaks around $\omega/\omega_{ci}=0.3$ are due to the KAW, whereas the broad peak is due to the surface mode of the fast wave. The power obtained with ISMENE is negative for $\omega/\omega_{ci}<0.293$ and $\omega/\omega_{ci}>0.69$, therefore a "negative logarithmic" scale has been used for the lower part of the plot.

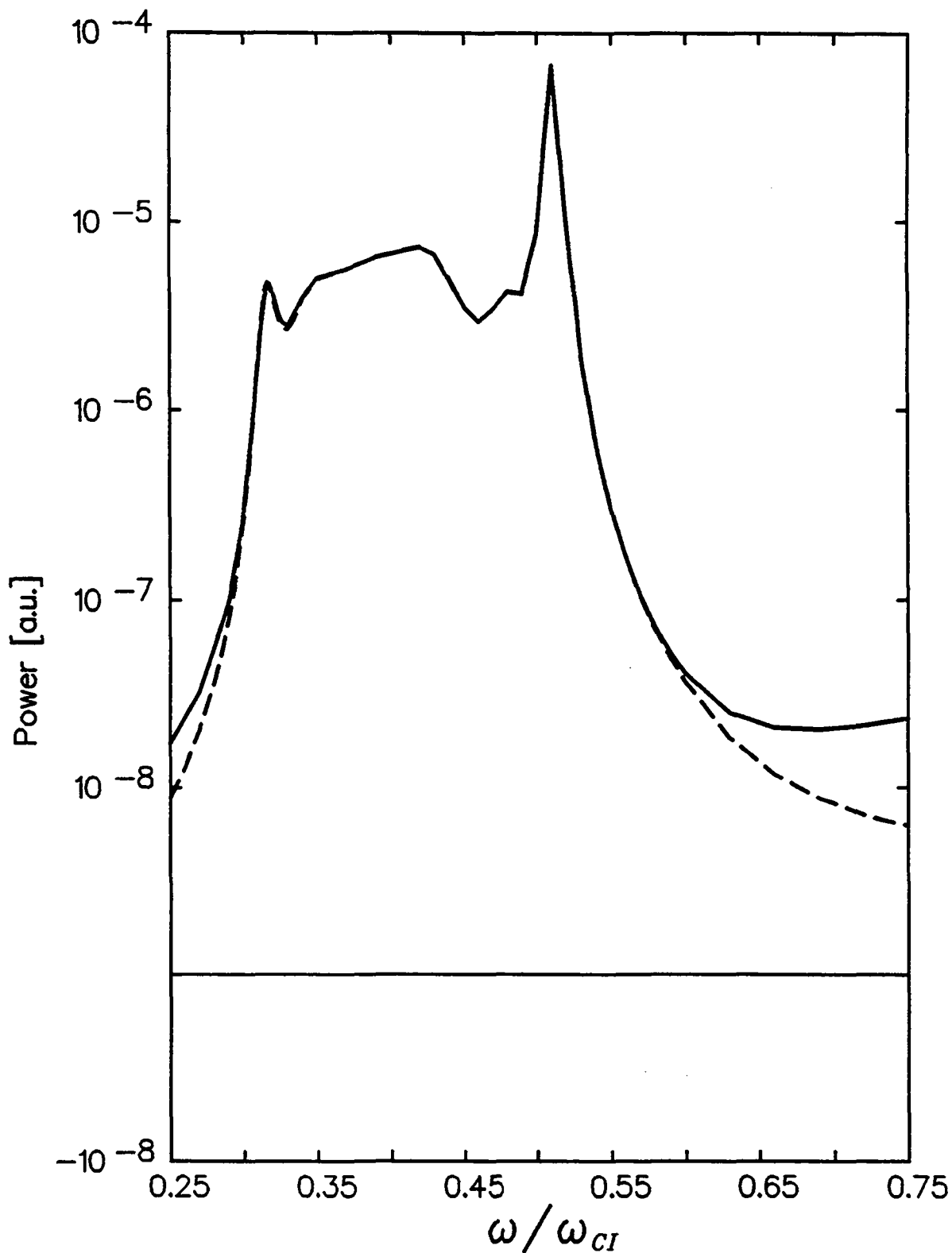


Fig.7.4b: The same plot as in Fig.7.4a, but with inhomogeneous density and temperature profiles. Note that the equilibrium gradients are needed in ISMENE (dashed line) in order to have positive power at both edges. With SEMAL, we had to pack points very close to the edge to avoid numerical problems, as the power is very low near $\omega/\omega_{ci}=0.7$.

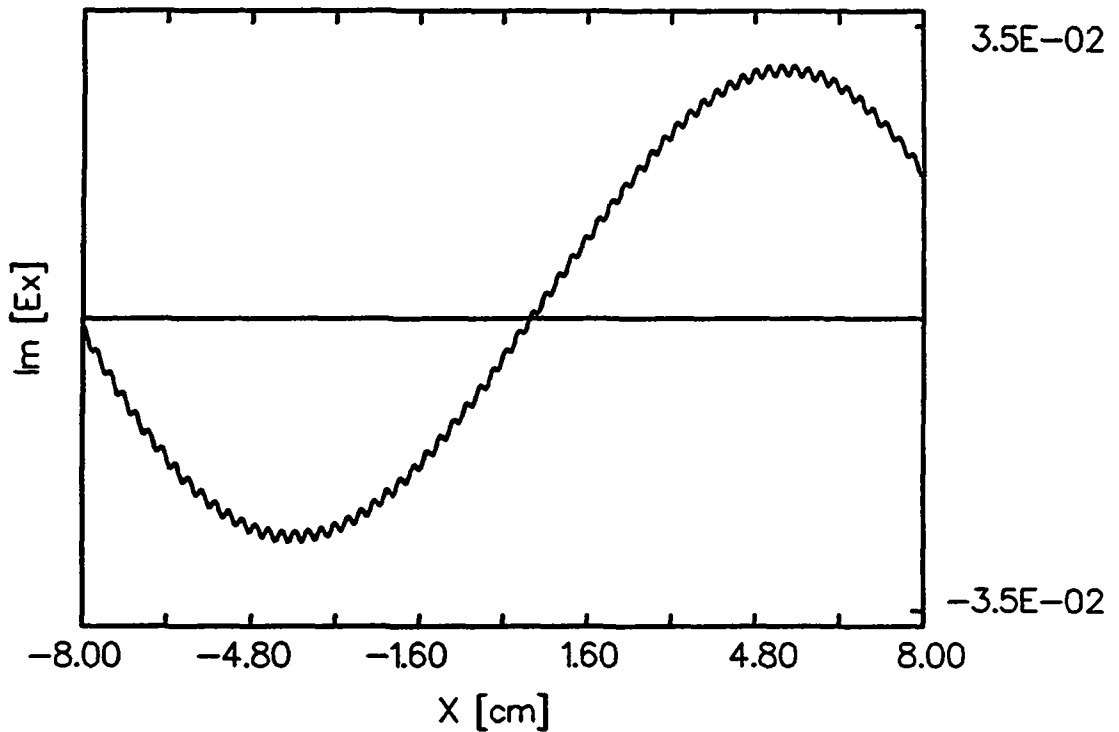


Fig.7.5: $\text{Im}[E_x]$ obtained with ISMENE for the first mode of the KAW, at $\omega/\omega_{ci}=0.296$, with the same parameters as in Fig.7.4. The small oscillation is due to the extra root of the dispersion relation.

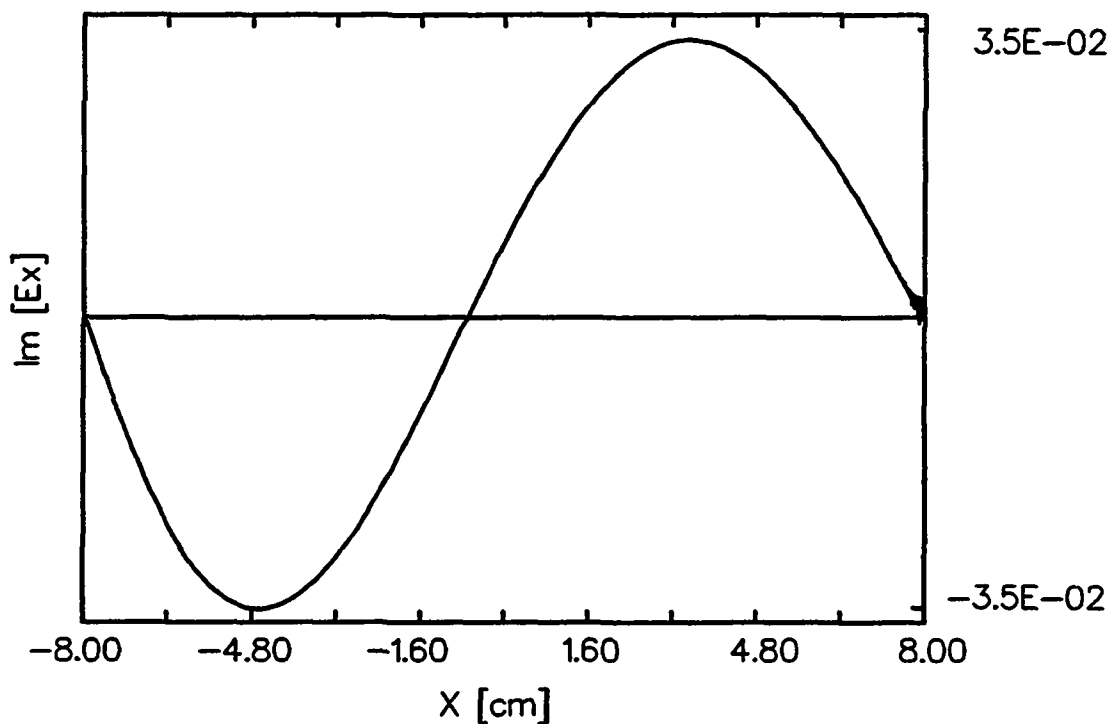


Fig.7.6a: Imaginary part of E_x obtained with SEMAL for the first mode of the KAW, at $\omega/\omega_{ci}=0.298$, with the same parameters as in Fig.7.4. The edge parts of the wave field have been cut at $x=\pm 7.94\text{cm}$. They are shown in Fig.7.6b.

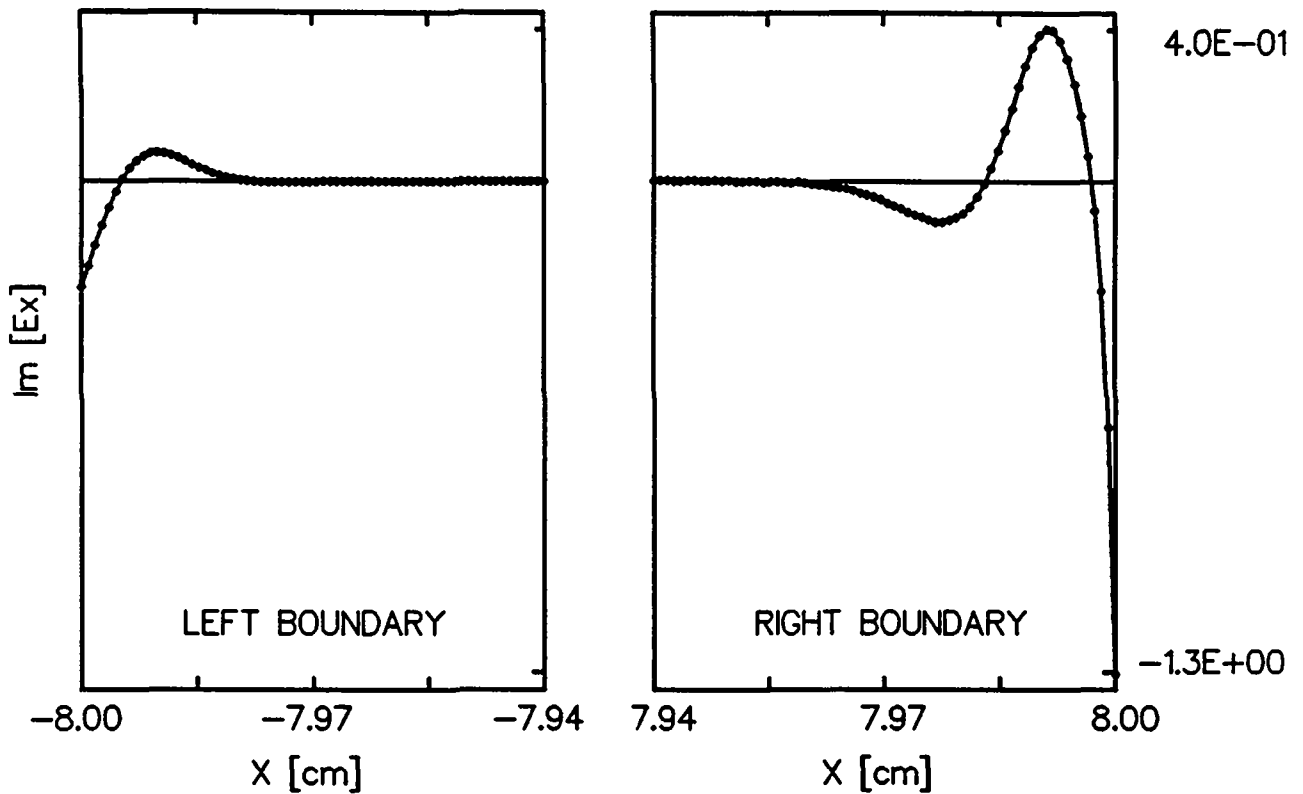


Fig.7.6b: Edge parts of $\text{Im}[E_x]$ shown in Fig.7.6a. The same units have been used. The dots represent the mesh points, showing that this fine structure is resolved numerically. In this case, $\rho_e \cong \lambda_{De} = 7.4 \cdot 10^{-3}$ cm and $\lambda_{Di} = 7.4 \cdot 10^{-4}$ cm.

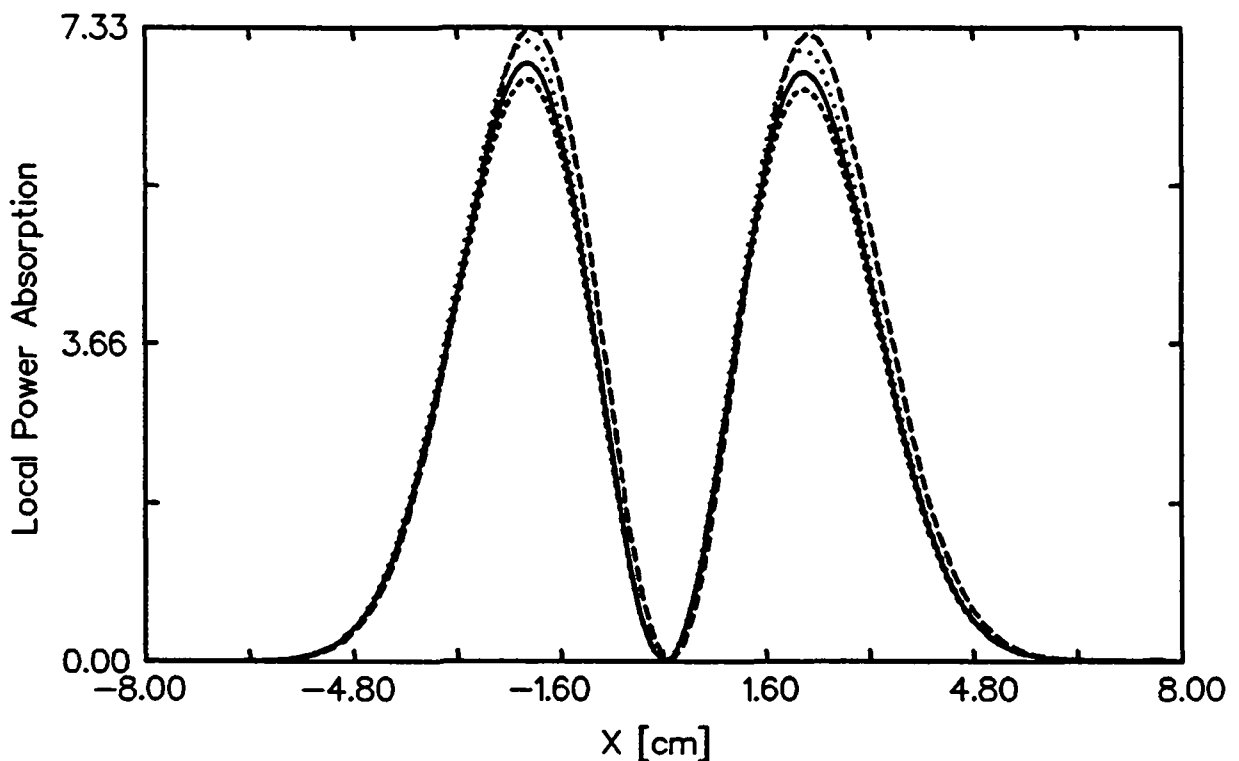


Fig.7.7: $P_L(x)$ of the electrons vs x for the same case as in Fig.7.1. The top curve (long dashes) is obtained with a second order expansion with respect to $k_{\perp} \rho_e$ of $P_L(x)$. The three other curves are calculated using the complete formula with different x'' and θ' meshes: $N''=N'=25$ (short dashes); $N''=N'=50$ (solid line) and $N''=N'=150$ (dotted line).

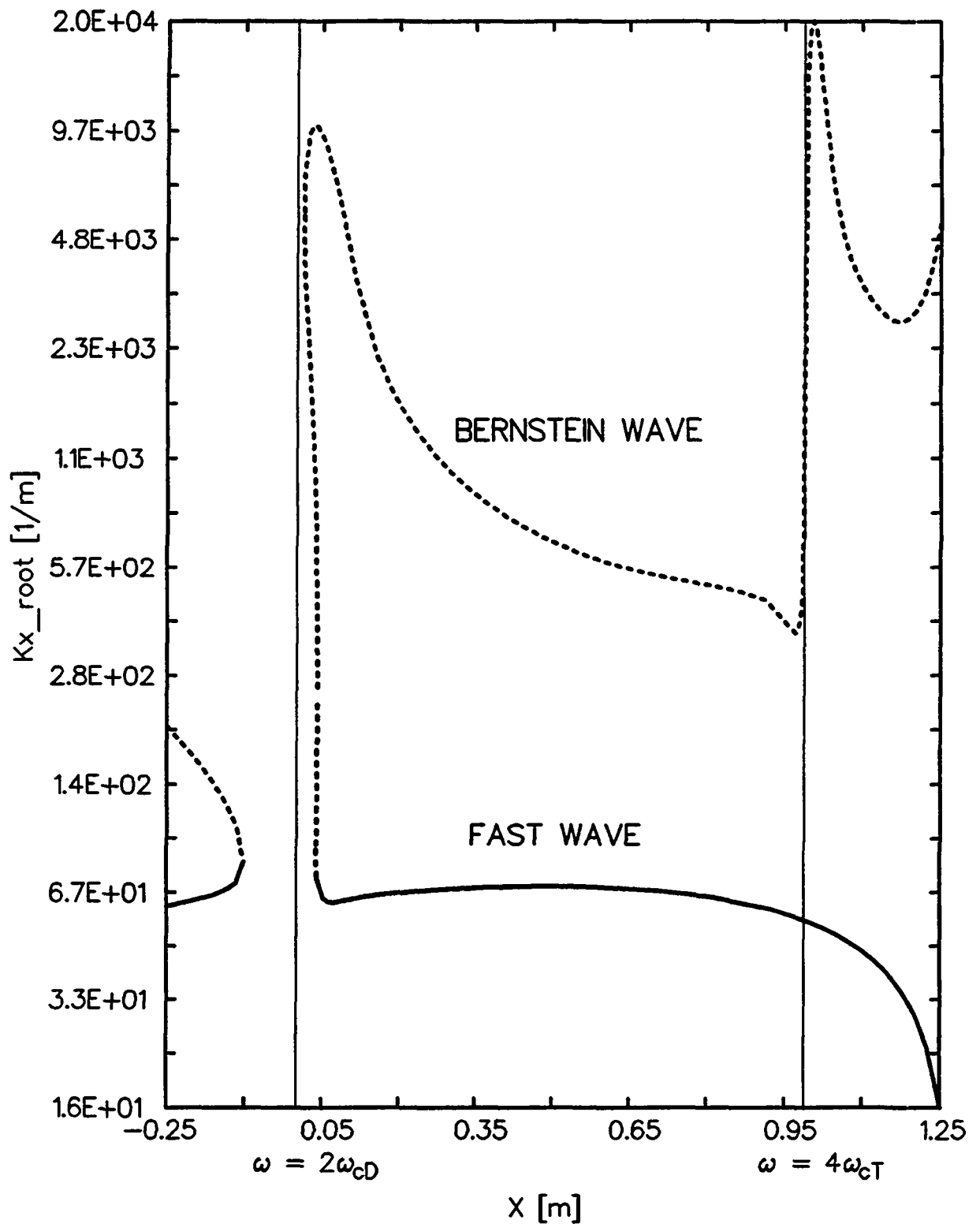


Fig.7.8: Full hot plasma dispersion relation, using the code DISPAL, for the standard D-T- α plasma parameters (Sec.7.2), with $n_\alpha/n_e=1\%$ and homogeneous alpha particle temperature profile. At $x=0$, $\omega=2\omega_{cD}=4\omega_{c\alpha}=3\omega_{cT}$ and at $x=1m$, $\omega=4\omega_{cT}$.

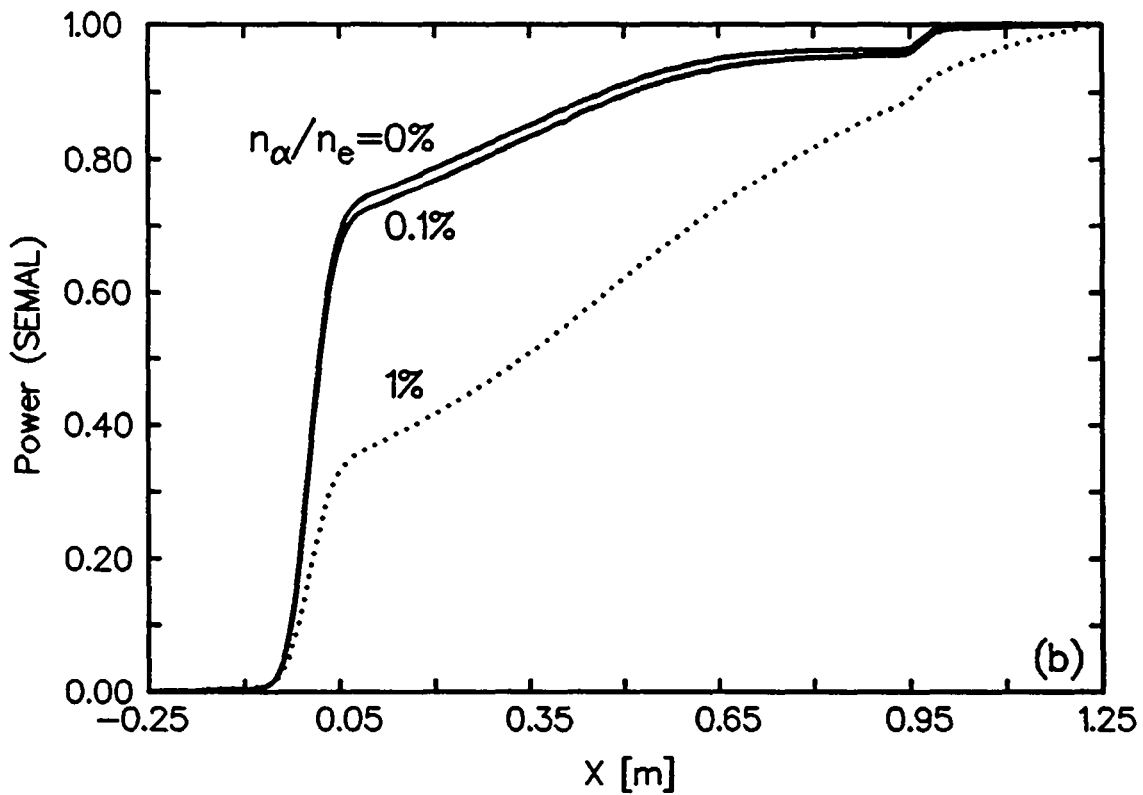
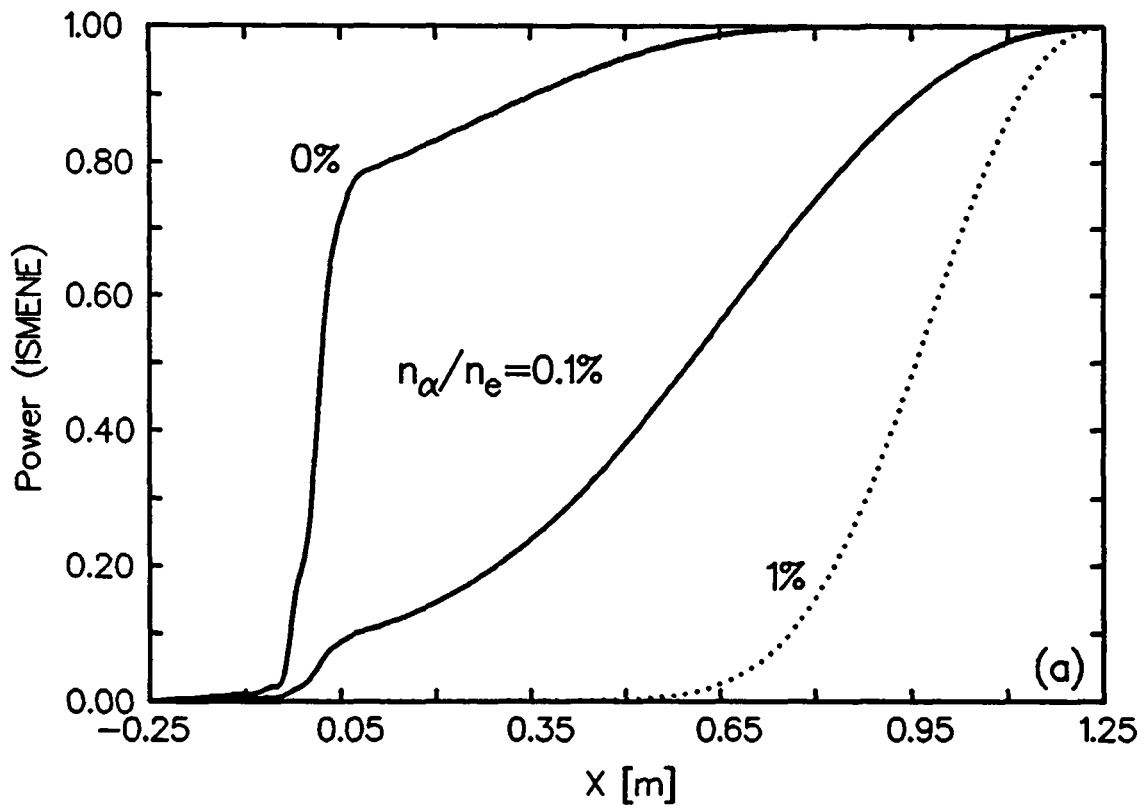


Fig.7.9: Power not yet absorbed by the particles, $1 - \bar{P}_L(x) / \bar{P}_L(x_{pl})$, vs x for the standard parameters with $n_\alpha/n_e = 0\%$, 0.1% and 1% . (a) Local model (ISMENE). (b) Nonlocal model (SEMAL). The dotted lines correspond to the same parameters as in Fig.7.8.

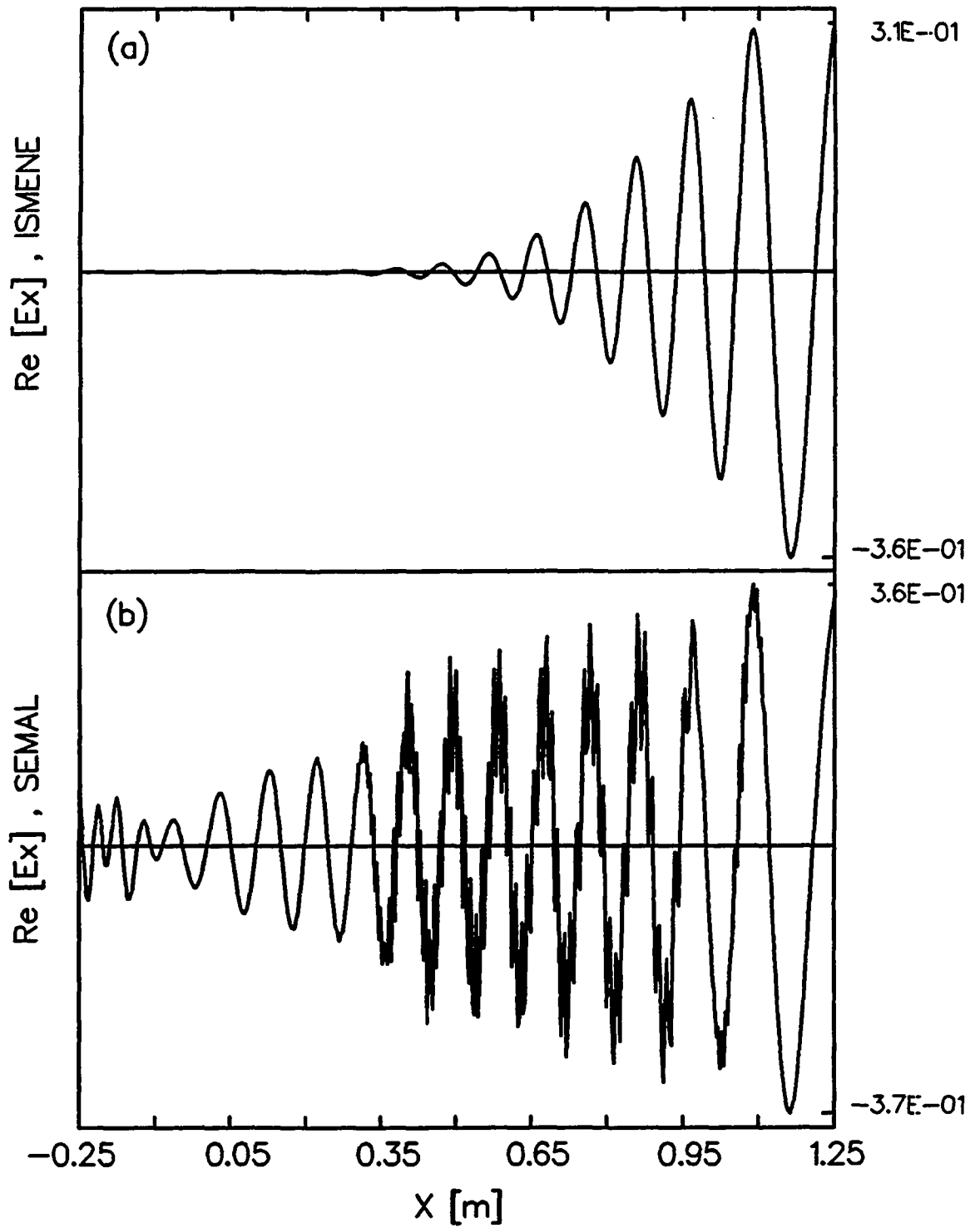


Fig.7.10: Real part of E_x for the cases shown in Fig.7.9 with $n_\alpha/n_e=1\%$ (dotted lines).

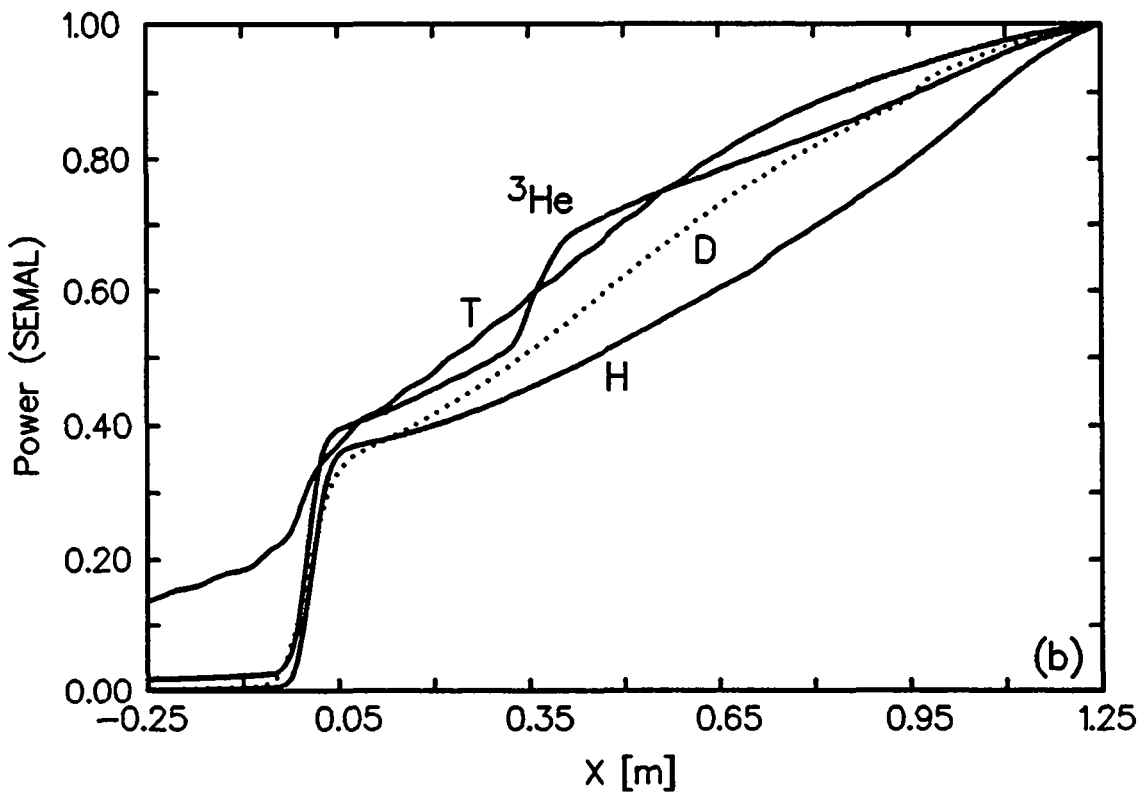
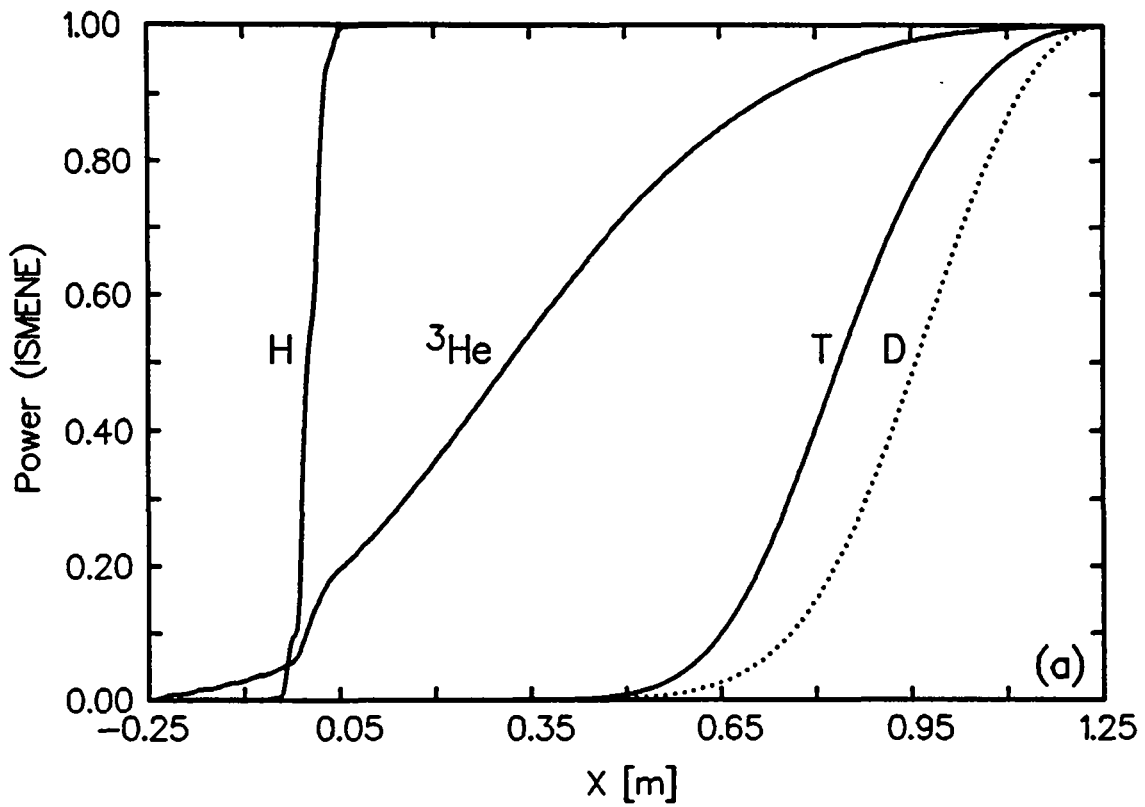


Fig.7.11: $1 - \bar{P}_L(x)/\bar{P}_L(x_{pl})$ vs x for different scenarii with $n_\alpha/n_e=1\%$: (H) $\omega=2\omega_{cH}$; (^3He) $\omega=2\omega_{c^3\text{He}}$; (T) $\omega=2\omega_{cT}$; and (D) $\omega=2\omega_{cD}$. 20% of H or ^3He has been added in the first two scenarii. (a) Local model (ISMENE). (b) Nonlocal model (SEMAL). The dotted lines correspond to the same cases as shown in Fig.7.9.

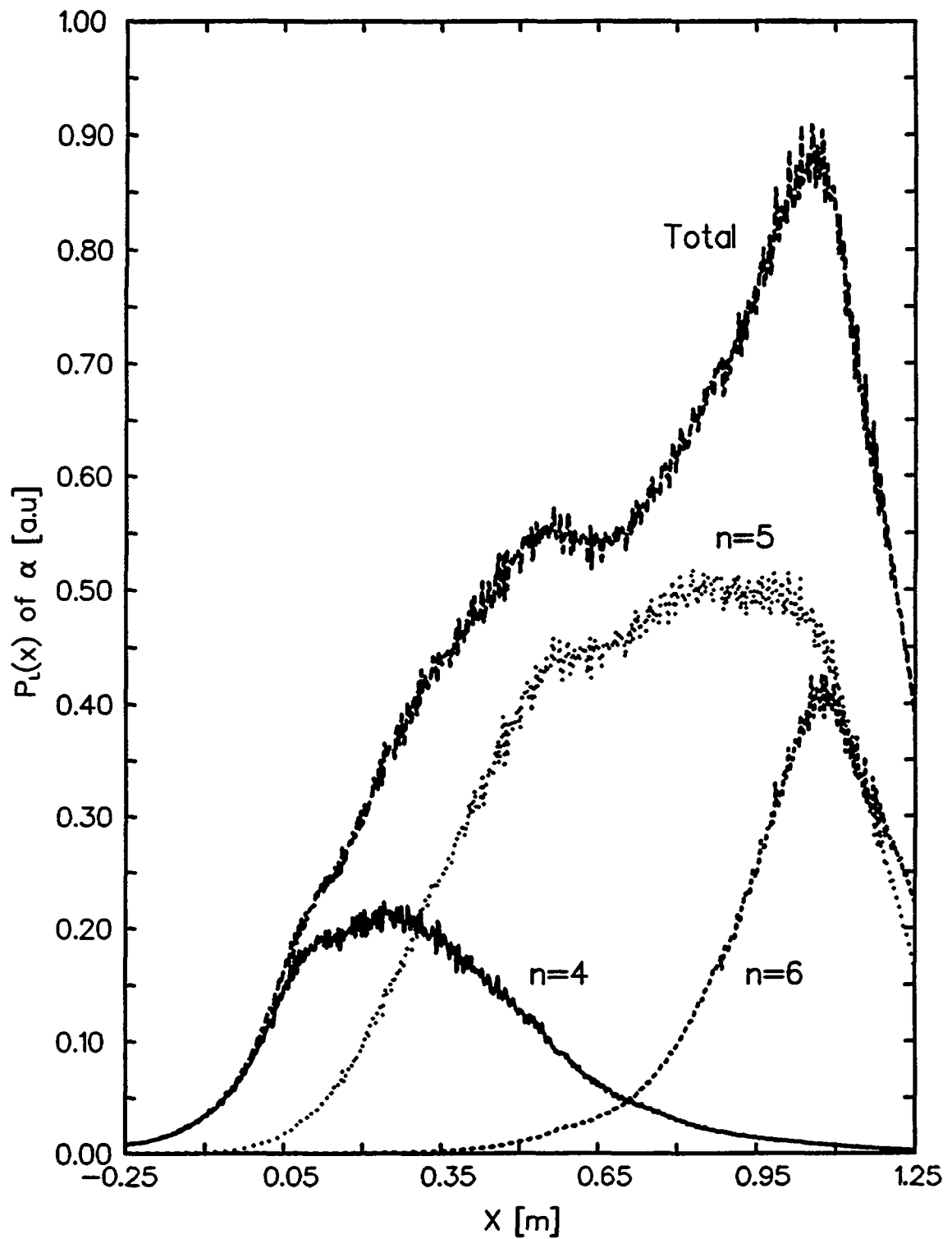


Fig.7.12: Local power absorption of alpha particles (total) for the scenario with hydrogen (H) shown in Fig.7.11b. The contributions of each harmonic $n=4, 5$ and 6 are also shown.

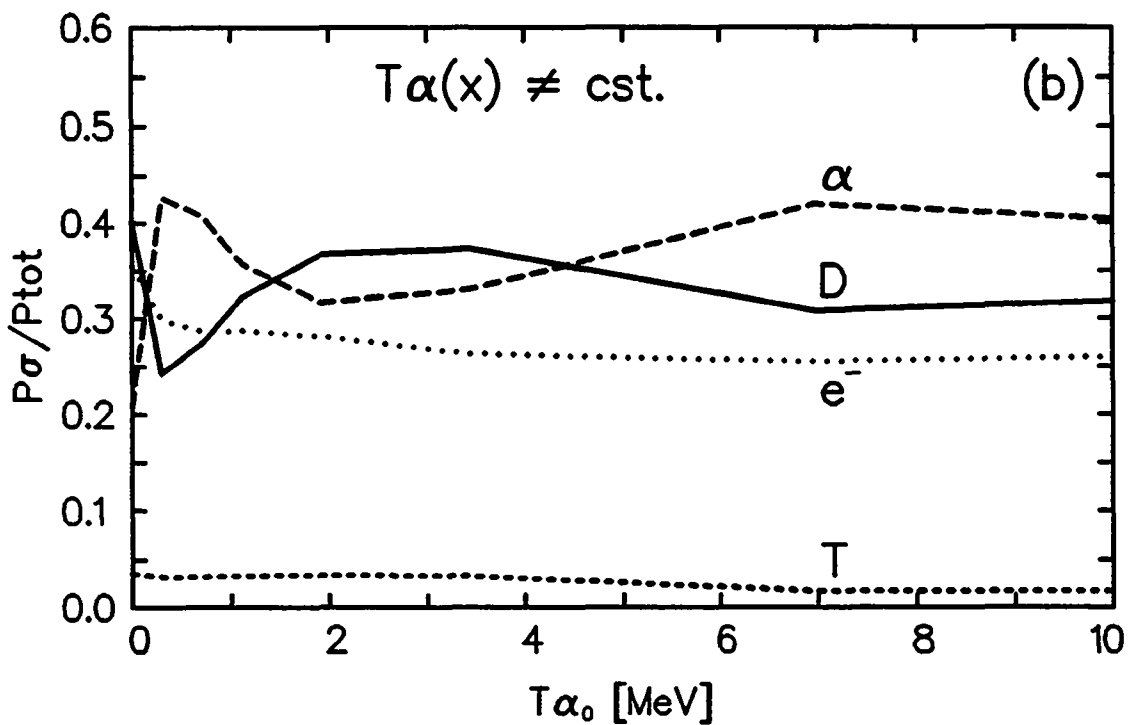
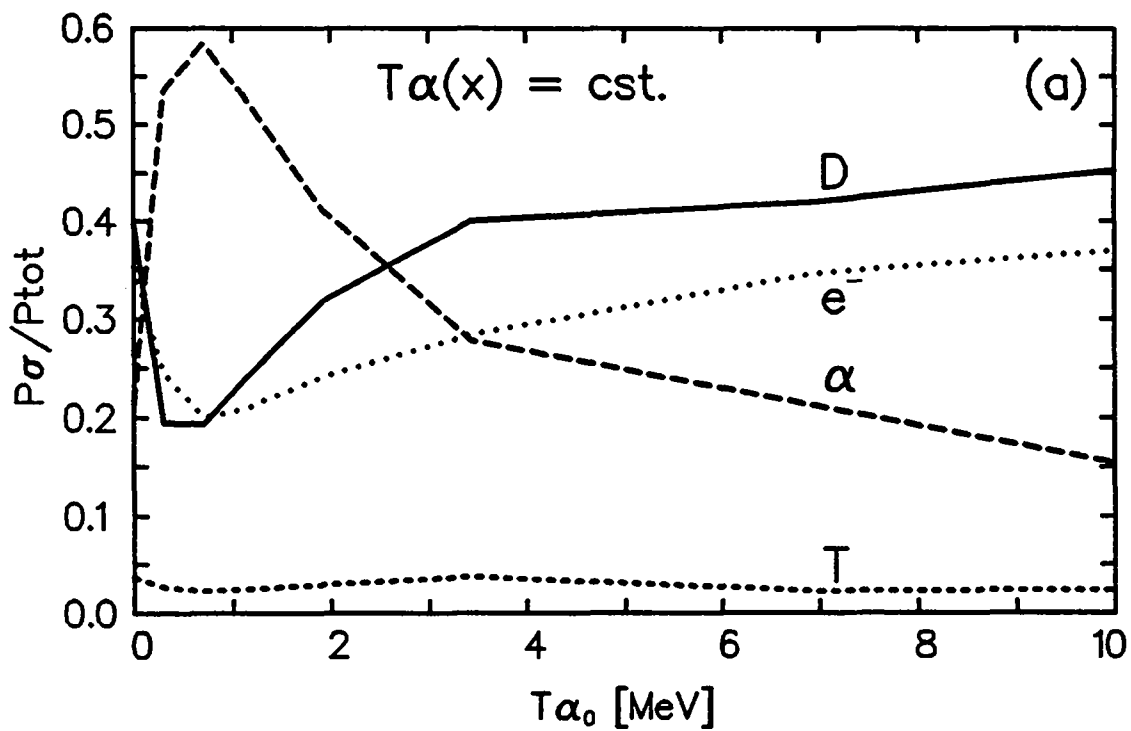


Fig.7.13: $\bar{P}_{L\sigma}(x_{pl})/\bar{P}_L(x_{pl})$ vs the central alpha particle temperature for the standard parameters, with $k_{\parallel}=5\text{m}^{-1}$ and $n_{\alpha}/n_e=1\%$. The alpha particle temperature profile is constant (a) or bi-quadratic (b).

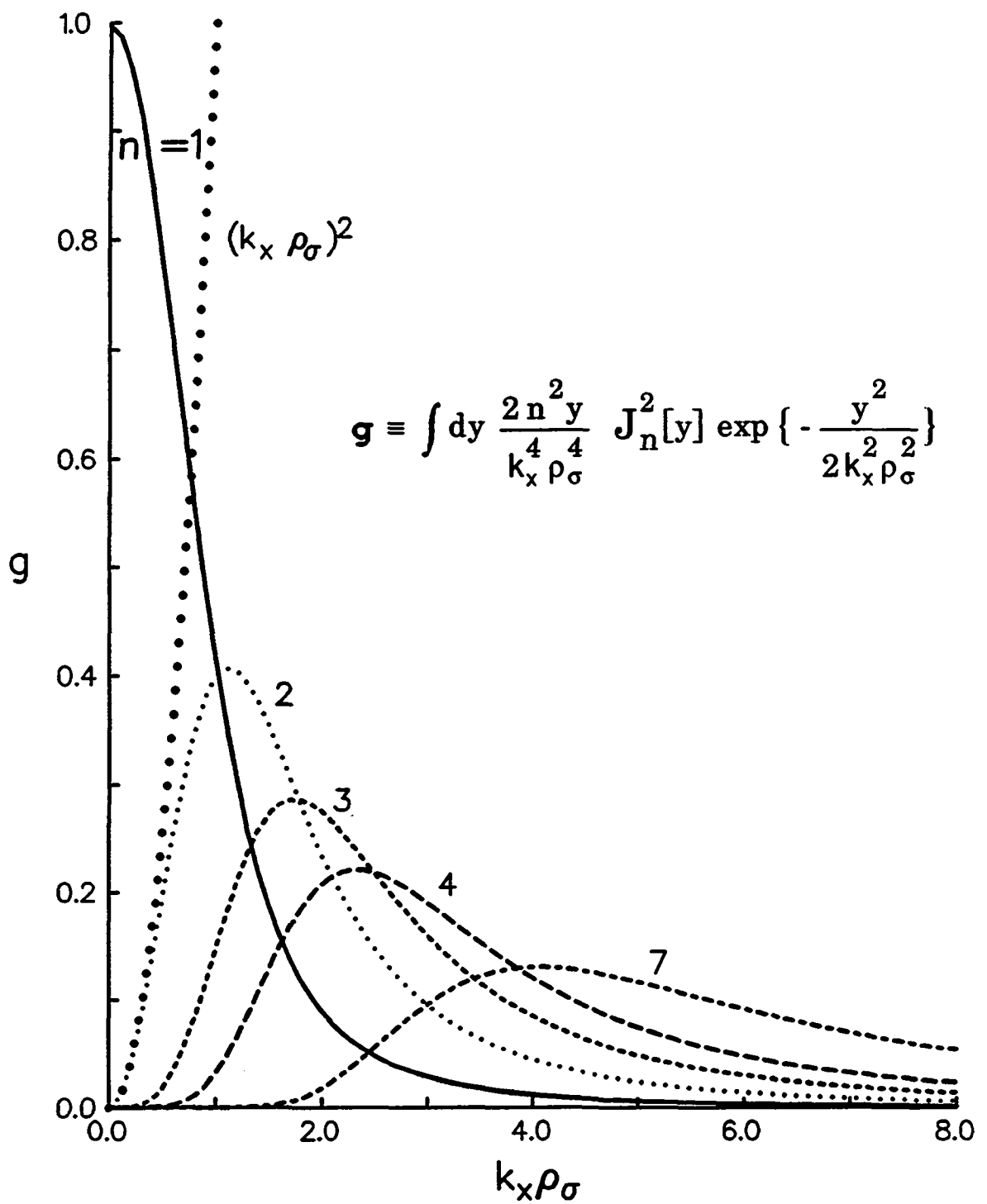


Fig.7.14: Form factor $g(k_x \rho_\sigma, n)$ (Sec.7.2.2) for different harmonic numbers: $n=1, 2, 3, 4$ and 7 . For $n=2$, g expanded to second order in $k_x \rho_\sigma$ [$=(k_x \rho_\sigma)^2$] is also plotted (large dots).

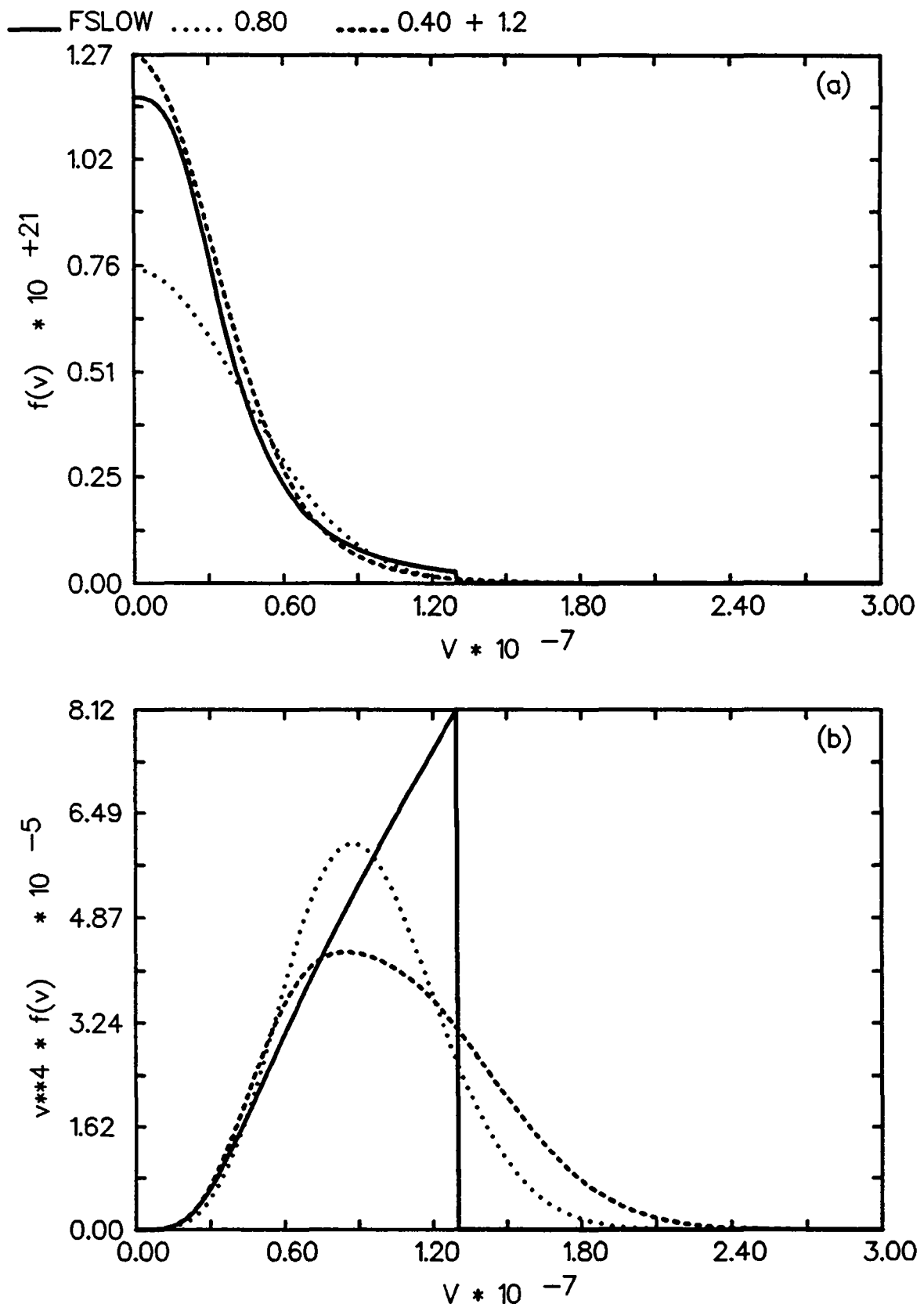


Fig.7.15: (a) Isotropic distribution functions $f(v)$ and (b) integrand of $\langle v_{\perp}^2 \rangle$, $v^4 f(v)$, vs velocity. The solid line corresponds to the slowing-down distribution function with $T_e=5\text{keV}$ and the dotted line to a Maxwellian with $T=0.8\text{MeV}$. The dashed line represents a bi-Maxwellian with $T_1=0.4\text{MeV}$, $T_2=1.2\text{MeV}$ and $n_1=n_2$. The three distributions have the same total density and the same averaged perpendicular velocity squared $\langle v_{\perp}^2 \rangle$.

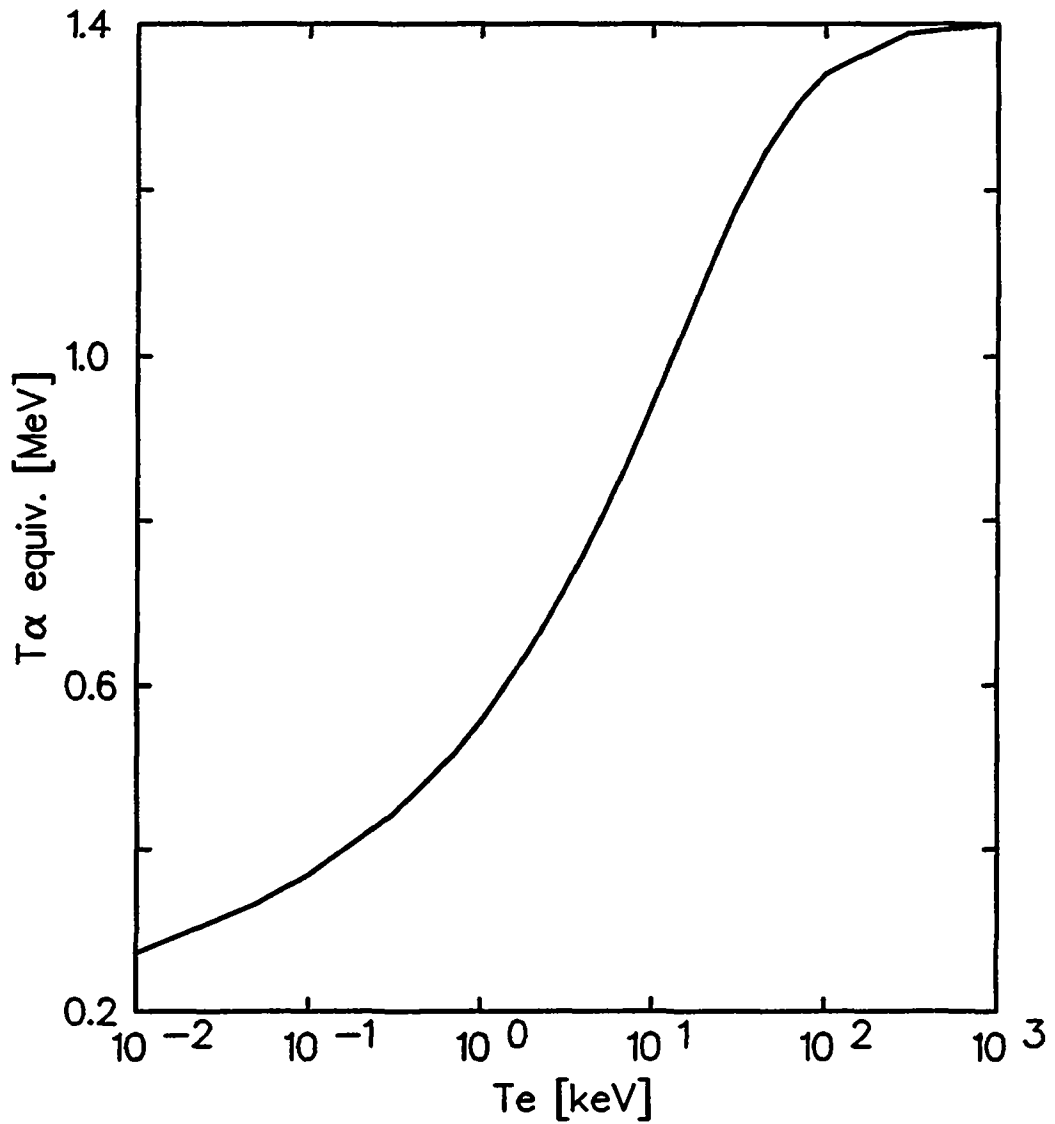


Fig.7.16: Equivalent Maxwellian alpha particle temperature T_α vs the electron temperature. T_α is calculated such that $v_{T_\alpha}^2 = \langle v_\perp^2 \rangle_{\text{slow}}$, where v_\perp^2 is averaged over the slowing-down distribution considered.

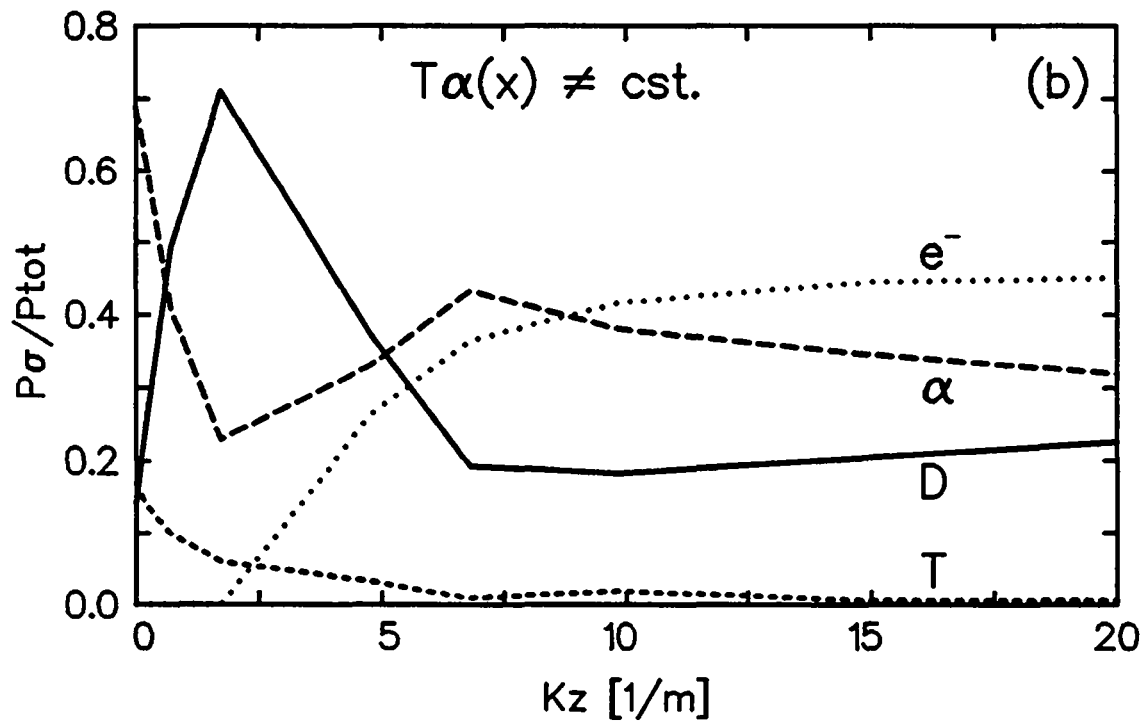
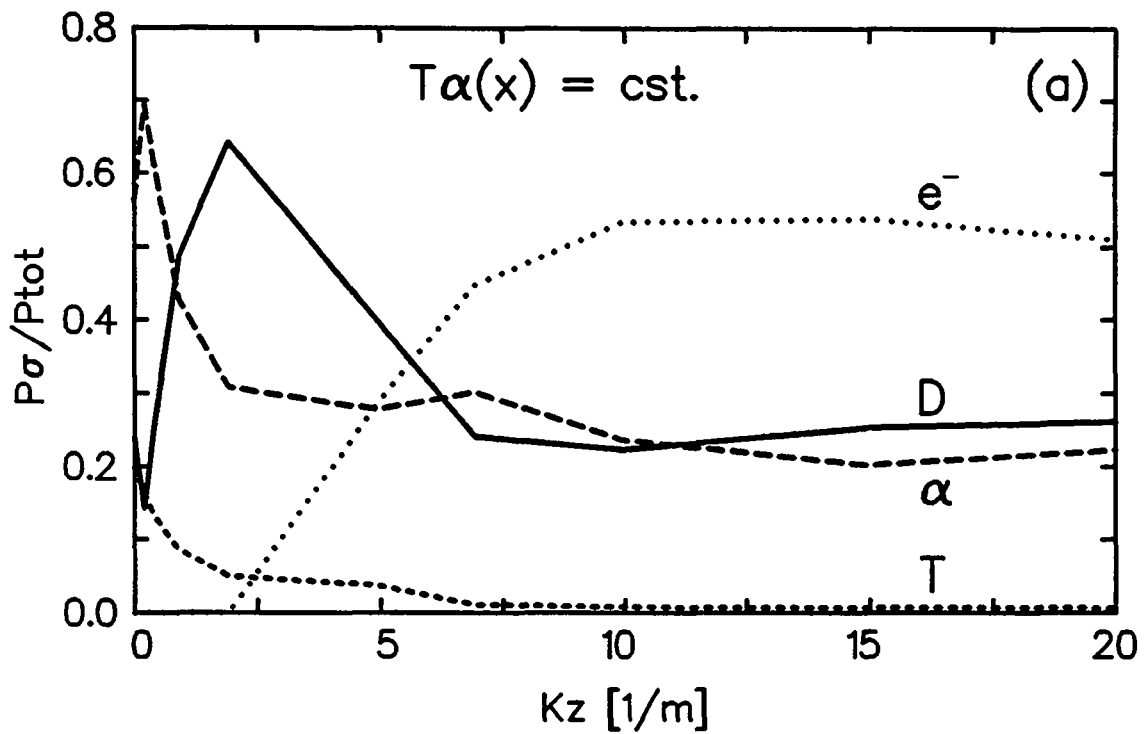


Fig.7.17: The same plot as in Fig.7.13, but vs k_z , with $T_{\alpha}=3.5$ MeV and $n_{\alpha}/n_e=1\%$. (a) Homogeneous and (b) inhomogeneous alpha particle temperature profiles.

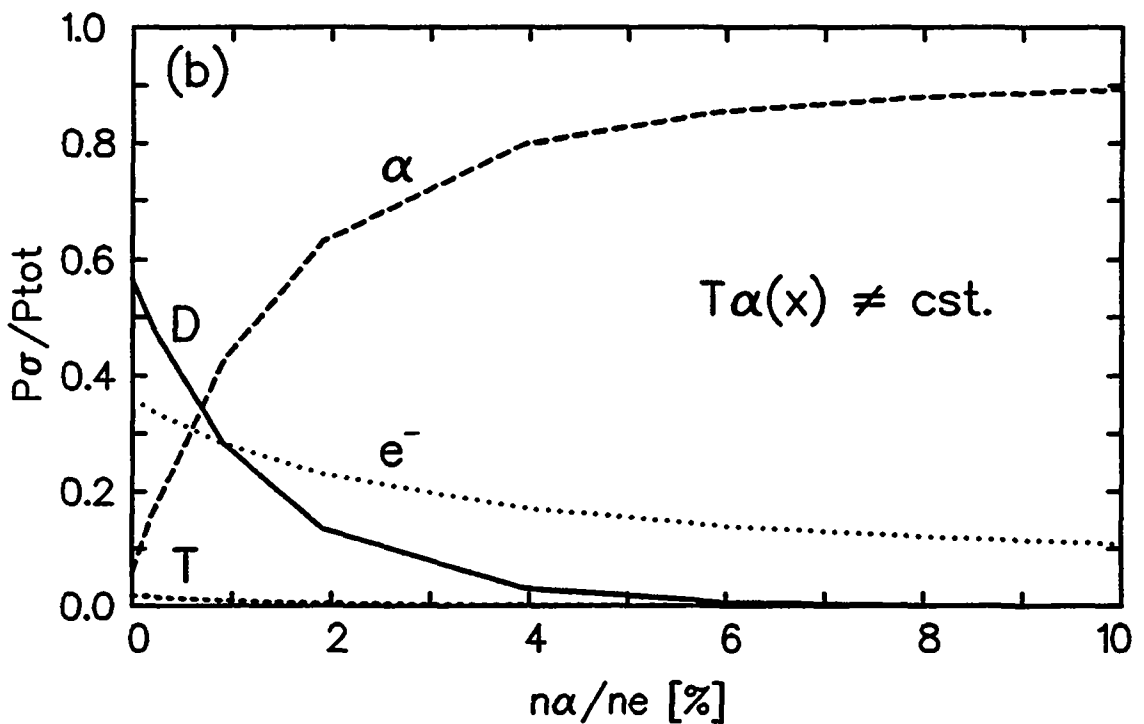
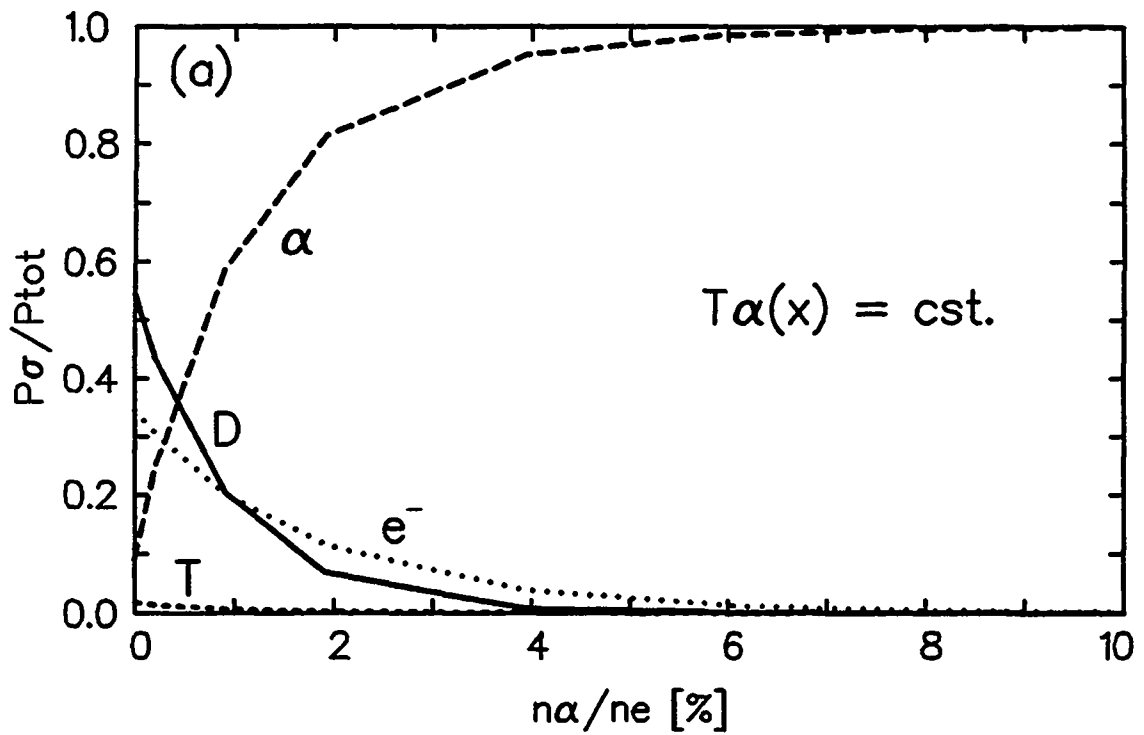


Fig.7.18: The same plot as in Fig.7.13, with $k_z=5\text{m}^{-1}$, for different values of alpha particle concentration, but with $T_\alpha=0.8$ MeV at the center. (a) Homogeneous and (b) inhomogeneous alpha particle temperature profiles.

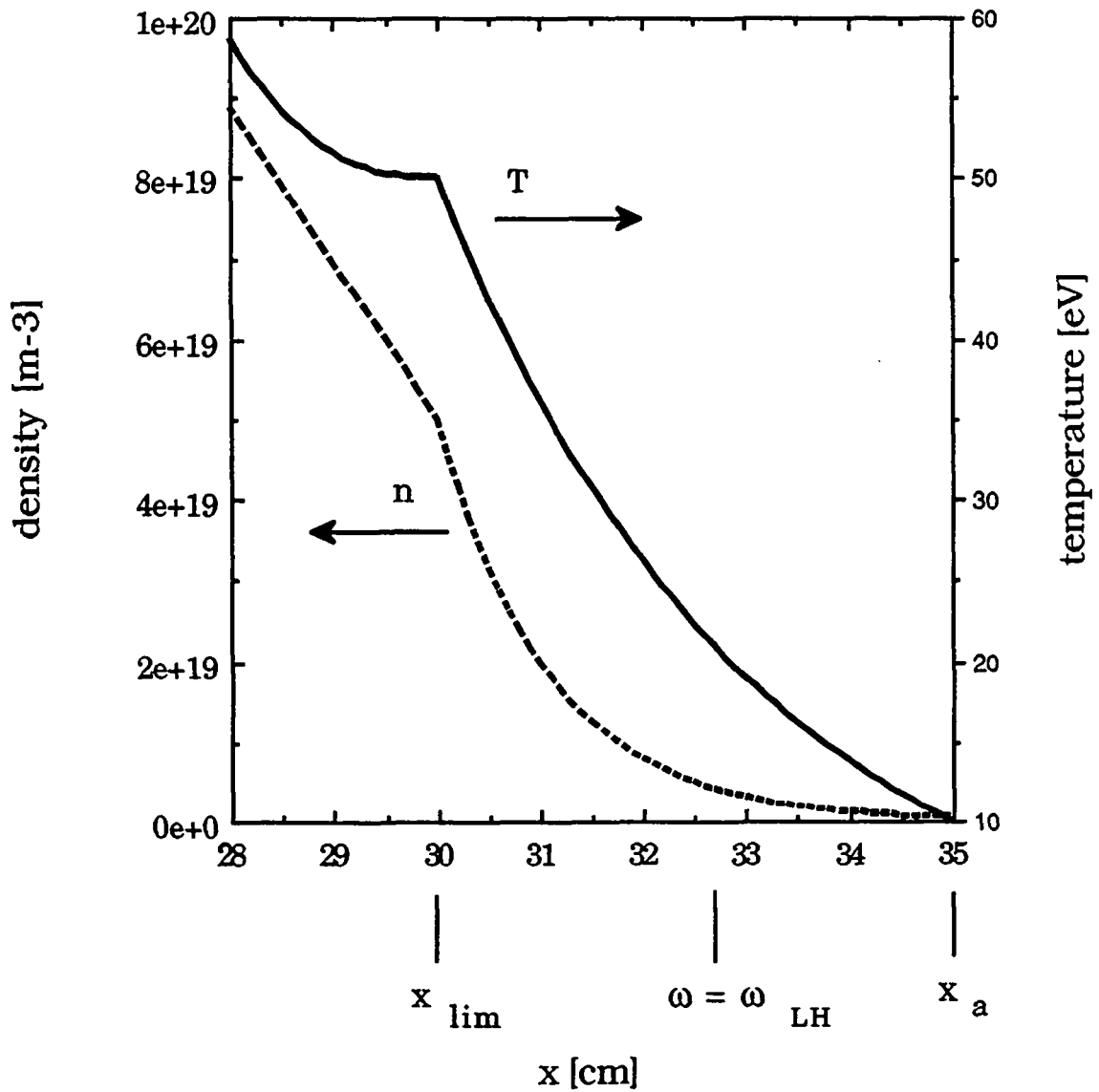


Fig.7.19: Typical density (dashed line) and temperature (continuous line) profiles for the simulation of the FTU tokamak scrape-off layer. The limiter is located at $x_{\text{lim}}=30\text{cm}$, the waveguide mouth at $x_a=35\text{cm}$ and the lower-hybrid layer at 32.7cm ($f=433\text{MHz}$).

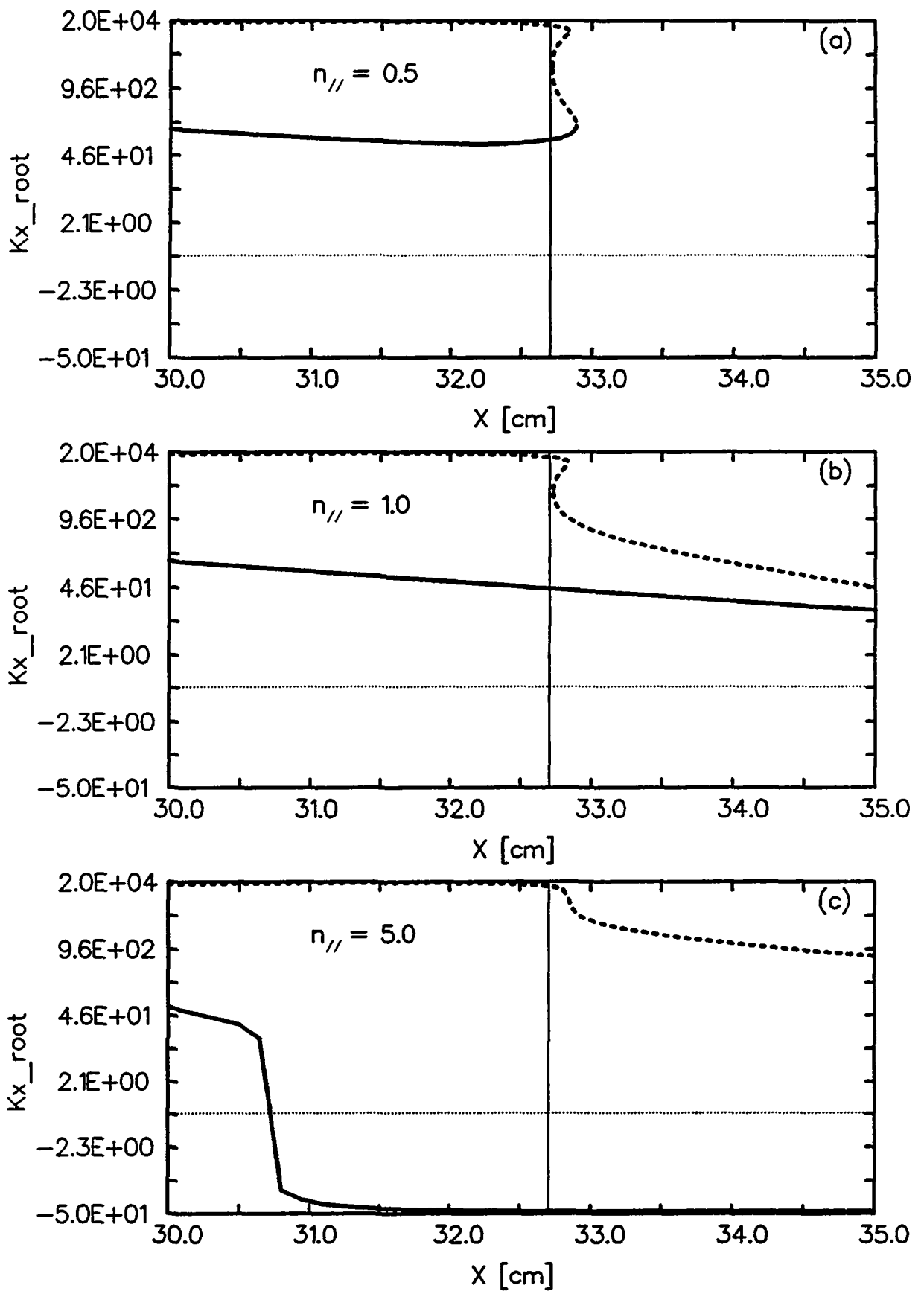


Fig.7.20: Dispersion relation for the parameters shown in Fig.7.19 with $B_0=7.9242$ and $R_0=93$ cm. The dispersion relations (DISPAL) obtained with three different values of $k_{//}$ are shown: (a) $n_{//}=0.5$; (b) $n_{//}=1.0$; (c) $n_{//}=5.0$. The vertical line at 32.7cm corresponds to the lower-hybrid layer. An "asinh" scale has been used for the vertical axis where $k_{x_root}=\text{sign}(k_x^2) \cdot |k_x^2|^{1/2}$.

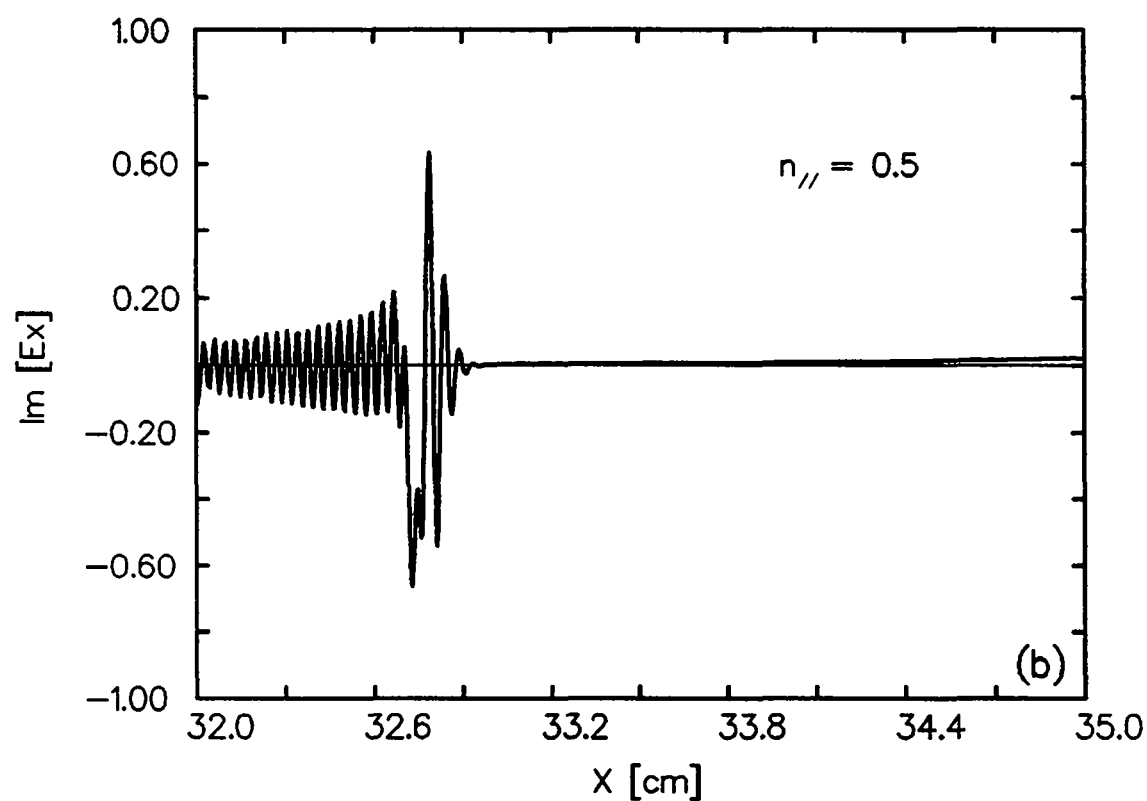
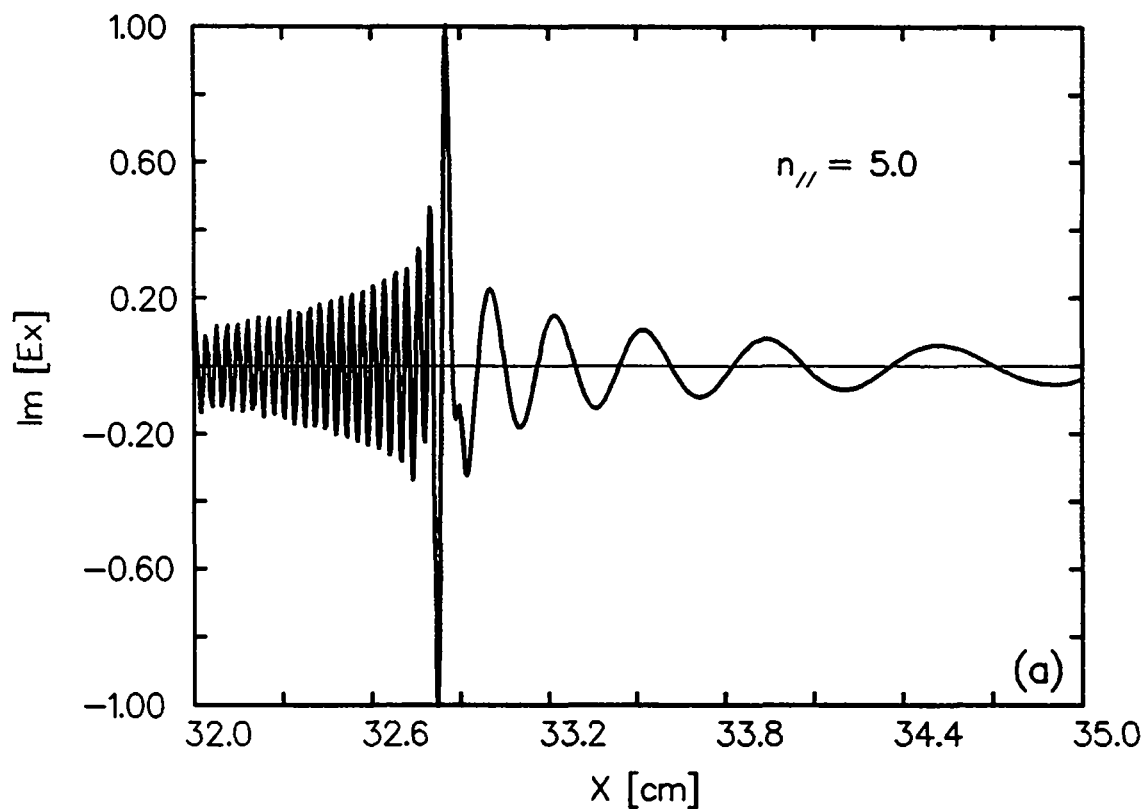


Fig.7.21: Imaginary part of E_x [a.u.] for the same parameters as in Fig.7.20 with $n_{//}=5.0$ (a) and $n_{//}=0.5$ (b). The same units, chosen such that $\max(E_x)=1$ in Fig.7.21a, have been used for both plots.

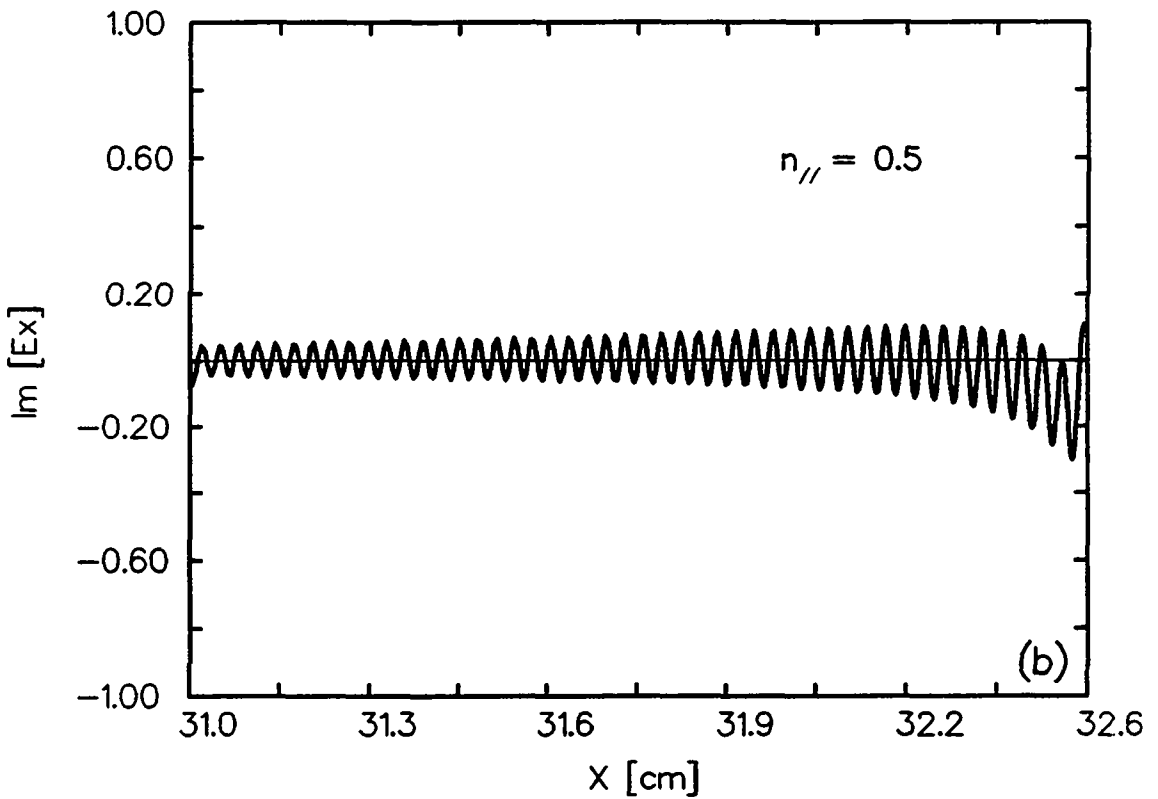
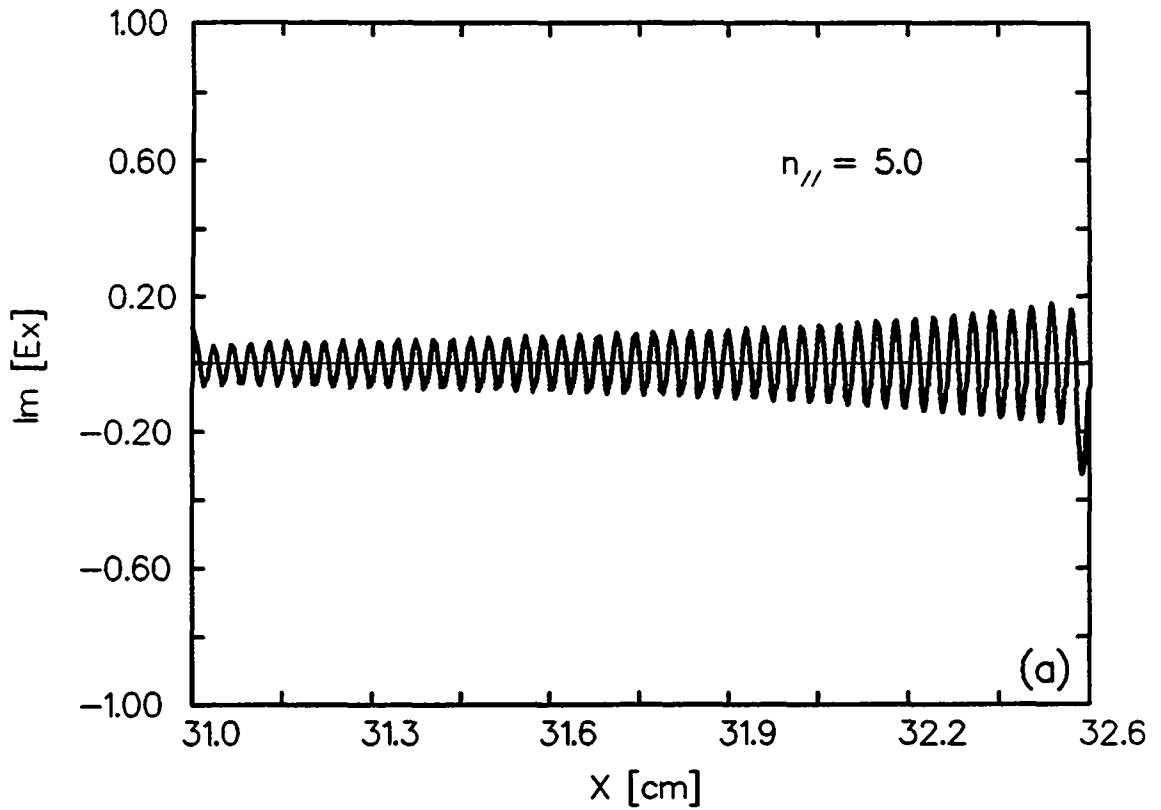


Fig.7.22: Imaginary part of E_x for the same parameters and using the same units as in Fig.7.21, but with $x_a=32.6$ cm. That is, the waveguide mouth is on the high field side of the lower-hybrid layer. (a) $n_{//}=5.0$ and (b) $n_{//}=0.5$.

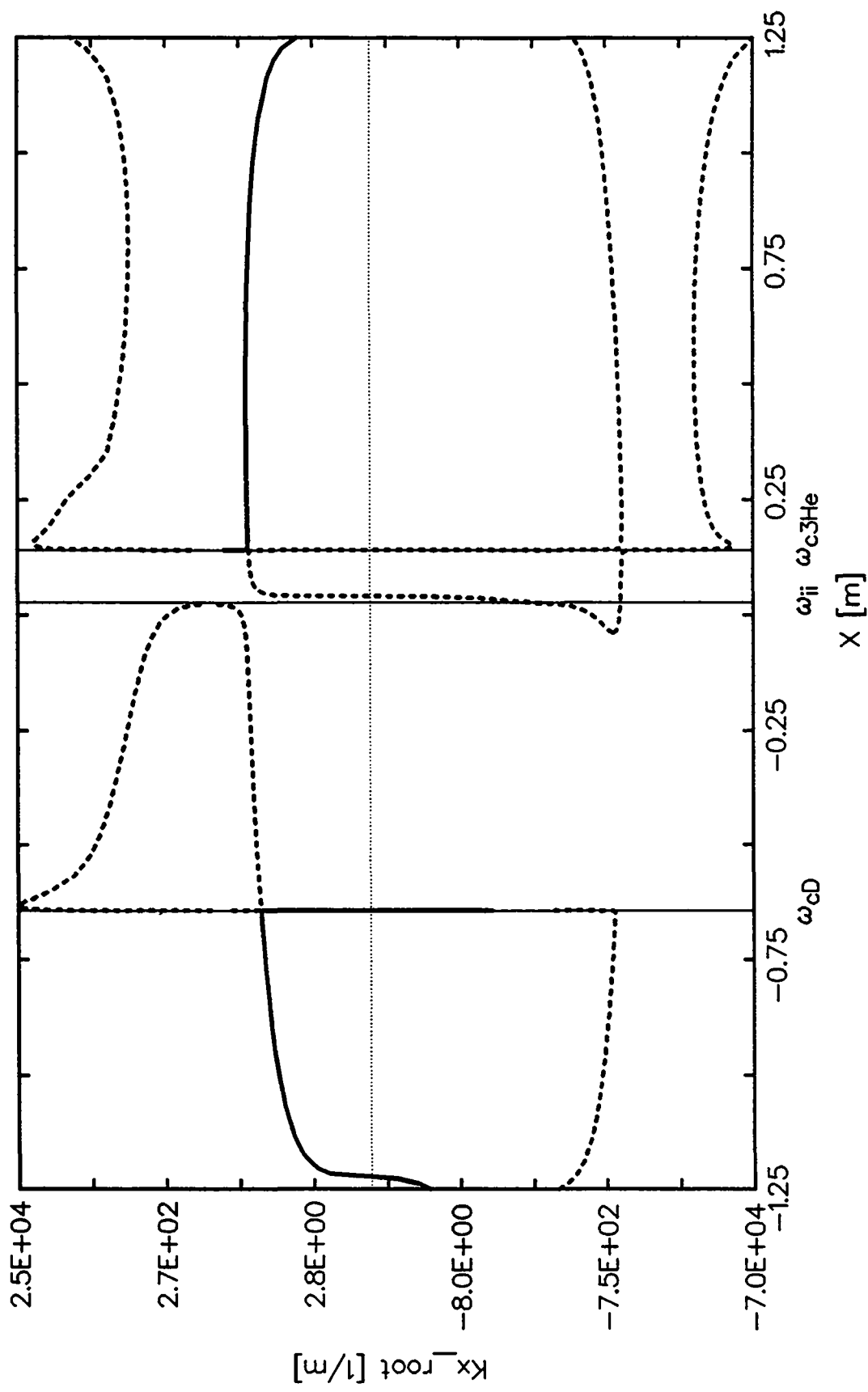


Fig.C.1: Dispersion relation obtained with DISPAL for a D-³He plasma with: $n_D=2.8 \cdot 10^{19} \text{m}^{-3}$, $n_{^3\text{He}}=2.06 \cdot 10^{18} \text{m}^{-3}$, $T_e=T_D=2 \text{keV}$, $T_{^3\text{He}}=600 \text{eV}$, $B_0=3.4 \text{T}$, $R_0=3 \text{m}$, $f=33 \text{MHz}$, $k_y=0$, $k_{||}=3 \text{m}^{-1}$, parabolic density and bi-quadratic temperature profiles. An "asinh scale" is used for the vertical axis, where $k_x \text{ root} = \text{sign}(k_x^2) \cdot |k_x^2|^{1/2} \text{m}^{-1}$. The locations of the deuterium (ω_{cD}) and ³He (ω_{c3He}) fundamentals and the cold ion-ion hybrid resonance (ω_{ii}) are shown.

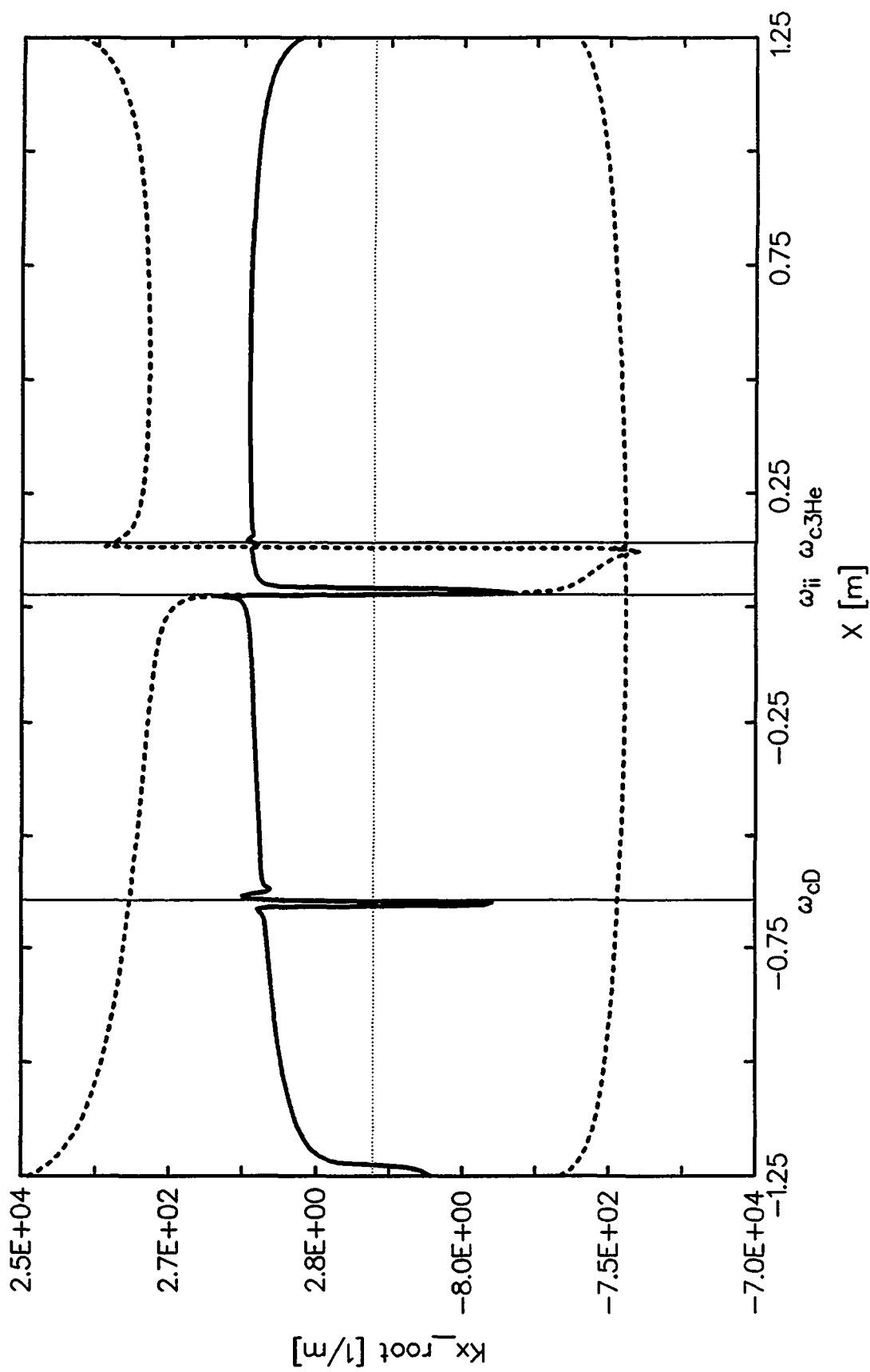


Fig.C.2: Dispersion relation for the same parameters as in Fig.C.1, but obtained with the code ISMENE, which corresponds to the second order expansion, which is why there are always three roots. In this case, $kx_root = \text{sign}(\text{Re}[k_x^2]) \cdot |\text{Re}[k_x^2]|^{1/2} \text{ m}^{-1}$.

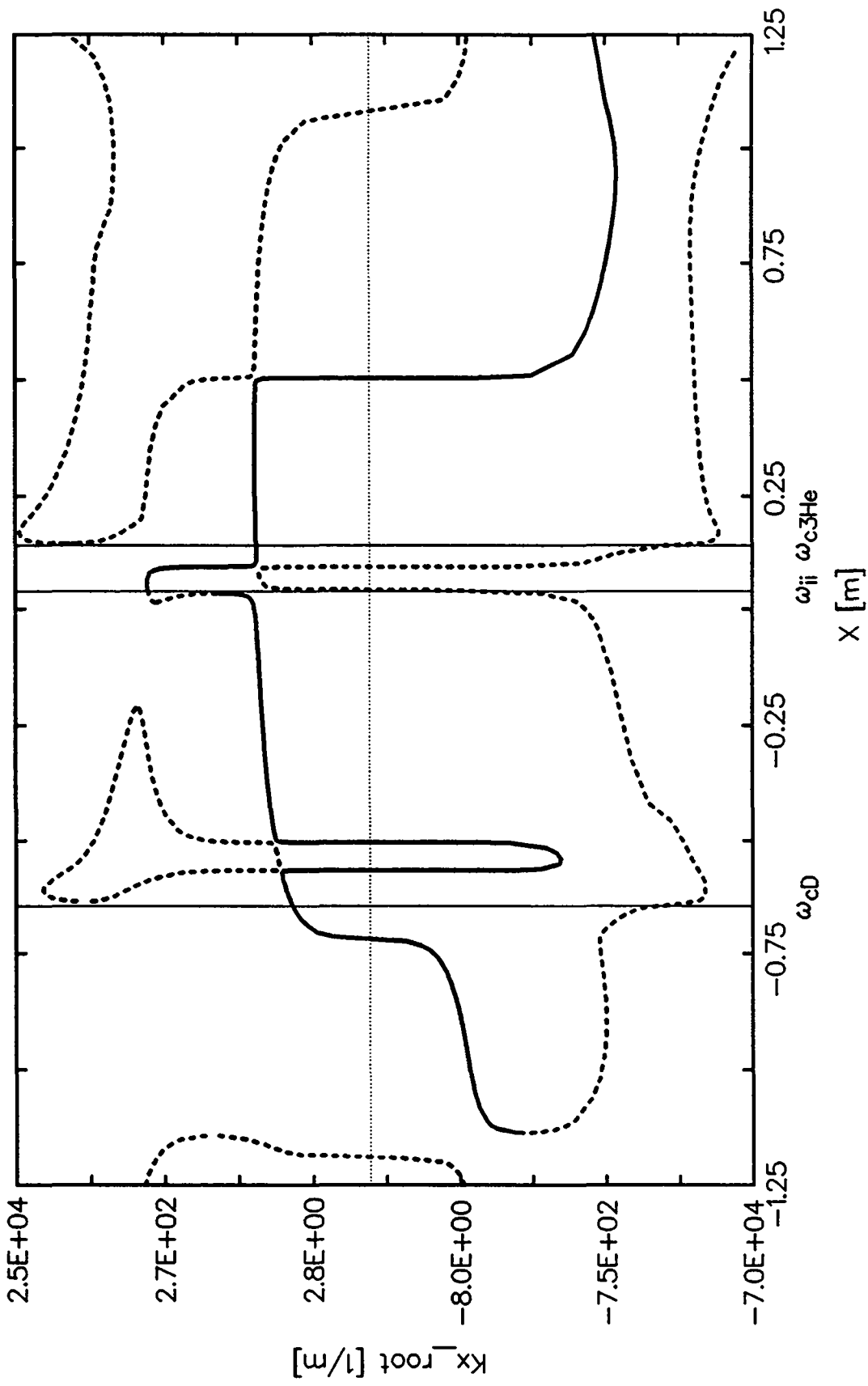


Fig.C.3: Dispersion relation (DISPAL) for the same parameters as in Fig.C.1, but with $k_{\parallel}=10m^{-1}$. Note that in this case, there is a region, at the left of $\omega=\omega_{ji}$, where there is only one propagatory mode. This means that the Bernstein wave is strongly damped in this region.

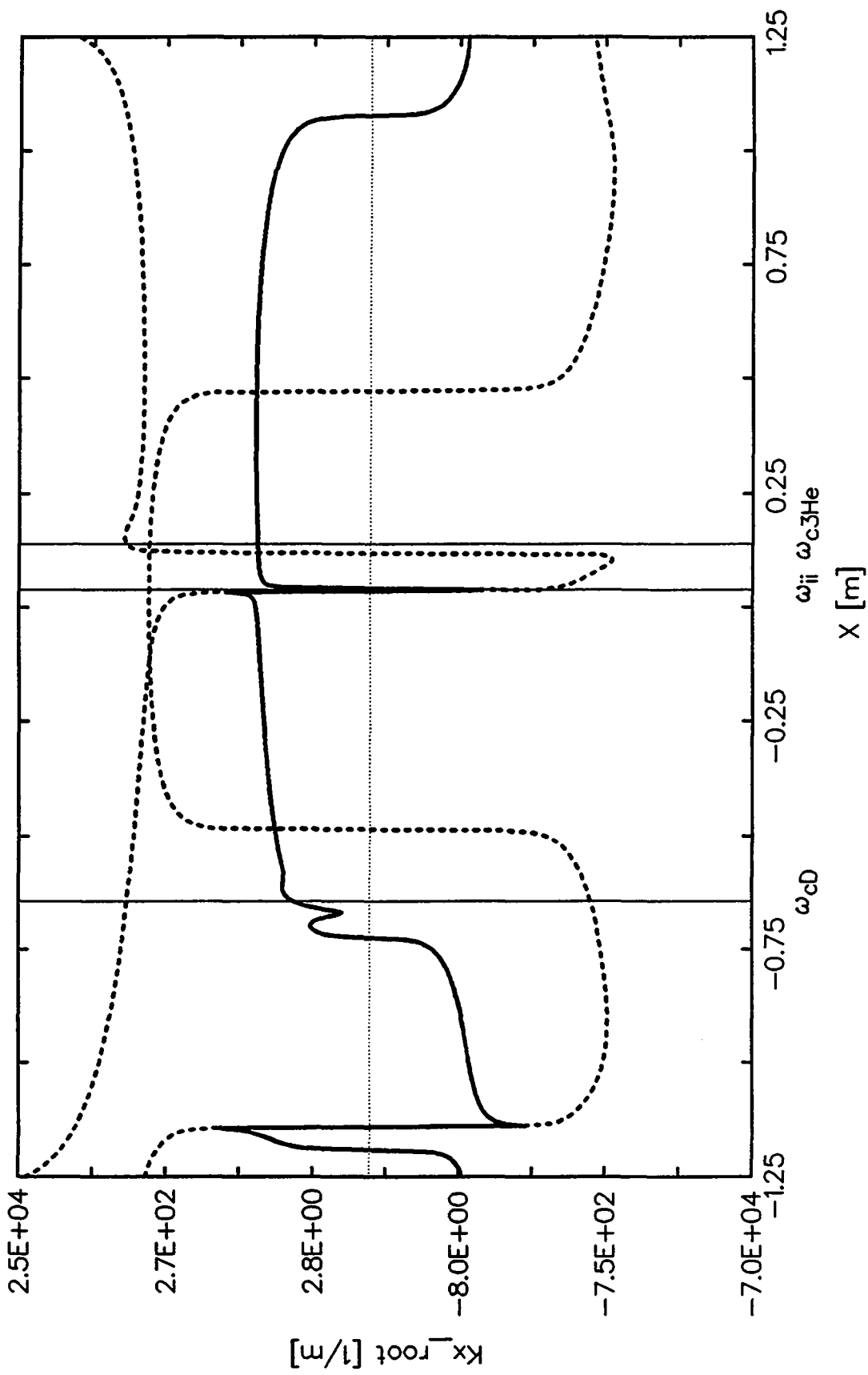


Fig.C.4: Dispersion relation for the same parameters as in Fig.C.3, but obtained with the code ISMENE. Note that with the local model, there is no longer a gap at the left of $\omega=\omega_{jj}$.

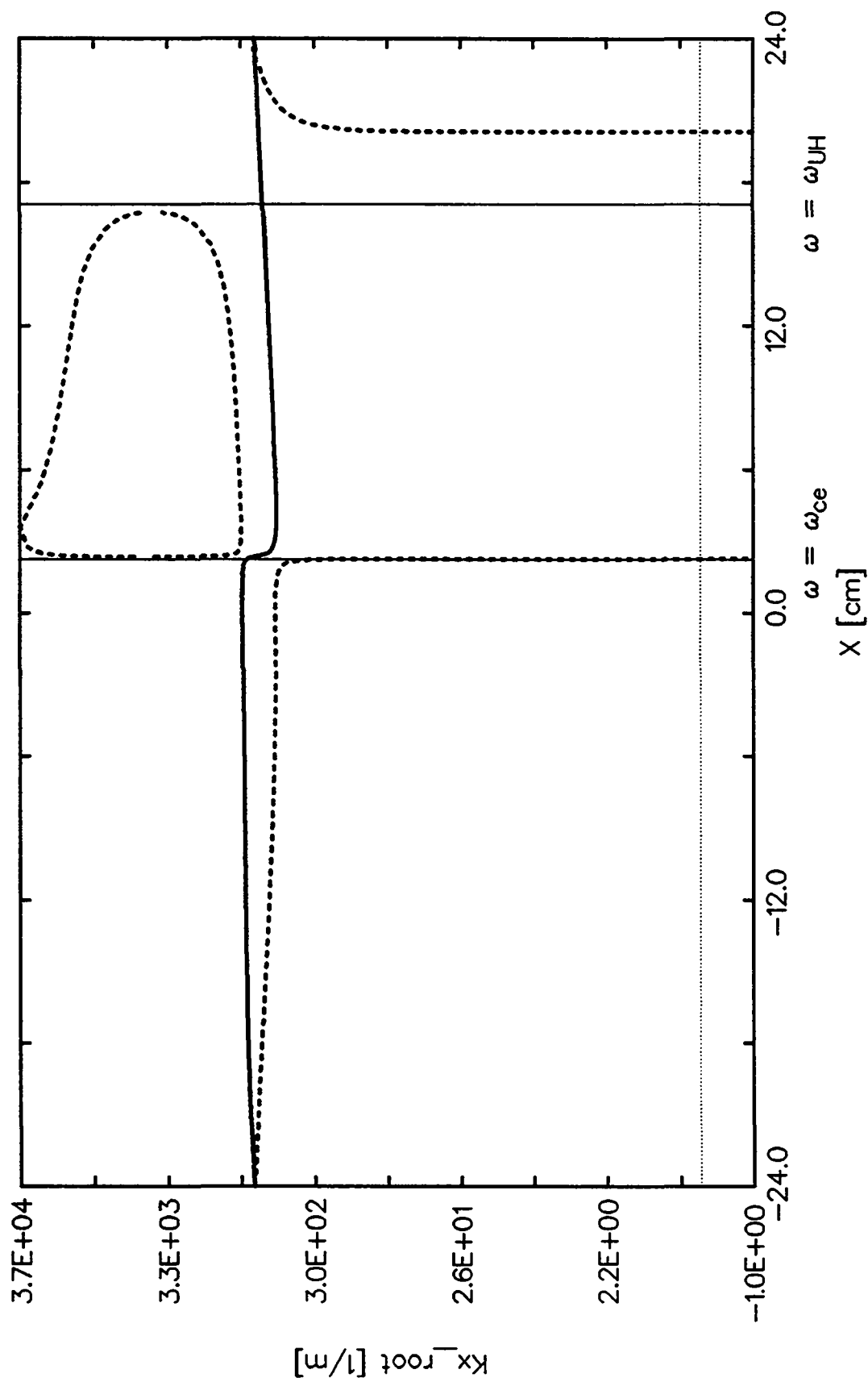


Fig.C.5: Dispersion relation in the electron cyclotron range of frequency near the fundamental and the upper-hybrid frequencies. Typical TCV parameters with $f=39$ GHz have been used.

CURRICULUM VITAE

Originaire de Zürich (ZH) et Vallorbe (VD), je suis né le 5 avril 1962 à Pompaples. J'ai suivi l'école primaire à Vallorbe, puis l'école secondaire et le gymnase à Lausanne. Après l'obtention de la maturité fédérale ès-sciences en 1980, j'ai vécu une année aux Etats-Unis, où j'ai effectué la dernière année de high school. De retour en Suisse, je suis entré à l'EPFL et y ai obtenu mon diplôme d'ingénieur physicien en janvier 1986. Depuis lors, je travaille en tant qu'assistant-doctorant au Centre de Recherches en Physique des Plasmas.